Carbon dioxide capture and utilization by VPSA: a sustainable development

Angel Eduardo Gutiérrez Ortega

UNIVERSITAT RAMON LLULL

DOCTORAL THESIS

Title	Carbon dioxide capture and utilization by VPSA: a sustainable development.
Presented by	Angel Eduardo Gutiérrez Ortega
Centre	IQS School of Engineering
Department	Chemical Engineering and Materials Science
Directed by	Dr. Rosa Nomen Ribé Dr. Rafael González Olmos

To my parents and my brothers, the reason for my existence and my belief,

To my girlfriend Joanna, the reason for my love,

To my country, the reason to continue struggling.

Dedicado a mis padres y mis hermanos, la razón de mi existencia y mi convicción,

A mi novia Joanna, la razón de mi amor,

Y a mi país, la razón de mi lucha continua.

Acknowledgements

I wish to express my gratitude to all the people who have helped me during this time. Among them and trying not to forget anyone, I would first like to thank Dr. Rafael González for his technical advice and his scientific interest during this project, Dr. Rosa Nomen and Dr. Julià Sempere for helping me in my first steps and for their constant support during the Ph.D. research. To the Dr. Fèlix Llovell my friend and colleague who encouraged me to work with patience and for giving me the first guidelines about how to write this manuscript. Also, I want to express my special thanks to Oriol Martinez for his faith in me and for motivating me to make this researching project come to fruition.

I want to express my sincere gratitude to my friends, Nabi Ferrer, Beatrice Ravasio and Martha Izaguirre for bringing me their friendship and smile when I most needed it. I sincerely want to thank Dr. Miguel Montes and Dr. Jose B. Parra for their help in all experimental work during this project, especially with the adsorption analyzer and magnetic suspension microbalance; without their advice, the experimental work of this project would have been much more difficult. Also, I want to mention the advice and unconditional support of Bernat Clofent and Astrid Tulleuda. I also cannot forget to mention the day-to-day assistance, happiness, support and teachings that I received from my partners of the GasN2 family with special mention to Albert Melis, Ezequiel de Paz, Guillermo Parladé, Héctor Santos and Javier Expósito who have made it possible to run out the project from the laboratory and into the real world.

I am also deeply grateful, for the help and collaboration from Adrià Espiell, Oriol Serracant, Alex Crespo, Alexandre Pallejà, Álvaro Domínguez, Carlos Arregui, Cástor Soto, Marc Lizandara and lastly, to all my friends in Catalunya and México. Finally, I would like to thank the GasN2 company and the Sarrià Chemical Institute, with the support of the Secretary of the Universities and Research from the Department of Economy and Knowledge of the Generalitat de Catalunya and the European Social Fund for giving me the opportunity to do my PhD studies under the Industrial Doctorate Plan program 2014 DI 057, without their help this work would not have been possible.

Unió Europea
Fons Social Europeu
L'FSE inverteix en el teu futur

Generalitat de Catalunya
Departament d'Empresa
i Coneixement

Agradecimientos

Deseo expresar mi gratitud a todas las personas que me han ayudado durante este tiempo. Entre ellos y tratando de no olvidar a nadie, me gustaría agradecer al Dr. Rafael González por su asesoramiento técnico y su interés científico durante este proyecto, a la Dra. Rosa Nomen y al Dr. Julià Sempere por ayudarme en mis primeros pasos y por su constante apoyo durante la investigación doctoral. A el Dr. Fèlix Llovell mi amigo y colega por darme las primeras pautas sobre cómo escribir este manuscrito por animarme a trabajar con paciencia. Además, quiero expresar mi agradecimiento especial a Oriol Martínez por su fe en mí y por motivarme para hacer que este proyecto de investigación se realizase.

Quiero expresar mi sincera gratitud a mis amigos, Nabi Ferrer, Beatrice Ravasio y Martha Izaguirre por brindarme su amistad y sonrisa cuando más la necesitaba. Deseo sinceramente agradecer al Dr. Miguel Montes y al Dr. José B. Parra por su ayuda en todo el trabajo experimental durante este proyecto, especialmente con el analizador de adsorción y la microbalanza de suspensión magnética; sin su asesoramiento, el trabajo experimental de este proyecto hubiera sido mucho más difícil. Además, quiero mencionar los consejos y el apoyo incondicional de Bernat Clofent y Astrid Tulleuda. Tampoco puedo olvidar mencionar la asistencia diaria, la alegría, el apoyo y las enseñanzas que recibí de mis compañeros de la familia GasN2, con una mención especial a Albert Melis, Ezequiel de Paz, Guillermo Parladé, Hector Santos y Javier Expósito que han hecho posible ejecutar este proyecto desde el laboratorio hasta el mundo real.

También estoy profundamente agradecido por la ayuda y colaboración de Adrià Espiell, Oriol Serracant, Alex Crespo, Alexandre Pallejà, Álvaro Domínguez, Carlos Arregui, Cástor Soto y Marc Lizandara. Por último, quisiera agradecer a todos mis amigos en Cataluña y México por sus buenos deseos. Finalmente, me gustaría agradecer a la compañía GasN2 y al Instituto Químico de Sarrià que con el apoyo de la Secretaría de Universidades e Investigación del Departamento de Economía y Conocimiento de la Generalitat de Cataluña al y el Fondo Social Europeo por brindarme la oportunidad de realizar mis estudios de doctorado bajo el plan de Doctorado Industrial 2014 DI 057, sin su ayuda en este trabajo no hubiera sido posible.

Unió Europea
Fons Social Europeu
L'FSE inverteix en el teu futur

Generalitat de Catalunya
Departament d'Empresa
i Coneixement

Abstract

The continuously increasing share of renewable energy sources and European Union targets for carbon dioxide (CO_2) emission reduction need significant changes both on a technical and regulatory level. Carbon dioxide capture and utilization (CCU) is an effective method for achieving CO_2 mitigation while simultaneously keeping energy supplies secure. While the demand for reduction in CO_2 emissions is increasing, the improvement of energy-efficiency and the cost of CO_2 capture processes remains a limiting factor for industrial applications. The present work studies the Vacuum Pressure Swing Adsorption process (VPSA) using high selectivity adsorbents for separating CO_2 from flue gas as an alternative method to the traditional absorption process with amines.

A screening analysis for CO_2 capture was conducted on ten commercial adsorbents, including carbon molecular sieves (CMS) and zeolites. The textural properties, the adsorption capacities and the adsorbent cyclic behaviors were determined to compare their performance in the context of CO_2 separation from nitrogen (N_2). Subsequently, the single component adsorption isotherms were measured in a magnetic suspension balance at four different temperatures (283, 298, 232 and 323 K) and over a large range of pressures (from 0 to 10 bara). Data on the pure component isotherms were correlated using the Toth, Sips and Dual Site Langmuir (DSL) models.

Three laboratory units were designed and built to perform the VPSA experiments. The first was used for the production and control of CO_2 and N_2 gas mixtures at a maximum pressure of 9 bara. Adsorption equilibrium measurements with a mixture that resembles the composition of combustion gases (15/85% CO_2/N_2 v/v) were obtained using the second unit that was built. Afterwards, the Aspen Adsorption® program was used to simulate the experimental system, where the predictions of the DSL model agree with the breakthrough curves and the temperature profiles of the experimental fixed bed results. In addition, dynamic studies were performed to evaluate the zeolites 5ABL and 13XBL using a discontinuous VPSA process for the CO_2 separation of N_2. The process was automated and operated with a PLC interface, using a control strategy developed in this work. Based on the comparison results of the zeolites, it was found that the 13XBL zeolite was the one most suitable for the proposed VPSA process. The experimental results were verified by numerical simulations in the Aspen Adsorption® software and the validated model was used to perform a two-factor complete design of experiments (2^6) using 13XBL simulations in a discontinuous configuration.

The third experimental unit was built with three adsorption columns which included the developed control strategy and the recirculation of N_2 and CO_2 rich streams. Three experiments were carried out using zeolite 13XBL as an adsorbent for the proposed 8-step VPSA cyclic process by changing the control parameters of the automated process. Through the experiments, the objectives were achieved in terms of CO_2 purity (> 90%) and energy consumption (> 2.5 kWh/kgCO_2). Based on the experimental and simulated results, a pilot-scale demonstration plant for CO_2 capture from flue gas in an existing industrial boiler in a Spanish company was carried out.

The pilot-scale CO_2 capture plant consisted of a pre-treatment process for flue gases, a VPSA unit coupled with a dehumidification unit and an industrial application for the use of CO_2. In the pretreatment unit the flue gases were cooled from 70°C to 25°C and then denitrified. In the dehumidification unit, the water vapor was removed from the denitrified gas by adsorption with alumina. Subsequently, the three columns' eight-step VPSA process developed with zeolite 13XBL was used. The results were a product purity of 85 to 95% of CO_2, a recovery of 48 to 56%, a productivity of 0.20 to 0.25 $g_{CO2}/(g_{ads} \cdot h)$ and an energy consumption of 1.48 kWh/kg_{CO2}. The recovered CO_2 was then used to replace the use of mineral acids in the pH regulation stage of the existing wastewater treatment plant. Therefore, it is concluded that the developed process is an effective alternative to separate the CO_2 from the emission points of industrial combustion gases and to use the recovered CO_2 as raw material for industrial applications. The use of CO_2 captured in these emission sources has two clear advantages. On the one hand, it reduces the CO_2 emissions to the atmosphere. On the other hand, it allows the reuse and transformation of an environmental pollutant into neutral compounds.

Resumen

El continuo incremento en el uso de las energías renovables y los objetivos para la reducción de las emisiones de dióxido de carbono (CO_2) requieren cambios significativos tanto a nivel técnico como a nivel normativo. La captura y utilización de dióxido de carbono (CCU, por sus siglas en inglés) es un método eficaz para lograr la mitigación del CO_2 y al mismo tiempo mantener de forma segura los suministros de energía. Si bien la demanda en la reducción de las emisiones de CO_2 está aumentando, la eficiencia energética y el costo de los procesos de captura de CO_2 siguen siendo un factor limitante para las aplicaciones industriales. En el presente trabajo se estudia el uso del proceso de adsorción por oscilación de presión y vacío (VPSA, por sus siglas en inglés) con adsorbentes de alta selectividad para separar el CO_2 de los gases de combustión, como un método alternativo al proceso de absorción tradicional con aminas.

Se realizó una selección entre diez adsorbentes comerciales para la captura de CO_2, incluidos los tamices moleculares de carbón (CMS, por sus siglas en inglés) y las zeolitas. Se determinaron las propiedades texturales, la capacidad de adsorción y el comportamiento cíclico de los adsorbentes para comparar su comportamiento en la separación del dióxido de carbono del nitrógeno. Posteriormente, se midieron las isotermas de adsorción de un solo componente en la balanza de suspensión magnética a cuatro temperaturas diferentes (283, 298, 232 y 323 K) y en un amplio margen de presiones (de 0 a 10 bara). Los datos sobre las isotermas de componentes puros se correlacionaron utilizando los modelos Toth, Sips y Dual Site Langmuir (DSL).

Se diseñaron y construyeron tres unidades de laboratorio para realizar la experimentación del proceso VPSA. La primera unidad se usó para la producción y el control de mezclas gaseosas de CO_2 y N_2 a una presión máxima de 9 bara. En la segunda unidad se llevaron a cabo las mediciones de los equilibrios de adsorción con una mezcla de composición semejante a la de los gases de combustión (15/85% de CO_2/N_2 v/v). Con el programa Aspen Adsorption® se simuló el sistema experimental, obteniendo que las predicciones del modelo DSL reproducen suficientemente bien los resultados experimentales de las curvas de ruptura y los perfiles de temperatura en el lecho fijo. Además, se hicieron estudios dinámicos para evaluar las zeolitas 5ABL y 13XBL usando el proceso VPSA discontinuo para la separación CO_2 de N_2. La unidad dos se dotó de un sistema de control con una interfaz PLC que facilita su operación y automatización, usando una estrategia de control desarrollada en este trabajo. En base a los resultados obtenidos con la unidad dos y su simulación, se encontró que la zeolita

13XBL era la que la más adecuada para el proceso VPSA propuesto. Los resultados experimentales se usaron para alimentar el diseño de la unidad dos en Aspen Adsorption® y validar el modelo usado que a su vez se utilizó para realizar un diseño completo de experiencias de dos factores (2^6) en configuración discontinua.

La tercera unidad experimental consta de tres columnas de adsorción donde se incluyó la estrategia de control desarrollada para la unidad dos y se incluyó la recirculación de las corrientes ricas en N_2 y CO_2. Se llevaron a cabo tres experimentos en el proceso VPSA cíclico de 8 pasos cambiando los parámetros de control del proceso automatizado y usando la zeolita 13XBL como adsorbente. Se logró satisfacer los objetivos en términos pureza de CO_2 (>80%) y consumo energético (<2.5 kWh/kg_{CO2}). Sobre la base de los resultados experimentales y simulados, se realizó una demostración a escala piloto de la captura de CO_2 del gas de combustión de una caldera de vapor en una planta industrial situada en la provincia de Barcelona.

La planta piloto de captura de CO_2 consta de un proceso de pretratamiento de los gases de combustión, una unidad VPSA acoplada con una unidad de deshumidificación y una aplicación industrial para el uso del CO_2. En la unidad de pretratamiento, los gases de combustión se enfriaron de 70ºC a 25ºC y desnitrificaron. En la unidad de deshumidificación, se eliminó el vapor de agua del gas desnitrificado mediante adsorción con alúmina. Posteriormente, se empleó el proceso VPSA de ocho pasos con tres columnas usando zeolita 13XBL, en la que se obtuvo una corriente enriquecida de CO_2 de 85 a 95% de pureza de CO_2, con una recuperación del 48 a 56%, una productividad de 0.20 a 0.25 $g_{CO2}/(g_{ads} \cdot h)$ y un consumo energético de 1.48 kWh/ kg_{CO2}. El CO_2 recuperado se usó para reemplazar el uso de ácidos minerales en la etapa de regulación del pH de la planta de tratamiento de aguas residuales existente en la fábrica. Por lo tanto, el proceso desarrollado es una alternativa efectiva para separar el CO_2 de los puntos de emisión de gases de combustión industrial y utilizar el CO_2 recuperado como materia prima para aplicaciones industriales. El uso de CO_2 capturado en estas fuentes de emisión tiene dos ventajas claras. Por un lado, redujeron las emisiones de CO_2 a la atmósfera. Por otro lado, permitió reutilizar y transformar un contaminante ambiental en compuestos neutros.

Resum

El continu increment en l'ús de les energies renovables i els objectius per a la reducció de les emissions de diòxid de carboni (CO_2) requereixen canvis significatius tant a nivell tècnic com a nivell normatiu. La captura i utilització de diòxid de carboni (CCU, per les sigles en anglès) és un mètode eficaç per aconseguir la mitigació del CO_2 i al mateix temps mantenir de forma segura els subministraments d'energia. Si bé la demanda a la reducció de les emissions de CO_2 està augmentant, l'eficiència energètica i el cost dels processos de captura de CO_2 segueixen sent un factor limitant per a les aplicacions industrials. En el present treball s'estudia l'ús del procés d'adsorció per oscil·lació de pressió i buit (VPSA, per les sigles en anglès) amb adsorbents d'alta selectivitat per separar el CO_2 dels gasos de combustió, com un mètode alternatiu al procés d'absorció tradicional amb amines.

Es realitza un estudi preliminar mitjançant Anàlisi Tèrmica per determinar la capacitat d'adsorció i el comportament cíclic de la captura de CO_2 per deu adsorbents comercials, inclosos els tamisos moleculars de carboni (CMS) i les zeolites. L'anàlisi es va fer amb CO_2 pur, N_2 pur i mescles dels dos gasos en la proporció 15%/85% que correspon a la composició d'un gas de combustió normal; s'usen les zeolites comercials 13X, 5A, 4A sense i amb aglomerants i tres tamisos moleculars de carboni (CMS) en l'interval de pressió de 0 a 10 bar i a 283K, 298K, 232K i 323 K de temperatura. Els resultats s'han ajustat amb els models Toth, Sips i Dual Site Langmuir (DSL).

Es va realitzar una selecció entre deu adsorbents comercials per a la captura de CO_2, inclosos els tamisos moleculars de carbó (CMS, per les sigles en anglès) i les zeolites. Es van determinar les propietats texturals, la capacitat d'adsorció i el comportament cíclic dels adsorbents per comparar el seu comportament a la separació del diòxid de carboni del nitrogen. Posteriorment, es van mesurar les isotermes d'adsorció d'un sol component en la balança de suspensió magnètica a quatre temperatures diferents (283, 298, 232 i 323 K) i en un ampli marge de pressions (de 0 a 10 bara). Les dades sobre les isotermes de components purs es van correlacionar utilitzant els models Toth, Sips i Dual Site Langmuir (DSL). Es van dissenyar i construir tres unitats de laboratori per realitzar l'experimentació del procés VPSA. La primera unitat es va usar per a la producció i el control de mescles gasoses de CO_2 i N_2 a una pressió màxima de 9 bara. En la segona unitat es van dur a terme la determinació dels equilibris d'adsorció amb una barreja de composició semblant a la dels gasos de combustió (15/85% de CO_2/N_2 v/v). Amb el programa Aspen Adsorption® es va simular el sistema experimental,

obtenint que les prediccions del model DSL reprodueixen suficientment bé els resultats experimentals de les corbes de ruptura i els perfils de temperatura en el llit fix. A més, es van fer estudis dinàmics per avaluar les zeolites 5ABL i 13XBL usant el procés VPSA discontinu per a la separació CO_2 de N_2. La unitat dos es va dotar d'un sistema de control amb una interfície PLC que facilita la seva operació i automatització, usant una estratègia de control desenvolupada en aquest treball. En base als resultats obtinguts amb la unitat dos, tant experimentals com simulats, es va trobar que la zeolita 13XBL era la més adequada per al procés VPSA proposat. Els resultats experimentals es van emprar per alimentar el disseny de la unitat dos a Aspen Adsorption® i validar el model usat que al seu torn es va utilitzar per realitzar un disseny complet d'experiències de dos factors (2^6) en configuració continua.

La tercera unitat experimental consta de tres columnes d'adsorció on es va incloure l'estratègia de control desenvolupada per la unitat dos i es va incloure la recirculació dels corrents rics en N_2 i CO_2. Es van dur a terme tres experiments del procés VPSA cíclic de 8 passos canviant els paràmetres de control del procés automatitzat i usant la zeolita 13XBL com adsorbent. Es va aconseguir satisfer els objectius en termes puresa de CO_2 (> 80%) i consum energètic (<2.5 kWh/kg_{CO2}). Sobre la base dels resultats experimentals i simulats, es va realitzar una demostració a escala pilot de la captura de CO_2 del gas de combustió d'una caldera de vapor en una planta industrial a situada a la província de Barcelona. La planta pilot de captura de CO_2 consta d'un procés de pretractament dels gasos de combustió, una unitat VPSA acoblada amb una unitat de deshumidificació i una aplicació industrial per a l'ús del CO_2. A la unitat de pretractament, els gasos de combustió es van refredar de 70ºC a 25ºC i es van desnitrificar. A la unitat de deshumidificació, es va eliminar el vapor d'aigua del gas desnitrificat mitjançant adsorció sobre alúmina. Posteriorment, es va emprar el procés VPSA de vuit passos amb tres columnes usant zeolita 13XBL, en la qual es va obtenir un corrent enriquit de CO_2 de 85 a 95% de puresa de CO_2, amb una recuperació del 48 a 56%, una productivitat de 0.20- 0.25 $g_{CO2}/(g_{ads}\cdot h)$ i un consum energètic de 1.48 kWh/kg_{CO2}. El CO_2 recuperat es va usar per reemplaçar l'ús d'àcids minerals en l'etapa de regulació del pH de la planta de tractament d'aigües residuals existent a la fàbrica. Per tant, el procés desenvolupat és una alternativa efectiva per separar el CO_2 dels punts d'emissió de gasos de combustió industrial i utilitzar el CO_2 recuperat com a matèria primera per a aplicacions industrials. L'ús de CO_2 capturat en aquestes fonts d'emissió té dos avantatges clars. D'una banda, es van reduir les emissions de CO_2 a la atmosfera. De l'altra, va permetre reutilitzar i transformar un contaminant ambiental en compostos neutres.

Contents

List of figures

List of tables

Symbols and nomenclature

μ	Dynamic viscosity of gas mixture, Pa s
μ_g	Viscosity of gas mixture, cP
ACs	Activated carbons
b	Affinity constant parameter, 1/bara
BET	Brunauer-Emmett-Teller
CCS	Carbon Capture and Storage
CCU	Carbon Capture and Utilization
c_i	Molar fraction of component i
C_{in}	Inlet concentrations, % v/v
CMS	Carbon molecular sieves
CO_2	Carbon dioxide
C_{out}	Outlet concentrations, % v/v
C_{pai}	Specific heat capacity of the adsorbed gas, MJ/kmol K
C_{ps}	Specific heat capacity of the adsorbent, MJ/kmol K
C_{pw}	Specific heat capacity of the wall, MJ/kmol K
C_{vg}	Specific gas phase heat capacity at constant volume, MJ/kmol K
DA	Dubinin-Astakhov
D_B	Internal diameter of column, m
DEA	Diethanolamine
D_L	Dispersion coefficient, m^2/s
DP	Depressurization
DSC	Differential scanning calorimetry
DSL	Dual-site Langmuir model
EOR	Enhanced Oil Recovery
EP	Provided pressure equalization
ER	Received pressure equalization
e_{TSA}	Energy consumption
EU	European Union
FD	Feed
FP	Pressurization
GHG	Greenhouse gas
h_b	Heat transfer coefficient between column and ambient, W/m^2 K
h_t	Heat transfer coefficient between void tank and ambient, W/m^2 K
HTC	Heat transfer coefficient between gas and solid, W/m^2 K
h_w	Heat transfer coefficient between gas and wall W/m^2 K
IPCC	The International Panel of Climate Change
k_g	Heat conductivity of gas, W/m K
k_s	Heat conductivity of adsorbent, W/m K
k_w	Heat conductivity of wall, W/m K
LES	Required stoichiometric capacity
LUB	Length of unused bed
m_{ads}	Mass of the adsorbed phase
MEA	Monoethanolamide
MOFs	Metal organic frameworks
m_s	Mass of adsorbent, mg
MTC	Mass transfer coefficient
MTC_i	Mass transfer coefficient of component i, 1/s
MTZ	Mass transfer zone
MW	Adsorbate molecular weight, g/mol
M_w	Molecular weight of gas mixture, kg/kmol
n	Sips parameter
n	Component loading
NO_X	Nitrogen oxides
P	Gas pressure, bar (a)
P	Gas pressure, bar (a)
PC	Power consumption
p_i	Partial pressure of component i, bar (a)
Pr	Productivity
PR	Purge
PSA	Pressure Swing Adsorption
P_T	Adsorption pressure
P_V	Vacuum pressure on the regeneration step
q	Absolute amount adsorbed, mmol/g
Q_{EX}	Stop point by vacuum pump flowrate
q_{exc}	Excess amount adsorbed, mmol/g
Q_{FD}	Feed flowrate
q_i	Adsorbent loading of component i per unit mass of adsorbent, kg/kmol
q_i^*	Adsorbent in equilibrium with its partial pressure in gas phase, kg/kmol
Q_{RN}	Rinse flowrate
q_s	Saturation capacity, mmol/g
q_{TGA}	Adsorption capacity, mmol/g
Q_V	Vacuum flowrate
R	Ideal gas law constant, kJ/K·mol
R	Universal gas constant, $(kPa\ m^3)/(kmol\ K)$
r	Radial co-ordinate of the adsorbent, m
R&D	Research and Development
r_{AB}	Characteristic length, Å
Re	Reynolds number

LDF	Linear driving force kinetic model
RG	Regeneration
RH	Relative humidity
RN	Rinse
r_p	Particle radius, m
S_{BET}	Specific surface areas were calculated using the BET method, cm^2/g
Sc	Schmidt number
SC-CO_2	Supercritical CO_2
S_{eq}	Equilibrium selectivity
S_{FD}	Stop feed point
S_{kin}	Kinetic selectivity
SO_X	Sulfur oxide
S_{PR}	Stop purge point
S_{RN}	Stop rinse point
t	Toth heterogeneity parameter
T	Gas temperature, K
Tads	Adsorption temperature, K
t_{cycle}	Total cycle time
T_{env}	Environmental temperature, K
TGA	Thermogravimetric analysis
TRLs	Technology Readiness Level
T_s	Adsorbent temperature, K
TSA	Temperature swing adsorption
T_t	Column jacket temperature
t_V	Desorption time at the vacuum pressure
T_w	Column wall temperature, K
UNFCCC	United Nations Framework Convention on Climate Change
V_{ads}	Adsorbed volume of the gas, L
VDA_{CO2}	Narrow micropore volumes obtained from the CO_2 applying DA equation, cm^3/g
v_g	Superficial gas velocity, m/s
V_m	Molar volume, L
VPSA	Vacuum Pressure Swing Adsorption
VSA	vacuum swing adsorption
w_i	Working capacity
W_r	Wall thickness, m
z	Axial distance coordinate, m
α_p	Specific particle surface area per unit length of bed, 1/m
ΔH_{ads}	Adsorption heat, kJ/mol
ΔH_{des}	Desorption heat, kJ/mol
ΔH_i	Enthalpy of adsorption for component i, kJ/mol
ΔH_{indium}	Melting heat of indium, J/gindium
ΔT_W	Difference between the adsorption and desorption temperature
ρ	Gas specific density, kg/m^3
ρ_b	Bulk density of adsorbent, kg/m^3
ρ_g	Density of the gas, g/L
ρ_g	Gas molar density, $kmol/m^3$
ρ_L	Adsorbed phase density, g/L
ρ_w	Column wall density, kg/m^3
ψ	Particle shape factor
ε_i	Bed voidage
ε_p	Particle voidage

1. Introduction

Carbon dioxide (CO_2) emissions result in the global warming effect, which is one of the most urgent problems that threatens the habitability of the Earth. Although some governmental laws and protocols have limited the amount of emissions, the rates remain so high that the accumulation of CO_2 has caused the global climate to change (Leung et al., 2014). Efforts are being made continuously to limit the degree of further climate changes due to the increase in greenhouse gas (GHG) emissions. The International Panel of Climate Change (IPCC) estimates that by the year 2100, the CO_2 content in the atmosphere shall reach 570 ppmv, the sea level will increase by 3.8 m and the global mean temperature will rise by 2ºC (IPCC, 2014). Continued emission of GHG will cause further warming and long-lasting changes in all components of the climate system, increasing the likelihood of severe, pervasive and irreversible impacts for people and ecosystems (see Figure 1).

Limiting climate change would require substantial and sustained reductions in GHG emissions. In December 2015, the Paris Agreement was signed by 195 Parties at the United Nations Framework Convention on Climate Change (UNFCCC) where the Chinese and US governments made their historic participation. The purpose of the Paris agreement is to prevent the global temperature from rising by 2 ºC above preindustrial levels within this century, and try to control the rise to no more than 1.5 ºC (UNFCCC. Conference of the Parties (COP), 2015). The European Union (EU) has committed to achieve an economy-wide domestic target of at least 40% GHG emission reductions (from 1990 levels) by 2030 and at least 80% GHG reductions by 2050. This should allow the EU to contribute in keeping global warming well below 2°C (Fortunato and Heuer, 2018). However, on the 1st of June 2017, the U.S. declared to withdraw from the Paris Agreement. Trump's formal declaration of withdrawal caused worldwide reaction. Trump will use the withdrawal to build his political reputation and to renegotiate the Paris Agreement despite its negative effects on the political credibility, international relationships, and potential long-term economic growth of the U.S. (Zhang et al., 2017). In general, the withdrawal of the U.S. from the Paris Agreement will not change the development of low-carbon technologies and the transformation trend of the global climate governance regime. However, the long-term goals and international cooperation on climate change will be affected by budget cuts in American climate change research and the cancelation of donations from the multilateral environmental fund of the U.S (Dai et al., 2017; Zhang et al., 2017). If the Paris Agreement is renegotiated, the common but differentiated principle of responsibility of the UNFCCC will be challenged again.

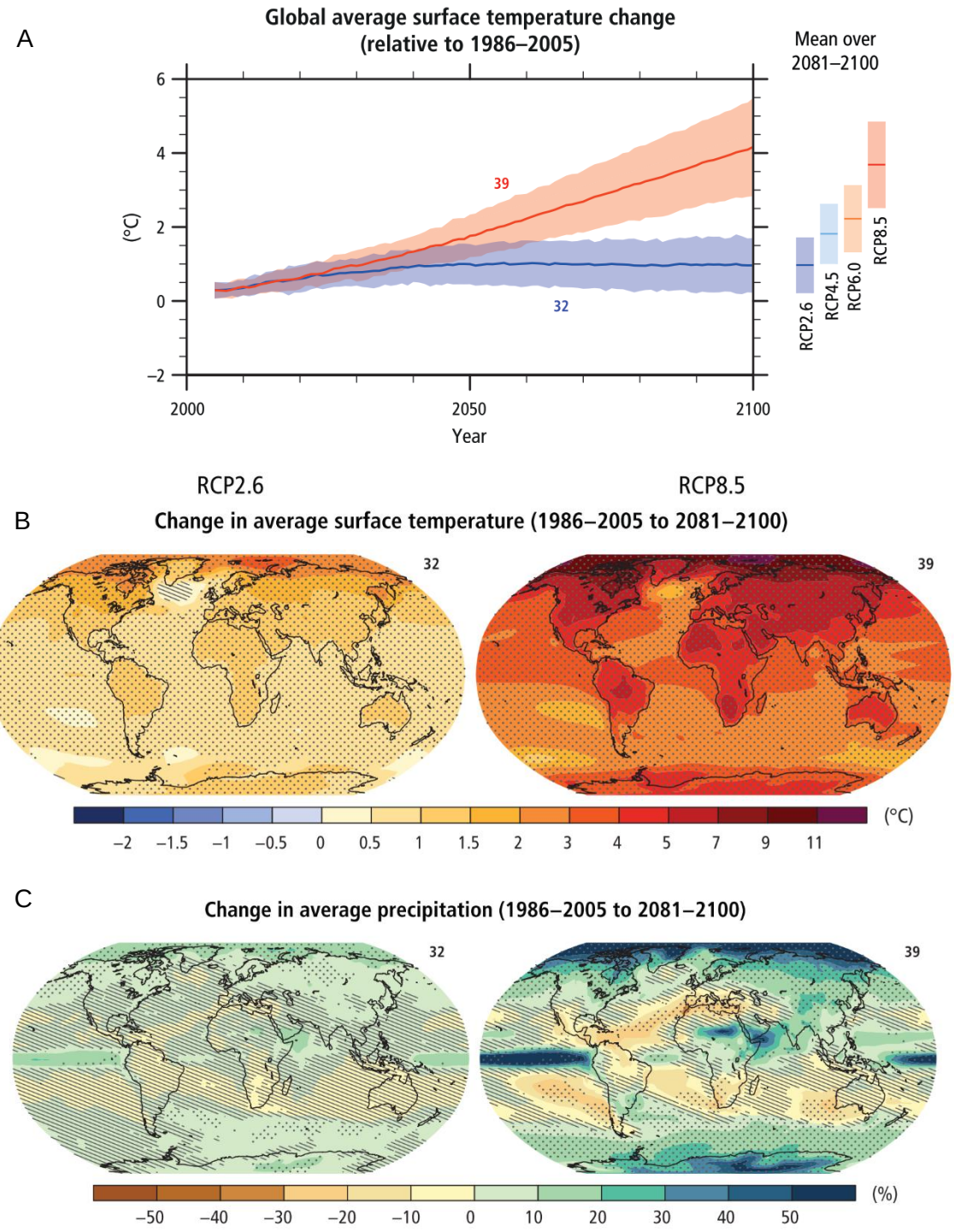

Figure 1: (A) Global average surface temperature change, (B) change in average surface temperature from 2006 to 2100 and (C) change in average precipitations as determined by multi-model simulations (IPCC, 2014). Time series of projections and a measure of uncertainty (shading) are shown for scenarios RCP2.6 (blue) and RCP8.5 (red).

Nevertheless, climate change governance remains a main theme of future sustainable development. Instead of national governments, local governments and non-governmental organizations will develop strategies for technical innovation and emphasize pragmatic cooperation, thus expanding their roles in climate change governance. From a global view, although the effectiveness of the Paris Agreement is

not as high as before because of the withdrawal of the U.S., other parties will still make active efforts to implement its policies and fulfill their commitments (Zhang et al., 2017).

Achieving those reduction targets requires the deployment of new and efficient technologies, appropriate policies and legislative initiatives, as well as investments in research and development (R&D) and an appropriate financial framework to facilitate the demonstration and deployment of technologies in the higher level of TRLs (Technology Readiness Level). The EU is part of the Clean Energy R&D Focus Area on carbon capture and utilization (CCU) and carbon capture and storage (CCS) ("European Union – Mission Innovation," n.d.). A total of 61 projects on CCU technologies were funded from 2008 until 2018 under FP7 and Horizon 2020 for a total of 243 M€. A prize is funded under Horizon 2020 ("Horizon prize CO_2 reuse") to reward innovative products utilizing CO_2 that could significantly reduce the atmospheric emissions of CO_2 when deployed at a commercial scale (European Commision, 2018).

Carbon based fossil fuels have the precise energy concentration and most probably will continue to be the main energy source in the short-medium term, but it is necessary to control the CO_2 emissions to the atmosphere(Tan et al., 2016). About 80% (Figure 1) of the world's energy needs are currently supplied by fossil fuels (Quadrelli and Peterson, 2007). CO_2 emissions from industrial sources are very important and represent 25% of the global emissions (*The global status of CCS 2015*, 2015).

The concentration of CO_2 in the atmosphere now is greater than at any other time in modern history. Although the transition of the existing infrastructures from carbon-based sources to cleaner alternatives would be ideal in this regard, such a change requires considerable modifications to the current energy framework, and many of the proposed technologies are not yet sufficiently developed to facilitate largescale industrial implementation. Thus, CCS and CCU technologies that efficiently capture CO_2 from existing emission sources will play a vital role until more significant modifications to the energy infrastructure can be implemented.

One scenario in which CO_2 capture technologies could be rapidly implemented is at stationary point sources, such as coal and natural gas-fired power plants. In the EU 41,6% of the total electricity generation is generated by fossil fuel combustion (European Climate Foundation, 2010), and hence the installation of effective capture systems to existing plant configurations could offer a large reduction in emissions. The captured CO_2 would then be subjected to permanent sequestration, where the CO_2 is injected into underground geological formations, such as depleted oil reservoirs or salt water aquifers. Similar technologies are already established in the context of processes such as enhanced oil recovery (EOR), and several trial CO_2 sequestration sites are in

construction (Feron, 2010). Note that the reuse of the captured CO_2 as a reactant in chemical transformations presents an alternative sequestration pathway, although it would not be a viable long-term strategy owing to the tremendous scale of worldwide CO_2 emissions (ca. 30 Gt per year) (Thambimuthu et al., 2005) resulting in the market for any commodities prepared therefrom being rapidly saturated.

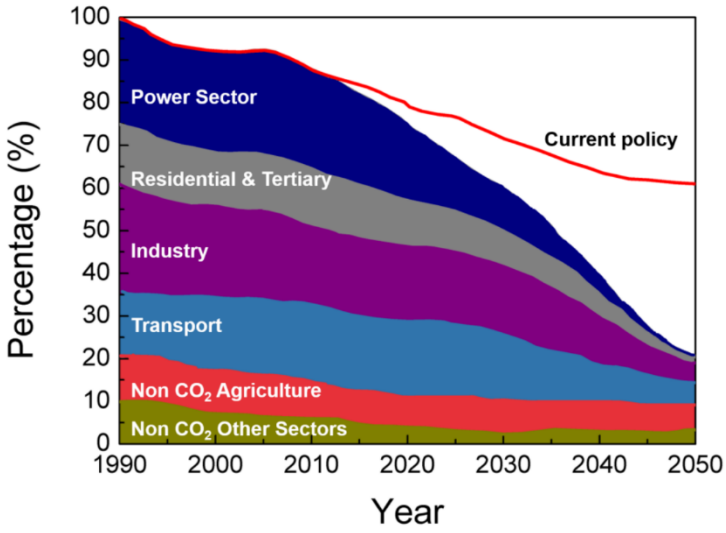

Figure 2: EU CO_2 emission reduction pathways towards an 80% reduction by 2050 (European Climate Foundation, 2010)

CCU is one of the most promising strategies to achieve these emissions reductions, together with the improvements on the energy efficiency and the switch from fossil fuels to renewable energy. A significant reduction in the energy consumption of CO_2 capture systems remains a challenge. Furthermore, the source and type of the energy used by the capture plants will play an important role in the overall operating cost (Zenz et al., 2009). Many researchers are currently exploring energy integration options with power plants for the potential use of cheaper, low-grade thermal energy or heat recovered from flue gas cooling in order to offset part of the energy requirements for the CO_2 capture systems as a means of reducing operating cost (Sculley et al., 2013).There are three general approaches to CO_2 capture for fossil-fuel power plants, which are: pre-combustion, post-combustion and oxy-combustion (Leung et al., 2014).

1.1. Pre-combustion Capture

It is a process in which the fuel (normally coal or natural gas) is decarbonated prior to combustion, resulting in zero carbon dioxide production during the combustion step (Sumida et al., 2012a) (see Figure 3). Here, coal is gasified, generally at high

temperature and pressure, to produce synthesis gas, which is a mixture of mostly H_2, CO. This gas mixture is then run through the water-gas shift reaction to produce H_2 and CO_2 (syn gas) at high pressure and slightly elevated temperature (5 to 40 barg and 40 °C, depending on the production plant) (Leung et al., 2014). Pre-combustion CO_2 capture, which refers to the separation of CO_2 from H_2 within this gas mixture, can then be performed to obtain pure H_2, which is subsequently combusted in a power plant to generate electricity. For non-gaseous feedstock, the gas stream generally must be cleaned to remove species containing sulphur, nitrogen (cyanides and ammonia), chlorides and others which either pose a threat to hardware or which are regulated by environmental requirements.

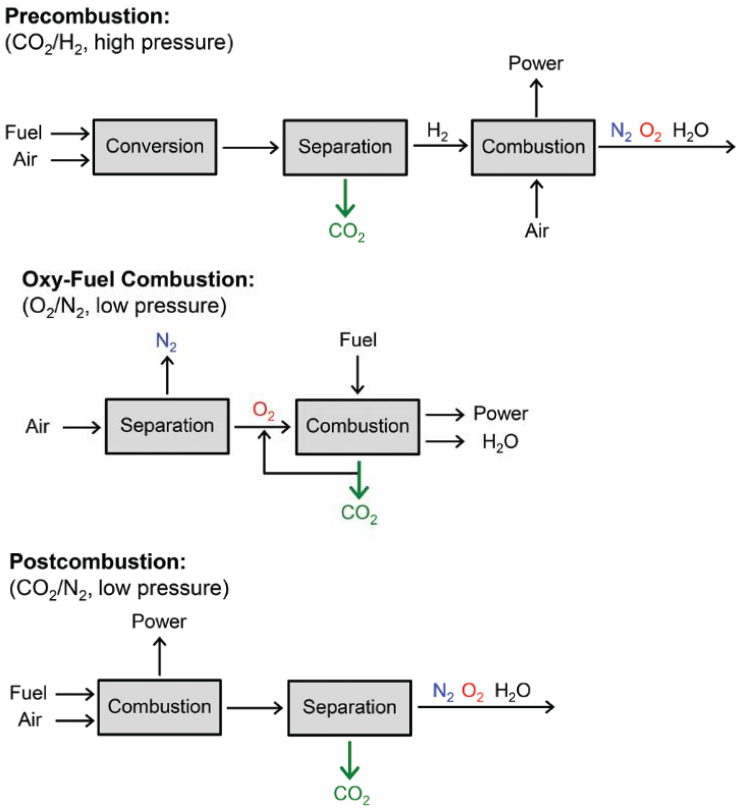

Figure 3: Basic schemes showing the types of CO_2 capture relevant to the present doctoral thesis. The processes for post-combustion capture, pre-combustion capture, and oxy-fuel combustion (Sumida et al., 2012b).

1.2. Oxy-combustion Technology

The oxyfuel combustion technology involves replacement of combustion air with a mixture of recycled CO_2 rich flue gas recycle and high purity oxygen for combustion (see Figure 3) (Sumida et al., 2012b). An air separation unit is required to supply a stream of

highly pure oxygen. A major part of the flue gas must be recycled back to the boiler plant for providing a primary flue gas recycle stream to transport pulverized fuel and a secondary oxyfuel flue gas recycle to the burners and furnace. The resulting flue gas from an oxyfuel boiler is predominantly CO_2 and water, with trace species such as NO_x and SO_2. The CO_2 rich flue gas needs to be cleaned and dried prior to compression for storage or other uses. The most widely considered technology for oxygen production is cryogenic air separation (García et al., 2014; Leung et al., 2014). The auxiliary power consumption of a cryogenic air separation unit is high and has a major impact on the overall efficiency of the power plant. Integration of the heat cycle of plants fitted with oxyfuel capture is essential to minimize the impact of the capture process on the overall plant efficiency.

1.3. Post Combustion Capture

CO_2 is removed from the flue gas that results after combustion of the fuel in air (see Figure 3). The combustion of fossil fuel in air generates a flue gas composed of mostly N_2, CO_2 (15-16%) and other minor components such as H_2O, O_2, CO, NO_X, and SO_X. The gas stream is released at a total pressure of approximately 1 bara. Since SO_x and NO_x removal would precede CO_2 capture, the flue gas would be expected at temperatures between 40 and 60 °C (Sumida et al., 2012a).

The major challenges for CO_2 capture methods are stated briefly as follows. In oxyfuel combustion capture the main problems are related to the high energy consumption for the supply of pure oxygen and the lack of readiness for this technology, given that there is very little experience on the commercial scale (Quadrelli and Peterson, 2007). In pre-combustion capture, the challenges include high cost, insufficient technical know-how for good operability, absence of single concise process for overall operational performance; and lack of development for industrial application. For the post-combustion capture case, the difficulties include: the additional energy requirement for compression of captured carbon dioxide, need for treatment of high gas volumes, because CO_2 has low partial pressure and concentration in flue gas and large energy requirement for regeneration of sorbent e.g. amine solution.

In recent years, post-combustion capture has been the topic of much research, because it is easier to integrate into an existing plant, without needing to substantially change the configuration or combustion technology of the plant. Moreover, it is more suitable for gas plants than the Oxy-Combustion or the Pre-Combustion plants, its maintenance does not stop the operation of the power plant and it can be easily regulated or controlled (Ben-Mansour et al., 2016; Songolzadeh et al., 2014). Post-combustion CO_2 capture

technology is widely employed in chemical processing. However, the application of this technology to specific applications needs further investigation, especially in optimizing CCU systems for fixed and mobile sources. The priority activities in this task are: the development of better materials for post-combustion CO_2 capture, identifying optimal capture process designs including ways of integrating the capture systems with the emission sources to minimize the energy losses and environmental impact, identifying advantages and limitations of precipitating systems (e.g., carbonates) (Songolzadeh et al., 2012; Sumida et al., 2012a) and carrying out a detailed assessment of the environmental impact of various CO_2 capture technologies (Songolzadeh et al., 2014; Tan et al., 2016). Post-combustion capture technologies would enable the world to continue to use fossil fuels, but with much reduced net emissions of CO_2 while other low CO_2 emission energy sources are developed and introduced on a large scale (Ben-Mansour et al., 2016).

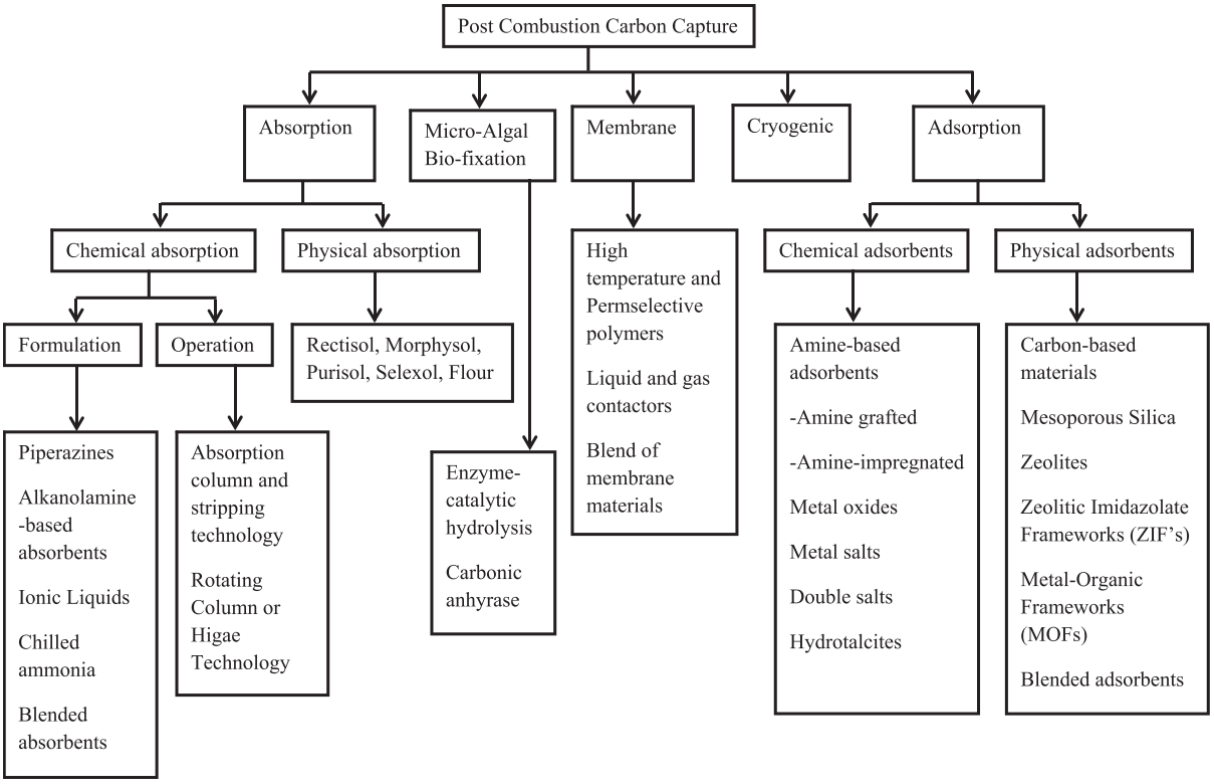

Figure 4: Post combustion carbon capture processes (Metz et al., 2005).

Based on economic and environmental considerations, it is necessary to apply efficient and suitable technology for CO_2 separation with low operating costs and energy consumption. There are several gas separation technologies being investigated for post-combustion capture such as absorption, membranes, cryogenics, adsorption, and other advanced concepts as the micro-algae bio-fixation (Ben-Mansour et al., 2016). Figure 4 briefly describe these methods (Metz et al., 2005).

In absorption of CO_2, Figure 5 (or "scrubbing") a liquid sorbent is used to separate the CO_2 from the flue gas. The sorbent can be regenerated through a stripping or regenerative process by heating and/or depressurization. This process is the most mature method for CO_2 separation. Typical sorbents include monoethanolamine (MEA), diethanolamine (DEA) and potassium carbonate (Leung et al., 2014). The process takes place in columns ("towers") known as scrubbers, in which turbulent flow promotes rapid CO_2 transfer from gas to liquid. Differences in density make it easy to separate the emerging gas and liquid. To recover the captured CO_2, the loaded solvent is pumped to a "stripper" in which it is exposed to a hotter CO_2-free gas, typically steam. Heating of the solvent causes the desorption of the CO_2 (and traces of nitrogen). The stripped liquid is pumped back to the scrubber, while the steam/CO_2 mixture is cooled to condense the steam, leaving high-purity CO_2 suitable for compression and, after transportation to an appropriate site sequestration or use (Metz et al., 2005).

Some of the absorption disadvantages are: high heat/power requirement for solvent regeneration, the need for corrosion control measures and the sensitivity of the solvents to losses in chemical purity or quality due to infiltrations from other by-products (e.g. SO_x, NO_x, etc.) in the flue gas streams, which leads to reduction in efficiencies and increment in costs of power supply (Ben-Mansour et al., 2016).

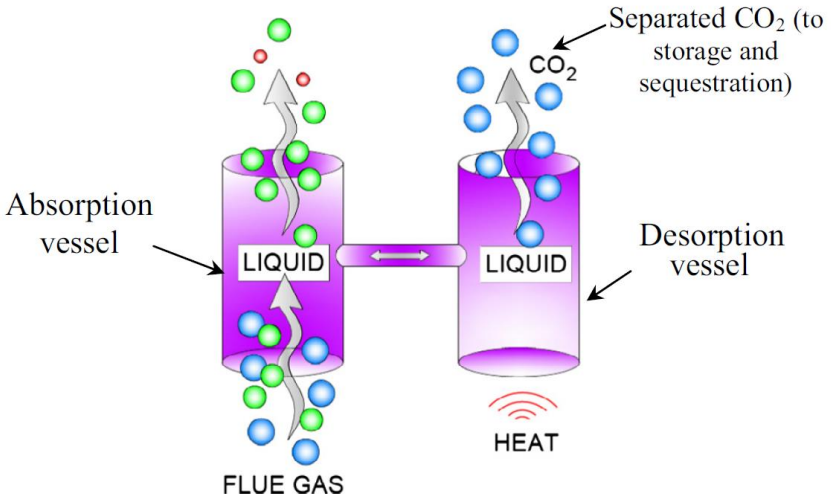

Figure 5: Schematics of absorption carbon capture process using amines (Ben-Mansour et al., 2016).

Microalgal bio-fixation is another potential technique for the removal of CO_2 from flue gases. This technique entails the use of photosynthetic organisms (microalgae) for anthropogenic CO_2 capture (see Figure 6). Aquatic microalgae have been suggested to have greater potential because of their higher carbon fixation rates than land plants (Kassim and Meng, 2017; Zhou et al., 2017). Nonetheless, the implementation of large-scale microalgae-based carbon sequestration technologies has yet to be realized.

Innovation and improvement in the following areas are necessary before microalgae based technologies can be commercialized: development of technologies to address carbon sources with different chemical forms and distribution characteristics, screening and genetic engineering of high performance strains, improved utilization of industrial waste gases, better understanding of microalgae-based carbon fixation mechanisms, enhanced CO_2 transfer and oxygen desorption, cultivation process optimization including scaling up, cost-effective photobioreactors, high efficiency microalgae harvesting and conversion technologies, value-added products development, and system integration (Ravindran et al., 2016; Zhou et al., 2017). The understanding and improvement of economic feasibility must be achieved through techno-economic analysis using production facilities with reasonable scales (Ho et al., 2011; Nakamura et al., 2003).

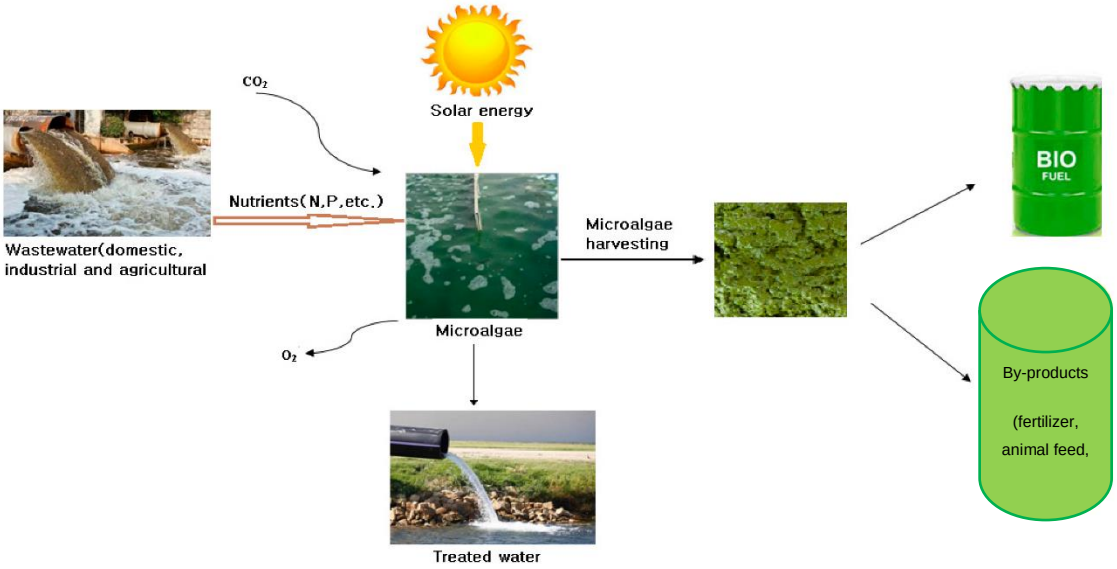

Figure 6: Principles of the microalgae production integration with wastewater treatment (Ravindran et al., 2016).

Membrane separation of carbon dioxide (Figure 7) involves the use of polymer ceramic membranes to sieve out the CO_2 gas from the flue gas (Khalilpour et al., 2015). Differences in permeation rates are generally due (in the case of porous membranes) to the relative sizes of the permeating molecules or (in the case of dense membranes) their solubilities and/or diffusion coefficients (i.e., mobilities) in the membrane material. Because permeation rates vary inversely with membrane thickness, membranes are made to be as thin as possible without compromising mechanical strength (which is frequently provided by non-selective, porous support layers) (Song et al., 2017b).

Challenges are still being faced in the application of this technique on a large scale, and in the design of membranes that would operate efficiently for the desired purpose at relatively high temperatures (Khalilpour et al., 2015). Membrane permeation is generally pressure-driven, the feed gas is compressed and/or the permeate channel operates

under vacuum and/or a sweep gas is employed. Due to the low partial pressure of CO_2 in the flue gas, this constitutes a major challenge for the membrane-based approach compared to liquid absorbents or solid adsorbents that are thermally regenerated (i.e., heated to strip the captured CO_2). Most significantly, for membranes to be competitive with amine-based absorption for capturing CO_2 from flue gases, their CO_2/N_2 selectivity (i.e., permeability ratios) must be in the range of 200 (Brunetti et al., 2010).

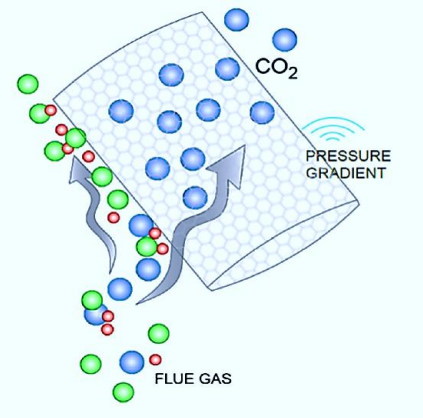

Figure 7: Schematics of membrane carbon capture process (Ben-Mansour et al., 2016).

Cryogenic distillation (Figure 8) is a gas separation process using distillation at very low temperature and high pressure (due to the low boiling points). For CO_2 separation, flue gas containing CO_2 is cooled to de-sublimation temperature (-100ºC to -135ºC) and then solidified CO_2 is separated from other light gases and compressed to a high pressure of 100 to 200 atm. The amount of CO_2 recovered can reach 90 to 95% of the flue gas. Since the distillation is conducted at extremely low temperature and high pressure, it is an energy intensive process (Tuinier et al., 2011). Typically high CO_2 concentrations (higher than 50%) are more suitable for this process (Song et al., 2012). Several patented processes have been developed and research has mainly focused on cost optimization (Song et al., 2017a, 2012; Tuinier et al., 2010).

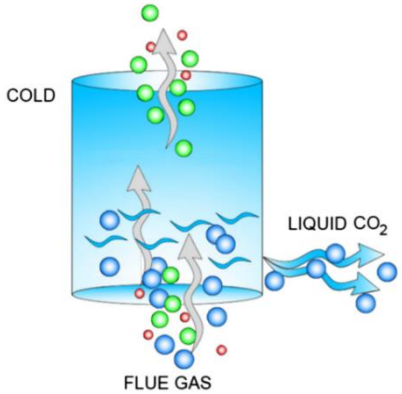

Figure 8: Schematics of cryogenic carbon capture process (Ben-Mansour et al., 2016).

In chemical adsorption by chemical looping, a metal oxide is used as an oxygen carrier instead of directly using pure oxygen for the combustion, as in the case of oxyfuel combustion (see Figure 9). During this process, the metal oxide is reduced to metal while the fuel is oxidized to CO_2 and water. The metal is then oxidized in another stage and recycled in the process. Water, the process by-product, can be easily removed by condensation, while pure CO_2 can be obtained without consumption of energy for separation (Leung et al., 2014). There are a wide variety of metal oxides that are of low-cost and suitable for this process including CaO, Fe_2O_3, NiO, CuO and Mn_2O_3. The effectiveness of different metal oxides in this process has been studied by various researchers (Kang et al., 2018; Nandy et al., 2016; Protasova and Snijkers, 2016; Zhu et al., 2018, 2017). Challenges are still being faced in the application of this technique since: the process is still under development and there is no large-scale operation experience, operational problems exist due to low fluxes, there are high energetic requirements and fouling (Erlach et al., 2011; Nazir et al., 2017).

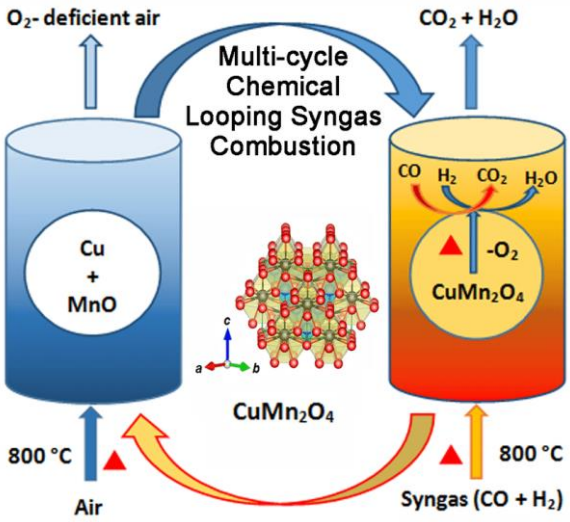

Figure 9: Schematics of chemical looping carbon capture process (Nandy et al., 2016).

Adsorptive separation is a mixture separating process, which works on the principle of differences in adsorption/desorption properties of the constituents of the mixture. The word adsorption is defined as the adhesion of ions, atoms or molecules from a liquid, gas or dissolved solid to a surface. The adhered ions, atoms or molecules are called the adsorbate, while the surface onto which they are attached is called the adsorbent. Adsorption is different from absorption because in absorption, the fluid (absorbate) is dissolved by a solid or liquid (absorbent). Adsorption occurs on the surface while absorption entails the whole material volume. Adsorption may take place physically via weak Van der Waals forces (physisorption), which consumes relatively less energy, resulting in better adsorbent durability and greater stability after several

adsorption/desorption cycles (see Figure 10). In physisorption, new chemical bonds are not formed between the adsorbate and adsorbent, therefore much less energy is required for CO_2 regeneration when compared with chemical absorbents such as amines (Songolzadeh et al., 2012).

Adsorption has a major advantage to other approaches due to the ease of adsorbent regeneration by temperature or pressure modulation, reducing the energy consumption of post-combustion carbon capture. Important factors in adsorption processes include: ease of regeneration of adsorbed CO_2, durability of adsorbent, selectivity of adsorbent for CO_2, adsorption capacity and stability of adsorbent after several adsorption/desorption cycles (Songolzadeh et al., 2012). Regarding to CO_2 capture by adsorption, the most used technology in industrial scale is Pressure Swing Adsorption (PSA). It is a cyclic adsorption process, but it is commonly adapted via the use of multiple adsorption columns for operating in a continuous mode. PSA is performed by periodic changes of pressure which aim to minimize the amount of product contaminants, and is considered energetically viable for separation of CO_2 from flue gases containing about 5-15% v/v (Dąbrowski, 2001; Kast, 1985).

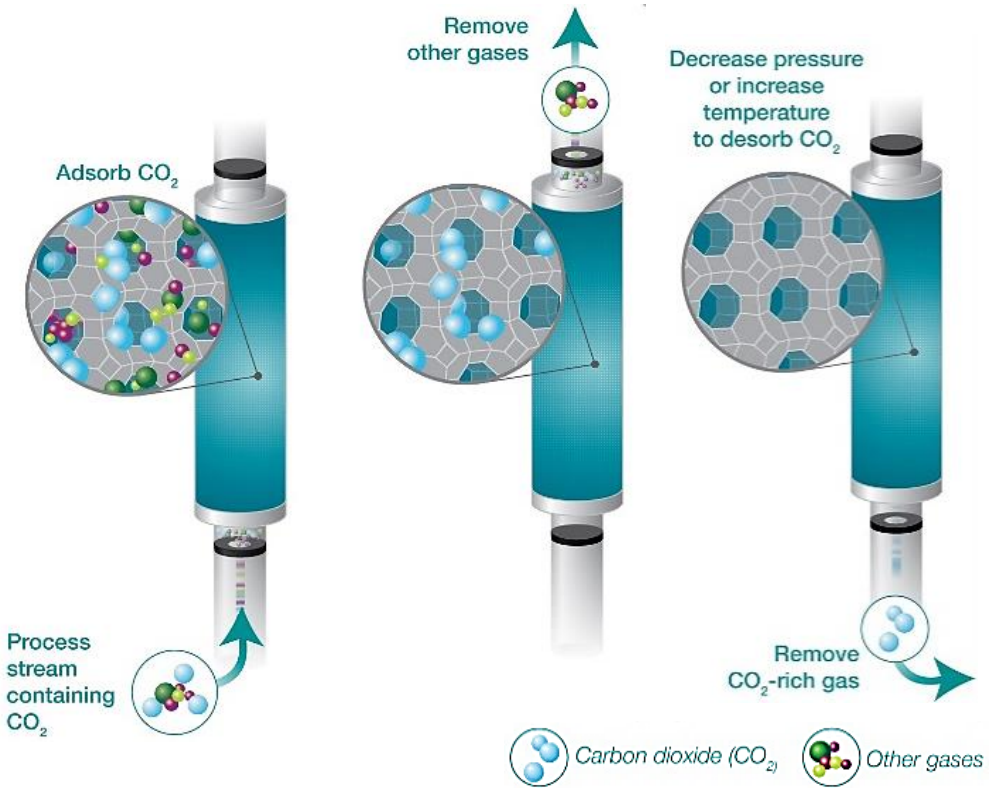

Figure 10: The principle of adsorption capture (APEC, 2012)

Adsorption technology is becoming increasingly popular for CO_2 capture because of its potential low energy consumption, simple operation, easy maintenance and flexibility in

design to meet different demand requirements (Ling et al., 2014; Riboldi and Bolland, 2017a; Yu, 2012). The interest in applying this technology in the industrial scale is driving further developments in the energy efficiency of the CO_2 adsorbent regeneration. Available regeneration techniques include pressure swing adsorption (PSA), vacuum swing adsorption (VSA), temperature swing adsorption (TSA) (see Figure 11) and hybrid processes (PTSA or VPSA). There are several variants of the TSA technique which use different methods to increase the temperature, one such example being electric swing adsorption (ESA) which conducts electricity through the adsorbent.

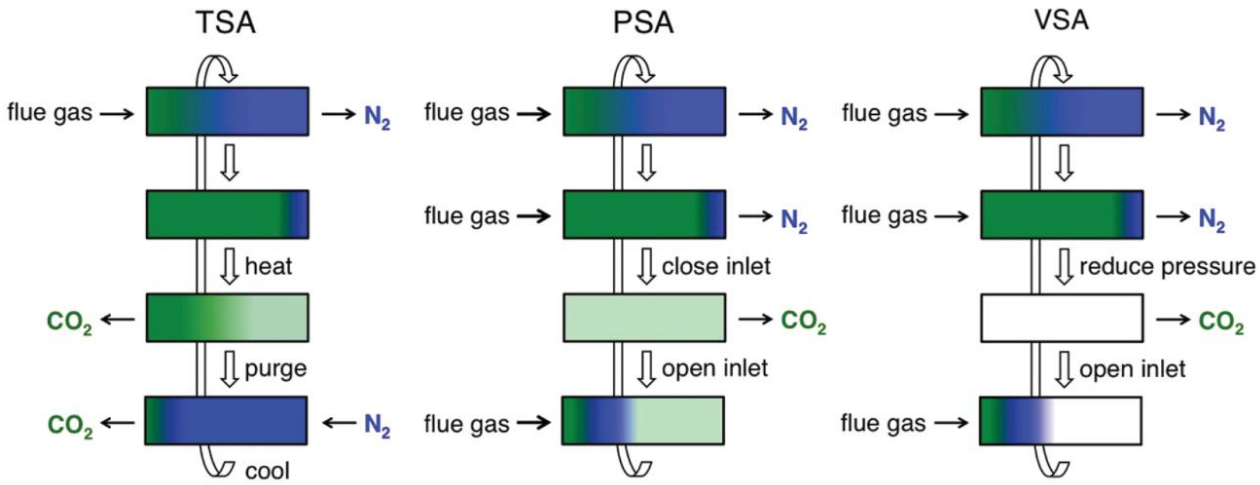

Figure 11: Schematic diagrams of idealized temperature swing adsorption (TSA), pressure swing adsorption (PSA), and vacuum swing adsorption (VSA).

In PSA, adsorption is typically performed at pressures higher than atmospheric pressure, while desorption is performed at atmospheric pressure. In VSA, adsorption operates at atmospheric pressure and near-room temperature, while desorption operates at lower pressures. Both PSA and VSA are performed by altering the pressures. Generally, the adsorbents with high adsorption capacity and high selectivity toward CO_2 are preferred. Because the pressure in flue gas streams is approximately equal to 1.0 bara and CO_2 concentration in the feed gas is commonly higher than 10%, VSA is considered more economical for CO_2 capture than PSA (where significant compression of the feed gas is required) (Kacem et al., 2015; May et al., 2017; Wang et al., 2013a; Webley et al., 2017). The TSA technique can be designed to directly utilize cheaper, low-grade thermal energy resources from power plants for regeneration to reduce the operating cost. However, the longer time required for heating/cooling limits its application for CO_2 capture. With the long cycle time, productivity will be lower compared to other adsorption technologies. The product may also be diluted by the purge gas if regeneration is performed by direct hot gas purge as used in conventional systems (Joss et al., 2017; Ntiamoah et al., 2016; Pahinkar, 2016; Zhao et al., 2017).

The temperature range of flue gases varies by their sources and pre-treatment processes that may be available. Taking a typical coal-based power plant for instance, the flue gas stream may be available at a temperature ranging from 70 to 90ºC or even higher, depending on the extent of heat recovery from the stream(Ling et al., 2014). The VSA performance is sensitive to the feed gas temperature, so a further heat treatment may be required to condition the flue gas before feeding it to the VSA plant, which will inevitably impact on the separation efficiency and economics of the process.

A variety of PSA cycle configurations have been developed for concentrating CO_2 from stack and flue gases. Given the atmospheric pressure level of these gases, the most common PSA processes in post-combustion applications rely on sub-atmospheric adsorbent regeneration (VPSA). As an alternative to vacuum pressures, an upstream flue gas compression has been studied, but this approach has demonstrated to be unfeasible due to the large energy requirement involved (Riboldi and Bolland, 2015). Many combinations of process steps may be able to meet the targets in terms of CO_2 purity and recovery, so the primary factor to optimize becomes the energy consumption for implementing the gas separation process.

Some recent studies have highlighted the true potential of the two adsorption technologies, including vacuum pressure swing adsorption (VPSA) (Fujiki et al., 2017; Kacem et al., 2015; Li et al., 2016; Ling et al., 2015; Maring and Webley, 2013; Wang et al., 2013a) and pressure-temperature swing adsorption (PTSA), for CO_2 capture (Joss et al., 2017; Pahinkar, 2016; Plaza et al., 2010; Song et al., 2015). Adsorption based technologies, are attractive due to the non-volatility of solid sorbents, the potential low energy consumption, the moderate heat of adsorption (between 30 kJ/mol and 70 kJ/mol) and the moderate regeneration temperature, which might offer attractive heat integration opportunities using low-grade heat sources (Lively et al., 2010).

Table 1 shows some VPSA capture systems of CO_2 from a desulfurized flue gas was demonstrated on a pilot plant scale in an existing coal-fired power plants with flow rates between 32- 60 Nm^3/h (Torkkeli, 2014; Wang et al., 2013a, 2013b). The best performance achieved for VPSA cycle in a two-stage configuration was 95% purity, 73% recovery with a productivity of 0.036 $g_{CO2}/(g_{Ads} \cdot h)$ and an energy consumption of 0.6 kWh/ton CO_2 (Wang et al., 2013b). The reported works are based on dry flue gas with no impurities (SO_X, NO_X), therefore it does not address the real process economics.

A 2-stage VPSA system is likely necessary to efficiently meet the requested separation performance. Commonly, the first stage provides high CO_2 recovery, while the second stage achieves the CO_2 purity level desired. Some studies seem to show that a single stage process may become able to reach similar performance with competitive energy consumption (Andersen et al., 2013; Du et al., 2017; Fujiki et al., 2017; Maring and Webley, 2013; Webley et al., 2017) but would require high vacuum conditions, which are not simple to implement on large systems (Riboldi and Bolland, 2017b). Moreover, experimental results on the same PSA system arrangements do not always fully agree with the simulation outputs (Torkkeli, 2014), stressing the degree of complexity of these systems and the necessity of further results validation. Table 1 gives an overview of the expected performances of the adsorption techniques, and reports some of the most meaningful results from the literature.In general, it was found that the power consumption of the vacuum pump VPSA unit accounts for two-thirds of the total power consumption in the carbon capture experiments (Wang et al., 2013a), so it is very important to reduce the power consumption of the vacuum pump under a high vacuum to improve this process. Also, the effect of the fuel gases temperature, moisture and impurities are important issues that should be taken in to consideration when applying this technology on an industrial scale. Some studies on carbon capture from wet flue gas demonstrate the negative impact on the adsorbent performance for adsorption based capture process (Li et al., 2008; Zhang et al., 2009).

While the demand for reduction in CO_2 emissions is increasing, the cost of CO_2 capture processes remains a limiting factor for large-scale applications. Reducing the cost of the capture system by improving the process and the adsorbent used must be prioritized to apply this technology in the future. Experimental and theoretical work on a pilot-scale VPSA separation of CO_2 with a suitable adsorbent is essential for the evaluation of CO_2 capture from power plants.

Table 1: Performances of various PSA arrangements for CO_2 capture from flue gas.

Type	Cycle Config.	Adsorbent	Flue gas Temp. (ºC)	Pres. (barg)	Reg. Vac. or Temp. (barg) or (ºC)	Purity %	Rec. %	Enr. cons. (kWh/kg_{CO2})	Prod. ($g_{CO2}/g_{Ads}·h$)	Result type	Flue gas source	Flue gas comp. CO_2/N_2 (% vol)	Feed flowrate (Nm^3/h)	Ref.
VPSA	3-bed 7-step	Zeolite 5A	25-30	1.2	0.02	85	79	0.7	0.041	Exp.	Coal-fired power plant*, desulfurized.	15/85	46	Liu et al., 2012
VPSA	3-bed 9-step	Granulated Activated Carbon	25	2.0	0.05	90-99	55	-	-	Exp.	Synthetic.	13/87	6	Na et al., 2002
VSA	3-bed 9-step	Zeolite 13X APG 3	60	1.1	0.08	53	87	-	-	Exp.	Synthetic.	15/85	0.08	Ling et al., 2015
VPSA	3-bed 9-step	UiO-66 MOF	55	2	0.05	60	70	-	-	Exp.	Synthetic.	15/85	0.02	Andersen et al., 2013
PSA	3-bed 9-step	Zeolite 5A binderless	35	4	0.3	62	80	0.4	0.035	Exp.	Synthetic.	20/80	0.03	Patrícia A P Mendes et al., 2017
TSA	2-bed 5-steps	Zeolite 13X	30	1.3	147	88-99	70-90	0.9	-	Sim.	Simulated	15/85	1.3	Joss et al., 2017
Two-stage VPSA	4-bed 7-steps	Zeolite 5A	25	1.5	0.1	96	89	0.2	0.020	Sim.	Simulated	15/85	0.06	Liu et al., 2011a
VSA	2-bed 4-steps	Zeolite 13X	20	1.5	0.01	95	89	0.5	0.038	Pilot scale	Coal-fired power plant, dry and desulfurized.	15/85	60	Torkkeli, 2014
VPSA	3-bed 8-step	13X APG	30-50	1.2	0.02	73-82	84-95	0.5-0.6	0.036-0.044	Pilot scale	Coal-fired power plant* desulfurized	16.5/83.5	32-45	(Wang et al., 2013a)
Two-stage VPSA	3-bed 8-step	1^{st}:13X APG 2^{nd}: A. Carbon	30	1.3	0.07	95	83	0.7	-	Pilot scale	Coal-fired power plant, desulfurized	16.5/83.5	37	Wang et al., 2013b

** The energy used to dry the flue gas not included in the energy consumption estimation*

1.4. Adsorbents

The adsorbent determines the overall CO_2 capture performance in VPSA technology. With a relatively low concentration of CO_2 (15-16%) and large quantities of N_2 (73-77%) on the fossil fuel exhaust stream, a high selectivity toward CO_2 is crucial. Several challenges are being faced by scientists and engineers alike with respect to the commercialization of these materials. The researched materials require further work to improve their performance and stability. Suitable materials for carbon capture must account for the size of gas molecules and the electronic behavior of such molecules. There is not much difference in the kinematic diameters of gas molecules; this makes it difficult to base CO_2 separation solely on gas molecule size (CO_2: 3.30 Å, N_2: 3.64 Å) (Li et al., 2011). However, electronic properties like quadrupolar moments and polarization have been of great help, as bases of separation as they are significantly different for each gas (Ben-Mansour et al., 2016).

An ideal adsorbent for capturing CO_2 from post-combustion flue gas would exhibit a high selectivity for CO_2 over the other flue gas components, high gravimetric and volumetric CO_2 adsorption capacities, minimal energy penalty for regeneration, long-term stability under the operating conditions, and rapid diffusion of the gas through the adsorbent material (Songolzadeh et al., 2012). Adsorption processes rely on the use highly porous organic or inorganic materials which are either commercially available or under development through research on material science and engineering. Different adsorbents have been developed for CO_2 capture (Zhao et al., 2015) such as activated carbons (ACs) (Rashidi and Yusup, 2016; Zhao et al., 2015), zeolites (Cheung and Hedin, 2014; Gleichmann et al., 2016; Linda Shi and Hurst, n.d.; Patrícia A.P. Mendes et al., 2017; Silva et al., 2012), metal organic frameworks (MOFs) (Ben-Mansour et al., 2016; Sreenivasulu et al., 2015; Zhang et al., 2014), silica or porous polymers (Lee and Park, 2015). Every type of adsorbent has different properties (such as the specific surface area, total micropore volume, etc.), which make them more appropriate for different operational conditions. The choice of the adsorbent is critical to the effective operation of an adsorption unit. The properties of the adsorbents are one of the most important aspects of the unit performance for a given cycle configuration (Maring and Webley, 2013). For adsorption processes, carbon molecular sieves (CMS) and zeolites are feasible adsorbents and are the current adsorbent of choice in many instances, while MOF and amine functionalized adsorbents have displayed interesting potentials but are still under development (Sumida et al., 2012b). MOFs require further research in their chemical and thermal stability as well as their large-scale production process. In contrast, these properties are already well-established for the case of zeolites. A comparison of

the CO_2 capture characteristics of zeolites and MOFs is given by Krishna and Van Battem (Krishna and Van Baten, 2012).

The pore structures of adsorbents such as zeolites and metal-organic frameworks comprise regular arrays of uniform channels of molecular dimensions, thus offering the possibility of size selective (molecular sieve) separations (Ruthven, 2011). The concept of size exclusion is straightforward: Molecules that are too large to enter the pores are simply excluded, giving rise (at least in principle) to a highly selective separation. In this context, the most appropriate measure of molecular size is the critical molecular diameter, which is defined as the diameter of the smallest cylinder that can just circumscribe the molecule in its equilibrium conformation.

While the number of new adsorbent materials reported has proliferated, only a very select few will undergo bench-top testing and even fewer will pass on to pilot testing stage. This is partly due to the limited availability of production materials in the large scale which is often overlooked in the initial materials research. Therefore, the adsorption process design for CO_2 capture still focuses on commercially available materials such as zeolites, ACs and CMS which can be purchased in bulk and tested in pilot or field installations (Ben-Mansour et al., 2016; Siriwardane et al., 2001; Songolzadeh et al., 2012).

1.4.1. Commercial CO_2 Adsorbents

Due to their unique properties, zeolite molecular sieves are one of the most utilized adsorbents in industry (Yang, 2003). Typical applications for the zeolite types A (Figure 12 A) and X (Figure 12 B) are drying, purification and separation of gases and liquids. Many syntheses and shaping technologies for molecular sieves were developed over the last decades. In dynamic adsorption processes, where the adsorbent must be regenerated frequently, the fluid dynamics (e.g., the pressure drop over the fixed bed of molecular sieves) must be considered. Therefore, the zeolite must be applied in a suitable particle size (usually in the form of stable mechanically shaped macroscopic particles such as beads/spheres or extrudates/cylinders).

Because pure zeolite powder does not exhibit binding properties, an appropriate binder needs to be applied to form the above-mentioned macroscopic particles. Mineral binders such as bentonite, attapulgite, or kaolin are common as well as synthetic binders such as alumina, silica or a mixture thereof. To create a defined secondary pore system thermally or chemically, removable spacers (e.g., cellulose fibers or soluble salts) are

added to the pre-mixture. In most of the bulk zeolite molecular sieves, a binder content of around 20% (anhydrous basis) is used. But also lower (down to around 5%) and higher (above 30%) binder amounts are described (Gleichmann et al., 2016).

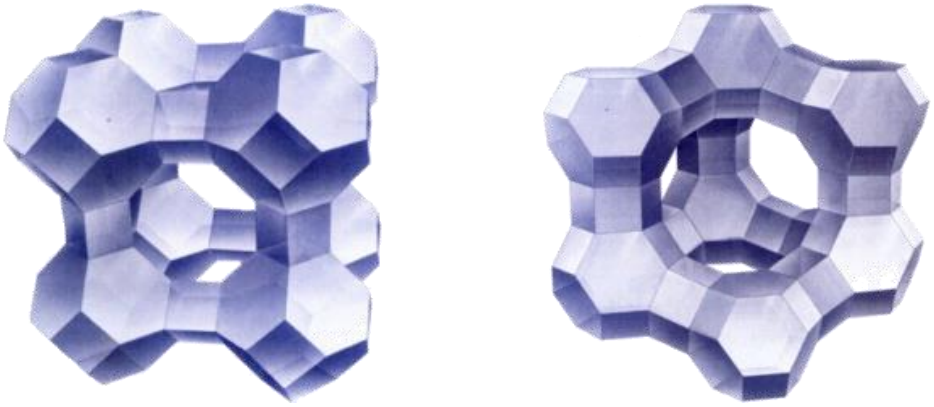

Figure 12: (A) Molecular Sieve Type X, (B) Molecular Sieve Type A. (Xinyan Technology, 2014)

The binding mechanism of activated binder-containing zeolite molecular sieves is based on the generation of a network of binder material, wherein the zeolite crystals are embedded. Figure 13 shows SEM pictures of zeolite 13X crystal agglomerates (A) and the binder (B). Figure 13 (C) shows the surface of a zeolite 5A bead with binder and (D) shows the physical shape bound formed. To avoid the above-mentioned disadvantages of binder-containing zeolite molecular sieve bulk materials such as adsorption capacity reduction by the adsorption of inert binders or influence of the secondary pore structure of the binder material, the so-called 'binderless' zeolite molecular sieves were developed.

Commercial zeolites contain 20% or more of adsorptive inert clay binder (cement) to give the necessary mechanical strength to the pellets or beads to be used in packed-columns. Such binder usually does not contribute to the adsorption. That means the total adsorption capacity is reduced at about the percentage of the added binder. Recently a new type of 13X zeolite made with a binder that is itself zeolite 13X (binderless beads) (Schumann et al., 2012) proved to increase the sorption capacity of CO_2 and CH_4 by 20% (Silva et al., 2012) equal to the proportion of otherwise inert binder material. In another study it was also shown that binderless zeolite 5A has a superior CH_4 adsorption capacity over H_2 (Yu et al., 2012).

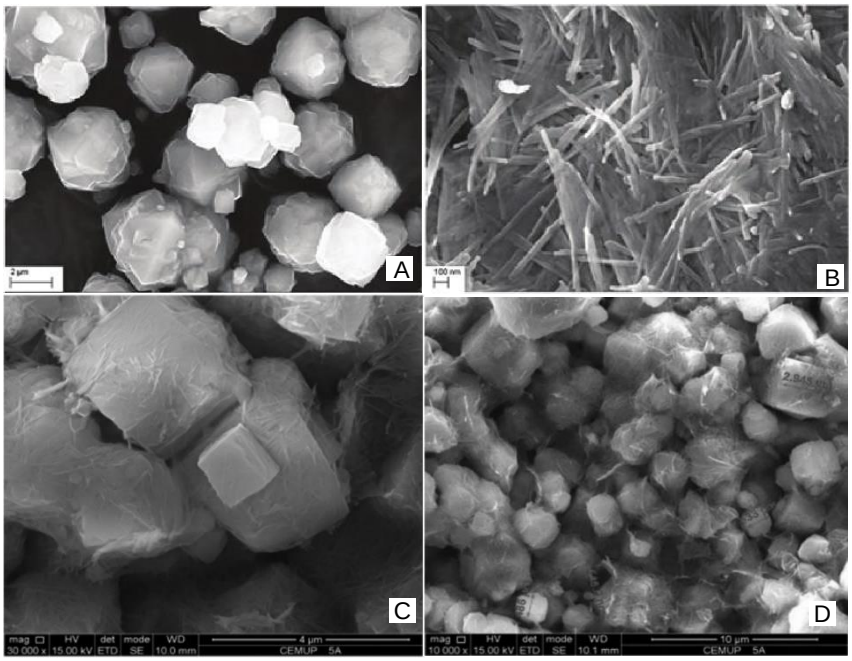

Figure 13: SEM pictures of the raw materials. (A) (Gleichmann et al., 2016) zeolite 13X crystal agglomerates, (B) (Gleichmann et al., 2016) Mineral binder, (C) (Liu et al., 2011b) Bead surface of zeolite 5A binder containing, (D) (Liu et al., 2011b)Bead fracture of zeolite 5A binder containing

There are different manufacturing procedures for binderless molecular sieves described in the literature (Gleichmann et al., 2016). Thus, it is possible to generate binderless zeolite shapes using temporary binder. A mixture of temporary binder material such as kaolin, metakaolin Figure 14 (B) or silica, and zeolite powder Figure 14 (A) are converted into zeolite matter. During the chemical conversion of the non-zeolitic components into zeolite matter, the binding mechanism changes. In the case of kaolin/metakaolin-based systems, the mechanical stability of the shapes is now based on intergrowths between zeolite crystals in the single shape Figure 14 (C and D). Said intergrowths are formed during the conversion of the metakaolin into a polycrystalline zeolite matter (Schumann et al., 2012).

Despite the different manufacturing procedures of binder-containing and binderless zeolite bulk material, the mechanical stability of the resulting shapes is similar (Gleichmann et al., 2016). A further interesting observation is, that in the above-described special manufacturing process for binderless molecular sieves, a very open secondary pore system is generated, which allows faster kinetics compared to conventional binder-containing zeolite molecular sieves with the (usual) binder content of around 20% (Schumann et al., 2012).

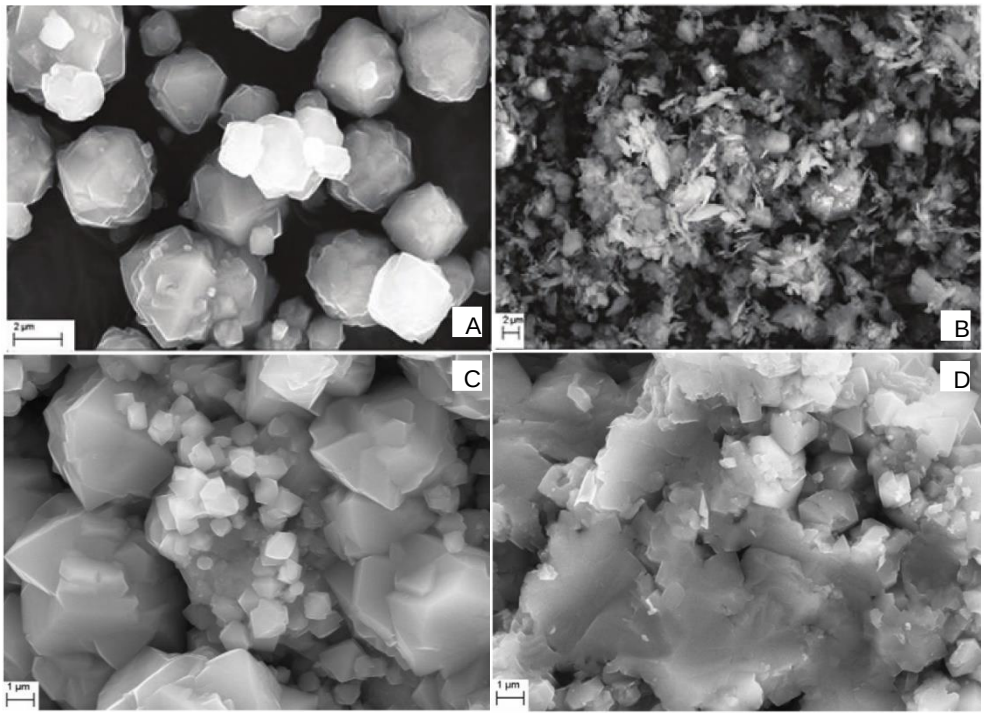

Figure 14: Binderless zeolite molecular sieve shapes (bulk material) (A) (Gleichmann et al., 2016) Zeolite 13X, (B) (Gleichmann et al., 2016) Mineral temporary binder (Metakaolin), (C) (Gleichmann et al., 2016) Bead surface of binderless zeolite 13X, (D) (Gleichmann et al., 2016) Bead fracture of binderless zeolite 13X.

However, besides all obvious advantages of binderless over binder-containing molecular sieves mentioned earlier, noted that, at least in the case of the kaolin/metakaolin based systems, the structure of the binderless shapes is more rigid than the related binder-containing shapes. This can easily be explained by the different binding mechanisms: intergrowths in the case of the binderless structures, embedment in the case of binder-containing structures.

CMSs have been extensively used for the separation of nitrogen and oxygen from the air (Ahmad et al., 2008; Son et al., 2005), carbon dioxide and methane (Liu et al., 2016; Technologies, 2007; Vu et al., 2002) and, propane and propylene (Liu et al., 2015). Because they are less hydrophilic than zeolites but have molecular sieving properties, CMS can be used more efficiently in separation processes involving wet-gas streams. Their molecular sieving properties derive from their unique pore structure (see Figure **15**).

Because of the aforementioned and several other promising features, CMS's have attracted considerable interest. Because the finishing step in producing CMS's is carbon deposition in an inert atmosphere at a moderately high temperature, the surface of CMS's is quite uniformly covered by carbon. Unlike activated carbon that has a

considerable amount of surface functionality, CMS's do not have a detectable surface functionality. Moreover, they should have fewer exposed inorganic compounds than activated carbon, and do not have cations. Consequently, the adsorption of gas molecules on CMS's involves only nonspecific dispersion forces.

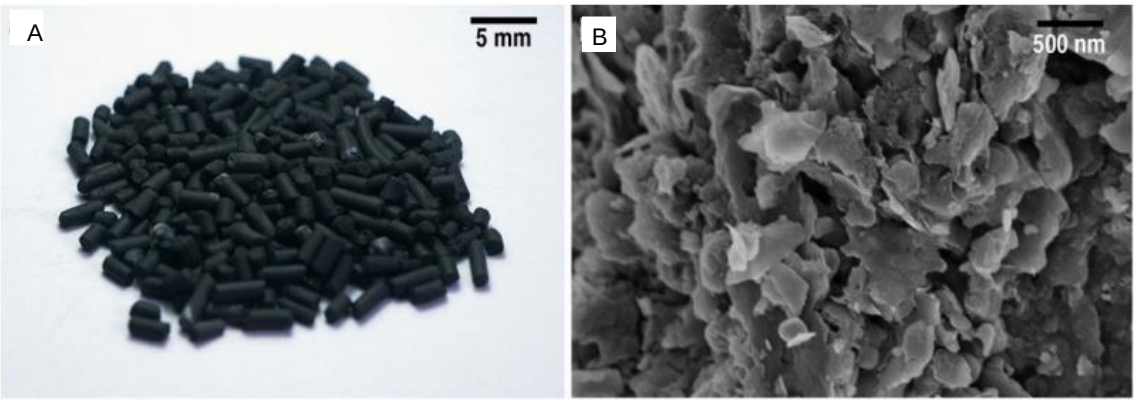

Figure 15: (A) Photograph, (B) SEM images of CMS (Liu et al., 2015).

For these reasons, CMS's should also be more hydrophobic than activated carbon. The main use for CMS's is nitrogen production from air and CH_4/CO_2 separation, both by PSA. Separations using CMS are based on kinetics and not on equilibrium, i.e., separations are obtained by differences in the diffusion rate and/or adsorption rate constants of the species involved. The adsorption kinetics do not always depend only on molecular size, it is a complex function of size, shape and electronic structure to absorb the gas molecules in relation to the micropore type, size and to the surface functional groups present on the material (Nabais et al., 2006).

In addition to CCU, efforts are also being focused on using captured CO_2, both directly as a working fluid and in chemical conversion processes, as a key strategy for mitigating climate change and achieving resource efficiency. CO_2 is used as a refrigerant for food preservation, beverage carbonation agent, supercritical solvent, inert medium (such as fire extinguisher), pressurizing agent, chemical reactant (urea, etc.), neutralizing agent, and as gas for greenhouses (see Figure 16).

Supercritical CO_2 (SC-CO_2) can be used as either a solvent for separation or as a medium for chemical reaction, or as both a solvent and a reactant. The use of supercritical SC-CO_2 allows contaminant free supercritical extraction of various substances ranging from beverage materials (such as caffeine from coffee beans), foods (such as excess oil from fried potato chips), and organic and inorganic functional materials, to herbs and pharmaceuticals. (Koytsoumpa et al., 2018) Various chemicals, materials, and fuels can be synthesized using CO_2. These processes require large amounts of energy, which should be provided sustainably in the long term when

renewable sources of energy such as solar energy is used as the energy input for the chemical processing (Alper and Orhan, 2017). CCU stands for the capture of anthropogenic CO_2 and its subsequent use in an industrial process, transforming CO_2 into another product with commercial value (Jarvis and Samsatli, 2018).

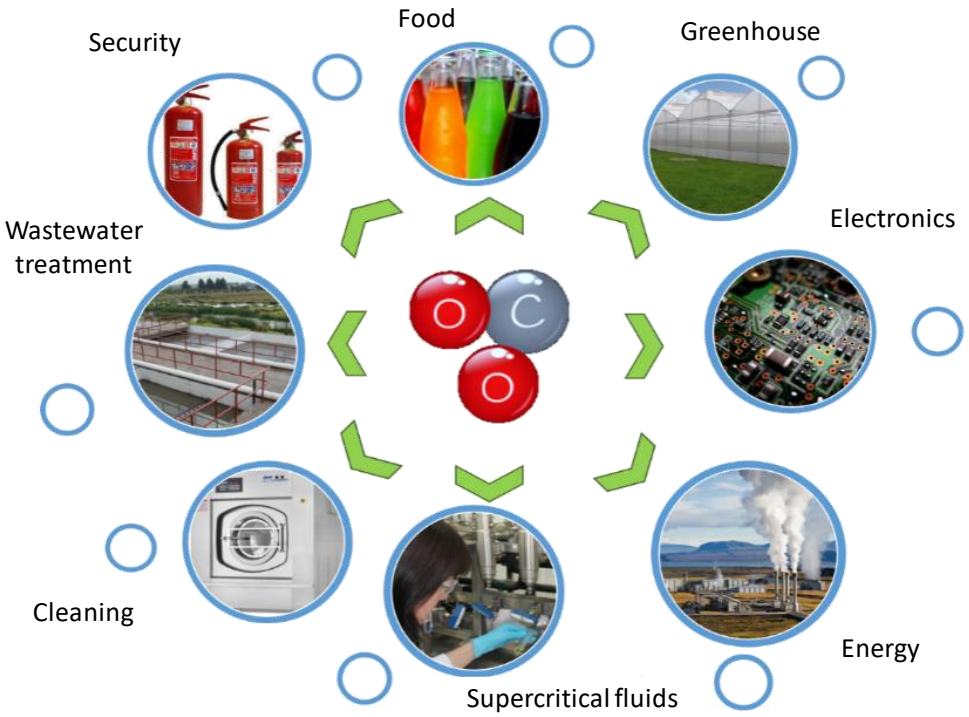

Figure 16: Carbon dioxide applications and uses.

GasN2 as a company which provides of technology for the separation of gases together with the PQAT laboratory of IQS detected an opportunity area to develop a technology for CO_2 capture from combustion gases which can be used inside a variety of industrial processes, including both the recovery and the utilization as added-value product. In 2015 in collaboration with the Catalan government, the research project for developing technology for CO_2 capture was started through the industrial doctorate program with European founding (2014 DI 057).

GasN2 is a Catalan company on which business growth is based on the continuous search of innovative solutions to their clients. To achieve this, the company participates in internal R&D projects, as well as in R&D projects of their clients, collaborators and academic partners. One of the main interests of the company is the business line based in the development of technology for gas separations for their clients. GAN2 has a wide experience in the development of equipment to separate nitrogen and oxygen from air.

1.5. Objectives

The main objective of this thesis is to develop a cyclic adsorption process to obtain carbon dioxide from flue gas streams with a purity higher than 95%, with high recovery efficiency, and with a feasible and cheap adsorbent.

To do that, the following partial objectives are stablished:

1. Study approach of the Temperature Swing Adsorption (TSA) process by Thermal Analysis.
2. Study approach of the Vacuum Pressure Swing Adsorption (VPSA) to determine equilibrium data and capacity of several commercial adsorbents.
3. Single column binary dynamic adsorption experiments and simulations of VPSA.
4. Multicolumn VPSA binary dynamic adsorption experiments and simulations.
5. Design, construction and operation of a multicolumn VPSA pilot plant to produce CO_2 from a real industrial flue gas.

2. Materials and experimental methodology

2.1. Materials

A large number of materials have been synthesized and examined at laboratory scale as candidates for CO_2 adsorbents, but only very few undergo field testing due to the limited availability of kilogram scale amounts (Choi et al., 2009; Hedin et al., 2013; Seul-yi and Park, 2014). Two groups of commercial adsorbent materials were used in this work for CO_2 capture: zeolites and carbon molecular sieves (CMSs). The main characteristic properties of the selected adsorbents were summarized in Table 2. The studied zeolites were divided into two types, zeolites with binder (5A, 13XNa, 13X-APG and APG-III) and binderless zeolites (13XBL, 5ABL and 4ABL). Zeolite 13X was selected as a ''benchmark'' commercial adsorbent for CO_2 capture because of its high CO_2 adsorption capacity and high CO_2 selectivity (Ling et al., 2015). Commercially available zeolite 13X, is a sodium form of the type X crystal structure, an alkali metal aluminosilicate of faujasite framework type (FAU). Its Si/Al molar ratio is 2.35 (Schumann et al., 2012), which is widely used in gas separation applications which adsorb molecules with critical diameters of up to 10 Å. Zeolite 13X-APG is a FAU framework type with a Si/Al ratio of 1.23. This zeolite was designed to be regenerated at high temperatures repeatedly (Wang et al., 2012). The APGIII zeolite is an advanced type of 13X zeolite that has a higher capacity to work at temperatures of up to 60 °C (Ling et al., 2015). The preparation and activation of these commercial zeolites was similar to the classical 13X zeolite. Zeolites 4A and 5A are alkali metal aluminosilicates with type A framework (LTA). These zeolites possess different charge-balancing cations (calcium in zeolite 5A and sodium in zeolite 4A) which tune the effective pore size in Å to approximately that given in its name. The binderless zeolites 13XBL (Schumann et al., 2012; Silva et al., 2014), 5ABL (Patrícia A.P. Mendes et al., 2017) and 4ABL (Müller et al., 2015) were produced with metakaolin (Kaorock) instead of the use of inert binder materials (Gleichmann et al., 2016).

CMSs belong to the activated carbon (AC) family. The modification of these carbons to a molecular sieve type is made by a thermal treatment of the porous structure (Jüntgen et al., 1981; Vaduva and Stanciu, 2007). Three different CMSs were used in this work. The CMS-F sample from bituminous coal, which will be named as CMS-I in this work. The commercial molecular sieves CMS-260 and CMS-330, which will be named as CMS- II and CMS-III respectively, are both produced using coconut shells and are activated with steam at temperatures of approximately 800° C (Mokhatab and Corso, 2016; Xiaowei et al., 2016).

Table 2: Main characteristics of adsorbents.

Adsorbent	Origin	Form	Particle diameter (mm)	Nominal Pore Diameter (Å)	Average Bulk Density (g/L)	Supplier
Zeolites						
13X-APG	FAU with binder	Spherical	1.6 - 2.4	8	609	UOP
APG-III	FAU with binder	Spherical	1.2 - 2.0	8	775	UOP
13X	FAU with binder	Spherical	1.2-2.0	8	677	CWK
13XBL	Binderless FAU	Spherical	1.2-2.0	8	660	CWK
5A	LTA with binder	Spherical	1.2-2.0	5	660	CWK
5ABL	Binderless LTA	Spherical	1.2-2.0	5	660	CWK
4ABL	Binderless LTA	Spherical	1.2-2.0	4	660	CWK
Carbon molecular sieves						
CMS-I	Hard coal based	Cylindrical	1.6 - 2.0	>10	630	Carbotech
CMS-II	Coconut shell based	Cylindrical	1.3 - 1.7	>10	630	SHL
CMS-III	Coconut shell based	Cylindrical	0.8 - 1.2	>10	650	SHL

2.2. Characterization of textural properties of materials

The textural properties studied in this work (surface area and narrow micropore volume) of the different adsorbents were measured with a nitrogen adsorption isotherm at 77 K and a carbon dioxide isotherm at 273 K on a static adsorption analyzer ASAP 2020 (Micrometrics, USA). The isotherms of CO_2 and N_2 adsorption on the adsorbent were also obtained with the same apparatus at discrete temperatures within the pressure range of 0–114 kPa. To remove any remaining water in the pores, the samples were degassed for 6 hours at 623 K for zeolites, and 393 K for ACs and CMSs, applying in all cases vacuum under 3 mm Hg for 17 hours prior to each adsorption experiment. Specific surface areas were calculated using the Brunauer−Emmett−Teller (S_{BET}) method, with an appropriate relative pressure range selected to ensure a correct fitting for the correlation coefficient (Parra et al., 1995; Rouquerol et al., 2007). Narrow micropore (<0.7 nm) volumes (VDA_{CO2}) were obtained from the CO_2 isotherms by applying the Dubinin-Astakhov (DA) equation to the adsorption data.

2.3. Methodology for fast screening adsorbent materials for CO_2 adsorption for TSA process.

The main challenge on the design of TSA systems is to achieve a high efficiency in the heat transfer. The operational cost due the heating and the cooling processes during the cyclic adsorption/desorption represents an important constraint in terms of the total

energy consumption. So, to reduce the column regeneration time and energy consumption can lead to recovering more of the adsorbed CO_2 per unit of time with a lower cost. The standard methods used to determine the adsorption capacity of adsorbents in the studies found in the literature are mainly differential gas adsorption manometry (Liu et al., 2011b; Su and Lu, 2012; Webley et al., 2017) and gas adsorption gravimetry (Cavenati et al., 2004; Garcia et al., 2013; Rouquerol et al., 2014a). However, these methods are very time consuming (between 1 to 2 days each measurement). In this work is described a faster screening methodology to select the suitable adsorbent and working temperature range (adsorption and desorption) for a TSA process with a simple thermogravimetric analysis (TGA) and differential scanning calorimetry (DSC). The presented methodology allows the evaluation of the adsorption/desorption capacity of an adsorbent over an entire temperature range; and similarly, qualitative information about the initial adsorption/desorption rates.

2.3.1. Determination of the CO_2 adsorption capacity and adsorption heat for TSA process.

The adsorption capacity (q_{TGA}), adsorption heat (ΔH_{ads}) and desorption heat (ΔH_{des}) of the selected materials were determined to evaluate their practicability in a TSA process, comparing q_{CO2} at a low-pressure value (0.30 barg) and the heat required to regenerate the adsorbents. q_{CO2} was determined in TGA by measuring the mass difference between the CO_2 adsorption and the desorption process by increasing the temperature. The characteristic curve for the TGA/DSC experiments for CO_2 adsorption is shown in Figure **17**.

TGA experiments were carried out on a Mettler Toledo horizontal balance TGA/DSC-1 with simultaneous TGA and DSC. The temperature and calorimetric accuracies were 0.5 °C and 0.0001 mg respectively. This instrument has up to 6 temperature sensors which were in the measurement pan. CO_2 ΔH_{ads} and ΔH_{des} were determined using a differential scanning calorimeter DSC 821, Mettler Toledo with 50 temperature sensors, which makes it more precise than the TGA/DSC-1. The temperature and calorimetric accuracies of the DSC 821 were 0.01 °C and 0.01 mJ respectively. Prior to the adsorption experiments, the temperature of the instrument's furnace and heat flow of both equipment were calibrated using a single point indium melting event. The TGA balance requires a minimum protection flow of N_2 of 20 ml/min to secure the instrument from any possible chemical interaction between the reactive gas and the sensors. The balance of both equipements were calibrated using a certified weight of indium. The

melting point and melting heat of indium (ΔH_{indium}) at atmospheric pressure is 156.6 °C and 28.43 J/g respectively.

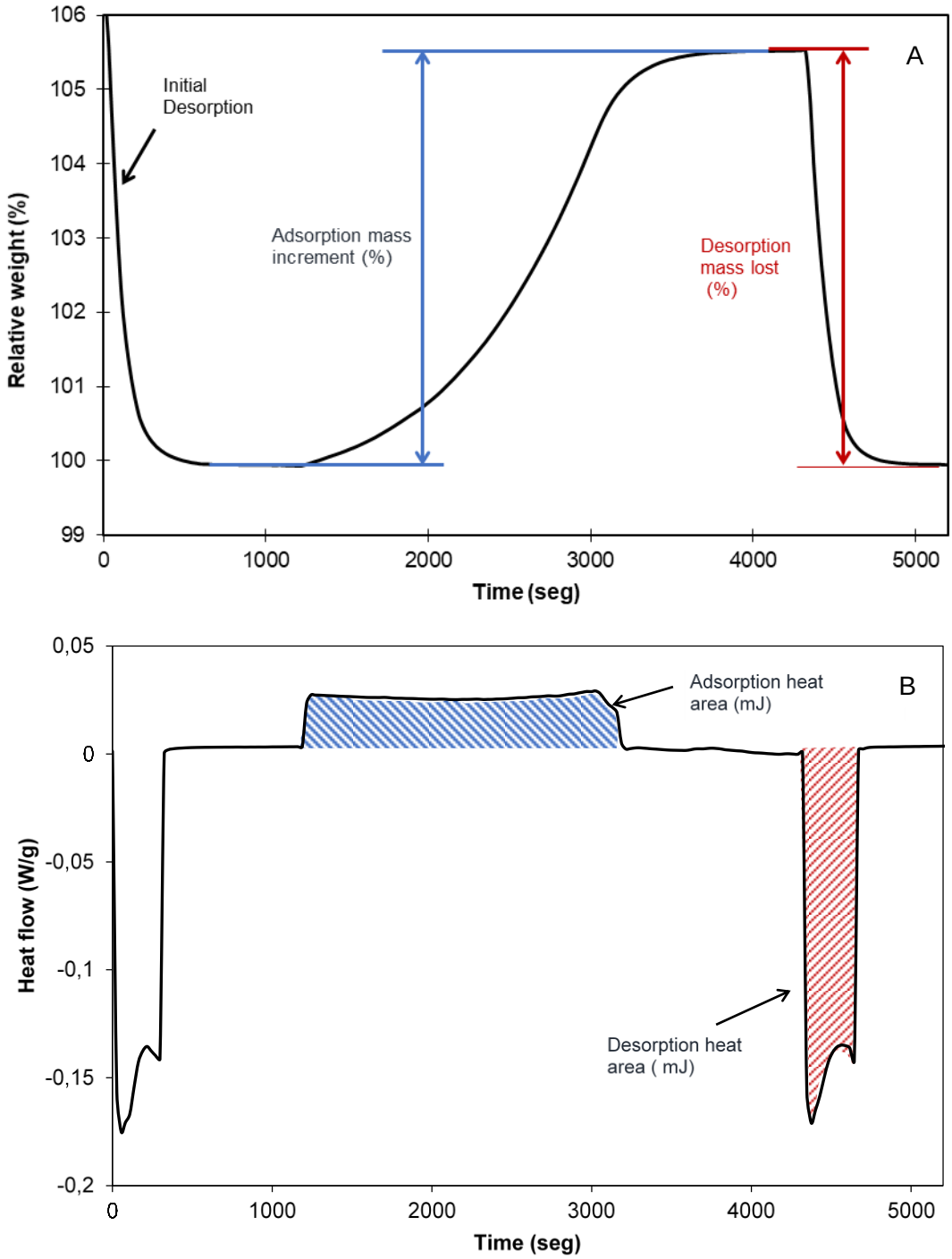

Figure 17: (A) CMS-I TGA curve for adsorption of CO_2, (B) CMS-I DSC curve for adsorption of CO_2.

The $q_{TGA,}$ ΔH_{ads} and ΔH_{des} were determined following the methodology described in Table **3**. First, carbonaceous adsorbents and zeolites were dehydrated at 200ºC for 15 minutes and 350 °C for 60 minutes respectively. Subsequently, the adsorbents were cooled down

to 40 °C and then the CO_2 adsorption was performed with 70 ml/min of a mixture of 15% CO_2/ 85% N_2 at 40°C until the adsorption equilibrium was reached. All gases used were provided by Linde Group and used as received: carbon dioxide 4.5 and nitrogen 5.0 (purity greater than 99.995% and 99.999%, respectively). The mixture of 15% CO_2/ 85% N_2 was produced setting the flow ratio of the feed gases into the TGA/DSC-1 or DSC 821 control system and measuring the feed CO_2 concentration with a non-dispersive infrared sensor (GSS, UK).

Table 3: TGA/DSC analysis method for the determination of q and ΔH for CMSs and zeolites.

Stage	CMS		Zeolites	
	Temperature (°C)	Time (min)	Temperature (°C)	Time (min)
Dehydration	200	15	350	60
Cool down	200-40	32	350-40	62
Adsorption	40	20	40	80
Desorption	40-200	6	40-350	10
Isothermal	200	10	350	60

The q_{TGA} (mmol/g) ΔH_{ads} (kJ/mol) and ΔH_{des} (kJ/mol) were calculated with Equation (1) and Equation

(2), respectively.

$$q_{TGA} = \frac{(w_{eq} - w_0) \times 10^3}{m_{adsorbent} \times MW} \quad (1)$$

$$\Delta H_{ads} = \frac{\Delta H_{indium} \cdot \left(\frac{A_{sample}}{A_{indium}}\right) \cdot \left(\frac{m_{indium}}{m_{adsorbent}}\right)}{q} \quad (2)$$

where w_{eq} is the weight (mg) when the adsorption reaches the equilibrium and w_0 is the initial weight of the adsorbent (mg) obtained from the TGA analysis. $m_{adsorbent}$ is the mass of the adsorbent (mg) and *MW* is the molecular weight of CO_2 (44 g/mol). In the determination of ΔH_{ads}, ΔH_{indium} is the melting heat of indium (J/g_{indium}), A_{sample} is the integral area of exothermic peak due to the adsorption of CO_2, A_{indium} is the integral area of endothermic peak due to the melting of indium, m_{indium} is the mass of indium (mg). Blank tests without adsorbent were also conducted to correct buoyancy effects subtracting the blank curve from the experimental curve. The calibration of these instruments is done periodically by the technician of the service, however the result of equation 2 is directly calculated by the instrument and is not directly handled by the user.

The reproducibility of the methodology was validated using different amounts of zeolite APG-III beads (from 1 to 5 beads) by triplicate.

2.3.2. Study of the Temperature Swing Adsorption cyclic behavior.

The TSA cyclic behavior was carried out during 7 cycles of adsorption/desorption with a flow of 70 ml/min of a mixture of 15% CO_2/ 85% N_2. For this study three methodologies were used. The first methodology is shown in Table 4 and it was used to compare the behavior of zeolites and CMSs at conventional TSA working temperatures (40 ºC for adsorption and 120 ºC for desorption). In this part of the study the selected adsorbents CMS-I and APG-III were used as representative of carbonaceous and zeolite materials.

Table 4: Methodology for the cyclic performance analysis of CMS-I and APG-III.

Stage	Temperature (°C)	Time (min)
Cool down	120 - 40	20
Adsorption	40	20
Desorption	40 - 120	5
Isothermal	120	5

With this first methodology, it was observed that zeolite APG-III was not completely regenerated during the desorption stage at 120ºC. For that reason, an additional experiment was carried out with APG-III increasing the desorption temperature up to 350ºC (Table 5) with the objective of comparing the cyclic performances of APG-III and CMS-I under conditions of complete regeneration.

Table 5: Methodology for the cyclic performance analysis at complete regeneration of APG-III.

Stage	Temperature (°C)	Time (min)
Cool down	350-40	70
Adsorption	40	20
Desorption	40-350	15
Isothermal	350	5

The influence of the desorption temperature on the TSA performance was studied with the methodology described on Table 6, a set of experiments was carried out varying the desorption temperature from 60ºC to 150ºC while the adsorption temperature was kept at 40°C.

Table 6: Methodology for study the influence of desorption temperature in the cyclic performance of APG-III.

Experiment	Adsorption Temperature (ºC)	Desorption Temperature (ºC)	Cycle time (min)
1	40	60	142
2	40	90	156
3	40	120	163
4	40	150	161

On the other hand, flue gases typically are at high temperatures (90ºC to 120ºC). Therefore, the influence of the adsorption temperature on the TSA performance was studied with the methodology described on Table 7. To investigate this impact a set of experiments was carried out using different adsorption temperatures, from 40ºC to 120ºC while the desorption temperature was kept at 150°C. The selected range of temperatures in this study was selected according to the literature (Ling et al., 2015). Zeolite APGIII was used in the experiments, and all the experiments were performed with 70 ml/min of a mixture of 15% CO_2/ 85% N_2.

Table 7: Methodology for study the influence of adsorption and desorption temperatures for APG-III.

Experiment	Adsorption Temperature (ºC)	Desorption Temperature (ºC)	Cycle time (min)
1	40	150	161
2	60	150	155
3	90	150	148
4	120	150	144

2.4. Adsorption equilibrium isotherms for pure components.

Adsorption equilibrium isotherms of pure gases on different adsorbents were performed in a magnetic suspension microbalance (Rubotherm-VTI, Germany) operated in a closed system. The sample of adsorbent is weighted and placed in a basket suspended by a permanent magnet through an electromagnet (magnetic suspension coupling). The cell in which the basket is housed is then closed, and vacuum is applied. An analytical balance connected to the magnetic coupling receives the weight values measured inside the cell, and through an acquisition system, records the data in a computer (see Figure **18**). A description of the gravimetric unit operation is given elsewhere (Cavenati et al., 2004). Prior to the experiment, the adsorbents were degassed under a vacuum at 350°C

for zeolites and 150ºC for CMSs at high vacuum conditions ($1x10^{-8}$ mbara). Monocomponent adsorption of N_2 and CO_2 were measured at 283 K, 298 K, 323 K, 343 K in the range of 0 to 1000 KPa. The reversibility of the isotherms was confirmed performing the desorption measurements without hysteresis. The heating rate to reach this temperature was 5 K/min with an accuracy of 0.01 K and an accuracy for weight measurement of 1µg. Corrections for buoyancy effects were performed in the pressure range studied.

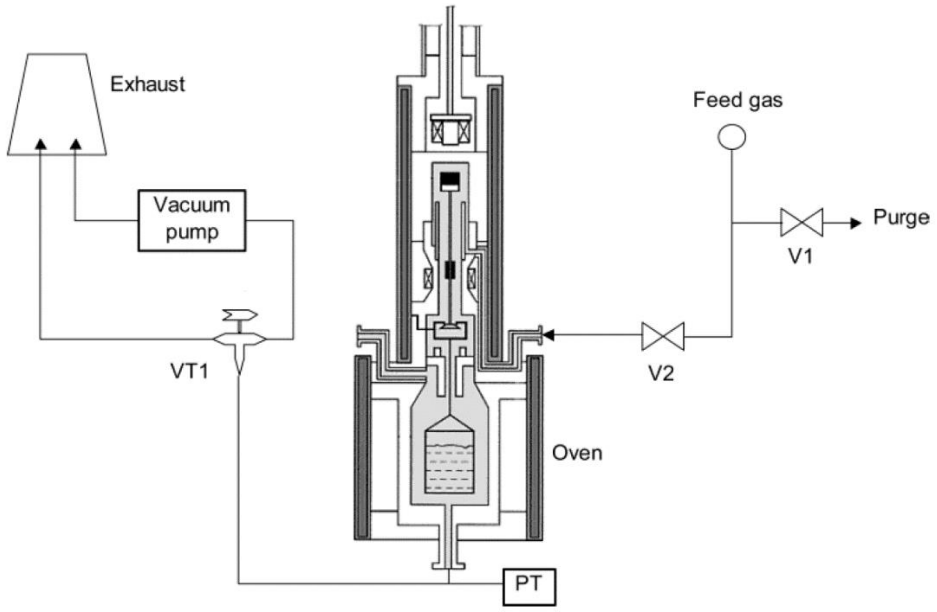

Figure 18: Experimental set-up of the closed unit used for gravimetric measurements: V1 and V2, on-off valves; VT1, three-port valve; PT, pressure transducer; VP, vacuum pump (Dreisbach et al., 1999)

2.4.1. Monocomponent adsorption data handling

In the high-pressure magnetic suspension balance, absolute adsorption cannot be obtained directly from the gravimetric measurement, and the excess mass adsorbed is obtained instead. The excess and absolute adsorption are correlated as follows (Cavenati et al., 2004):

$$q = q_{exc} + \frac{\rho_g V_{ads}}{m_s MW} \quad (3)$$

where q (mmol/g) is the absolute amount adsorbed, q_{exc} (mmol/g) is the excess amount adsorbed, ρ_g *(g/L)* is the density of the gas, V_{ads} (L) is the adsorbed volume of the gas, m_s is the mass of adsorbent (g), and *MW* (g/mol) is the adsorbate molecular weight. Although in gas adsorption under a sub-atmospheric pressure range V_{ads} is negligible, it cannot be neglected in a high pressure range (Hamon et al., 2014; Murata et al., 2002).

In this case, either the density or volume of the adsorbed phase must be known, which are not readily accessible by an experimental measurement. Thus, estimates of the adsorbed phase density or volume are usually employed. Herein, the volume of the adsorbed phase is approximated by (Dreisbach et al., 1999)

$$V_{ads} \cong \frac{m_{ads}}{\rho_L} \tag{4}$$

where m_{ads} (g) is the mass of the adsorbed phase and ρ_L *(g/L)* is the adsorbed phase density, which is assumed to present a density similar to that of the liquid phase at the adsorption temperature (T_{ads}). The adsorbate liquid phase density is then calculated as

$$\rho_L = \frac{M}{V_m} \tag{5}$$

V_m (L) is the molar volume calculated by the Gunn-Yamada method (Poling et al., 2001) when $T_{ads} < T_c$ (T_c is the critical temperature of the adsorbate) and equals the van der Waals co-volume of the adsorbate, b, when $T_{ads} \geq T_c$. By replacing equation (4) into equation (3), we get that the absolute adsorption capacity can be calculated from the following equation (Garcia et al., 2013):

$$q = \frac{\Delta m + \rho_g (V_S + V_i)}{m_s M} \cdot \frac{\rho_L}{\rho_L - \rho_g} \tag{6}$$

where Δm (g) is the microbalance signal when adsorption equilibrium is reached, ρ_g *(g/L)* is the density of the gas at measuring conditions, and (V_S+V_i) are the adsorbent volume and measuring cell volume, respectively. These volumes are measured by adsorption isotherm measurements with helium as adsorbate and assuming that it accesses the total pore volume of the sample without being adsorbed. Helium measurements were done at 338 K and pressures that were similar to conditions during an adsorption run with adsorptive gases. Prior to the measurements, the measuring cell with the adsorbent was dried under vacuum at 373 K for 120 min. The cell was then cooled down to the measuring temperature, and pressurization was attained with He in a stepwise mode (Garcia et al., 2013).

2.4.2. Monocomponent isotherm models

The Langmuir equation (equation (*7*), describes monolayer surface adsorption on an ideal and flat surface assuming surface homogeneity, localized adsorption on the solid surface, and energetically equivalent adsorption sites, were q (mmol/g) is the total

adsorbed amount and *P* (bara) is the pressure in the system (Do, 1998). The equation contains two parameters: the saturation capacity, q_s (mmol/g), and the affinity constant parameter, *b* (1/bara). It is important to have the temperature dependence form of an isotherm equation, so that adsorption equilibrium at various temperatures can be described. The affinity constant's dependence on temperature is described using an Arrhenius-type equation (equation

(2) with parameters b_0 (1/bar) and ΔH_i (kJ/mol), which correspond to a pre-exponential factor and the isosteric heat of sorption respectively. *T* (K) is the system's temperature, and *R* (kJ/K·mol) is the ideal gas law constant.

$$q = \frac{q_s b P}{1 + bP} \tag{7}$$

$$b_i = b_0 \exp\left(\frac{-\Delta H_i}{RT}\right) \tag{8}$$

Adsorption in real solids, however, is a heterogeneous process because solids present complex porous and surface structures, which rarely satisfy the basic assumptions made in the Langmuir theory. This heterogeneity is characteristic of the specific solid-adsorbate pair rather than the solid alone. Thereby, many semiempirical approaches have been successfully developed to describe equilibrium data, such as the ones described next.

The Sips equation (equation (9) sometimes called the Langmuir-Freundlich equation in the literature because it has the combined form of Langmuir and Freundlich equations, has three model parameters, the saturation capacity, q_s (mmol/g), the affinity constant parameter, *b* (1/bar) and the parameter "*n*". Parameter *n* characterizes the system heterogeneity for ideal surfaces. The system heterogeneity could stem from the solid or the adsorbate or a combination of both. The parameter *n* is usually greater than unity, and therefore the larger is this parameter the more heterogeneous is the system. The temperature dependence of *b* is taken from that of the Langmuir equation. The difference between this equation and the Langmuir equation is the additional parameter "n" in Sips equation. If the parameter "n" is one, the Langmuir equation is recovered.

$$q = \frac{q_s (bP)^{1/n}}{1 + (bP)^{1/n}} \tag{9}$$

The Freundlich equation is not valid at the low and high ends of the pressure range because it does not possess the correct Henry's law type behavior. One of the empirical equations that is popularly used and satisfies the low and high limits is the Toth equation. This equation describes well many systems with sub-monolayer coverage, and it has the following form

$$q = \frac{q_s bP}{[1 + (bP)^t]^{1/t}} \tag{10}$$

Here "*t"* is the Toth heterogeneity parameter, which is usually less than unity. The parameters *b* (1/bar) and *t* are specific for adsorbate-adsorbent pairs. When *t* is one, the Toth isotherm reduces to the famous Langmuir equation; hence like the Sips equation the parameter *t* is said to characterize the system heterogeneity. If it deviates more from unity, the system is said to be more heterogeneous. Because of its simplicity in form and its correct behavior at low and high pressures, the Toth equation is recommended as the first choice of isotherm equation for fitting data of many adsorbates such as hydrocarbons, carbon oxides, hydrogen sulfide and alcohols on activated carbon as well as zeolites. The Sips equation presented in the last section is also recommended but when the behavior in the Henry's law region is needed, the Toth equation is the better choice (Do, 1998).

An alternative model to fit the pure component data is the single gas dual-site Langmuir (DSL) four parameters model q_{s1} (mmol/g), q_{s2} (mmol/g), b_1(1/bar) and b_2 (1/bar), which describes the adsorption of a pure component on a heterogeneous adsorbent that is composed of two homogeneous but energetically different sites (Bhadra et al., 2012; Ritter et al., 2011). All the assumptions of the Langmuir model apply to each patch, with no interactions between the two patches. The amount adsorbed would be given by equation (11):

$$q = \frac{q_{s1} b_1 P}{1 + b_1 P} + \frac{q_{s2} b_2 P}{1 + b_2 P} \tag{11}$$

where q_{s1} and q_{s2} are the saturation capacities at site 1 and 2, respectively, so the total saturation capacity is the sum of those on each patch or site (q_s=q_{s1}+q_{s2}); b_1 and b_2 are the affinity parameters or free energy for site 1 and 2, respectively, which are considered to be temperature-dependent as expressed in equation (12), where the subscript *j* represents the free energy level of site 1 or 2, b_0, *j* are the pre-exponential factors or adsorption entropies, and ΔH_j (kJ/mol) are their corresponding adsorption energies.

$$b_j = b_{0,j} \exp\left(\frac{-\Delta H_j}{RT}\right) \tag{12}$$

In equation (12), *j=1* always denotes the higher adsorbate-adsorbent free energy as opposed to *j*=2 that always denotes the lower adsorbate-adsorbent free energy. The free energy of site 1 is always higher than that of site 2 for single-gas adsorption (Ritter et al., 2011).

2.4.3. Binary dynamic adsorption experimental procedure.

Binary dynamic experiments were carried out in a fixed bed previously saturated with N_2 with 13XBL and 5ABL. The experiments were performed at 293 K, 313 K, 333 K and 363 K over a range of absolute pressures from 1.3 bara to 8 bara. These values cover the temperature conditions likely to be found in a post combustion capture scenario, where CO_2 needs to be separated from a CO_2/N_2 gas stream. The experiments were performed using a mixture of 15% CO_2 and 85% N_2, with a flowrate of 5 L/min. The adsorbent saturation is reached when the concentrations on the inlet (C_{in}) and the outlet (C_{out}) streams are the same, in order to assess the maximum dynamic adsorption capacity of the adsorbent.

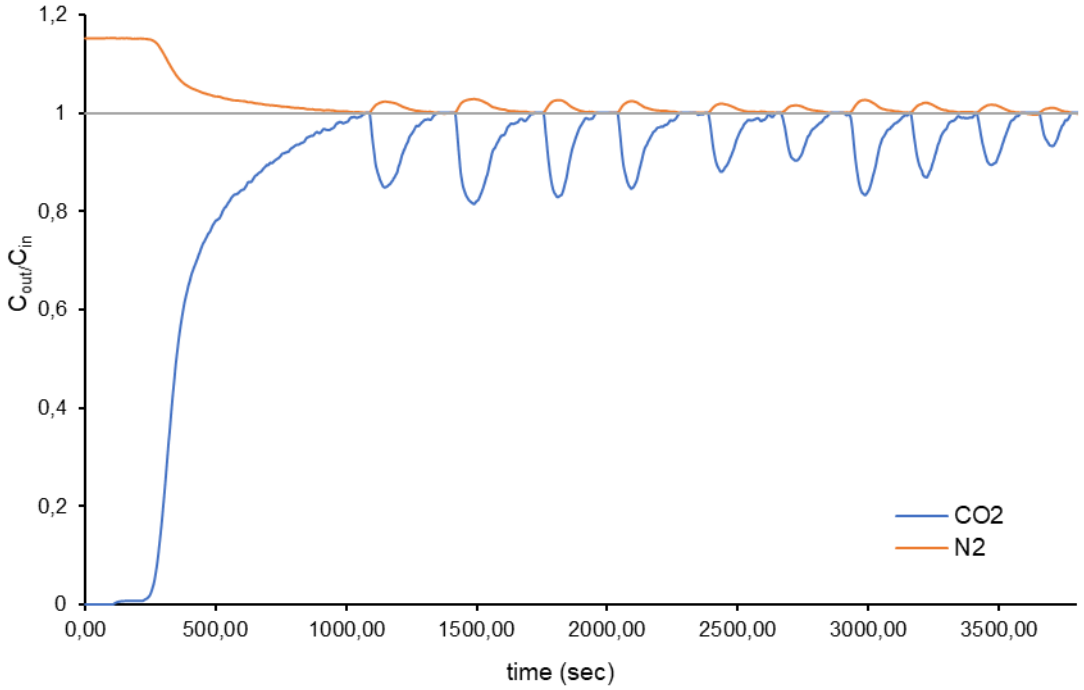

Figure 19: N_2 and CO_2 binary adsorption breakthrough curves of binderless zeolite 5ABL in a fixed bed at 298 K.

The concentration profiles of N_2 in Figure 19 show that this component is detected from the beginning of the adsorption step since it is not adsorbed on the solids bed, while CO_2 is not detected over a period of time and thus adsorbed. Once reached the saturation of CO_2 and N_2, the pressure is increased from 1.3 to 8.0 bars, reaching on each pressure the column saturation. Through the breakthrough curves it is possible to calculate the accumulated moles of CO_2 and N_2 of the binary adsorption by subtracting the area under the curves of the input and the output streams and multiplying by the molar flow of each substance (see Figure 19). As the column is previously saturated with nitrogen, the volume of nitrogen must be subtracted for the calculation of the initial adsorption. Prior

to each experiment, degassing of the adsorbent was carried out under vacuum at 423 K overnight. All gases used were provided by Linde Group and used as received: carbon dioxide 4.5 and nitrogen 5.0 (purity greater than 99.995% and 99.999%, respectively).

2.4.4. Binary adsorption equilibrium equations.

Successful prediction of binary adsorption equilibria relies entirely on an accurate measurement of single component data and on a reliable correlation of these data with an isotherm model (Garcia et al., 2013). Using the pure component isotherm parameters, adsorption equilibria of binary mixtures can be predicted by extending the corresponding single component equations to binary adsorption equations.

Thus, the amount adsorbed of component i of a binary mixture is given by equations (*13*), (*14*) and (*15*), which are known as the extended binary Toth, Sips, and DSL equations, respectively.

$$q_i = \frac{q_{s,i} b_i y_i P}{[1 + (\sum_{k=1}^{n} b_k y_k P)^{t_i}]^{1/t_i}} \tag{13}$$

$$q_i = \frac{q_{s,i} (b_i y_i P)^{1/n_i}}{1 + (\sum_{k=1}^{n} b_k y_k P)^{1/n_i}} \tag{14}$$

$$q_i = \frac{q_{s1,i} b_{1,i} y_i P}{1 + \left(\sum_{k=1}^{n} b_{1,k} y_k P\right)} + \frac{q_{s2,i} b_{2,i} y_i P}{1 + \left(\sum_{k=1}^{n} b_{2,k} y_k P\right)} \tag{15}$$

In equations (*13*), (*14*) and (*15*), *i* stands for the species for which the isotherm q_i is being evaluated, *y* would be the gas mole fraction of the corresponding component (denoted by subscript *i* or *k*), and *n* is the total number of components in the gas mixture.

2.5. Key adsorption performance indicators.

The optimization of a TSA or VPSA process involves minimizing its costs, namely both the capital and operating costs, which are controlled primarily by the productivity and the specific energy consumption, respectively (Joss et al., 2017).The performance of an adsorbent for a separation depends on several factors. One of the most important is its working capacity (w; mmol/g). This is defined as the difference between the uptake at the feed pressure and the uptake at the regeneration pressure.

$$w_i = \frac{(m_{adsorbed} - m_{desorbed}) \times 10^3}{m_{adsorbent} \times MW} \quad (16)$$

MW (g/mol) is the molecular weight, $m_{adsorbed}$ (g) and $m_{desorbed}$ (g) were the mass of CO_2 adsorbed and desorbed respectively. For any given adsorbent, working capacity depends partly on the isotherm shape. Figure 20 shows the pressure-swing and temperature swing cycles in PSA and TSA, where *n* is the equilibrium amount adsorbed and *P* is pressure, and the working capacity i in each case is given by n_{ads}-n_{des}. Lowering P_{des} in VPSA increases n_{ads}-n_{des}, as does increasing T_{des} in TSA. Then, for TSA, the working capacity is the difference between the uptakes at the feed temperature and the regeneration temperature at the working pressure and for VPSA it is the difference between the uptakes at the feed pressure and the regeneration pressure at the working temperature. The steeper the isotherm in the operating pressure range at the process temperature, the greater the working capacity (for an adsorbent with a given saturation uptake).

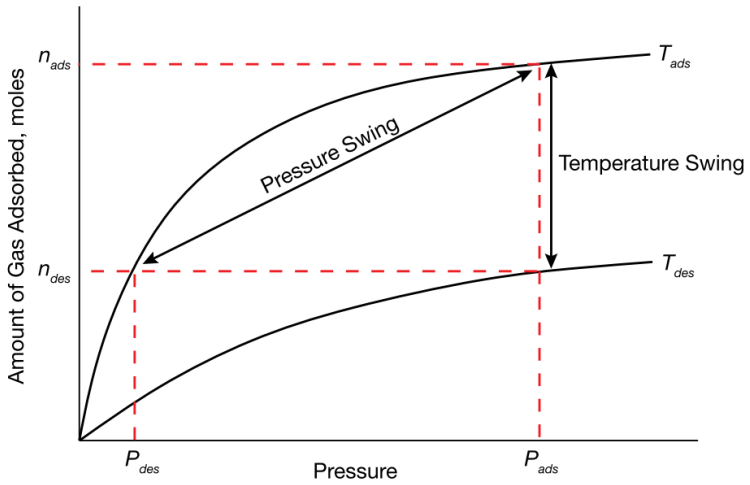

Figure 20: Adsorbent's working capacity depends on the shape of its isotherm (Broom, 2018).

The adsorbent used in a TSA or VPSA process must thereby fulfill certain specifications, which are a minimum working capacity, mechanical and thermal stability. However, for an optimal separation the equilibrium selectivity is more important. Selectivity (S_{eq}), is usually defined as:

$$S_{eq} = \frac{n_1/n_2}{p_1/p_2} \quad (17)$$

where n_1 (mol) and n_2 (mol) are the molar loadings of Species 1 and 2 at partial pressures of p_1 (bar) and p_2 (bar), respectively under the process conditions. For an adsorption process the kinetic selectivity (S_{kin}) depends on the ratio of the uptakes in a given time

which, for a diffusion controlled process, kinetic selectivity meanwhile, can be expressed as (Ruthven, 2011):

$$S_{kin} = \frac{q_1}{q_2} = \frac{K_1}{K_2}\sqrt{\frac{D_1}{D_2}} \tag{18}$$

where q_1 and q_2 are total adsorbed amount of species 1 and 2, the K_1 and K_2 are the Henry's law constants and D_1 and D_2 are the diffusivities of species 1 and 2, respectively. Equilibrium selectivity therefore depends on the relative equilibrium quantities of each component adsorbed under the process conditions, whereas kinetic selectivity depends on differences in diffusion rates. The productivity (*Pr) i*s defined as the working capacity divided by the total cycle time. The productivity was given with the following equation:

$$Pr = \frac{m_{CO2}}{t_{cycle} \cdot m_{ads}} \tag{19}$$

Where t_{cycle} (h) is the total cycle time, m_{ads} is the mass of the adsorbent and m_{CO2} is the weight of CO_2 recovered (g_{CO2}). Besides, the energy consumption (e_{TSA}) of the TSA/VPSA was evaluated measuring the amount of energy used to adsorb and desorb the CO_2 over the cycle time. For TSA process, the energy consumption was determined with DSC analysis by integrating the heat by mass of adsorbent (kJ/g_{ads}) used during the desorption (ΔH_{des}) and adsorption (ΔH_{ads}) steps in each cycle per unit time and CO_2 adsorbed amount (mmol/g_{ads}).

$$e_{TSA} = \frac{\Delta H_{des} + \Delta H_{ads}}{q_i \cdot t_{cycle}} \tag{20}$$

In the case of VPSA, the energy consumption was determined measuring the power consumption (PC) used during the process with a power meter measuring watts per unit time (W·h) divided by the weight of CO_2 recovered.

$$e_{VPSA} = \frac{PC}{m_{CO2}} \tag{21}$$

3. Cyclic adsorption design and experimental procedure.

3.1. Process description based on the VPSA process for CO_2 capture from flue gas.

For CO_2 capture from flue gases needs to be concentrated from a low concentration stream (9 to 15% CO_2 v/v). Therefore, the scheduling of the VPSA process should be based on this requirement (Ling et al., 2014; Riboldi and Bolland, 2017b). Usually, two modifications to the Skarstrom cycle have been proposed to improve the heavy product purity or enrichment, namely, the addition of a cocurrent depressurization step or the addition of a high pressure rinse (i.e., heavy reflux) step.(Liu et al., 2011a) The use of residual flows is applied to reduce energetic consumption related to compression energy to economize the process. In this work, an eight step VPSA process was employed to produce high-purity CO_2 as follows: The steps of this cycle are displayed in Figure 21

(1) Pressurization (FP): The pressure is increased from low pressure to a higher pressure with feed of flue gas.

(2) Feed (FD): When the working pressure is achieved, the column outlet is opened. In this step, the CO_2 is preferentially absorbed, and the N_2 as the element less retained (termed as raffinate) flows through the adsorbent to the outlet.

(3) Depressurization (DP): After the feed step, the pressure of the column is reduced to atmospheric pressure (concurrently to feed).

(4) Rinse (RN): Part of the CO_2 is recycled to the column before desorption. The product gas, which is already highly enriched in CO_2, displaces the N_2 from the adsorbed phase near the feed end of the column and flushes it downstream towards the N_2 end of the column.

(5) Provided pressure equalization (EP). This step is performed by putting two columns at different pressure levels into contact to save energy. The high pressure of the column can be reduced.

(6) Regeneration (RG). In this step, CO_2 is removed from the adsorbent. In VPSA technology for CO_2 capture, high-purity CO_2 will be recovered in this step. The blowdown is carried out at lower pressure.

(7) Purge (PR): To remove the CO_2 from the adsorbent, a counter-current purge with N_2 exiting from the other column at the feed step is carried out. This step is also carried out at the lowest pressure of the system.

(8) Received pressure equalization (ER): The column is connected with the provided pressure equalization column to receive the compression energy and reduce the energy consumption on the pressurization stage.

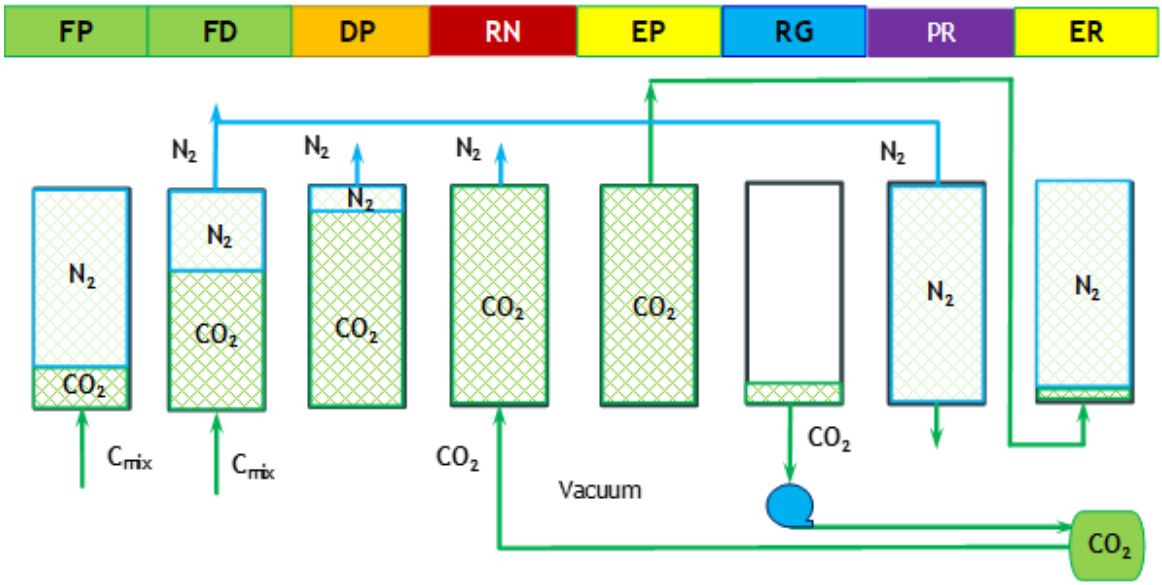

Figure 21: Eight steps VPSA cycle in a column representation.

3.1.1. Single column batch configuration.

To study the competitive adsorption kinetics of CO_2 and N_2 in a fixed-bed experiment, a batch configuration of the cycle previously described is shown in Figure 22. In the process sequence, each cycle is explained in a series of steps or events. These batch configuration steps are the co-current pressurization with feed, high pressure feed, countercurrent depressurization to atmospheric pressure, counter-current regeneration at low pressure, countercurrent purge at low pressure with nitrogen to displace carbon dioxide from the product end and a pressure equalization using an auxiliary tank.

The operating conditions and each step duration employed in the VPSA single column batch configuration are the following: column jacket temperature (T_t), constant adsorption pressure (P_T), desorption time at the vacuum pressure (t_V). The kinetic control based on the continuous monitorization of section 3.4.1 is included in said configuration. The control parameters for the process of each step are: the three-output stop point variables S_{FD}, S_{PR} and S_{RN}, the vacuum pressure on the regeneration step (P_V) and the flowrates on the feed (Q_{FD}), rinse (Q_R) and the vacuum (Q_V) streams.

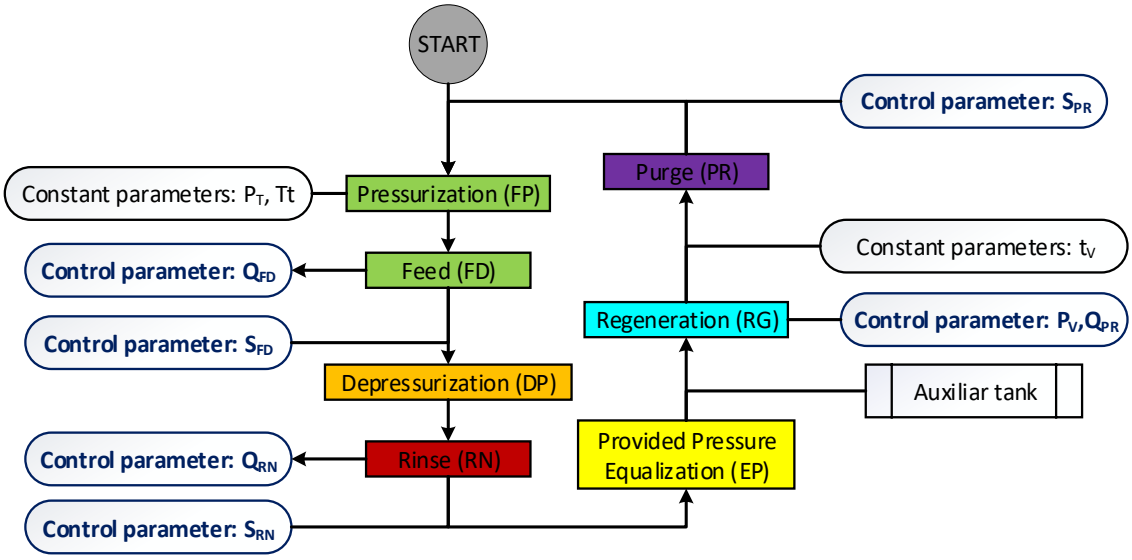

Figure 22: Schematic diagram of a VPSA batch description for fixed bed experiments.

3.1.2. Three-column cyclic configurations for VPSA for CO_2 capture from flue gas

To arrange the steps in continuous sequence, three columns were chosen for this work (Liu et al., 2012). The Figure 23 shows the different interconnections in the three column VPSA process steps. When the column is in the feed step, the stream is rich in nitrogen from the raffinate stream, and this is then used for the purge step in a different column. The CO_2 separated in the process is then recirculated in the rinse step. In the equilibrium step the energy pressure of one column filled with CO_2 after the rinse step is transferred to another column that is going to be pressurized for the pressurization step.

Figure 23 also shows the scheduling of the eight process steps combined sequentially in three columns represented through the numbers 1, 2 ,3. Each column step and step stream is represented with a different color as follows: Feed and pressurization, green; depressurization, orange; rinse, red; provided or received equalization, yellow; regeneration, blue and purge, purple. The CO_2 is stored in a tank after the desorption through the vacuum pump (VP) for later reflux.

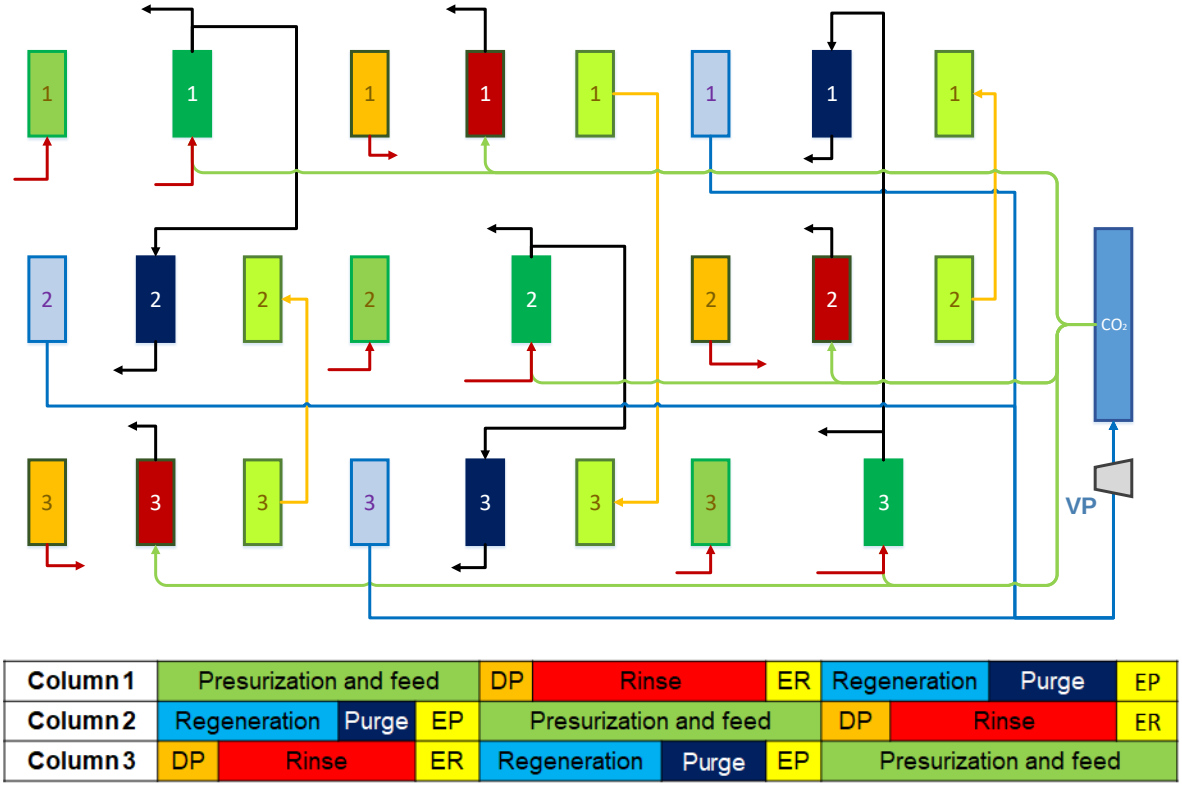

Figure 23: Interconnections on the three column VPSA process. VP; vacuum pump.

3.2. Experimental set-ups.

3.2.1. Equipment to produce gas mixtures.

The experimental set-up allows to work with binaries gas mixtures from 1 to 99% v/v of CO_2/N_2. The diagram of the experimental apparatus employed to produce CO_2/N_2 mixtures is shown in Figure 24. The apparatus consists of a gas static mixer connected to a N_2 generator GN-03 (GasN2, Spain) of 99.999% of N_2 purity and a CO_2 gas cylinder of 99.995%of purity. The system can work between 0.1 to 4 bara of pressure on the low-pressure mixture tank and until 9 bara in the high-pressure tank, with a product flowrate between 1.2 to 69.1 g/min of mixture 15% CO_2, 85%N_2 v/v. The CO_2 concentration was analyzed with a nondispersive infrared absorption sensor I-208 (Gas Sensing Solutions, Scotland). The flow of CO_2 was controlled with a mass-flow controller I-207 (M+W Instruments GmbH, Germany), the flow of N_2 was fixed with a needle valve V-201. The pressure of both gases is controlled by pressure controllers I-206 and I-207 (SMC, Japan), and the setup is equipped with two pressure transmitters I-210 and I-211 (Wika, Spain) for monitoring the pressure on the mixture generation. The pure gas streams are previously filtered by two centrifugal filters (one on each gas line). A static mixer with intern deflectors ensures the constant mixing profile and avoid the stratification of the

mix and a solenoid valve (Metalwork, Italy) control the mixture gas generation. A programmable logic controller (PLC) with a data-acquisition system (Schneider Electric, France) was used to automate the processes. Figure 25 shows a photograph of the installation of the developed mixture equipment system.

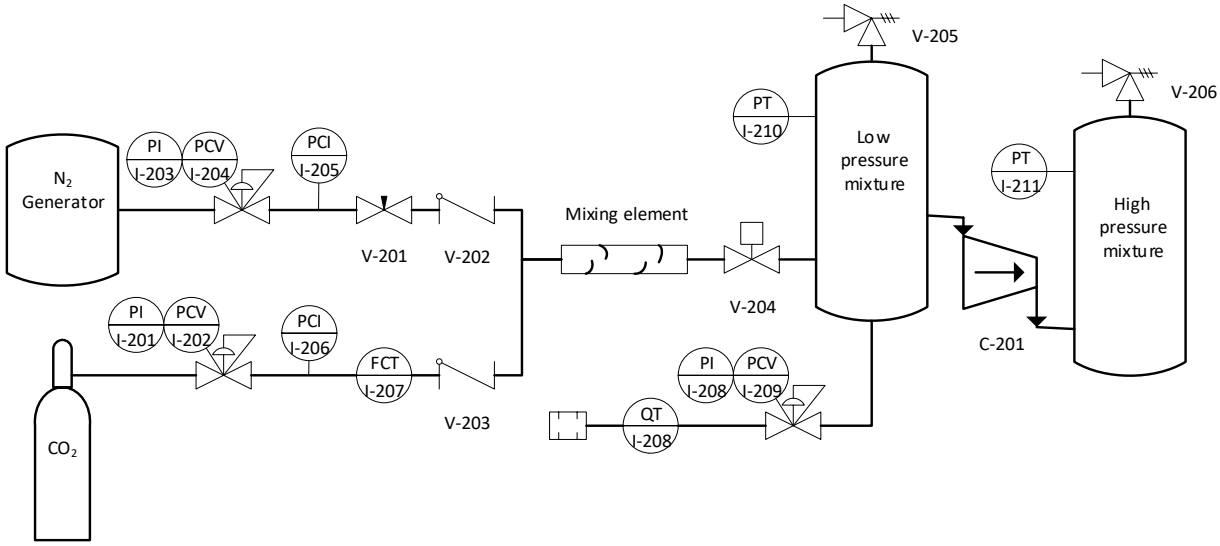

Figure 24: Equipment to produce gas CO_2/N_2 gas mixtures. Symbols: PCV, Pressure controller valve; PCI, Pressure controller and indicator; PI, Pressure Indicator; FTC, flow transmitter and controller, pressure transmitter; QT, Concentration transmitter.

Figure 25: Picture of the mixer equipment developed.

The pipes are made of stainless steel of ¼ diameter (Inoxpress, Italy), the flexible tubing is made polyamide (Parker, U.S.) and all connections are automatic push in fitting "R" series (Metalwork, Italy). The nitrogen was provided by a nitrogen generator GN-03 (GasN2, Spain) of 99.999% of N_2 purity.

3.2.2. Single column VPSA laboratory setup for dynamic equilibrium experiments.

A single column VPSA laboratory setup was built to carry out dynamic equilibrium experiments. The adsorption column was designed with Solidworks® as a tube and shell exchanger with service fluid to control the temperature of the adsorbent in the column. The column was built with an inner aluminum tube of 25 mm of diameter, 340 mm of length and 3.4 mm of thickness. The tube is enclosed by a second aluminum tube of 53 mm of diameter with a 2.5 mm of thickness, the total length of the column is 340 mm. In both cases an aluminum alloy 6060 (Aalco, England) was used as a construction material. The jacket formed between the two concentric tubes is used to keep the internal bed temperature constant. The temperature of the column was controlled and adjusted by a thermostat (JULABO GmbH, Germany) for the adsorption process and for adsorbent degassing. Figure 26 shows the 3D design of the adsorption column.

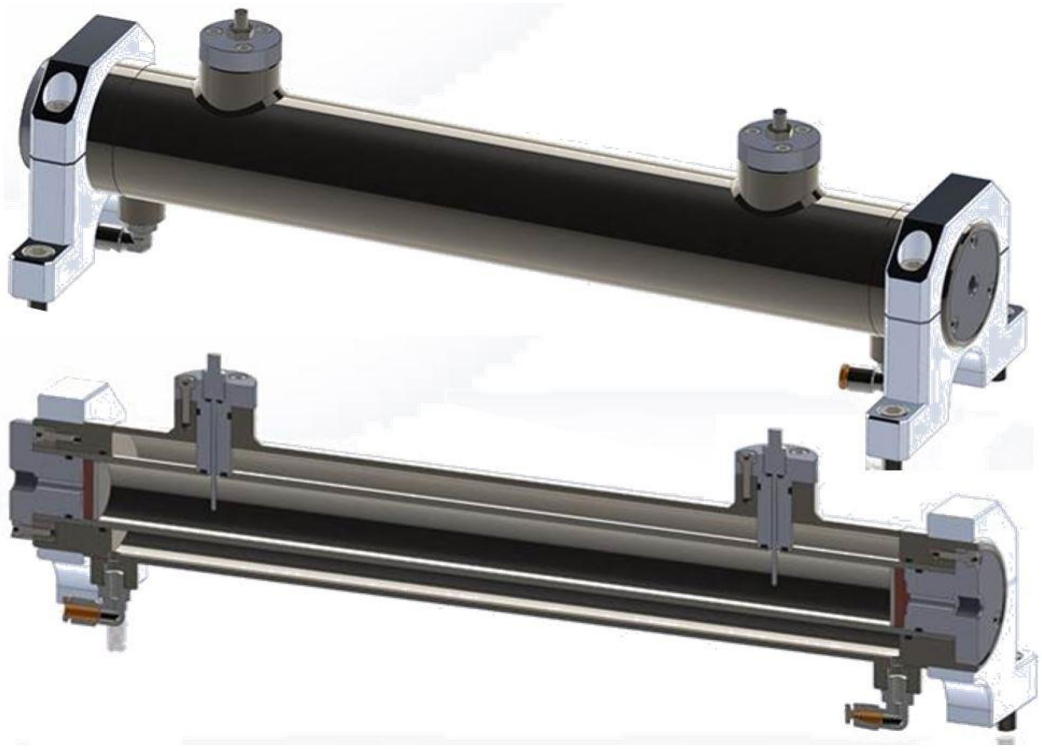

Figure 26: 3D design of the adsorption column.

The diagram of the experimental apparatus is shown in Figure 28, the column is equipped with three pressure transmitters I-106, I-111 and I-120 and a vacuum pressure transmitter I-115 (Wika, Spain). The temperature of the column was monitored with two thermocouples (Electricfor, Spain) located at 5 cm I-113 and 33 cm I-114 from the bottom of the column. The range of operating conditions was between 0.1 to 8 barg of pressure and temperatures between 10ºC to 160ºC, with a feed flowrate between 0.2 to 69 g/min

of a mixture 15% CO_2, 85% N_2 v/v. The inlet and the outlet gas temperature were measured with two thermocouples I-110 and I-114 respectively (Electricfor, Spain). The flow of the gas in the column inlet I-107 was controlled with a mass-flow controller (M+W Instruments GmbH, Germany), the column outlet I-118 and the regeneration I-123 streams were measured with two mass-flow meters (M+W Instruments GmbH, Germany).

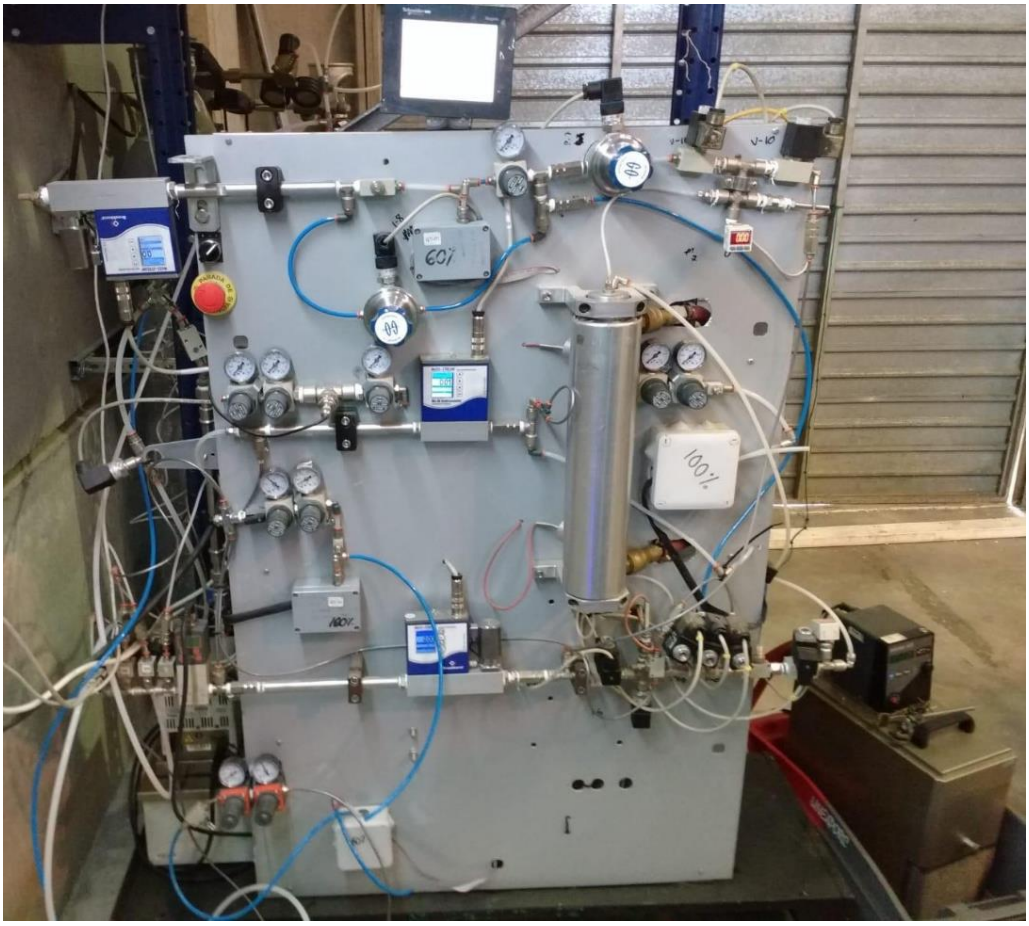

Figure 27: Picture of the single column VPSA laboratory developed.

The CO_2 concentration was analyzed with nondispersive infrared absorption (Gas Sensing Solutions, Scotland) sensors I-109, I-117 and I-122. The pressure of all the columns is controlled by a backpressure regulator valve I-116. To keep the pressure constant over the CO_2 sensors, a second backpressure regulator valve I-119 and two pressure regulator valves I-108, I-121 were used. For the desorption steps a diaphragm vacuum pump P-101 (Thermo Fisher Scientific, Spain) was used. A PLC with a data-acquisition system (Schneider Electric, France) was used to automate the processes. Figure 27 shows the installation of the developed VPSA system setup installed with a single column.

The diagram of the experimental apparatus employed to measure the dynamic adsorption equilibrium is shown in Figure 28. Table 8 gives the details of the column used in the fixed bed experiments. The instrument specifications and accuracies are listed along the Table 11 and Table 12 on section 3.4.3 for the control and automatization set-up.

Table 8: Column specifications used in the fixed bed experiments and simulations.

Parameter		Value
Column radius	m	0.025
Column length	m	0.38
Density of column wall	kg/m^3	2720
Column wall thickness	m	0.0034
Wall heat capacity	$J/(kg \cdot K)$	887
Wall thermal conductivity	$W/(m \cdot K)$	147

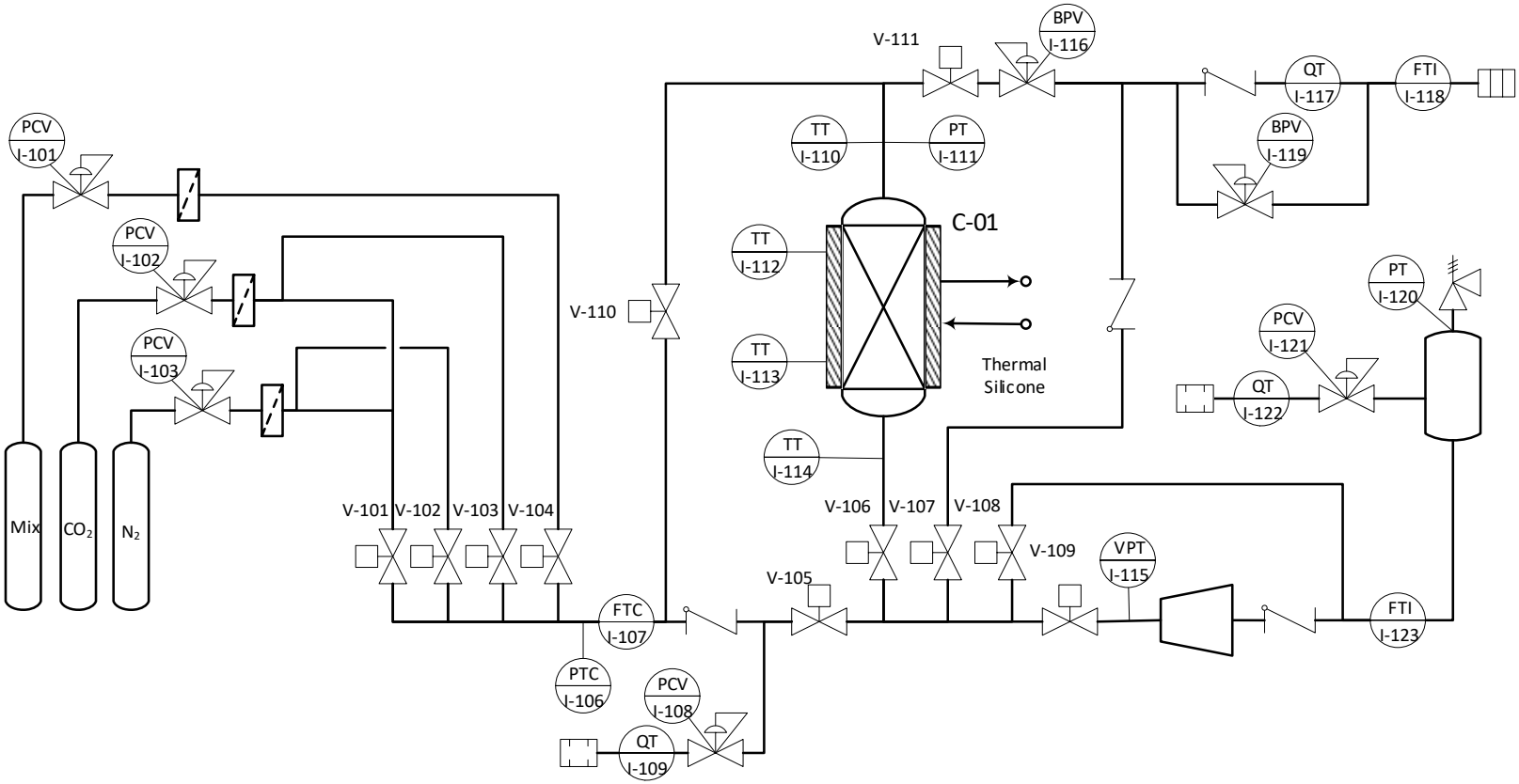

Figure 28: Schematic experimental set-up for single column VPSA. Symbols: PCV, Pressure controller valve; FTC, flow transmitter and controller; FTI, flow transmitter and indicator; PT, pressure transmitter; VPT, vacuum pressure transmitter, QT, concentration transmitter.

3.2.3. Three columns VPSA setup for cyclic experiments.

The equipment was designed for two column sizes, a set of three jacketed columns of same as those described on section 3.2.2 and a set of three columns with jackets (a tube and shell exchanger) of internal diameter 5.0 cm and packing length 70.0 cm. The tube is enclosed by a second tube of 76 mm of diameter with a 3.0 mm of thickness. In both cases an aluminum alloy 6060 (Aalco, England) was used as a construction material. The VPSA prototype was designed with Solidworks®. Figure 29 (A) shows the VPSA apparatus design represented with a 3D model with the 5.0 cm diameter set of columns, Figure 29 (B) displays the internal configuration of the apparatus and Figure 29 (C) shows how the VPSA apparatus was as built with the 2.5 cm diameter set of columns.

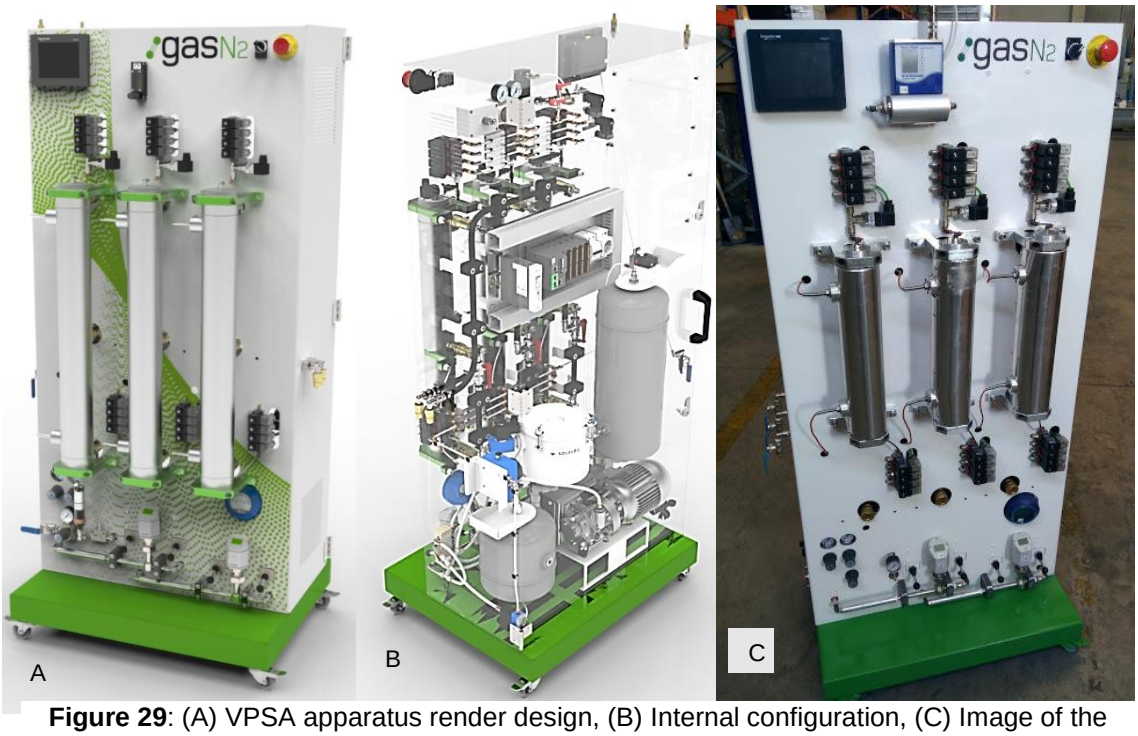

Figure 29: (A) VPSA apparatus render design, (B) Internal configuration, (C) Image of the VPSA cyclic prototype.

The diagram of the VPSA experimental prototype employed to measure the cyclic adsorption is shown in Figure 30. The experimental prototype allows to work in a wide range of operating conditions for a cyclic VPSA process. The pilot setup can work between 0.1 to 8 barg of pressure and temperatures between 10ºC to 160ºC, with a feed flowrate between 0.5 to 138 g/min of a mixture 15% CO_2, 85% N_2 v/v.

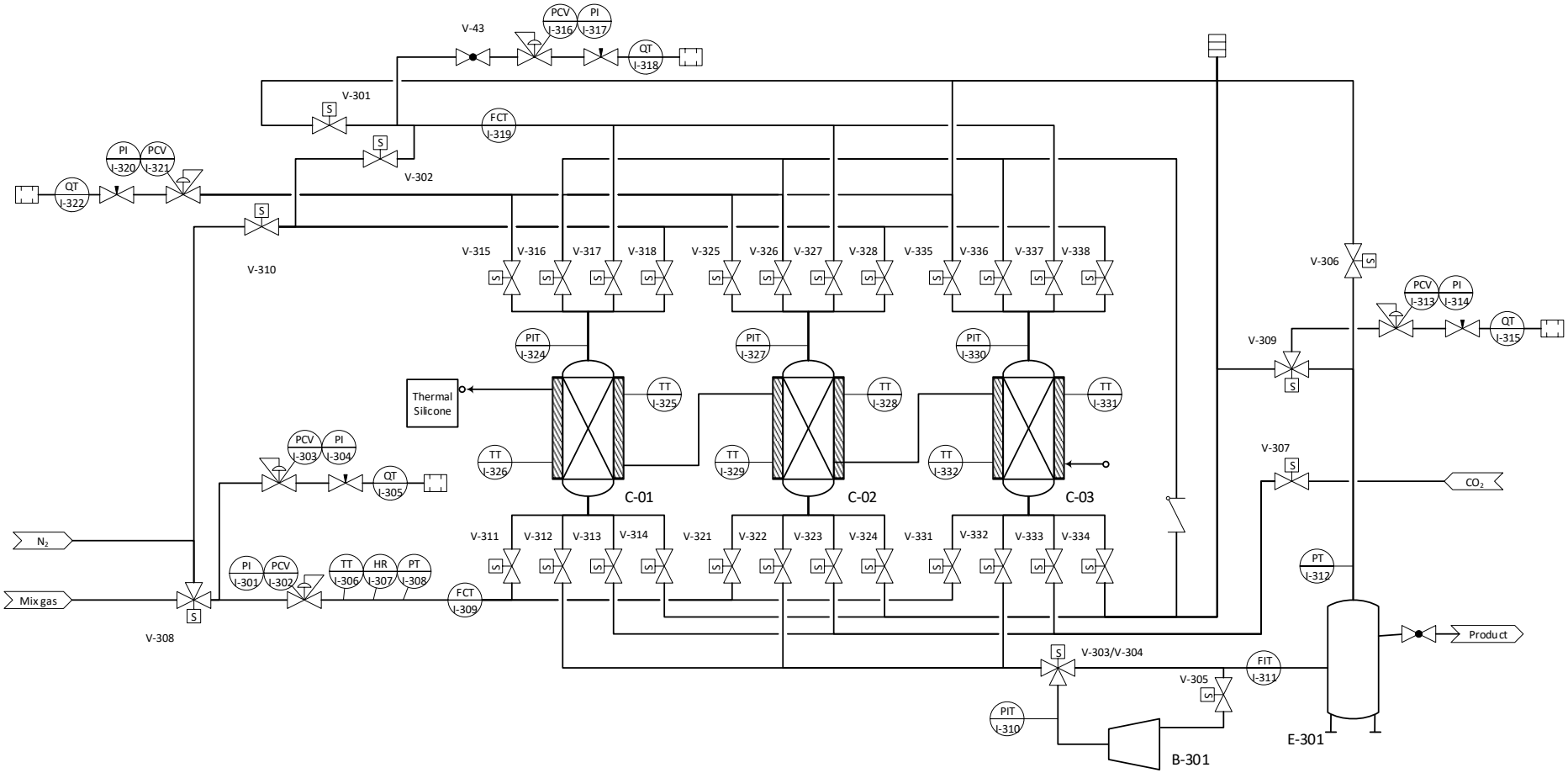

Figure 30: Simplified schematic diagram of the three bed VPSA experimental prototype. Symbols: PCV, Pressure controller valve; FTC, flow transmitter and controller; FTI, flow transmitter and indicator; PT, pressure transmitter; VPT, vacuum pressure transmitter, QT, concentration transmitter.

The temperature of the columns was monitored with two thermocouples (Electricfor, Spain) located at 5 cm (I-326, I-329 and I-332) and 60 cm (I-325, I-328 and I-331) from the bottom of each column, the inlet gas temperature was measured with the thermocouple I-306. A control flowmeter and two flow meters (M+W Instruments GmbH, Germany) were installed on the feed I-309, raffinate I-319 and product lines I-311 to measure the designed flowrates, while purge, rinse and pressure equalization rates are controlled by needle valves. A dry claw vacuum pump (Busch, United States) was used for regeneration. During the runs, gas samples were continuously analyzed with nondispersive infrared absorption CO_2 sensors (Gas Sensing Solutions, Scotland) from product/purge I-315, rinse I-322, feed I-305 and raffinate lines I-318. In addition, a product storage tank E-301 is also provided. Cycle operation is entirely automated and realized by switching solenoid valves (Metalwork, Italy) to change the direction of gas flow for the different steps of the cycle according to a programmed PLC logic. A PLC with a data acquisition system (Schneider Electric, France) was used to automate the processes. The equipment is operated from a PLC controller interface HMISTU655 LCD touch screen of 5.7". The pipes are made of flexible polyamide tubing (Parker, U.S.) and all connections are automatic fitting series (Metalwork, Italy). The instrument specifications and accuracies are listed along the Table 13 and Table 14 on section 3.4.3 for the control and automatization set-up.

3.3. Industrial VPSA setup.

The industrial plant set-up for CO_2 capture and the in-site utilization is divided in three stages: Flue gases pre-treatment, CO_2 capture and storage plant and CO_2 utilization for pH control.

3.3.1. Flue gases pretreatment setup.

The diagram of the pretreatment setup is shown in Figure 31. The pretreatment was designed to cool down the flue gases from an industrial boiler from 75 ºC (+/- 5ºC) to 28 ºC (+/- 5ºC) and to remove NO_x, SO_x without adversely affecting the concentration of CO_2. The pretreatment setup allows to work in a range of operating conditions between 10ºC and 100ºC, with a feed flowrate between 100 to 350 m^3/h. Flue gas is conducted from the chimney with a polypropylene multilayer pipe of diameter of 160 mm reinforced with mineral fibres (ABN, Spain). The pipe has external protection to ultraviolet radiation

(UV), internal protection to chemical corrosion, incrustations and it is resistant in a range of temperatures from -20°C to 90°C. An adiabatic cooling unit E-401 works with a cooling water stream at a flow rate of 6 m^3/h. The unit dimensions are 800 mm of internal diameter and 2000 mm of high. The E-401 is made of galvanized steel with a coating of a bicomponent polyurethane polyurea waterproofing membrane (Maris Polymers, Spain). The water is stored and returned to the cooling water return through a centrifugal pump E-402 (Bloch, Spain) controlled by a float level switch connected to a frequency inverter (Coelbo, Spain). The unit has three automatic purge and a strainer filter to collect all the condensed water on the cooling stage.

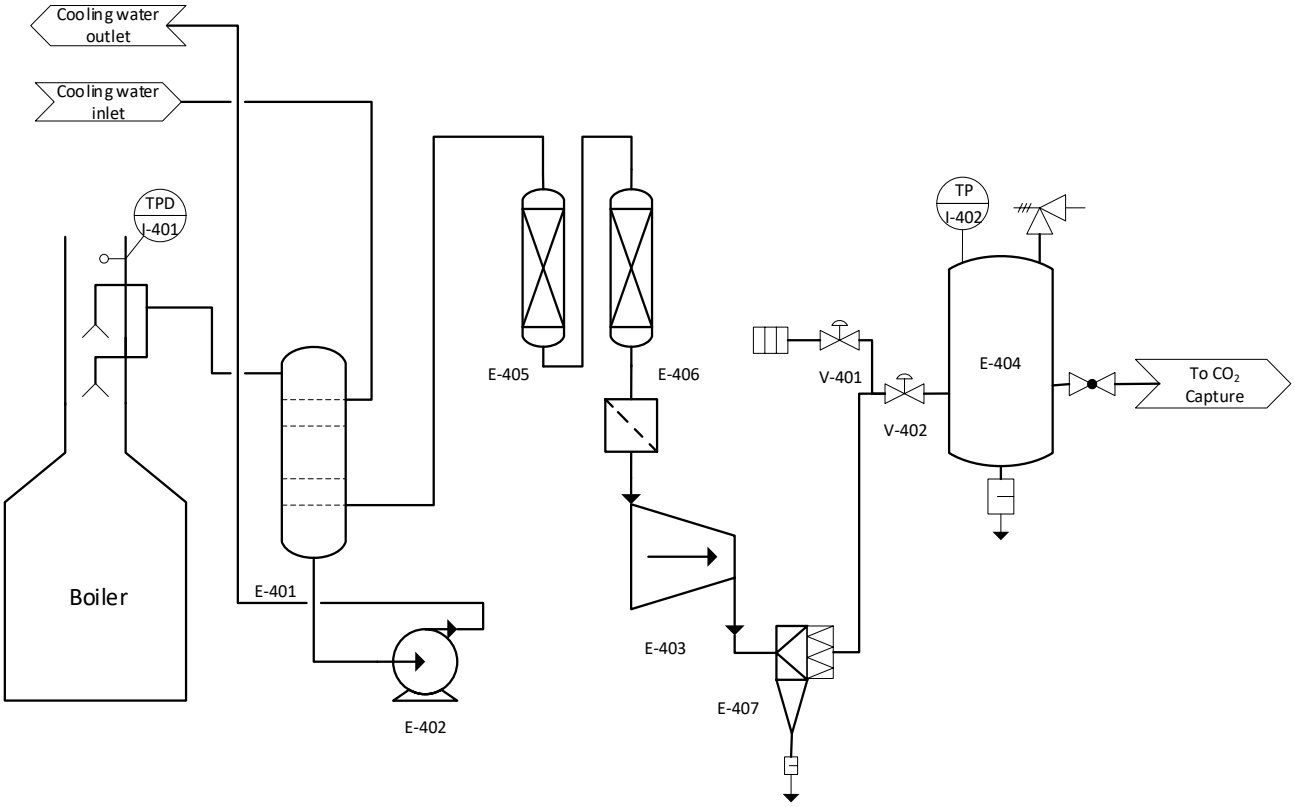

Figure 31: Schematic of the flue gas pretreatment setup system.

E-405 and E-406 are connected in series to decrease the humidity and to remove the NO_x from the combustion gases. The first column (E-405) is filled with two different adsorbents, the first adsorbent is Sorbead WS (BASF, Germany) an alumina resistant to temperatures up to 60ºC, this material removes a small part of the humidity and acts as protection to the second adsorbent. The second section of adsorbent is the molecular sieve alumina water resistant KC-Trockenperlen WS (BASF, Germany), this material has a surface area of 650 m^2/g. The humidity is decreased using physical adsorption to a relative humidity (RH) between 20 to 30%. The second column (E-406) is filled with a

molecular sieve alumina Alphasorb 8 (Alphachem, Spain) impregnated with potassium permanganate ($KMnO_4$) to remove NO_X by chemical adsorption from the flue gas stream. The two columns are made of galvanized steel with a coating of a bicomponent polyurethane polyurea waterproofing membrane (Maris Polymers, Spain). The dimensions of the both columns are 355 mm of diameter and 1000 mm of high.

Figure 33: Picture of the pretreatment system.

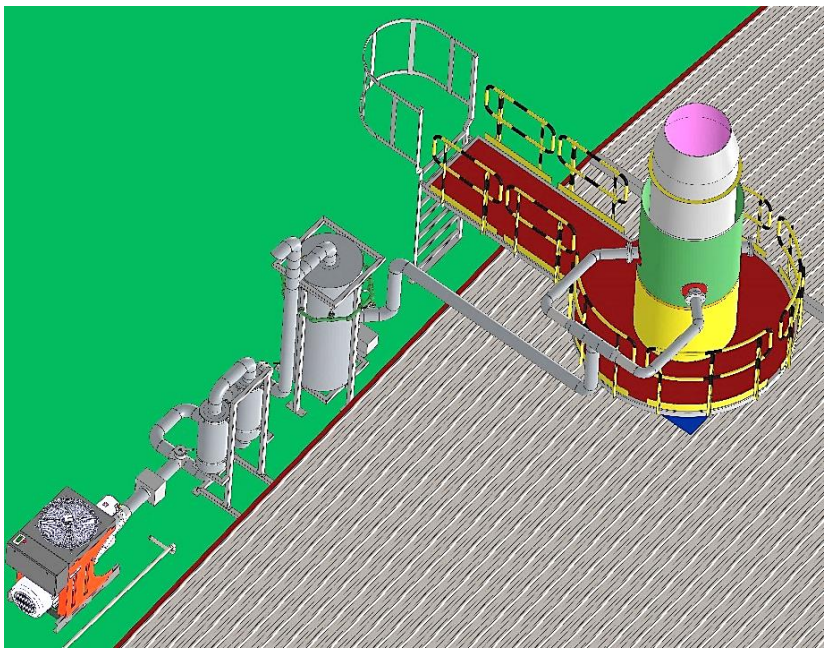

Figure 32: 3D design of the pretreatment system.

A filter holder E-403 was made with two type of particle filters, the first one was a prefilter of 50 to 70% efficiency on particles from 3.0 to 10 µm (Venfilter, Spain). The second filter

is water resistant fine particles filter of 64 to 79% of efficiency on particles from 1.0 to 3.0 µm (Venfilter, Spain). A centrifugal gas compressor E-403 (Mattei, Italy) aspirates flue gas through the pre-treatment system to compress it from 2 to 8 barg. After the compressor unit a centrifugal water separator E-407 is installed to remove condensed water (Beko, Germany), and a set of 20 µm and activated carbon filters are used to remove solid particles and oil traces (Beko, Germany). The desulfurized/denitrified gas is stored in a 2000 L tank at a maximum pressure of 8 barg. The diameter of the tank is 1100 mm with a height of 2490mm, the tank is made of carbon steel with internal coating RAL 5005 anticorrosive ALM (Baglioni, Italy). The pneumatic valves V-401 and V-402 (Bürkert, Germany) of 1 ½" allows to purge the initial load for 2 minutes to ensure the homogeneity of the treated gas. The pipes for high pressure treated gas are stainless steel of 1 ½" of diameter (Inoxpress, Italy). The pretreatment system was designed with Solidworks® using Aspen Hysys® for energy mass balances. Figure 32 shows a 3D drawing of the pretreatment system on the installation point, Figure 33 shows a picture of the installation of the built system.

3.3.2. CO_2 capture and storage plant.

A simplified schematic of the pilot plant is shown in Figure 35 along with the instrument specifications. The industrial carbon capture plant consisted of two main units. The dehumidifying unit removes the water vapor from the denitrified flue gas before it enters the VPSA process. Six columns of 156 mm diameter and 2 m height made of aluminum alloy 6060 were packed with 26 kg alumina KC-trockenperlen WS of a 3-5 mm pellet diameter (BASF, Germany). The alumina is used as the desiccant (dew point, around - 50°C) the six columns were set in two groups and connected in series to operate in PSA configuration. The flue gas humidity was measured continuously with a dew point sensor I-502 (Beko, Germany). A representative render made with SolidWorks software ® of the dryer unit is shown in Figure 34.

The VPSA unit was used to capture and concentrate CO_2 from the dehumidified flue gas, where a three-bed VPSA process was employed. The unit is equipped with three identical sets of six adsorption columns of 156 mm diameter and 2 m height made of aluminum alloy 6060 where each one was packed with 23 kg of 13XBL (bed voidage of 0.35 and particle size in the range 1.2-2.0 mm). The columns where mounted onto aluminum plugs with internal distribution channels were the pipe, valves and pressure sensors were set.

Figure 34: PSA dryer unit render made with SolidWorks software ®

The equipment was designed to work in a range of operating conditions for a cyclic VPSA process. The industrial setup can work between 0.5 to 8 barg of pressure and temperatures between 10ºC to 50ºC, with a feed flowrate between 100 to 450 Nm^3/h. Two flow meters (SMC, Japan) were installed on the feed (I-503) and raffinate (I-504) lines to measure the designed flowrates, while purge, rinse and pressure equalization rates are controlled by needle valves. A dry claw vacuum pump E-501 (Busch, United States) was used for evacuation. During the runs, gas lines are continuously analyzed with nondispersive infrared absorption CO_2 sensors (Gas Sensing Solutions, Scotland) from the feed (I-505), product (I-501), rinse (I-502), purge (I-503) and raffinate lines (I- 504). A low-pressure product storage tank E-502 of 1100 mm diameter and 2490mm height, made of carbon steel with internal coating RAL 5005 anticorrosive ALM (Baglioni, Italy) is provided from which the recovery gas can be compressed by the piston compressor E-503 (Frascold, Italy). The compressed stream rich on CO_2 recovered is stored in a second storage tank E-504 of 1200 mm diameter and 2990mm height, made of carbon steel with internal coating RAL 5005 anticorrosive ALM (Baglioni, Italy) from which the CO_2 recuperated can be recycled to the columns when required by the cycle design. The pressures at the inlet and outlet of the columns were measured using the pressure transducers I-511, I-521 and I-531 and a vacuum pressure transmitter I-515 (Wika, Spain). The working pressure and the flowrate were controlled with a pneumatic regulator valves (SMC, Japan).

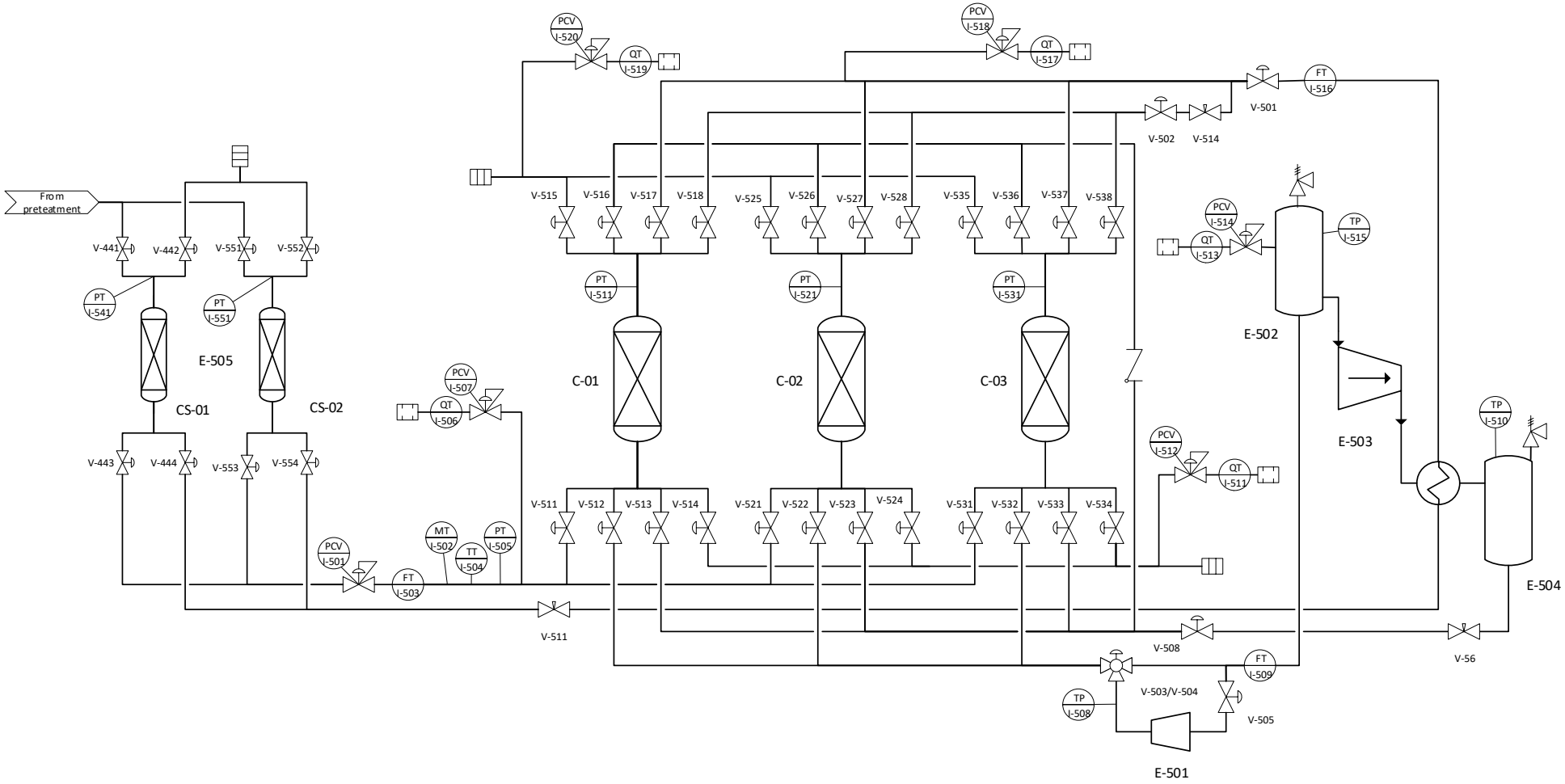

Figure 35: Simplified schematic diagram of the VPSA pilot plant. Symbols: PCV, Pressure controller valve; FTC, flow transmitter and controller; FTI, flow transmitter and indicator; PT, pressure transmitter; VPT, vacuum pressure transmitter, QT, concentration transmitter.

The temperature of feed gas was monitored with a PT- 100 thermocouple (Electricfor, Spain). A plate heat exchanger (Swep, Sweden) was installed at the compressor outlet to recover the heat energy to heat the raffinate stream and regenerate the columns of the drying unit by countercurrent flow. The pipes are inox stainless of 1" diameter (Inoxpress, Italy). The CO_2 separation plant was designed with Solidworks®. Figure 36 (A) shows the VPSA industrial plant represented with a 3D model render, Figure 36 (B) display the internal configuration of the plant.

Figure 36: VPSA industrial plant design represented with a 3D model render (A) Front, (B) Back.

All the pneumatic valves, flow controllers and meters, pressure transducers, thermocouples and CO_2 analyzers were connected to a PLC with a data-acquisition

system (Schneider Electric, France) which was used to automate the processes, and the equipment is operated from a PLC controller interface HMISTU655 LCD touch screen of 5.7". Both a dehumidifying unit and a CO_2 capture unit were operated automatically by the PLC. Figure 29 (C) shows a representative picture of the CO_2 capture industrial plant. The instrument specifications and accuracies are listed along the Table 16 and Table 15 on section 3.4.3 for the control and automatization set-up.

Figure 37: Picture the VPSA industrial plant for CO_2 capture and storage.

3.3.3. CO_2 utilization for pH control.

The CO_2 separated from flue gases is used to reduce the pH of the wastewater of the factory replacing the prior usage of a mineral acid (sulfuric acid). A simplified schematic of the injection control unit is shown in Figure 38 along with the instrument specifications. The application was developed to inject CO_2 into the pipe that transports the wastewater from the production plant to the storage tank E-602 for further treatment in the wastewater plant. The CO_2 injection application setup allows to work in a range of operating injection conditions between 2 to 8 barg, with a feed flowrate between 2 to 50 nm^3/h of CO_2. The CO_2 is transported from the storage tank E-601 to the dual in-line injection control unit with stainless steel pipes 316L of ½" diameter using press-fitting systems (Inoxpress, Italy) for the interconnection. The working pressure is set with a membrane pressure regulator I-602 (SMC, Japan), the pressure is monitored with a pressure transmitter I-602 (Wika, Spain). The flow is measured with a CO_2 flowmeter I- 604 (Beko, Germany) and two needle valves (Metalwork, Italy) are calibrated with different flowrates at 10 nm^3/h (V-61 named as the high flow line) and 6 m^3/h (V-62

named as the low flow line). Two stainless steel solenoid valves V-63 and V-64 (SMC, Japan) control the gas flow of each pipe; when the two valves are open the flowrate is named as maximum flow (16 nm^3/h). The pH is measured upstream with pH transmitters with temperature compensation (Hanna Instruments, Germany) in three points, 1 meter before the first injection point I-605, 1 meter before the second injection point I-606 and on the storage tank I-60. CO_2 is injected in the wastewater pipe with two fine bubble diffusers to increase the gas-liquid contact and homogenization. A PLC with a data-acquisition system (Schneider Electric, France) was used to automate the processes, and the equipment is operated from a PLC controller interface HMISTU655 LCD touch screen of 5.7". The instrument specifications and accuracies are listed along the Table **17** and Table 18 on point 3.4.3 for the control and automatization set-up. Figure **39** shows some pictures of the CO_2 injection application setup.

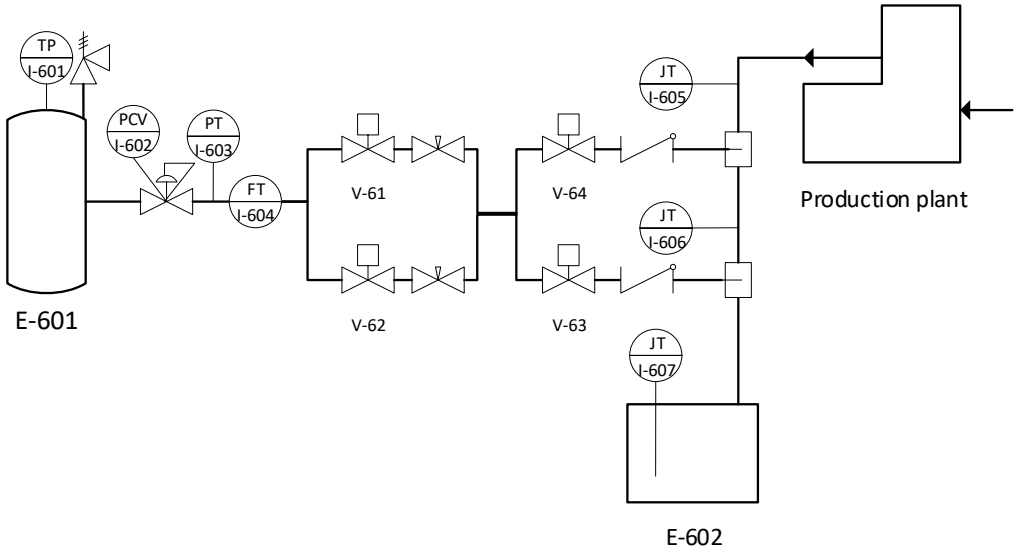

Figure 38: Simplified schematic diagram of the use of CO_2 for waste water treatment. Symbols: PCV, Pressure controller valve; FT, flow transmitter; PT, pressure transmitter and JT, pH transmitters.

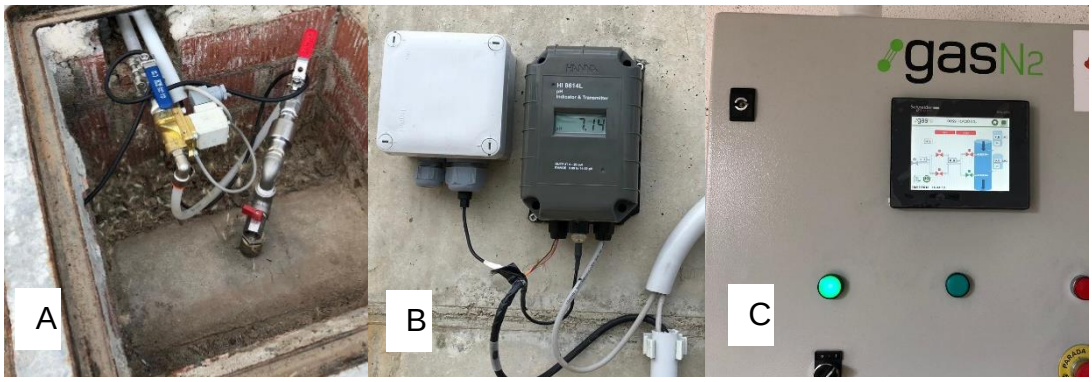

Figure 39: Picture of the CO_2 injection application setup. (A) Injection point on 800 mm tube diameter, (B) pH transmitter I-605, (C) CO_2 injection control unit for pH

3.4. Control and automatization set-up.

3.4.1. CO_2 separation kinetic control strategy based on VPSA system

The behavior in a fixed bed is based on the concept of the mass transfer zone (MTZ). This concept corresponds to a macro approach, the structured movement of the MTZ during adsorption operation, and is considered as the portion of the bed on which the adsorbate in the feed solution is transferred to the solid phase-adsorbent. As a result of this treatment, a complete design method is obtained considering equilibrium and kinetics. This method is applicable to the system when there is a rapid formation on the stable zone of mass transfer. Due to these facts, the adsorption process becomes limited, preferably to a partial region of the bed, which flows gradually at a constant rate within a short time after the beginning of the process (Ruthven, 2002). This shift is determined by the operation flow of adsorbate concentration and the maximum adsorption capacity of the adsorbent.

The monitoring of the MTZ is accomplished by monitoring the concentration of the adsorbate at the outlet of the fixed bed column. The progressive movement of the MTZ in the bed is known as the breakthrough curve; illustrated in Figure 40.

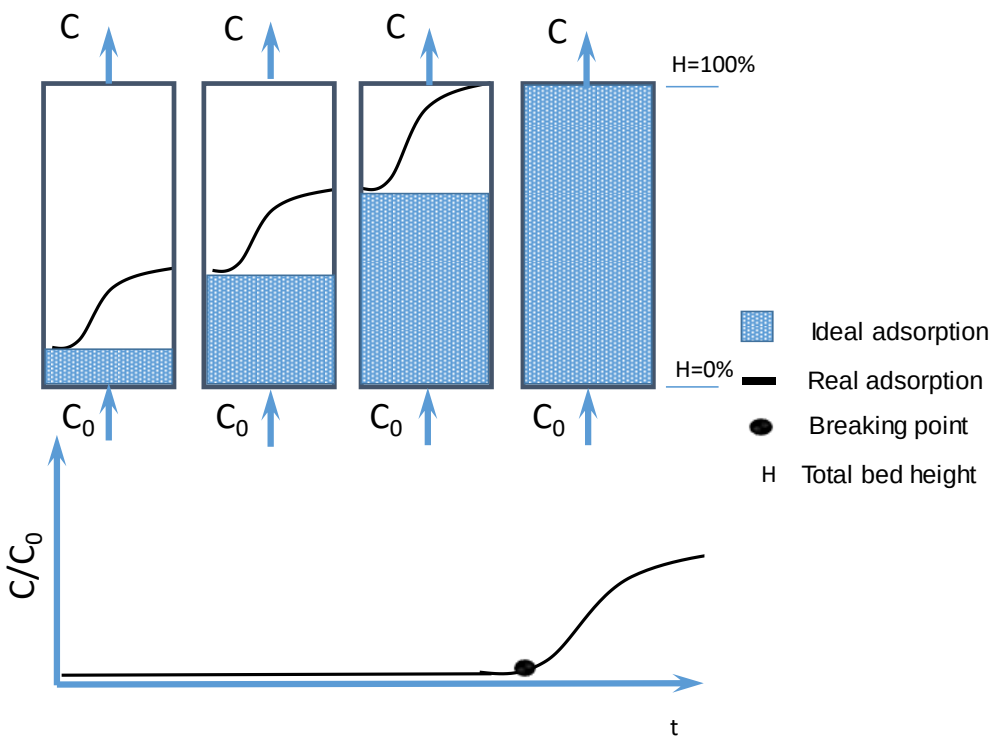

Figure 40: Scheme of a breakthrough curve at fixed bed

The curvilinear behavior of the breakthrough curve delineates a region of the bed in which MTZ is taking place. A short MTZ length indicates a higher efficiency, representing a system closer to ideality.

The breakthrough curve is the behavior of adsorption on a fixed bed column adsorbent over time, where the dispersion effects and the mass transfer to its full saturation is considered, that is to say, when equilibrium is achieved. Therefore, from a breakthrough curve it is also possible to obtain the adsorption equilibrium capacity as obtained in the equilibrium adsorption isotherm. In a kinetic PSA process, the duration of the adsorption and the desorption steps are critical design elements. Conventional PSA cycles have been developed for enrichment of the raffinate product, such as the N_2 separated from the air. However, the recovery of the retained product, as it is the case of CO_2 capture, has been limited. During the adsorption step in PSA cycles, species with faster diffusing capacity are retained inside the column, and the components with slower diffusing capacity are recovered as a raffinate product at the high-pressure outflow.

In fixed-bed adsorption, the concentrations in the fluid phase and the solid phase change with time and the position in the bed, as the concentration in the fluid decrease exponentially when reaching the end of the bed. This concentration gradient becomes *S* shaped, and the region where most of the change in concentration occurs is called the

mass transfer zone. In a separation where the retained substance is the desired product, the process productivity will depend on the maximum use of the transfer area.

For a step-function feed with constant concentration introduced into a clean bed, the concentration front will change in every cycle until the Cyclic Steady State (CSS) is reached. CSS is defined as the equilibrium between the uptake at the adsorption pressure and the uptake at the regeneration pressure over the cyclic repetitions. Then, for an efficient operation the run must be stopped just before the concentration increases exponentially. In the present study, the kinetic control system is referred to the determination of the process times of the different stages thought the constant CO_2 monitoring on three different process streams.

Consequently, the control of the stop point in the feed stage is defined as the stop feed point (S_{FD}). On the other side, purge and rinse times have a direct impact on the global production performance parameters. The principle of the rinse step is to displace the light component (N_2) from the adsorbed phase near the end of the column (at H=100%, see Figure 40) and flush it downstream toward the light-product end of the column. In an opposite way, the purge step removes the heavy gas (CO_2) from the gas phase, and then a contercurrent inert gas (N_2 in this case) is introduced to displace the heavy gas (CO_2) from the end of the column to the feed point in downstream configuration. The correct duration of these steps can improve the extract product purity when the lighter species are co-adsorbed in large amounts with heavier components. Hence, the rinse and purge stop points were selected as control variables, named as the stop purge point (S_{PR}) and stop rinse point (S_{RN}).

In an industrial application with different client facilities, different emission gas composition and different CO_2 specifications, there will be a need for a robust control strategy flexible enough to adapt to different conditions. The fuel type or the substance calorific value can lead to different CO_2 concentration on the fuel streams. The fuel stream rates on an industrial boiler operation depend on the production campaigns and the season influence. In the open-loop model, the desired purity and recovery cannot be exactly tracked due to its errors and disturbances. Thus, a feedback control strategy is necessary for the compensation of control errors of the VPSA plant. Such a multivariable system requires a strong control strategy to track the set-point of the product performance indicators. The use of conventional methods, such as PID tuning, is not efficient in handling cases interacting within two control loops. Therefore, CO_2 separation kinetics control has been implemented to eliminate the effects of the different CO_2

composition on the flue gas and to handle the control parameters without effect on the scale.

The control system was built using SoMachine software® (Schneider electric, France), based on the continuous monitorization of the three-output stop point variables S_{FD}, S_{PR} and S_{RN} with the CO_2 concentration measured by inline sensors and switching the corresponding valve set (ON-OFF operation). The kinetic control system is referred to the determination of the process times of the different stages thought the constant CO_2 monitoring on three different process streams. The logic-mathematical criteria of each parameter are not published in the present work because of confidentiality purposes. The publication of any information related to the process or the program design is property of the company GasN2 and it is protected by the patent application send to the European patent office with reference number 18382203.0-1104 “Process for separating a heavy gas component from a gaseous mixture”.

3.4.2. PLC programing

Once the whole CO_2 capture operation unit has been characterized, the control and automatization of the designed units were developed using PLC. PLCs have been widely used for many applications, e.g. pumping systems, motor control, energy research, system monitoring, etc. Although PLCs are similar to conventional computers in terms of hardware architecture, they have several advantages suited for industrial control: (Alphonsus and Abdullah, 2016)

(i) They are more rugged and have noise immune capability.
(ii) Modular approach in construction, allowing easy replacement/addition of units (e.g. I/O).
(iii) Standard I/O miniaturized connections and signal levels, offering powerful machine control at a low price (less than 300 €).
(iv) High-end control grows exponentially: although cost and size are dropping on the low end, the capabilities of large PLC systems expand as well.
(v) The ability to network and distribute the control using numerous proprietary and international network standards permits PLCs to take control of entire manufacturing systems and production plants.

PLCs are designed to be programmed with schematic or ladder diagrams instead of common computer languages. All the control systems designed in the present work were programed with Grafcet language. GRAFCET (from the French acronym of GRAphe Fonctionnel de Commande Etape/Transition meaning Step Transition Function Charts) is a graphical method for specifying industrial automation. Simple syntax, graphical representation, powerful and concise commands make Grafcet easy to learn and use (Baracos, 1992). In its most simple form, Grafcet includes the full power of Boolean logic and has the capability to handle the arithmetic used in many continuous functions and more complex functions such as PID.

A graph is a drawing of steps, transitions, links and statements. Typically, steps are arranged into a sequence corresponding to some series of control actions to be executed by the controller. The actions to be executed are written in a box to the right of each step. The transitions and steps are connected by links, but two steps cannot be directly linked, as the link must pass through a transition (Bolton, 2009). Each step has a trigger condition which specifies when to stop executing one step and start executing the next.

SoMachine software ® (Schneider electric, France), is a user tool designed to develop projects in to a usable program and commission all of the elements in Schneider Electric

controllers. It can convert applications created in an operator interface for a remote graphic display unit. The program is organized in POUs (program organization units) or sections. These sections consist of rungs (networks) to simplify both reading and navigation within the program. The POUs are associated with various tasks of the application: master, periodic, and events. They can be programmed in: Instruction List (IL) language, Ladder (LD) language, Grafcet graphic language, Structured Text (ST) operations or User-defined function blocks.

A simplified block diagram of the CO_2 prototype is shown in Figure 41. Due to confidentiality purposes the logic diagrams and the programming code are not published in the present work, as mentioned in section 3.4.1 this information is protected by the application number 18382203.0-1104.

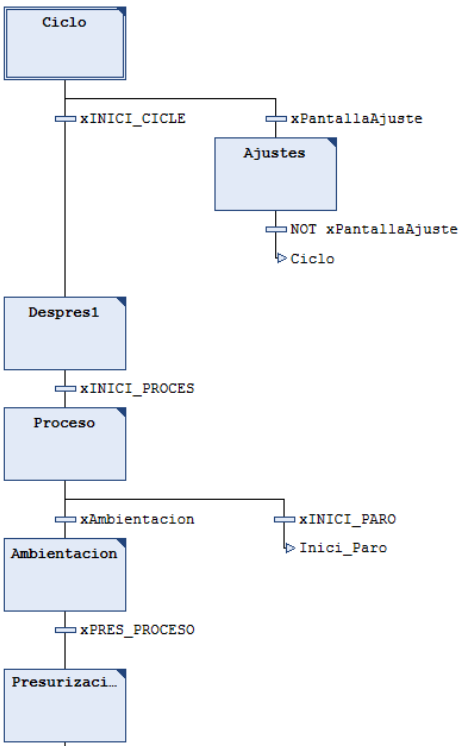

Figure 41: Diagram block used for the programming in SoMachine software®

Vijeo designer ® (Schneider electric, France) was used as the configuration software for creating operator interface applications for Human Machine Interface (HMI). It offers advanced script functions, alarm and data management, remote access, e-mail and multi-protocol connectivity. Vijeo designer® features a screen graphics editor, including simple objects, a library of animated objects (bara graphs, meters, charts and tanks), and preconfigured advanced objects (buttons, lamps, numeric and message displays and enumerated lists). Figure 42 shows the developed design for one of the multiple human interface applications for the VPSA pilot plant unit.

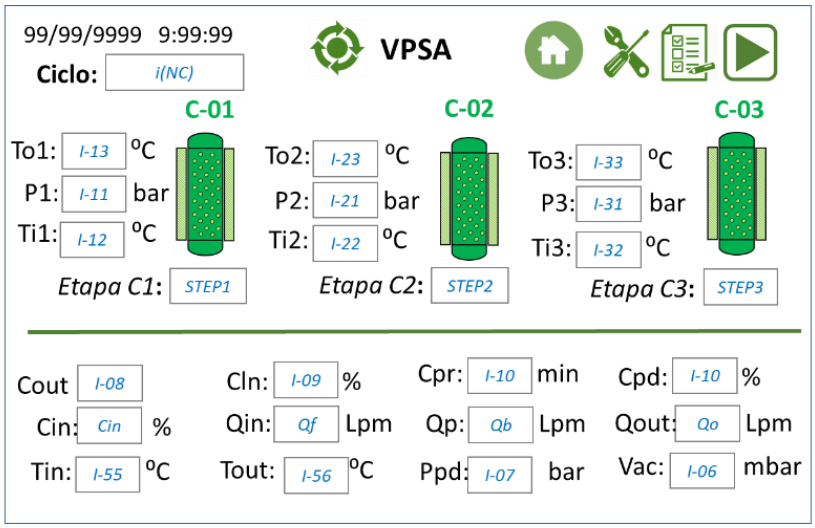

Figure 42: HMI example from Vijeo Designer ® (Scheider electric, France) developed in this work.

3.4.3. Instrumentation and PLC set-up

The automatization through a PLC provides an intelligent control system for the different experimental apparatus developed, and it belongs to the technical field of control systems. All designed control systems in the present work comprise a microcontroller unit Modicon M251 Logic Controller (Schneider electric, France), with a display screen HMISTU655 LCD touch screen of 5.7". The intelligent control system has the advantages of a simple modular structure and compact design, and it can collect parameters such as yield, CO_2 purity, flow, pressure, dew point and temperature in real time, being able to analyze and process data to automatically regulate the process parameters according to set control parameters thereby realizing self-adaptive regulative full-automatic running.

The M251is a PLC, a special form of microprocessor-based controller that uses programmable memory to store instructions and to implement functions such as logic, sequencing, timing, counting, and arithmetic calculations to control machines by logic conditions and processes parameters. The M251 include an embedded SD card slot to storage process data that allows export on ".txt" format for further data processing. The M251 Logic Controller was configured and programmed with the SoMachine software®.

A PLC configuration consists of a controller with its embedded input and output signal channels arranged in expansion modules. The modules are used to customize the number of channels and/or functions with flexibility in the control design. Expansion modules are connected directly by simple interlocking with the controller. The input and

output sections are where the processor receives information from external devices and communicates information to external devices. Digital devices can essentially be considered discrete devices which give a sequence of on−off signals. Analogue devices give signals whose size is proportional to the size of the variable being monitored (Alphonsus and Abdullah, 2016). The following tables list the digital output relay modules of 24 V c 50/60 Hz and the analog input modules for each instrument or sensor communicated with the PLC interface with its corresponding specifications used to control each developed equipment.

a) Mixture equipment PLC expansion modules

Table 9: Mixture equipment output modules in PLC.

Chanel	Module	Position	Label	Signal	Description
1	TM3ATI4G	0	I-205	4…20 mA	Pressure controller 1 a 10 Barg; 0.01 barg
2		1	I-206	4…20 mA	Pressure controller 1 a 10 Barg; 0.01 barg
3		2	I-207	4…20 mA	Flow controller 1 a 50 L/min; 0.01 L
4		3	V-204	24 V	Solenoid valve 5 W, 24VDC

Table 10: Mixture equipment input modules in PLC

Chanel	Module	Position	Label	Signal	Description
5	TM3AI8G	0	I-205	4…20 mA	Pressure transmitter 0 -10 Barg, accuracy 0.1 barg
6		1	I-206	4…20 mA	Pressure transmitter 0 -10 Barg, accuracy 0.1 barg
7		2	I-207-	4…20 mA	Flow transmitter 1 a 50 L/min; 0.1 L
8		3	I-210	4…20 mA	Pressure transmitter 0 -16 Barg, accuracy 0.1 barg
9		4	I-211	4…20 mA	Pressure transmitter 0 -16 Barg, accuracy 0.1 barg
10		5	I-208	0…5 V	Infrared CO_2 sensor, 0-100% v/v; accuracy 0.01%
11		6	V-204	24V	Solenoid valve 5 W, 24VDC

b) Single column VPSA PLC expansion modules.

Table 11: Single column VPSA output modules in PLC.

Chanel	Module	Position	Label	Signal	Description
1	TM3DQ16TG	0	V-101	24V	Solenoid valve 5 W, 24VDC
2		1	V-102	24V	Solenoid valve 5 W, 24VDC
3		2	V-103	24V	Solenoid valve 5 W, 24VDC
4		3	V-104	24V	Solenoid valve 5 W, 24VDC
5		4	V-105	24V	Solenoid valve 5 W, 24VDC
6		5	V-106	24V	Solenoid valve 5 W, 24VDC
7		6	V-107	24V	Solenoid valve 5 W, 24VDC
8		7	V-108	24V	Solenoid valve 5 W, 24VDC
9		8	V-109	24V	Solenoid valve 5 W, 24VDC
10		9	V-111	24V	Solenoid valve 5 W, 24VDC
11		10	RC	24V	Contactor 230 V
12	TM3DQ16TG	0	I-107	4…20mA	Mass flow controller 0-100 g/min, 0.06 l/min
13		1	I-106	4…20mA	Pressure transmitter 0 -10 Bar, accuracy 0.1 bar

Table 12: Single column VPSA input modules in PLC

Chanel	Module	Position	Label	Signal	Description
17	TM3AI8G	0	I-106	4…20mA	Pressure transmitter 0 -10 Bar, accuracy 0.1 bar
18		1	I-107	4…20mA	Mass flow meter 0-100 g/min, accuracy 0.06 l/min
19		2	I-123	4…20mA	Mass flow meter 0-50 g/min, accuracy 0,06 l/min
20		3	I-118	4…20mA	Mass flow meter 0-5 g/min, accuracy 0.06 l/min
21		4	I-115	4…20mA	Vacuum transmitter-1-1 Bar, accuracy 0.001 bar
22		5	I-109	4…20mA	Infrared CO_2 sensor, 0-60% v/v; accuracy 0.01%
23		6	I-117	0…5 V	Infrared CO_2 sensor, 0-60% v/v; accuracy 0.01%
24		7	I-122	0…5 V	Infrared CO_2 sensor, 0-100% v/v; accuracy 0.01%
25	TM3AQ4G	0	I-111	4…20mA	Pressure transmitter 1 a 10 Bar, accuracy 0.01 bar
26		1	I-116	4…20mA	Pressure transmitter 1 a 10 Bar, accuracy 0.01 bar
27		2	I-119	4…20mA	Pressure transmitter 1 a 10 Bar, accuracy 0.01 bar
28		3	I-120	4…20mA	Pressure transmitter 1 a 10 Bar, accuracy 0.01 bar
31	TM3TI4G	0	I-114	PT100	Temperature transmitter -60 to 400ºC; accuracy 0.1ºC
32		1	I-113	PT100	Temperature transmitter -60 to 400ºC; accuracy 0.1ºC
33		2	I-112	PT100	Temperature transmitter -60 to 400ºC; accuracy 0.1ºC
34		3	I-110	PT100	Temperature transmitter -60 to 400ºC; accuracy 0.1ºC

c) Three columns VPSA PLC expansion modules.

Table 13: Three columns VPSA output modules in PLC.

Chanel	Module	Position	Label	Signal	Description
1	TM3DQ16TG	0	V-301	24V	Solenoid valve 5 W, 24VDC
2		1	V-302	24V	Solenoid valve 5 W, 24VDC
3		2	V-303	24V	Solenoid valve 5 W, 24VDC
4		3	V-304	24V	Solenoid valve 5 W, 24VDC
5		4	V-305	24V	Solenoid valve 5 W, 24VDC
6		5	V-306	24V	Solenoid valve 5 W, 24VDC
7		6	V-307	24V	Solenoid valve 5 W, 24VDC
8		7	V-308	24V	Solenoid valve 5 W, 24VDC
9		8	V-309	24V	Solenoid valve 5 W, 24VDC
10		9	V-311	24V	Solenoid valve 5 W, 24VDC
11		10	V-312	24V	Solenoid valve 5 W, 24VDC
12		11	V-313	24V	Solenoid valve 5 W, 24VDC
13		12	V-314	24V	Solenoid valve 5 W, 24VDC
14		13	V-315	24V	Solenoid valve 5 W, 24VDC
15		14	V-316	24V	Solenoid valve 5 W, 24VDC
16		15	V-317	24V	Solenoid valve 5 W, 24VDC
17	TM3DQ16TG	0	V-318	24V	Solenoid valve 5 W, 24VDC
18		1	V-321	24V	Solenoid valve 5 W, 24VDC
19		2	V-322	24V	Solenoid valve 5 W, 24VDC
20		3	V-323	24V	Solenoid valve 5 W, 24VDC
21		4	V-324	24V	Solenoid valve 5 W, 24VDC
22		5	V-325	24V	Solenoid valve 5 W, 24VDC
23		6	V-326	24V	Solenoid valve 5 W, 24VDC
24		7	V-327	24V	Solenoid valve 5 W, 24VDC
25		8	V-328	24V	Solenoid valve 5 W, 24VDC
26		9	V-331	24V	Solenoid valve 5 W, 24VDC
27		10	V-332	24V	Solenoid valve 5 W, 24VDC
28		11	V-333	24V	Solenoid valve 5 W, 24VDC
29		12	V-334	24V	Solenoid valve 5 W, 24VDC
30		13	V-335	24V	Solenoid valve 5 W, 24VDC
31		14	V-336	24V	Solenoid valve 5 W, 24VDC
33	TM3DQ16TG	0	V-337	24V	Solenoid valve 5 W, 24VDC
34		1	V-338	24V	Solenoid valve 5 W, 24VDC
35		2	V-339	24V	Solenoid valve 5 W, 24VDC
40		7	RC	24V	Triphasic power contactor; 0.75 kW

Table 14: Three columns VPSA input modules in PLC

Chanel	Module	Position	Label	Signal	Description
49	TM3AI8G	0	P_G	4…20mA	Pressure transmitter 0 -16 Bar, accuracy 0.1 bar
50		1	Hr	4…20mA	Dew Point Transmitter-20 to 30°C
51		2	Q_{in}	4…20mA	Mass flow meter 0-100 g/min, accuracy 0.06 l/min
52		3	Q_{out}	4…20mA	Mass flow meter 0-50 g/min, accuracy 0.06 l/min
53		4	Q_{pr}	4…20mA	Mass flow meter 0-5 g/min, accuracy 0.06 l/min
54		5	P_v	4…20mA	Vacuum pressure transmitter-1-0.6 Bar, accuracy 0.001 bar
55		6	C_{rn}	0…5 V	Infrared CO_2 sensor, 0-60% v/v; accuracy 0.01%
56		7	C_{out}	0…5 V	Infrared CO_2 sensor, 0-60% v/v; accuracy 0.01%
57	TM3AM6G	0	C_{pr}	0…5 V	Infrared CO_2 sensor, 0-100% v/v; accuracy 0.01%
58		1	P_{c1}	2.5…20mA	Pressure transmitter -1 a 10 Bar, accuracy 0.01 bar
59		2	P_{c2}	2.5…20mA	Pressure transmitter -1 a 10 Bar, accuracy 0.01 bar
60		3	P_{c3}	2.5…20mA	Pressure transmitter -1 a 10 Bar, accuracy 0.01 bar
61		0	Q_C	4…20mA	Mass flow controller 0-50 l/min, accuracy 0.06 l/min
62		1	P_C	4…20mA	Pressure controller 0 -10 Bar, accuracy 0.1 bar
63	TM3TI4G	0	$T1_{in}$	PT100	Temperature transmitter -60 to 400ºC; accuracy 0.1ºC
64		1	$T1_{out}$	PT100	Temperature transmitter -60 to 400ºC; accuracy 0.1ºC
57		2	$T2_{in}$	PT100	Temperature transmitter -60 to 400ºC; accuracy 0.1ºC
58		3	$T2_{out}$	PT100	Temperature transmitter -60 to 400ºC; accuracy 0.1ºC
59	TM3TI4G	0	$T3_{in}$	PT100	Temperature transmitter -60 to 400ºC; accuracy 0.1ºC
60		1	$T3_{out}$	PT100	Temperature transmitter -60 to 400ºC; accuracy 0.1ºC
61		2	T_{in}	PT100	Temperature transmitter -60 to 400ºC; accuracy 0.1ºC
62		3	C_{in}	0…5 V	Infrared CO_2 sensor, 0-20% v/v; accuracy 0.01%

d) Industrial plant PLC expansion modules.

Table 15: Industrial plant input modules in PLC

Chanel	Module	Position	Label	Signal	Description
49	TM3AI8G	0	I-505	4…20mA	Pressure transmitter 0 -16 Bar, accuracy 0.1 bar
50		1	I-502	4…20mA	Dew Point Transmitter-20 to 30°C
51		2	I-503	4…20mA	Mass flow meter 300-6000 L/min, accuracy 0.06 l/min
52		3	I-516	4…20mA	Mass flow meter 300-6000 L/min, accuracy 0.06 l/min
53		4	I-509	4…20mA	Mass flow meter 0-200 L/min, accuracy 0.01 l/min
54		5	I-508	4…20mA	Vacuum pressure transmitter-1 to 1 Bar, 0.01 bar
55		6	I-506	0…5 V	Infrared CO_2 sensor, 0-60% v/v; accuracy 0.01%
56		7	I-513	0…5 V	Infrared CO_2 sensor, 0-60% v/v; accuracy 0.01%
57	TM3AI8G	0	I-517	0…5 V	Infrared CO_2 sensor, 0-100% v/v; accuracy 0.01%
58		1	I-519	0…5 V	Infrared CO_2 sensor, 0-100% v/v; accuracy 0.01%
59		2	I-511	4…20mA	Pressure transmitter -1 a 10 Bar, accuracy 0.01 bar
60		3	I-521	4…20mA	Pressure transmitter -1 a 10 Bar, accuracy 0.01 bar
61		4	I-531	4…20mA	Pressure transmitter -1 a 10 Bar, accuracy 0.01 bar
		5	I-541	4…20mA	Pressure transmitter -1 a 10 Bar, accuracy 0.01 bar
		6	I-551	4…20mA	Pressure transmitter -1 a 10 Bar, accuracy 0.01 bar
62		7	I-510	4…20mA	Pressure transmitter -1 a 10 Bar, accuracy 0.01 bar
63	TM3TI4G	0	I-504	Pt-100	Temperature transmitter -60 to 400ºC; accuracy 0.1ºC
64		1	I-515	4…20mA	Pressure transmitter -1 a 10 Bar, accuracy 0.01 bar

Table 16: Industrial plant output modules in PLC.

Chanel	Module	Position	Label	Signal	Description
1	TM3DQ16TG	0	V-501	24V	Solenoid valve 5 W, 24VDC
2		1	V-502	24V	Solenoid valve 5 W, 24VDC
3		2	V-503	24V	Solenoid valve 5 W, 24VDC
4		3	V-504	24V	Solenoid valve 5 W, 24VDC
5		4	V-505	24V	Solenoid valve 5 W, 24VDC
6		5	V-506	24V	Solenoid valve 5 W, 24VDC
7		6	V-507	24V	Solenoid valve 5 W, 24VDC
8		7	V-508	24V	Solenoid valve 5 W, 24VDC
9		8	V-509	24V	Solenoid valve 5 W, 24VDC
10		9	V-511	24V	Solenoid valve 5 W, 24VDC
11		10	V-512	24V	Solenoid valve 5 W, 24VDC
12		11	V-513	24V	Solenoid valve 5 W, 24VDC
13		12	V-514	24V	Solenoid valve 5 W, 24VDC
14		13	V-515	24V	Solenoid valve 5 W, 24VDC
15		14	V-516	24V	Solenoid valve 5 W, 24VDC
16		15	V-517	24V	Solenoid valve 5 W, 24VDC
17	TM3DQ16TG	0	V-518	24V	Solenoid valve 5 W, 24VDC
18		1	V-521	24V	Solenoid valve 5 W, 24VDC
19		2	V-522	24V	Solenoid valve 5 W, 24VDC
20		3	V-523	24V	Solenoid valve 5 W, 24VDC
21		4	V-524	24V	Solenoid valve 5 W, 24VDC
22		5	V-525	24V	Solenoid valve 5 W, 24VDC
23		6	V-526	24V	Solenoid valve 5 W, 24VDC
24		7	V-527	24V	Solenoid valve 5 W, 24VDC
25		8	V-528	24V	Solenoid valve 5 W, 24VDC
26		9	V-531	24V	Solenoid valve 5 W, 24VDC
27		10	V-532	24V	Solenoid valve 5 W, 24VDC
28		11	V-533	24V	Solenoid valve 5 W, 24VDC
29		12	V-534	24V	Solenoid valve 5 W, 24VDC
30		13	V-535	24V	Solenoid valve 5 W, 24VDC
31		14	V-536	24V	Solenoid valve 5 W, 24VDC
33	TM3DQ16TG	0	V-537	24V	Solenoid valve 5 W, 24VDC
34		1	V-538	24V	Solenoid valve 5 W, 24VDC
35		2	V-539	24V	Solenoid valve 5 W, 24VDC
40		3	RC	24V	Triphasic power contactor; 0.75 kW
41		4	V-541	24V	Solenoid valve 5 W, 24VDC
42		5	V-542	24V	Solenoid valve 5 W, 24VDC
43		6	V-543	24V	Solenoid valve 5 W, 24VDC
44		7	V-544	24V	Solenoid valve 5 W, 24VDC
45		8	V-551	24V	Solenoid valve 5 W, 24VDC
46		9	V-552	24V	Solenoid valve 5 W, 24VDC
47		10	V-553	24V	Solenoid valve 5 W, 24VDC
49		13	V-554	24V	Solenoid valve 5 W, 24VDC
50		14	V-401	24V	Solenoid valve 5 W, 24VDC
51		15	V-402	24V	Solenoid valve 5 W, 24VDC

e) CO_2 Injection application

Table 17: CO_2 Injection application output modules in PLC.

Chanel	Module	Position	Label	Signal	Description
1	TM3DQ8TG	0	V-61	24V	Solenoid valve 5 W, 24VDC
2		1	V-62	24V	Solenoid valve 5 W, 24VDC
3		2	V-63	24V	Solenoid valve 5 W, 24VDC
4		3	V-64	24V	Solenoid valve 5 W, 24VDC

Table 18: CO_2 Injection application input modules in PLC

Chanel	Module	Position	Label	Signal	Description
49	TM3AI8G	0	I-603	4…20mA	Pressure transmitter 0 -16 Bar, accuracy 0.1 bar
50		1	I-604	4…20mA	Mass flow meter 0-100 g/min, accuracy 0.06 l/min
51		2	I-605	4…20mA	Ph meter 0-13, -5 to 80ºC; Pt100; 6 Bar
52		3	I-606	4…20mA	Ph meter 0-13, -5 to 80ºC; Pt100; 6 Bar
56		4	I-607	4…20mA	Ph meter 0-13, -5 to 80ºC; Pt100; 6 Bar

3.5. Process modeling and simulation.

3.5.1. Simulation of indirect heating exchange of column for CO_2 adsorption with TSA

Simulation experiments were performed to study the viability of CO_2 capture process using the zeolite 13XBL by TSA. Tdyn® software was used to simulate the suitable operating conditions of heat exchange and a possible design for a fixed bed TSA column. Three strategies were studied for heating exchange on the fixed bed. The first one, consists of a packed column with a CO_2 hot gas inlet to heat up the saturated adsorbent. In the second one, the column was designed as a tube and shell exchanger with hot water as a service fluid to heat up the adsorbent in the column, and the third was a hybrid model of the previous strategies.

The column model was designed with an inner aluminum tube of 25 mm of diameter, 340 mm of length and 3.4 mm of thickness. The tube is enclosed by a second aluminum tube of 53 mm of diameter with a 2.5 mm of thickness, and the total length of the column is 340 mm. The model of the column was drawn in Autocad® and has been exported to Tdyn®, to perform the simulation. The following assumptions were considered:

- Pressure changes have not been considered.
- The heating fluid circulates in the jacket formed by the space between the tubes and enters through the bottom of the column, considering the effect of gravity.
- The gas flows countercurrent through the inner tube.
- Stationary-wall-film boundary conditions were used, meaning the velocity of the fluid in contact with the walls of the column and the jacket is zero.
- The properties of the used fluids have been defined from the Tdyn® database.
- Large Eddy Simulation models (LES) were used on the flow simulations.
- The temperature increment due to the adsorption was not considered.

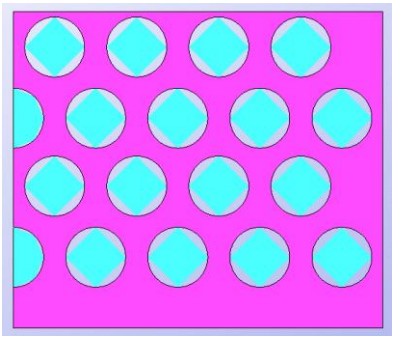

Figure 43: Adsorbents beads filling distribution in triangular arranged mesh.

To represent the filling in the three-dimensional model, beads of 1.5 mm of radius were arranged in a triangular mesh separated equidistantly (Figure 43). The equidistant disposition is caused by the presence of a second layer of pearls placed between the spaces first layer, forming a triangular arrangement of pearls between first and second layer. The three-dimensional adsorbent model filling was done by the repetition of this triangular 3D distribution along the column. Since Tdyn® did not have the characteristics of the zeolite 13XBL in its database, it has been indicated that the spheres were made of clay for the first approach. Figure 44 represents the model employed to simulate the heat exchange on the fixed bed.

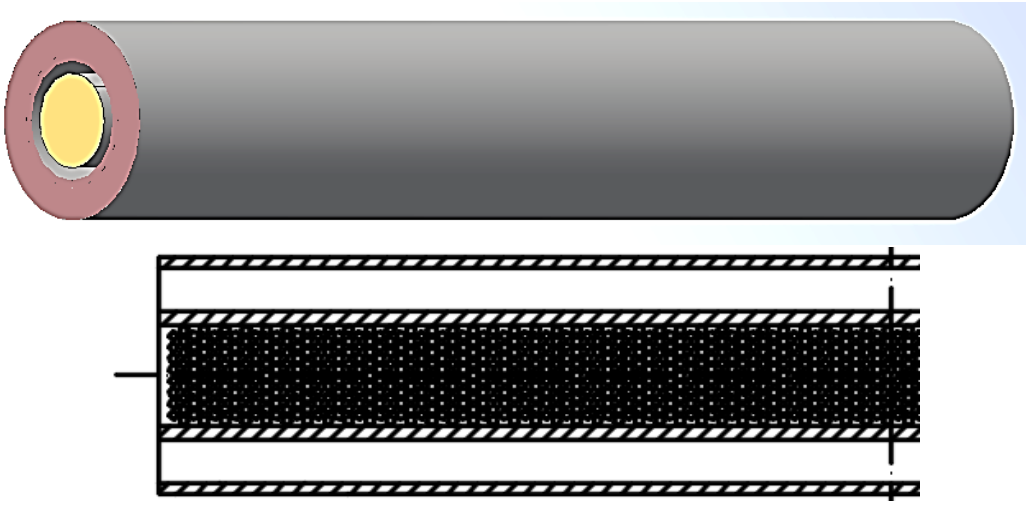

Figure 44: Column model employed to simulate heating exchange on the fixed bed

The model parameter values, kept constant while simulating all the runs, are listed in Table 19, whereas the values of the operating parameters (v_{IN}=inlet velocities and T_{HF}=temperatures of the heating fluid) that varied during the simulation of individual runs are listed in

Table **20**.

Table 19: Constant parameter values used for all simulations.

Design parameters	Symbol		Units
Length of column	L_c	340	mm
Length of jacket	L_j	340	mm
Diameter of column	D_{column}	25	mm
Diameter of jacket	D_{jacket}	53	mm
Density of column wall	ρ_w	8238	kg/m3
Specific heat of the column wall	Cp_w	500	J/(kg K)
Column wall thickness	x	25	Mm
Operating parameters			
Initial temperature gas	T_{Go}	20	ºC
Initial temperature adsorbent.	T_{So}	20	ºC
Working Pressure	P_W	1	barg
Adsorbent properties			
Radius of the adsorbent particle	r_P	1.5	mm
Bulk density	ρ_B	660	
Simulation Parameters			
Nodes	n_s	*9135*	
Simulation time	t_s	*30*	sec
Time steps	t_{st}	0.01	sec

Table 20: Values of the operating parameters used simulation experiments.

Run	Gas inlet velocity	Heating fluid velocity	Temperature feed gas	Temperature heating fluid
Heating by indirect fluid				
A	*0.10 m/s*	-	60ºC	-
B	*0.25 m/s*	-	60ºC	-
C	*0.50 m/s*	-	60ºC	-
D	*0.60 m/s*	-	60ºC	-
Heating by direct hot gas				
A	-	*0.01 m/s*	-	80ºC
B	-	*0.05 m/s*	-	80ºC
C	-	*0.10 m/s*	-	80ºC
D	-	*0.20 m/s*	-	80ºC
Direct and indirect heating				
A	*0.01 m/s*	*0.10 m/s*	60ºC	80ºC
B	*0.05 m/s*	*0.10 m/s*	60ºC	80ºC
C	*0.10 m/s*	*0.10 m/s*	60ºC	80ºC
D	*0.50 m/s*	*0.10 m/s*	60ºC	80ºC

Before the column simulation, a simple simulation of heat exchange on a bead was solved with three different mesh configurations as described in Table 21 . The first (Mesh number 1) has a total of 9135 nodes and 51899 elements (volumes delimited by the nodes). The second (Mesh number 2) has 615 nodes and 3248 elements. The last one (Mesh number 3) has only has 40 nodes that delimit 160 elements. In all three cases, the same time step was used: 0.01 seconds.

Table 21: Simple simulations of heat exchange on a bead was solved with three different mesh configurations

Run	Nodes	Time steps	Temperature	Simulation time
A	*9135*	0.01 s	80ºC	30 s
B	*615*	0.01 s	80ºC	30 s
C	*40*	0.01 s	80ºC	30 s

3.5.2. Modelling and simulation of fixed bed adsorption experiments in Aspen Adsorption®.

A simulation model was developed in Aspen Adsorption® to match the experimental equilibrium data obtained with zeolites 13XBL and 5ABL. The adsorption process is simulated by applying the so-called 'Single Bed Approach' with rigorous pressure flow relationships as well as mass and energy balances. The gas properties of the gas of the mixtures and the thermodynamic package are all imported from Aspen properties.

To reduce the computational effort while ensuring reliable simulation results, the following assumptions are considered in this work:

- Gas phase material balance was described by ideal gas behavior.
- Linear driving force kinetic model (LDF) was used to describe the flux between the gas and adsorbed phases with constant mass transfer coefficients.
- Convection with axial dispersion was considered with gas phase accumulation in the interparticle void space and flux between the gas and adsorbed phases.
- Constant axial dispersion was described by a fixed axial dispersion coefficient.
- Non-linear competitive adsorption isotherms were expressed as a function of partial pressures through the Dual site Langmuir model.
- Porosity of bed and adsorbent particle was uniform along the bed (each adsorbent was identical).
- Rigorous energy balance of gas-phase convection and solid-phase conduction was included.

Aspen Adsorption® solves the governing model equations for adsorption, consisting of a set of partial differential equations describing the mass, momentum and energy transport between the gas and solid phases (Zhang et al., 2016), as well as various equilibrium isotherm models. The basic assumptions and governing equations used in the simulation of the adsorbent bed are listed in Table 22. The pressure drop through the adsorbent bed is estimated by the Ergun equation (equation (22), which is valid for

both laminar and turbulent flow regimes. Mass transfer is described by the solid phase lumped parameter linear driving force model (equation (24). Values of the mass transfer coefficient (MTC) were estimated by considering resistances in the solid film and in the micropores of the particle (equation (30), thus accounting for limiting diffusivity (equation (31) (Poling et al., 2001).

Table 22: Governing equations used in the model

	Description	Equation	
Momentum balance	Pressure drop described by Ergun equation	$\frac{\partial \mathrm{P}}{\partial \mathrm{z}}=\pm(\frac{150\times10^{-5}\mu_{\mathrm{g}}(1\text{-}\varepsilon_{\mathrm{i}})^2}{(2\mathrm{r_p}\psi)^2\varepsilon_{\mathrm{i}}^3}\nu_{\mathrm{g}}+\frac{1{,}75\times10^{-5}M_w\rho_g(1-\varepsilon_i)}{(2r_p\psi)^2\varepsilon_i^3}\nu_g^2)$	(22)
Mass balance	Plug flow with axial dispersion	$\frac{\partial(\upsilon_g c_i)}{\partial z}+\left[\varepsilon_i+(1-\varepsilon_i)\varepsilon_p\right]\frac{\partial c_i}{\partial t}+\rho_b\frac{\partial q_i}{\partial t}-\varepsilon_i D_L\frac{\partial^2 c_i}{\partial t^2}=0$	(23)
Linear driving force kinetic model	Adsorption rate described by constant MTC	$\frac{\partial q_i}{\partial t}=MTC_i(q_i^*-q_i)$	(24)
Isotherm model	Dual site Langmuir with competitive adsorption	$q=\frac{q_{s1}b_1P}{1+b_1P}+\frac{q_{s2}b_2P}{1+b_2P}$	(25)
Energy balance	Gas phase	$-\mathrm{k_g}\varepsilon_{\mathrm{i}}\frac{\partial^2\mathrm{T}}{\partial z^2}+\mathrm{C_{vg}}\nu_{\mathrm{g}}\rho_{\mathrm{g}}\frac{\partial \mathrm{T}}{\partial \mathrm{z}}+[\varepsilon_{\mathrm{i}}+(1\text{-}\varepsilon_{\mathrm{i}})\varepsilon_{\mathrm{p}}]\mathrm{C_{vg}}\rho_{\mathrm{g}}\frac{\partial \mathrm{T}}{\partial t}+P\frac{\partial \nu_{\mathrm{g}}}{\partial z}+h_{gs}a_p(T-T_s)+\frac{4h_w}{D_B}(T-T_w)=0$	(26)
	Solid phase	$-k_s\frac{\partial^2 T_s}{\partial z^2}-k_s\frac{1}{r}\frac{\partial}{\partial r}\left(\frac{1}{r}\frac{\partial T_s}{\partial r}\right)+\rho_s C_{ps}\frac{\partial T_s}{\partial t}+\rho_s\sum_{i=1}^{n}(C_{pai}q_i)\frac{\partial T_s}{\partial t}+\rho_s\sum_{i=1}^{n}(\Delta H_l\frac{\partial q_i}{\partial t})-HTCa_p(T_g-T_s)=0$	(27)
	Column wall	$-k_w\frac{\partial^2 T_W}{\partial z^2}+\rho_w C_{pw}\frac{\partial T_w}{\partial t}-h_w\frac{4D_B}{(D_B+W_r)^2-D_B^2}(T-T_W)+h_b\frac{4(D_b+W_r)^2}{(D_b+W_r)^2-D_B^2}(T_W-T_{env})=0$	(28)
Heat transfer coefficient(Bird et al., 2007)	Gas−solid	$HTC=jC_{p,g}v_g\rho_g Pr^{-2/3}$	(29)
Mass transfer coefficient	with the solid film	$MTC_i=15\frac{D_{efci}}{r_c^2}$	(30)
Micropore diffusivity (Liu et al., 2011b)	at the adsorbent	$D_{efci}=D_{efci}^0\cdot\exp\left(\frac{-E_a}{R_gT_s}\right)$	(31)
Varying axial dispersion	Varying dispersion coefficient depending on υ_s	$D_L=2v_i r_p(\frac{20}{Re\cdot Sc}+\frac{1}{2})$	(32)
Heats of adsorption	Clausius−Clapeyron relation	$\Delta H_{ads}=-R\left[\frac{\partial In\, p}{\partial(1/T)}\right]_n$	(33)
Ideal gas behavior	Gas phase material	$Py_i=RT_g c_i$	(34)

The energy balance model selected is the rigorous energy balance incorporating both gas-phase convection and solid-phase conduction. The model considers independent balances in the fluid (equation (26), solid (equation (27), and wall phases (equation (28). The general wall balance equation includes a term for the heat transfer coefficient of the wall, which is based on the specified values of the wall density and the specific heat capacity of the wall material. Gas-solid heat transfer is expressed in terms of a film resistance, where the heat transfer area is proportional to the area of the adsorbent particles, as given in the rate of heat transferred per unit volume (HTC). HTC is also estimated by the software based on the Colburn j-factor correlation (equation (29). Heats of adsorption (ΔH_{ads}) of CO_2 and N_2 as a function of loading were calculated from the measured isotherm data by using the Clausius−Clapeyron relation (equation (34).

Heat transfer coefficients of zeolites 13XBL and 5ABL were not experimentally available but were estimated from standard correlations within the software. The input parameters used in the simulations including column and adsorbent characteristics, and gas physical properties are shown in Table 23.

Table 23: Adsorbent characteristics used in the Aspen

Parameter	Units	13XBL	5ABL
Sorbent mass used per bed	kg	0.195	0.125
Packing density	kg/m^3	689	700
Inter-particle porosity, ε_i	m^3 void/m^3 bed	0.35	0.35
Intra-particle porosity, ε_p	m^3 void/m^3 bead	0.6	0.6
Adsorbent shape factor (Sphericity), S_{fac}		0.83	0.83
Adsorbent specific heat capacity, Cps	kJ/kg·K	1.00	0.92
Heat of adsorption -ΔH_{CO2}	MJ/kmol	-35.00	-36.05
Heat of adsorption -ΔH_{N2}	MJ/kmol	-16.00	-16.84
constant mass transfer coefficient MTC_{CO2}	1/s	0.5	0.1
constant mass transfer coefficient MTC_{N2}	1/s	0.3	0.05
Constant adsorbed phase heat capacity CO_2	kJ/kmol·K	25.814	36.732
Constant adsorbed phase heat capacity N_2	kJ/kmol·K	15.50	29.105

A simulation flowsheet based on the ‘Single Bed Approach’, was adopted, which simulates the behavior of one bed. Dead volumes at both ends of the experimental system were estimated and are considered in the simulations. The typical flowsheet simulation from Aspen Adsorption ® is shown in Figure 45.

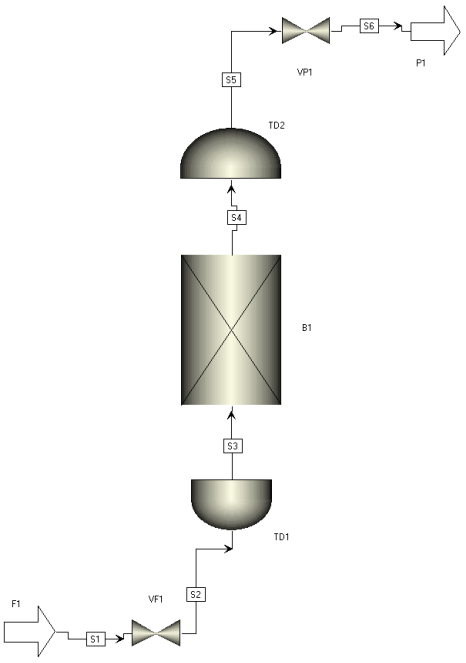

Figure 45: Simple flowsheet used for the simulation of the equilibrium relationship in Aspen Adsorpton®.

3.5.3. Simulation of VPSA cycles in Aspen Adsorption

VPSA dynamic cyclic experiments on a fixed-bed were performed to study the cycle performance of zeolites 5ABL and 13XBL. The commercial software Aspen Adsorption® simulator was used to simulate the process cycle for the purposes of interpreting the experimental data and understanding the process basics. The model equations were solved using the same assumptions and governing equations established in section 3.5.2 on single bed experiments. A rigorous model was used with the application of the DSL model, the linear driving force model and Ergun equation to represent the adsorption equilibrium, mass transfer rate and pressure drop across the bed respectively. The column/bed characteristics and the adsorbent properties are the same ones that were used in the section 3.5.2. Pure component isotherms equilibrium models of section 2.4 were used to predict the mixed-gas adsorption process simulations using the ideal adsorbed solution theory (IAS).

The single column configuration is the same used in the section 0. The cycle organizer of Aspen Adsorption® was used to specify the process steps, interactions and the events for step control on the cyclic operation. Rinse and purge steps were carried out with fresh carbon dioxide 4.5 and nitrogen 5.0 (purity greater than 99.995% and 99.999%, respectively). Cyclic Steady State (CSS), which is the nature of periodic adsorption processes, implies a steady state in which the conditions at the end of each cycle are identical to those at the beginning. The criteria used to confirm attainment of CSS was when thermal and concentration profiles at the end of a cycle is within a relative tolerance value of 0.01% compared to the values of the previous cycle.

4. Results and discussion

4.1. Adsorbent material screening for CO_2 adsorption for TSA.

CO_2 capture using organic and inorganic porous materials (e.g. carbonaceous materials and zeolites respectively) consumes less energy when compared to CO_2 capture with chemical absorbents such as amines. This is because new bonds are not formed between the adsorbate and the adsorbent, and therefore much less energy is required for the CO_2 regeneration. Different adsorbents have been developed on a commercial scale for CO_2 capture (Zhao et al., 2015) such as activated carbons (ACs) (Rashidi and Yusup, 2016; Zhao et al., 2015), carbon molecular sieves (CMS) (Liu et al., 2016; Nabais et al., 2006; Verma and Walker, 2015), zeolites (Cheung and Hedin, 2014; Gleichmann et al., 2016; Linda Shi and Hurst, n.d.; Patrícia A.P. Mendes et al., 2017; Silva et al., 2012), metal organic frameworks (MOFs) (Ben-Mansour et al., 2016; Sreenivasulu et al., 2015; Zhang et al., 2014), and silica or porous polymers (Lee and Park, 2015). Every type of adsorbent has different properties (such as the specific surface area, total micropore volume, etc.), which make them more appropriate for different operational conditions. Then CO_2 adsorption efficiency can therefore be improved by selecting an appropriate adsorbent material.

While the number of new adsorbent materials reported has proliferated, only a very select few will undergo bench-top testing and even fewer will pass on to pilot testing stage, partly due to the limited availability of production materials. Therefore, the adsorbent screening focuses on commercially available zeolites and CMS. For adsorbent material screening, the starting point for sorbent selection is to examine the fundamental properties that can influence the adsorptive separation. The adsorptive separation is achieved by one of three mechanisms: steric, kinetic, or equilibrium effect. The steric effect derives from the molecular sieving properties of zeolites and molecular sieves. In this case, only small and properly shaped molecules can diffuse into the adsorbent, whereas other molecules are totally excluded. Kinetic separation is achieved by the differences in diffusion rates of different molecules. A large majority of processes operate through the equilibrium adsorption of mixture and hence are called equilibrium separation processes. Steric separation is unique with zeolites and molecular sieves because of the uniform aperture size in the crystalline structure. This type of separation is generally treated as equilibrium separation. CO_2 separation by PSA using zeolite is based on the preferential adsorption of CO_2 over N_2.

4.1.1. Textural properties determination.

Textural parameters S_{BET} and VDA_{CO2} obtained from the N_2 and CO_2 adsorption isotherms of CMSs and zeolites are shown in Table 24. The results revealed that the S_{BET} and VDA_{CO2} of zeolites were higher than for CMSs. The presence of narrow micropores in the adsorbent is important because they can increase the diffusion rate of CO_2 compared to larger pores (Schroter and Carbon, 1993).

Table 24: Specific surface area (S_{BET}) and narrow micropore volume (VDA_{CO2}) on various adsorbents.

Sample	Adsorbent type	S_{BET} (cm^2/g)	VDA_{CO2} (cm^3/g)	Maximum CO_2 adsorbed at 0ºC (mmol/g)
CMS-I	Carbon Molecular Sieve	554	0.20	2.94
CMS-II		425	0.16	2.32
CMS-lll		450	0.18	2.36
13X	Zeolite with binder	725	0.25	5.62
13X-APG		655	0.26	5.50
5A		622	0.21	4.75
APG-III		756	0.26	5.68
13xBL	Zeolite binderless	782	0.30	6.59
5ABL		709	0.24	5.84
4ABL		573	0.22	4.95

Adsorption/desorption isotherms of N_2 for zeolites and CMS are shown in Figure 46. Zeolites exhibit a type I shape according to IUPAC classification. It can be observed, that at the beginning of the isotherms, a rounded knee is formed at a very low relative pressure (until 0.05 of relative pressure, defined as the sample pressure divided by the absolute pressure on the instrument). This effect is interpreted as the presence of the microporous structure. After an increase up to 0.95 of the relative pressure, the zeolites with binder, displayed a fast increment compared to the binderless zeolites, showing a steeper slope. This effect was produced by the different mesoporous structure between the two types of zeolite families and can be interpreted as a higher mesopore volume for the zeolites with binder. Thus, it can be deducted that the binder used in the production of the pellet beads, influenced directly on the mesoporous volume. Contrarily, the formation of a low mesopore volume in the binderless materials was achieved due to the application of spacers in the production process of this type of material (Gleichmann et al., 2016; Schumann et al., 2012). Finally, the volume of N_2 adsorbed on zeolite 4A and CMSs was practically zero because at cryogenic temperature N_2 has kinetic restrictions to enter the narrow micropores of these sieves (Martin-Calvo et al., 2014). As in the case of zeolites, it can be observed at low relative pressures a steeply slope associated to the

micropores and at relative pressures higher than 0.9 a slope related to the presence of mesopores.

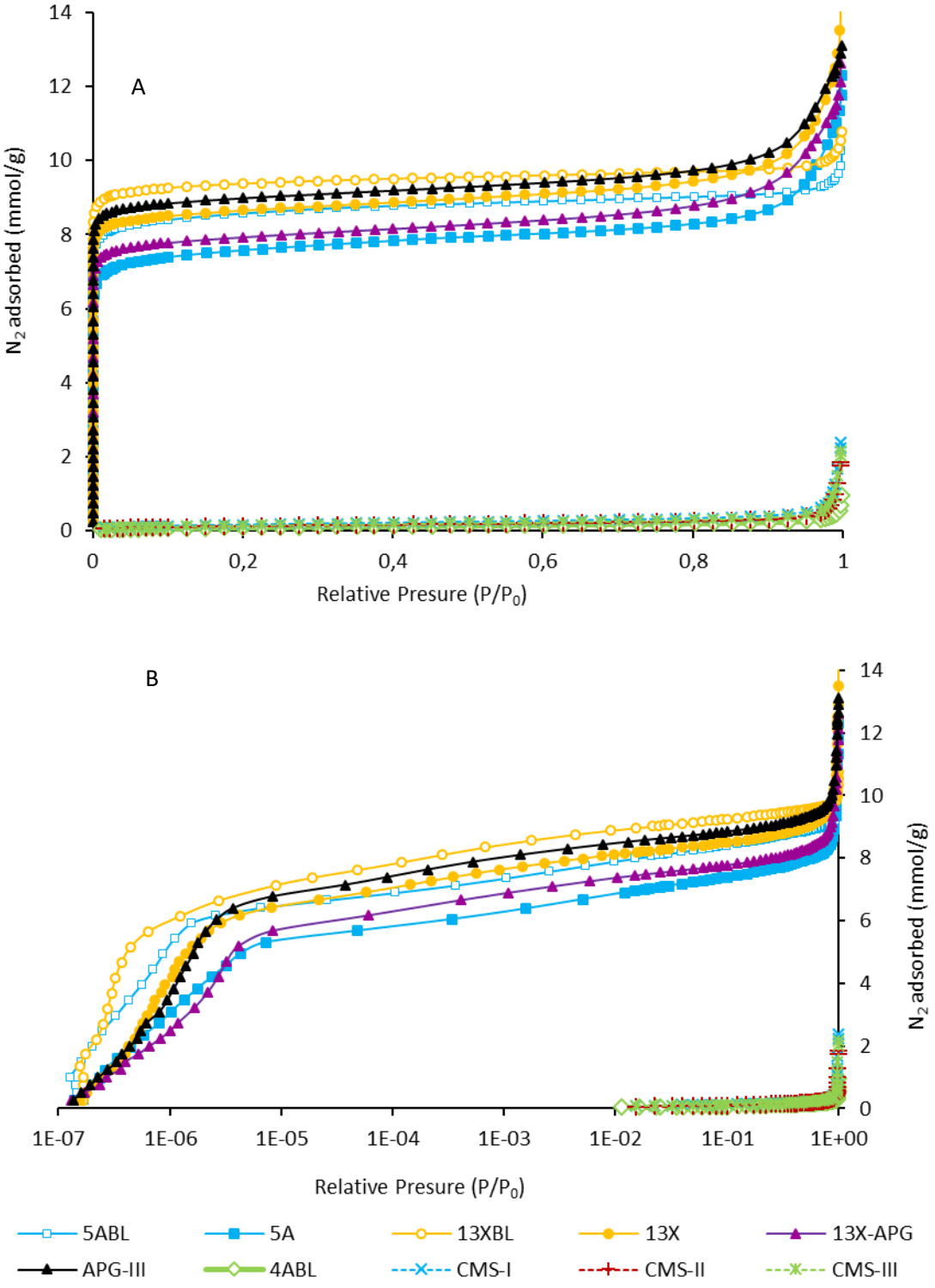

Figure 46: (A) N_2 adsorption isotherm for zeolites at 77 K, (B) N_2 adsorption isotherm zeolites at 77 K logarithmic plot.

Adsorption/desorption isotherms of CO_2 at 273 K are shown in Figure 47 for zeolites and CMS. Clearly, it can be observed that the CO_2 adsorption capacity is higher for zeolites than for CMSs. Increasing the relative pressure, 13XBL was the material with the highest CO_2 adsorption capacity (6.59 mmol/g). On the other hand, 4ABL and 5A were the zeolites with the lowest CO_2 adsorption capacity (4.75-4.95 mmol/g).

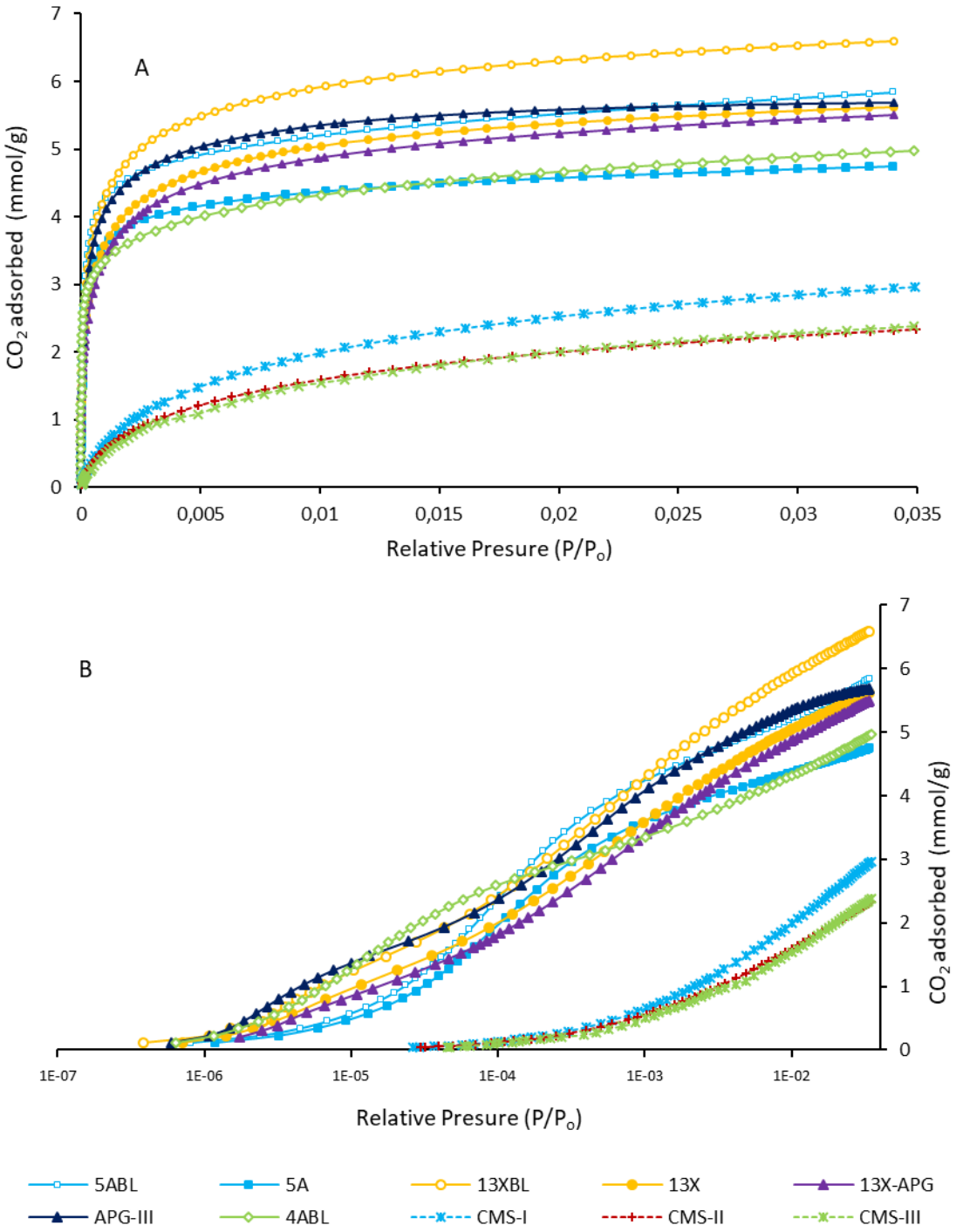

Figure 47: (A) CO_2 adsorption isotherms for zeolites at 273 K, (B) CO_2 adsorption isotherms for zeolites at 273 K logarithmic plot.

In Figure 47 (B) the isotherms were plotted on a logarithmic scale to differentiate the effects of the different materials at very low pressure, it can be observed that the CO_2 adsorption capacity was higher at low relative pressures with the binderless materials and the zeolite APG-III. On the other side, after 0.005 of relative pressure the CO_2 adsorption capacity had an asymptotic tendency (see Figure 47 A). The binderless materials adsorbed a higher amount of CO_2 (17% for 13XBL and 23% for 5ABL) than the analogous binder containing material (13X and 5A respectively). This percentage was proportional to the mass of the inert mineral binder in the adsorbent (about 20 wt% of binder for all commercial zeolites). Consequently, the adsorption capacities of binder zeolites were lower by approximately the amount of containing binder. Among the CMSs, CMS-I had the highest CO_2 adsorption capacity (2.94 mmol/g) and CMS-II and CMS-III had similar CO_2 adsorption capacity (2.3 mmol/g).

4.1.2. Determination of CO_2 adsorption capture, heat of adsorption and adsorption equilibrium time with the TGA-DSC method

The q_{TGA} and $\Delta H_{ads}/\Delta H_{des}$ and the time needed to reach adsorption equilibrium (t_{eq}) of the selected materials (Table 25) were determined from TGA and DSC characteristics curves shown in Figure 17. The total adsorption capacity between the adsorbate molecules and the adsorbent is the sum of their non-specific contributions (dispersion and repulsion energy) and the electrostatic contributions (electric fields created by dipole and quadrupole interactions) (Yang, 2003). As an approach, it can be considered that the determination of the ΔH represents the contribution of the total potential energies of adsorption (Yang, 2003). From Table 25, it can be observed that CMSs had approximately one third of the total capacity of the zeolites. This agrees with the previous results from CO_2 adsorption isotherms where it was observed that zeolites had a higher CO_2 adsorption capacity.

The zeolites had a higher q_{TGA} due to their adsorption potentials not only depends on their electrostatic energies as in the case of CMSs. These materials had an additive contribution on their non-electrostatic energies, such as the polarizability of the adsorbate molecule (Yang, 2003). Zeolites 13XBL and 5ABL showed the highest values of ΔH what agrees with the fact that they are the adsorbents with a higher q_{TGA}. These two materials also showed the highest adsorption capacity in the CO_2 adsorption isotherms experiments at 0ºC. It was observed from the experiments with TGA that the t_{eq} of zeolites was almost the double than for CMS.

Table 25: The adsorption capacity (q), adsorption heat (ΔH) and time to reach adsorption equilibrium (t_{eq}) on various adsorbents obtained from TGA and DSC analysis.

Sample	Adsorbent type	q (mmol/g)	ΔH (kJ/mol)	t_{eq} (min)
CMS-I	Carbon Molecular Sieve	1.13	45.74	65.40
CMS-II		0.92	32.64	60.95
CMS-lll		0.91	33.09	61.82
13XNa	Zeolite with binder	3.62	56.84	118.70
13X-APG		2.86	54.27	118.05
5A		3.96	57.23	117.98
APG-III		4.69	59.02	120.38
13xBL	Zeolite binderless	5.48	65.42	121.08
5ABL		4.95	62.41	108.01
4ABL		3.46	54.72	106.88

As it can be observed in Figure 48 (A), there is a linear correlation between q_{TGA} and ΔH_{ads} with the studied adsorbents. The maximum CO_2 adsorbed in the experiments with the ASAP 2020HD (Figure 48 B) equipment at 0ºC also correlates quite well with q_{TGA}. The methodology proposed in this work took from 3 to 5 hours (including set-up, degasification, adsorption, and desorption) in comparison with gravimetric and volumetric adsorption measurements that can need longer times (around 1-2 days) and more resources.

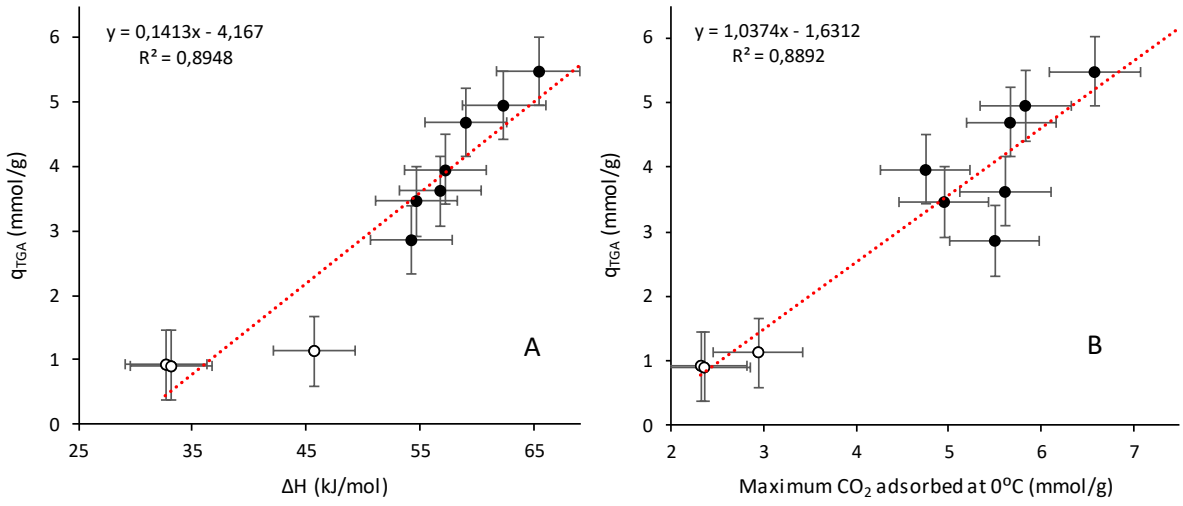

Figure 48: (A) Influence of ΔH on q_{TGA} of the studied adsorbents. B) Influence of the maximum CO_2 adsorbed at 0ºC on q_{TGA} on the of the studied adsorbents. ● Zeolites; ○ CMS's.

4.1.3. Influence of the textural Properties on CO_2 adsorption.

The influence of textural properties, S_{BET} and VDA_{CO2}, on q_{TGA} was also evaluated (Figure 49) in order to see which of both properties is more important in the prediction of the CO_2 adsorption capacity of the adsorbents. It can be observed how there is a lack of correlation of S_{BET} with q_{TGA} (Figure 49 A) and with VDA_{CO2} (Figure 49 B). Apparently S_{BET} is a more suitable parameter to predict the CO_2 adsorption capacity, but the points are a great distance away from the size of the error bars, so our results are inconsistent with a linear relationship between.

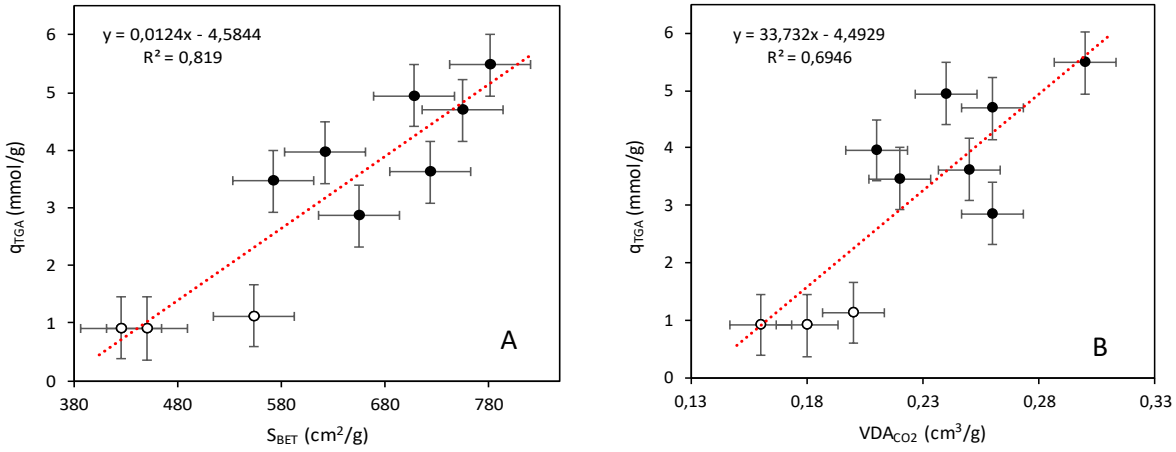

Figure 49: Influence of A) S_{BET} and B) VDA_{CO2} on q_{TGA} of zeolites and CMSs. ● Zeolites; ○ CMS's.

The zeolites with binder agent, present a lower S_{BET} than the binderless materials, this effect can be attributed to the higher volume of mesoporous created by the binder agent, that consequently contributes to a lower S_{BET} value. However, it is evident that a high S_{BET} value is not effective for the adsorption of CO_2, but it impacts on the transport of the adsorbate to the effective adsorbent zone (the narrow micropore structure) as discussed on section 4.1.1. On the other side, Figure 49 (B) shows the lack of correlation for q with VDA_{CO2}; as it is well known in zeolites, the electrostatic energies such as permanent dipole and quadrupole moments can make significant contributions toward the adsorption effect, and indeed can dominate the total energy. Zeolite 13X contains Na^+ ions and 5A zeolite contains Ca^{2+} ions (Rouquerol et al., 2014b). These atoms are present on the zeolites surface causing high electrostatic contributions for the CO_2 adsorption (Yang, 2003). From Table 25 it can be seen that the zeolite 13XBL has a higher adsorption capacity over 5ABL, this fact can be related to their difference in the

total electrostatic interactions potentials promoted by the polarizability values of the Na^+ ions over Ca^+ (Rouquerol et al., 2014a).

4.2. Temperature swing adsorption study approach.

4.2.1. Study of cyclic behavior of the materials for its use in TSA.

Cyclic adsorption separation processes are based on the selective adsorption of one or more components in a gas mixture, with the adsorbent regeneration by pressure (PSA/VSA) or by temperature (TSA). The adsorption is shown as an alternative of separation that has very efficient applicability since the adsorbent shows high adsorption capacity, high selectivity, good mechanical properties, ease of regeneration and stability to repeated cycles of adsorption/desorption.

The cyclic or periodic characteristic of the separation processes is fundamental from the viewpoint of intensification, because it determines the duration of the cycles, hence the productivity. As a result, the main objective is to shorten the duration of the cycles in order to intensify the process. One important feature of adsorption processes is that mass and heat transfer characteristics are strongly related. Low temperature promotes the adsorption while high temperature encourages the desorption (regeneration of the adsorbent). Hence the productivity of such a process depends strongly on the frequency at which we are capable of varying the temperature of the adsorbent bed, i.e. heating or cooling the adsorbent as quickly as possible to reach the temperature set-points for adsorption and desorption, respectively (Cruz et al., 2003).

To capture CO_2 with TSA, it is very important to understand the cyclic behavior of the adsorbents. Therefore, a methodology based in TGA/DSC was applied to study the CMSs and the zeolites using different operating conditions listed in the section 2.3.2. CMS-I and APG-III were previously selected as representative materials. CMS-I was selected since it showed a higher q_{TGA} in the previous section. APGIII was selected since it is a benchmark zeolite which is well-known to work well at high temperatures (>60°C) (Ling et al., 2015; Molsiv, 2015; Wang et al., 2013a, 2012). In Figure 50 (A), the evolution of q_{TGA} of CMS-I and APG-III during the adsorption-desorption cycles is observed. CMS-I was studied at a desorption temperature of 120ºC (methodology of Table 4). For APG- III two analyses were carried out, one with desorption at 120ºC (methodology of Table 4) and other with desorption at 350ºC (methodology of Table 5). For CMS-I, q_{TGA} was quite constant during the different cycles (see Figure 50 A), which means that the

desorption was complete at 120ºC. In the case of the cycling experiment with APG-III desorbing at 120ºC, q_{TGA} decreased from 1.4 mmol/g in the first cycle until stabilizing in 1.2 mmol/g at the fifth cycle. This was caused because at 120ºC APG-III was not completely regenerated, resulting in lost working capacity on each cycle. As discussed before, zeolites have a higher adsorption capacity than CMSs, and they require more energy in order to be regenerated completely. To compare the cyclic performance of both adsorbents at conditions of total regeneration, experiments with APG-III at desorption temperature of 350ºC were carried.

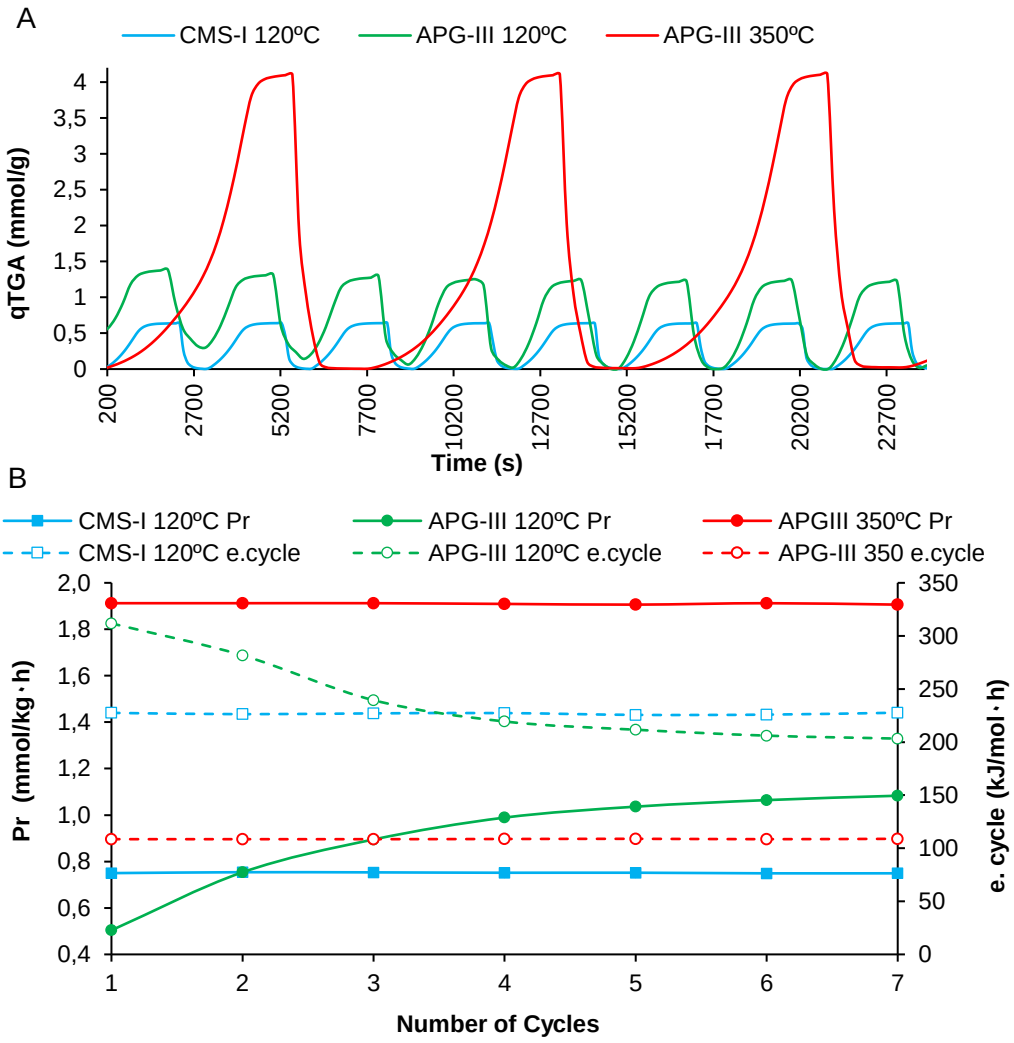

Figure 50: Adsorbents cyclic performance of CMS-I, APG-III at 120 ºC and 350 ºC of desorption temperature. (A) Cyclic CO_2 adsorption capacity, (B) Cyclic productivity performance and cyclic energy consumption.

In Figure 50 (A) it can be observed how q_{TGA} of APG-III regenerated at 350ºC was steady during all the cycles as in the case of CMS-I. It was evident that the increase of the desorption temperature increased the APG-III cycle time. In one cycle performed with APG-III desorbing at 350ºC, it was possible to carry out three cycles with CMS-I

desorbing at 120ºC during the same amount of time. Despite that, in one cycle of APG- III the q_{TGA} was higher (4.11 mmol/g) than the sum of all the q_{TGA} of the three cycles carried out with CMS-I (2.40 mmol/g) during the same period. Figure 50 (B) shows the evolution of productivity and energy consumption during these cycle experiments. After 7 cycles, the productivity of APG-III desorbing at 120ºC increases from 0.5 mmol/kg·h to 1.1 mmol/kg·h and the energy consumption went from 311 kJ/mol·h to 203 kJ/mol·h. The adsorption of CO_2 with APG-III on the first cycles was high but the recovered material was limited in each cycle due to the uncompleted desorption step which was not at the desorption temperature of 120ºC, therefore the amount of recovered material per cycle time is increased once the adsorbent reaches a steady state having an equilibrium between their adsorption and desorption rates. In the case of CMS-I, the productivity (0.75 mmol/kg·h) and the energy consumption (226 kJ/mol·h) remained constant along the consecutive 7 adsorption-desorption cycles.

This cyclic stability of CMS-I was explained by the total desorption of CO_2 at the desorption temperature of 120ºC. It can also be observed that at the regeneration temperature of 350ºC, APG-III presents an invariable productivity and energy consumption showing a good cycle stability. From Figure 50 (B) it can be concluded that the productivity of APG-III desorbing at 350ºC (1.92 mmol/kg·h) was 2.5 times higher than the one of CMS-I desorbing at 120ºC. The energy consumption of APG-III (108 kJ/mol·h) is reduced 52% in comparison with CMS-I despite the fact that the desorption temperature was increased up to 350ºC. Comparing the results of Figure 50, it can be concluded that the productivity and energy consumption of the zeolite APG-III was improved even by increasing the desorption temperature and cycle time. The energy consumption invested per gram of adsorbent was compensated by a higher desorption of CO_2 and a better utilization of the adsorption capacity on the same cycle time.

4.2.2. Effect of desorption and adsorption temperature on zeolite for TSA performance.

To study the influence of the desorption temperature on the TSA cyclic configuration a set of experiments was carried out using the methodology described in Table 5. In Figure **51** (A), it can be observed that the desorption temperatures have a considerable impact on the adsorption capacity, low desorption temperatures causes an increment on the q_{TGA} induced by the accumulation of non-desorbed CO_2. On the other hand, the study of the influence of the adsorption temperature was performed using the methodology

described on Table 6. Figure 51 (B) shows the results of the experiments, and the q_{TGA} keeps almost constant over the cycles; nevertheless, its capacity increments proportionally at low adsorption temperatures. Therefore, it can be affirmed that the higher is the difference between the adsorption and desorption working temperature (ΔT_w) the better is the working capacity for CO_2 capture.

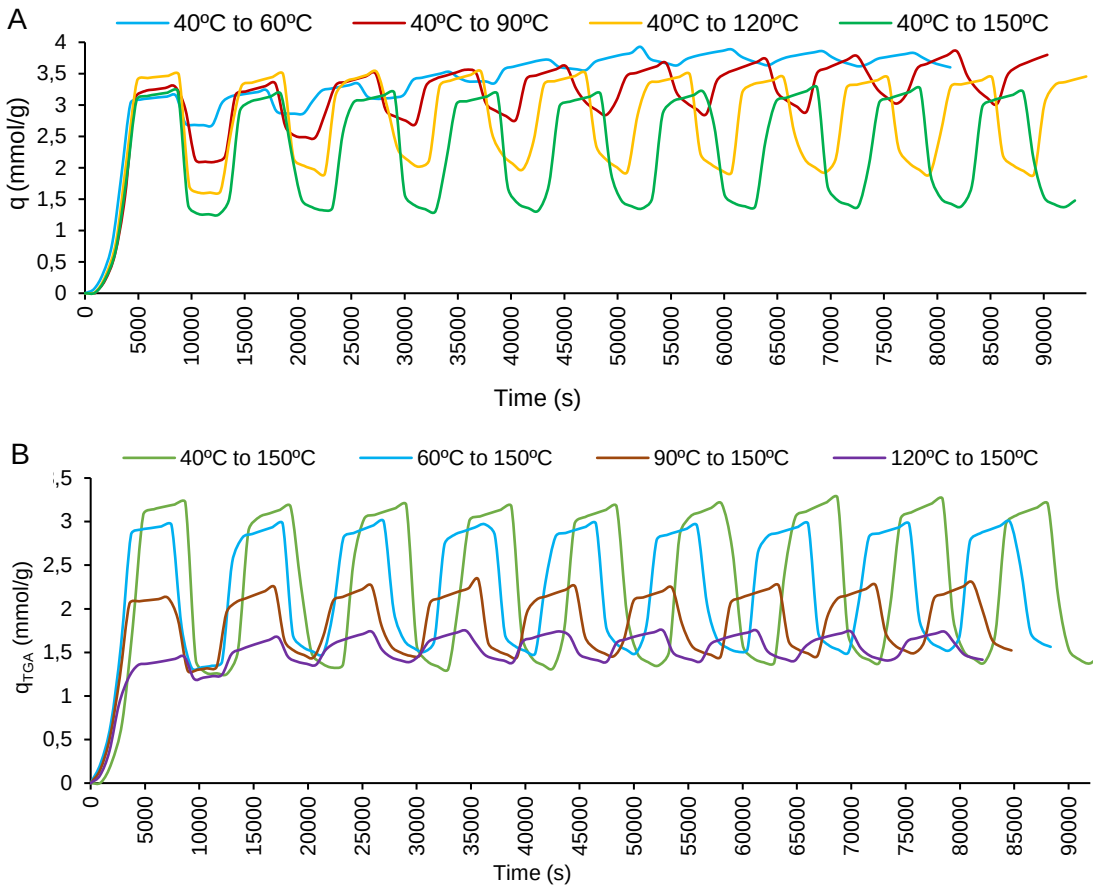

Figure 51: Zeolite APG-III cyclic performance, (A) Influence of desorption temperature, (B) Influence of adsorption temperature.

The CO_2 productivity and energy consumption are shown in Figure 52 for both sets of experiments. It can be observed in all experiments that the changes on adsorption and desorption temperatures had a high impact on the productivity and energy consumption in the first cycle. After the first cycle, the productivities were stabilized without significant variations through the consecutive cyclic repetitions. However, the behavior of the energy consumption in both sets of experiments was different. The energy consumption, when the adsorption temperature was kept at 40 ºC (Figure 52 A), was more stable at the desorption temperatures of 120ºC and 150ºC than at 60ºC and 90ºC (from 21 to 106 kJ/mol). The energy consumption was penalized by the poor CO_2 recovery during the desorption, inflicted by a low differential of temperature between adsorption and

desorption (ΔT) at the desorption temperatures of 60ºC and 90ºC (ΔT=20°C and ΔT=50°C respectively). In both figures, the values with a lower energy consumption were those with a higher ΔT. The highest productivities were obtained with the highest desorption temperatures (0.69 mmol/kg at 150ºC and 0.57 kJ/mol at 120ºC). On the other hand, when the desorption temperature was kept at 150 ºC (Figure 52 B) the adsorption temperatures with a higher productivity and lower energy consumption were 40 ºC and 60 ºC. Again, it was shown that a high ΔT is beneficial for both productivity and energy consumption.

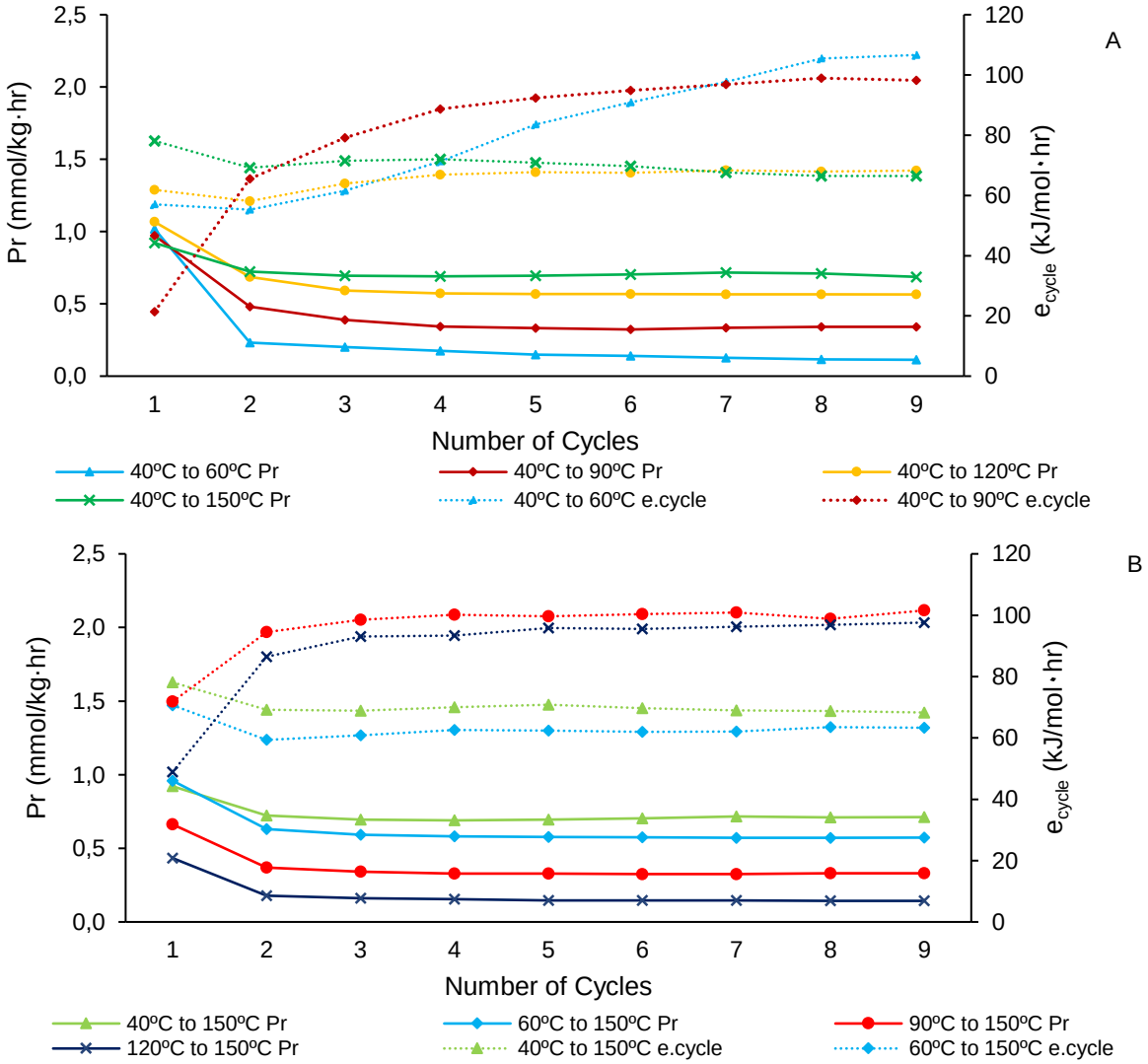

Figure 52: (A) APG-III productivity and energy consumption performance at 40°C of adsorption temperature and different desorption temperatures of cyclic CO_2 adsorption capacity, (B) APG-III productivity and energy consumption performance at 150°C of desorption temperature and different adsorption temperatures.

From these temperature intervals, the strategy for an optimal energy efficiency of TSA can be formulated using an adsorption temperature of 60ºC and a desorption temperature of 150 ºC, this means a saving of energy on the process due to less energy

being needed to cool down the gases in the adsorption stage. The decision can be formulated taking into consideration the heat integration of remaining energy sources available on an industrial scenario. For example, the use of residual steam from an existent industrial boiler or the use of existent cooling tower.

Finally, a new methodology (Table 26) was used to evaluate the TSA cyclic behavior of different zeolites (13X, 13X-APG, APG-III, 13XBL, 5A and 5ABL) under optimal energy efficiency working conditions.

Table 26: Optimized methodology for cyclic performance analysis of zeolites.

Stage	Temperature (°C)	Time (min)
Cool down	150-60	20
Adsorption	60	20
Desorption	60-150	5

Before each experiment, the zeolites were regenerated at 350ºC. The adsorption-desorption profiles of the cycle experiments are shown in Figure 53, where it is observed that the evolution of q_{TGA} was different for each zeolite. The zeolites adsorbed at their maximum capacity in the first cycle and then, they lose adsorption capacity during the next cycles due to their low desorption rate. Despite this effect at the beginning of the cycle, the q_{TGA} is stabilized in the after the sixth cycle.

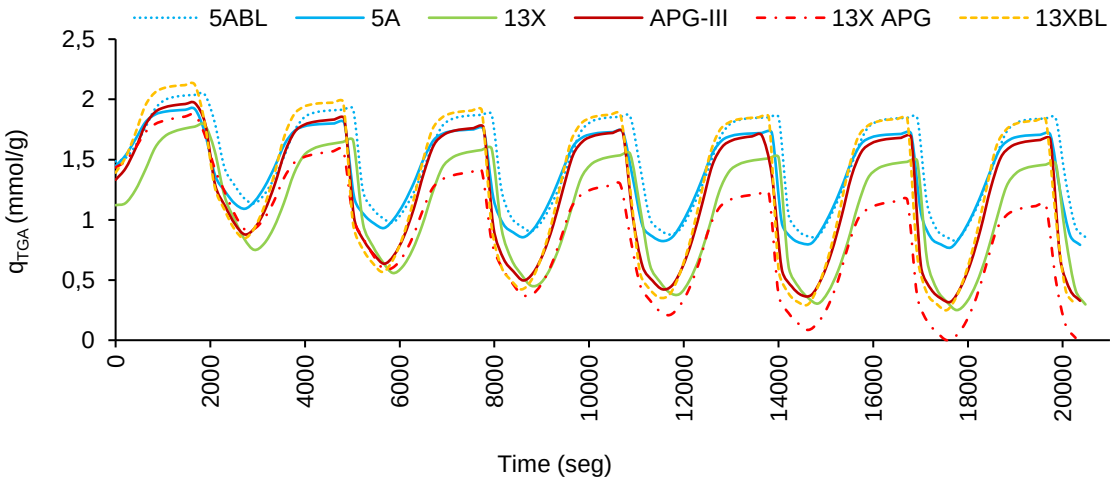

Figure 53: Zeolites cyclic performance at 60°C of adsorption temperature and 120ºC of desorption temperature.

The productivity and the energy consumption obtained with each zeolite was shown in Figure 54 (A) and Figure 54 (B) respectively. The zeolite with the highest productivity was 13XBL (1.94 mmol/kg·h) while 5A was the zeolite with the lowest (1.15 mmol/kg·h). The lower energy consumption was for 13XBL (98 kJ/mol·h) and the highest for 5A (165

kJ/mol·h). Likewise, the binderless materials (5ABL and 13XBL) showed higher productivity and lower energy consumptions than their analog binder-based materials (5A, 13X). These results confirmed that despite of the high mechanical and thermal resistance of the binder containing zeolites, the binderless zeolites have a stable cyclic behavior, since these materials did not show a decrease on their cyclic performance. On the other hand, it was confirmed that the zeolite APG-III had a better productivity than the 13X-APG with an equivalent energy consumption and that these two materials had a higher productivity and lower energy consumption than their analog zeolite 13X. In the last place, the 5A zeolites (binder and binderless) had the lowest productivity and the highest energy consumption.

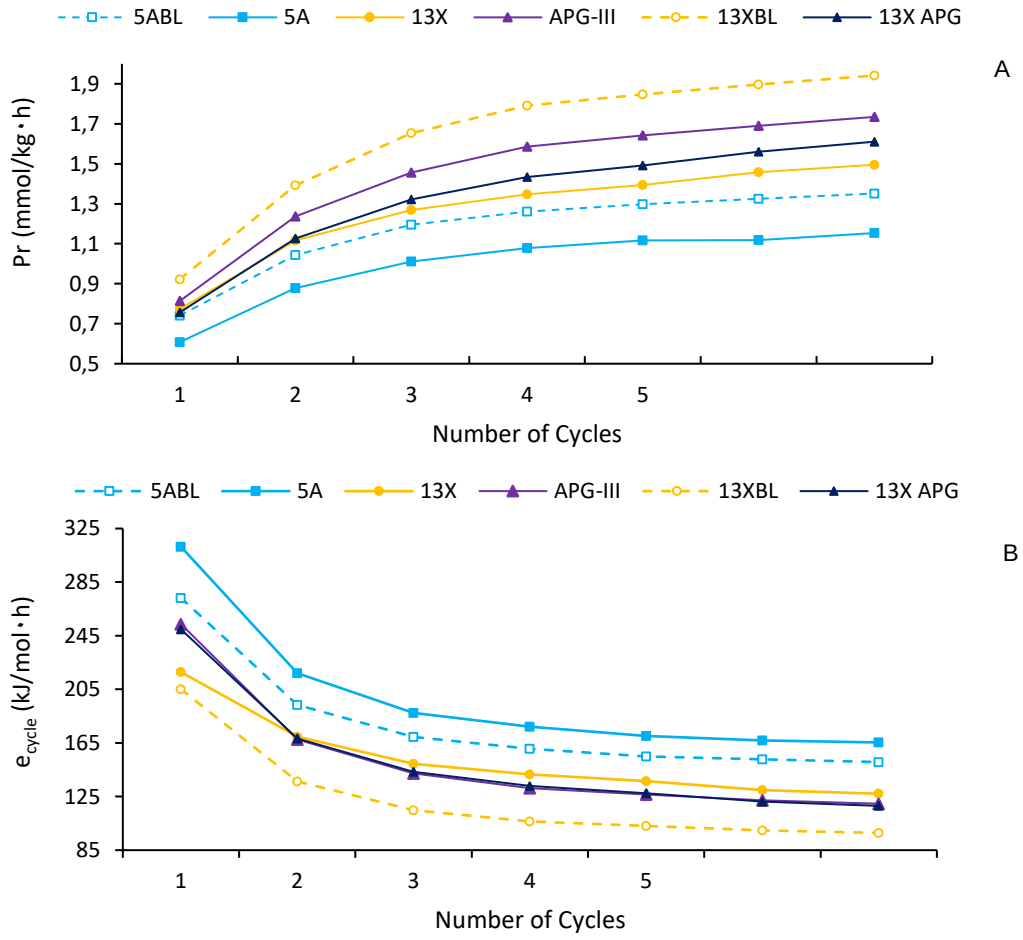

Figure 54: Zeolites (A) productivity and (B) energy consumption with 60°C of adsorption temperature and 120ºC of desorption temperature.

With these considerations, it can be concluded that for a TSA configuration, the material with a better performance is the zeolite 13X binderless, using as adsorption and desorption temperatures 60ºC and 150ºC respectively. As it can be noticed, the initial regeneration of the adsorbent had a considerable impact independent of working on low or high temperatures of adsorption. For this reason, it was interesting to study different

initial regeneration times to understand the influence of this stage on the overall TSA process performance. Figure 55 (A) shows three experiments carried out using zeolite 13XBL at 150 ºC as the regeneration temperature at different regeneration times.

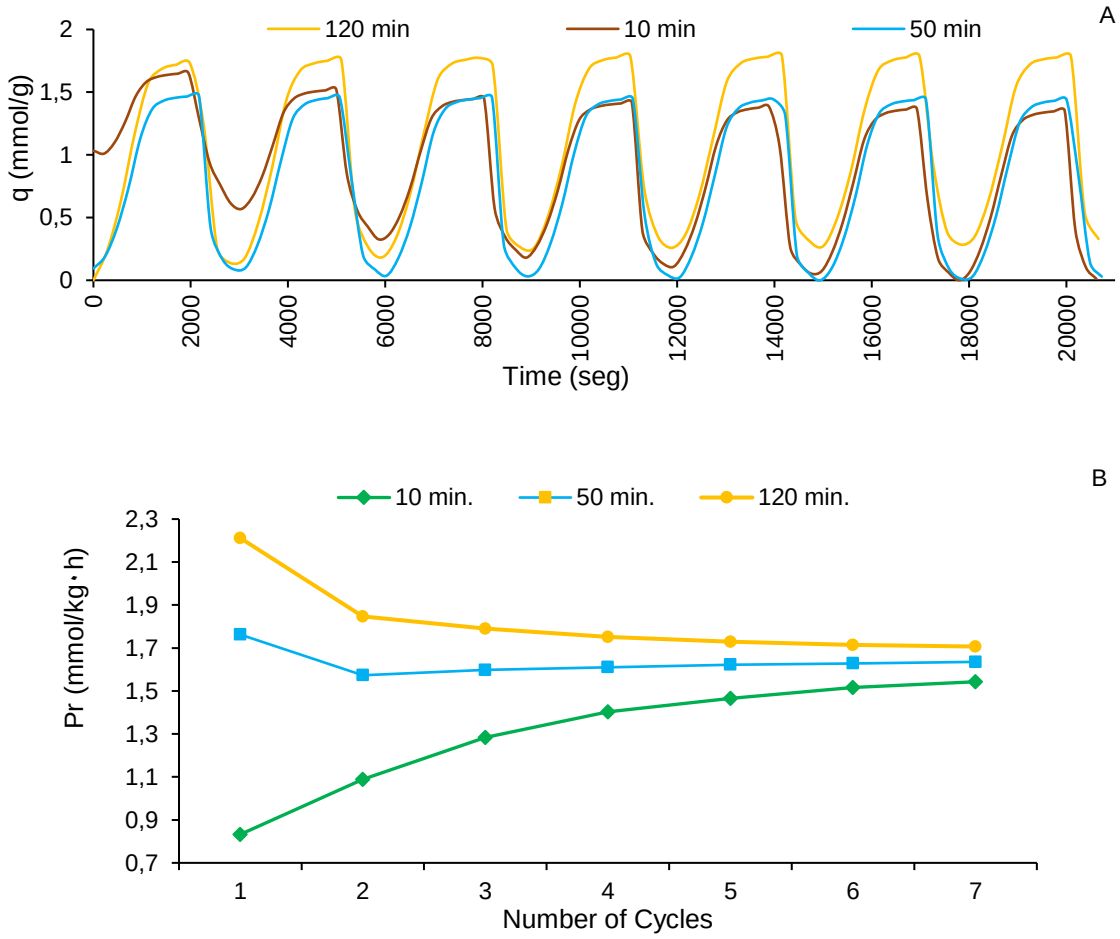

Figure 55: (A) Adsorbents cyclic performance and (B) Productivity at 40°C of adsorption temperature and 120ºC of desorption temperature at different initial regeneration times using 13XBL.

After the initial regeneration, the cycles were performed with zeolite 13XBL following the methodology of Table 26. It can be observed how the initial regeneration time had a strong effect at the beginning of the process, but this effect decreased along the cycle repetitions. Nevertheless, the productivity (Figure 55 B) showed a slight difference between the three initial regeneration times in the last cycle performed. With the cyclic repetitions, the adsorption productivity stabilized for all the initial regeneration times to a close value. With an initial regeneration time of 10 min the productivity was 1.54 mol/(kg·h), while with 120 min it was 1.70 mol/(kg·h). At longer initial regeneration times, other adsorbed molecules (such as H_2O and different fraction of atmospheric gases) were desorbed resulting in more available adsorption surface.

A qualitative methodology using TGA and DSC analysis has been developed to select adsorbents that could be applied in TSA for CO_2 capture in post combustion processes. The performed analysis unveiled the effect of the adsorption and desorption steps and the cyclic performance to show their potential on a continuous TSA process. The CO_2 adsorption capacity, adsorption heat and time to reach adsorption equilibrium for ten commercial adsorbents (3 CMSs and 7 zeolites) were determined using a mixture of 15% CO_2/ 85% N_2. The binderless zeolites 13XBL, APG-III and 5ABL showed the highest values of CO_2 adsorption capacity and heat of adsorption over the different studied materials. However, despite 5ABL having a high $q_{TGA,}$ it shows a low productivity (1.15 mmol/kg·h) limited by the poor desorption rate at the range of process temperatures (150ºC for desorption and 60ºC for adsorption) which is reflected by the high energy consumption (165 kJ/mol·h) of CO_2 recovery. On the other hand, the highest productivity (1.94 mmol/kg·h) and the lower energy consumption (98 kJ/mol·h) was achieved by 13XBL.

The productivity for CMSs is almost constant in every adsorption-desorption cycle, showing a complete and fast regeneration even working at low temperatures. In the case of zeolites, the difference between the adsorption and desorption temperatures, ΔT_W, has a strong effect on the adsorbent cycling performance. If the operating ΔT_W with zeolites is low, then the productivity is low, and the energy consumption is high. This is because the adsorption process is limited in each cycle by the desorption which is much slower than in CMSs. Binderless zeolites (5ABL and 13XBL) showed higher productivities and lower energy consumptions than their analog binder-based zeolites (5A, 13X).

For zeolites, an adsorption temperature of around 60ºC is preferred as this represents an appropriate balance on the adsorbent productivity and energy consumption. At maximum regeneration temperature (350ºC), the zeolites show a constant productivity and energy consumption, showing a good cycle stability. Two strategies for energy efficiency can be formulated, the first one using low working temperatures in a range of 60ºC for adsorption and 150ºC for desorption, and the second one, at high process temperatures in a range of 90ºC to 350ºC.

This fast screening methodology through TGA/DSC can be useful on the screening stages of the research of different adsorbents for CO_2 capture, taking into consideration the longer analysis times and resources needed on the application of the classic physical adsorption measurements methodologies of analysis (gravimetric and volumetric adsorption measurements). Because many operating conditions were considered, the

obtained results can serve as a basis to guide the cycle design adapted to given separation process targets, adsorbent design, adsorbent modification, or adsorbent optimization as the first approach, mainly when there is not enough time and resources.

4.2.3. Heating exchange simulations for CO_2 adsorption by TSA.

Significant reduction in the energy consumption of CO_2 capture systems remains a challenge. Clearly, the source and type of the energy used by the capture plant will play an important role in the overall operating cost. Many capture researchers are currently exploring integration options with power plants for the potential use of cheaper, low-grade thermal energy or heat recovered from flue gas cooling to offset part of the energy requirements of the capture process (Zenz et al., 2009). The TSA process is of interest due to its ability to directly utilize these low-grade thermal energy resources for regeneration. Table 27 shows the regeneration methods being employed in some studies at laboratory scale. In conventional TSA applications such as air and natural gas drying, the adsorbent is often regenerated by direct purge with a hot non adsorbing gas or steam.(Kast, 1985). Hence, as shown in Table 27, the bed is often first heated indirectly to the desired regeneration temperature using several means including heating jackets, electric heating tapes, or coils wrapped around the adsorbent, and hot/cold fluid carrying tubes.

The aim of the present section is to evaluate the potential of the combination of the indirect and direct heat TSA process for CO_2 capture. For this purpose, simulations were carried out with different operating conditions, and the performances were evaluated based on CO_2 productivity. The simulation was carried out using Tdyn® to provide an initial assessment of a column design for a TSA process. Tdyn® allows adding more elements in the mesh for sensitive areas, but also reduce the number of nodes in more trivial solution areas. A poorly planned and inefficient mesh can cause the calculation to not converge and/or cause excessively high calculation times. To determine the suitable number of mesh elements, some previous simulations were performed to assure the number of elements needed for reasonable results.

To have a correct precision and an operative simulation time, it is important to configure a correct model mesh. Three simulations of a single bead have been resolved with three different mesh configurations. The first mesh (case A) with 9135 nodes and 51899 elements. The second (case B) has 615 nodes and 3248 elements, 16 times smaller

than the first. The last one with 40 nodes and 160 elements. The time step used in the three cases was 0.01 seconds.

Table 27: Some studies on CO_2 capture by TSA, showing the regeneration methods used.

Description	Regeneration method	Adsorbent.	Ref.
Three TSA cycle configurations with heat integration by parametric analysis.	Indirect heating	Zeolite 13X	(Joss et al., 2017)
Modelling for energy-efficiency analysis based on carbon pump, two adsorption cycles based in carbon pump.	Indirect heating	Zeolite 5A	(Zhao et al., 2017)
Cyclic experiments using a hot CO_2 rich gas for regeneration on a single adsorption column.	Hot CO_2 rich gas	Zeolite NaUSY	(Ntiamoah et al., 2016)
Adsorbent-coated microchannels configuration	Indirect heating	Polymer matrix	(Pahinkar, 2016)
Chemical heat integration to reduce energy requirement	Indirect heating	Zeolium F9-HA	(Song et al., 2015)
Concentric tubes with heat-conducting oil and additional hot N_2 purge	Direct and indirect heating	Zeolite 13X-APG	(Wang et al., 2012)
Internal concentric tubes fin heat-exchanger packed in the annulus created by the tubes.	Indirect heating	13X and 5A	(Merel et al., 2008)
Bed is heated indirectly by means of steam condensation.	Indirect heating	Zeolite 5A	(Clausse et al., 2011)
Bed is heated by a heating tape coiled around the column and hot N_2 purge	Direct and indirect heating	Activated carbon	(Plaza et al., 2010)

Figure 56 shows the effect of the mesh size on the heat flow resolution. In all the simulations the adsorbent bead is exposed to CO_2 at 85ºC on three-time intervals (10, 20 and 30 seconds). In the simulation case C, it can be observed that there are some temperature profiles with a square contour which is clearly inconsistent. It is evident that case A is the simulation with more definition, showing more accurate results compared to the cases B and C. However, comparing case A and case B, the first one offers more precision on the results, but this configuration requires more calculation capacity and two times more calculation time (It took about 6, 3 and 2 minutes to solve meshes A, B and C, respectively). Therefore, the case A mesh configuration was used for the simulation of the three strategies described on Table 21. To reduce the calculation time, a square section of 2.5 cm of column was simulated.

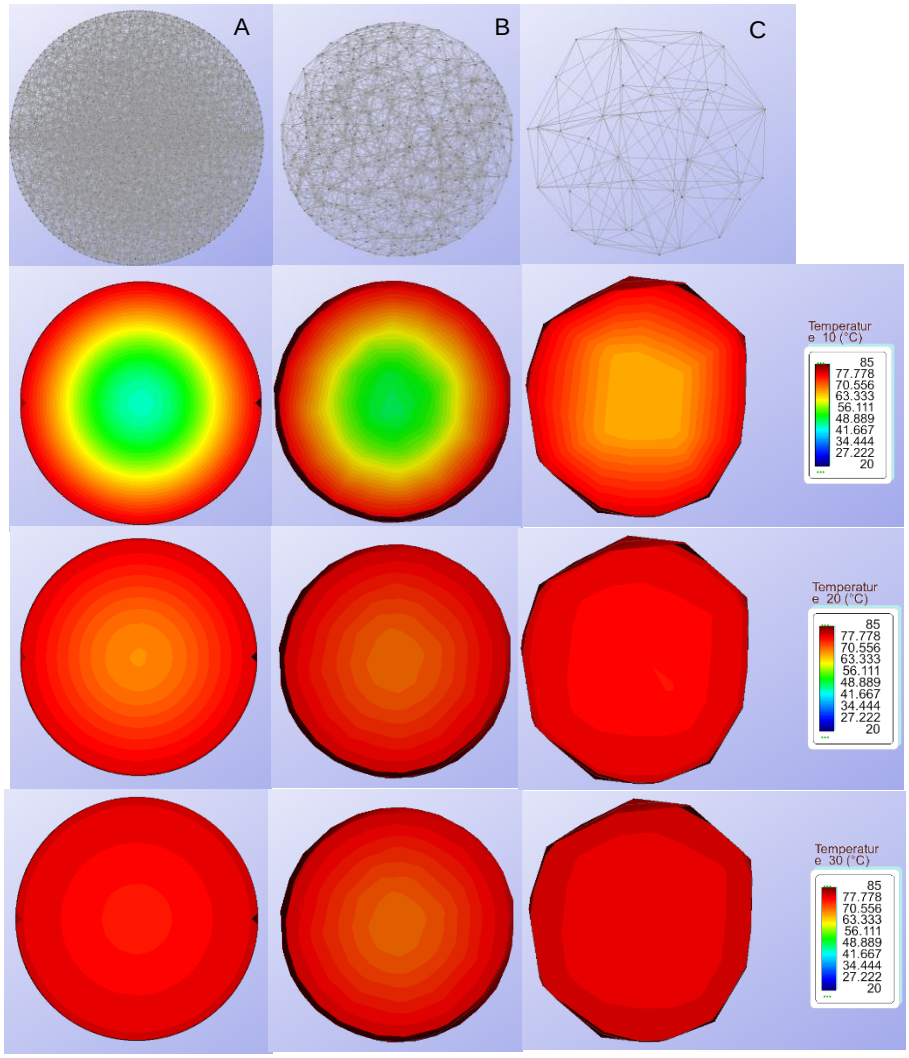

Figure 56: Simulated heat flow in an adsorbent bead at 10, 20 and 30 seconds. A) 9135 nodes, B) 615 nodes, C) 40 nodes.

4.2.4. Heating using direct hot gas strategy.

The used conditions for the simulation of the conduction heat transfer by a direct hot gas are described on

Table **20**. The Figure 57, shows the velocity profile and the heating flow over the simulated a section of the column. The adsorbent beads are placed in a triangular mesh separated equidistantly as described on section 3.5.1. The initial temperature in the system was fixed at 20ºC. The feeding process fluid was CO_2 at 60ºC entering from the top of the column. The simulation was performed over 30 seconds with four different inlet velocities: 0.10 m/s (case A), 0.25 m/s (case B), 0.50 m/s (case C) and 0.60 m/s (case D).

From Figure 57 it can be observed that the feeding velocity of CO_2 (profiles in A1, B1, C1 and D1) has an important effect on the heating exchange with the adsorbent (profiles in A2, B2, C2 and D2). In Figure 57 A2, the temperature of the first adsorbent layer is about 45ºC, while for the last layer it is about 30ºC. However, in Figure 57 D2 on the same referred adsorbent layers the temperature seems to reach a uniform temperature of about is 56ºC.

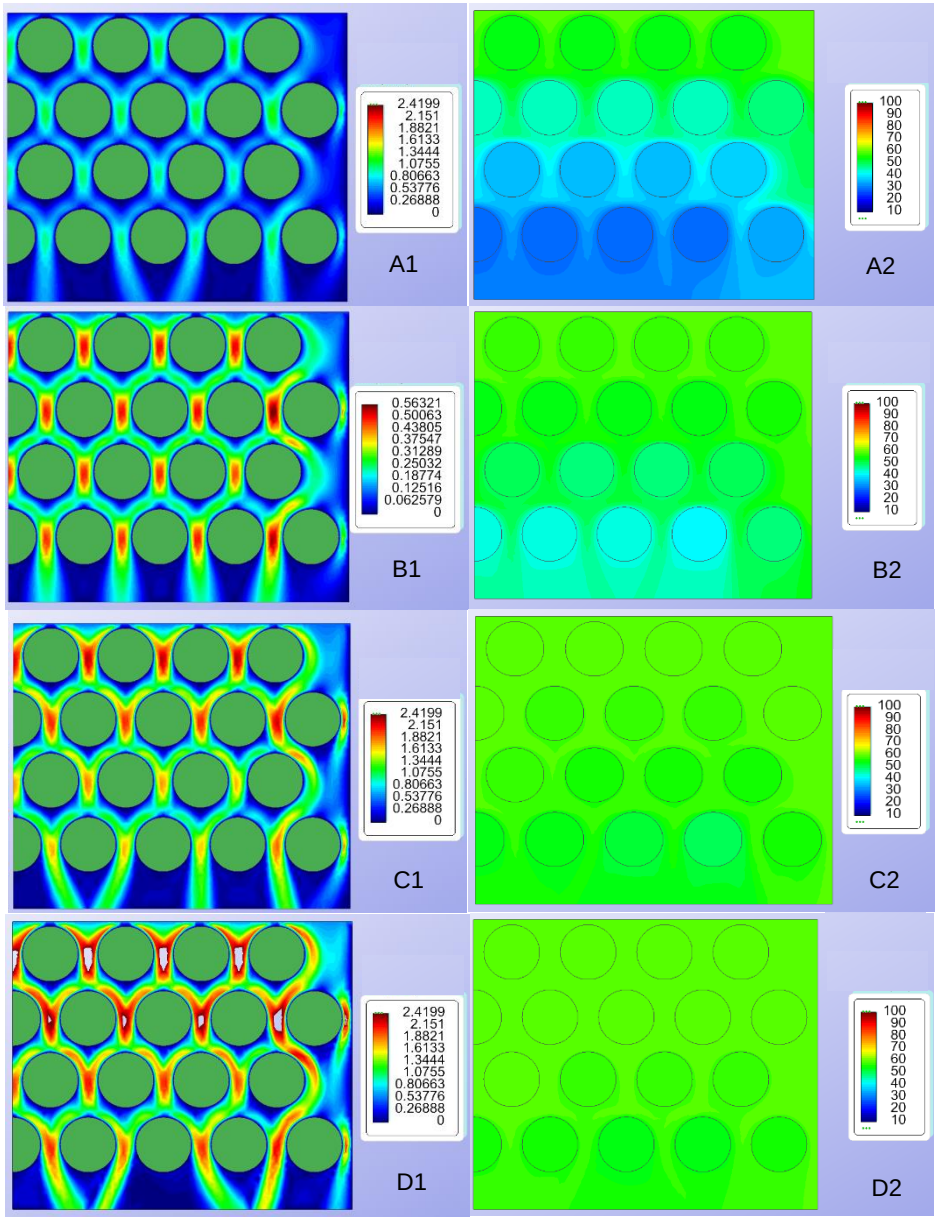

Figure 57: Simulated velocity profile at different gas inlet velocities: A1) 0.10 m/s, B1) 0.25 m/s, C1) 0.50 m/s, D1) 0.60 m/s. Simulated heat flow at different gas inlet velocities: A2) 0.10 m/s, B2) 0.25 m/s, C2) 0.50 m/s, D2) 0.60 m/s.

Figure 58 plots the temperature profile of the previous simulations with feed flow speeds from 0.01 m/s to 0.60 m/s over 30 seconds. The plotted temperatures profiles were the average temperature of the beads. It is evident that at higher speeds the heat exchange

between the hot gas and the solid increased. Nevertheless, this increment become less efficient on the heating exchange at feed flow speed higher than 0.25 m/s since the change of a speed of 0.60 m/s only increases the temperature 2ºC.

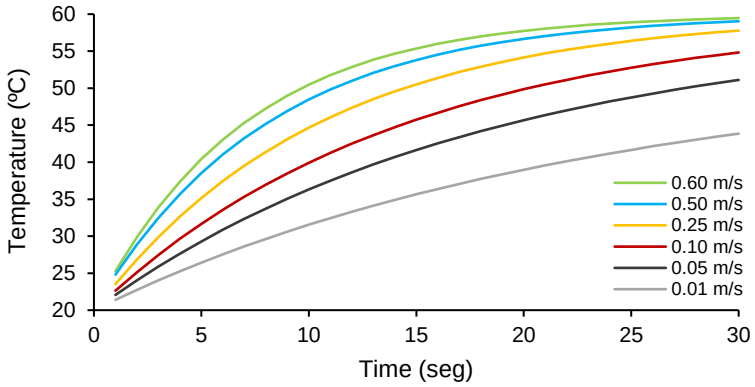

Figure 58: Temperature profile on the second adsorbent layer at different CO_2 feed

For the application of this heating strategy, the CO_2 stream can be heated by an electrical resistance or a thermodynamic cycle and be recycled until the desired desorption temperature on the adsorbent is reached.

4.2.5. Conductive heat transfer strategy by a heating fluid

To study the conduction heat transfer through the column wall by a heating fluid the column model was adapted to a concentric tube heat exchanger as described on section 3.5.1. The experimental conditions are described on

Table **20**, the initial temperature in all the columns was fixed at 20ºC and the temperature of the heating fluid was defined in the countercurrent flow at 80ºC. The simulation was performed over 30 seconds, changing the heating fluid speed flow from 0.01m/s to 0.20 m/s. Figure 59 shows the temperature profiles of the adsorbent beads, as well as the temperature profile on the jacket at the different hot fluid feed speeds flows.

It is possible to see that in Figure 59 (A) at 0.01 m/s of heating fluid feed flow speed, the adsorbent beads in contact with the column wall reached approximately the temperature of 40ºC, while the rest of the adsorbent kept at 20ºC of temperature. Due to the low speed value on the feed flow of the heating fluid, the column wall had a temperature of about 58ºC, with a low temperature transition profile from the hot liquid to the column wall, which makes it obvious that the low heating rate is due to the low feed flow speed.

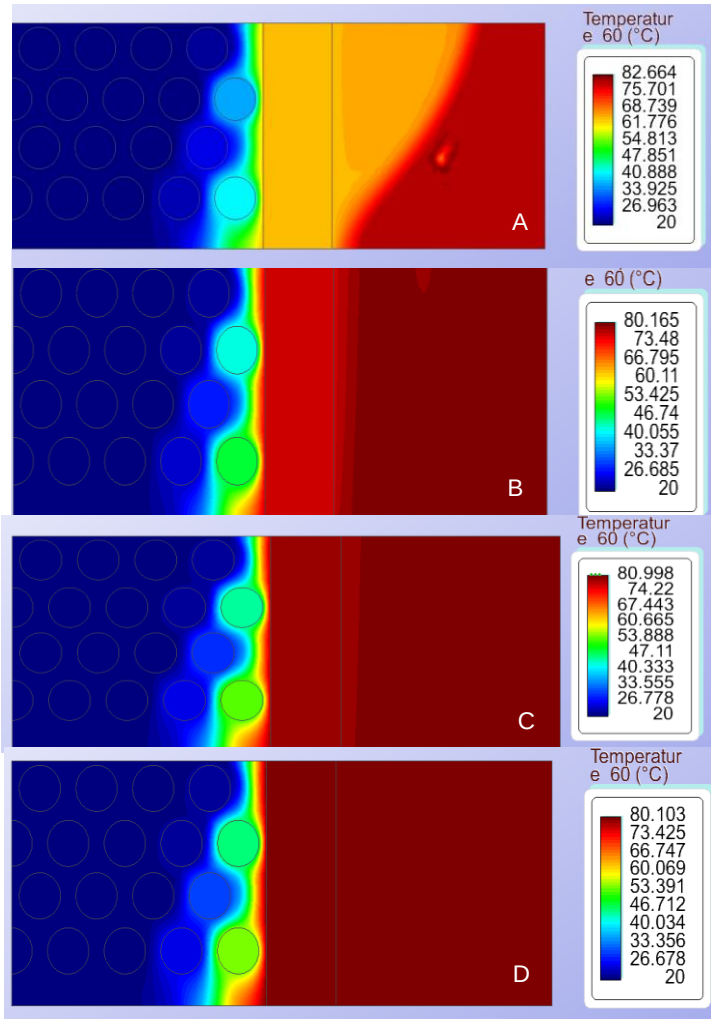

Figure 59:Simulated velocity profile at different gas inlet velocities: A) 0.10 m/s, B) 0.25 m/s, C) 0.50 m/s, D1) 0.60 m/s.

On the other hand, in Figure 59 (D) (at 0.60 m/s of flow speed) it can be observed that the adsorbent beads in contact with the wall had a temperature of about 62ºC were the column wall almost reached the same temperature of the heating fluid (85ºC). But the rest of the beads keep having the initial temperature of 20ºC.

Figure 60 plots the temperature profile of the different heating fluid feed flow speed (from 0.01 to 0.20 m/s) over 60 seconds of simulation time. The plotted temperature profiles were the average temperature of the beads in contact with the column wall.

From Figure 60 it can be observed that at higher fluid velocities, the heat exchange between the fluid and the adsorbent bead was also higher; but, the effect was negligible for the rest of the beads that were not in contact with the column wall. Increasing the feed flow speed from 0.01 to 0.2 m/s, the increment was about 13°C, while increasing the feed flow speed from 0.01 to 0.1, the increment was about 12°C. Therefore, the feed flow speed increments become less efficient on the heating exchange at feed flow speeds higher than 0.10 m/s.

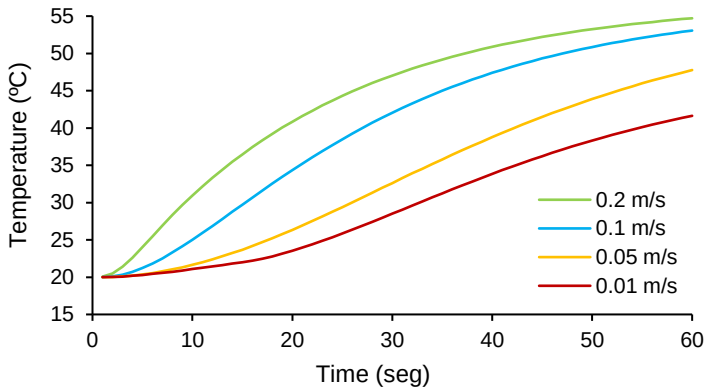

Figure 60: Temperature profile on the second adsorbent layer at different heating fluid speeds.

As it is well known, heat exchange can be promoted by including baffles on the column jacket. As seen in Figure 60, this heat exchange strategy has a low temperature transition through the adsorbent to the center of the packed column. The adsorbent beads don't have full contact between each other, leaving some free space occupied by the gas (CO_2). The low heat capacity of the gas as well as the adsorbent inhibit the heat flow, thus the heat exchange is poor across the rest of the package bead.

4.2.6. Heating transfer strategy by a heating fluid and hot gas feed.

To study the heat transfer through the column wall from a heating fluid and hot gas feed, the previous concentric tube heat exchanger column model was used, with experimental conditions as described on

Table 20. The initial temperature in the column was fixed at 20ºC, the CO_2 feed was set at 60ºC and the temperature of the heating fluid was defined in countercurrent flow at 80ºC and the heating fluid velocity was fixed at 0.1 m/s. The simulation was performed over 30 seconds with variations in the hot gas fluid feed flow speed between 0.01 m/s to 0.50 m/s. Figure 61 shows the temperature and the velocity profiles of the adsorbent bed, as well as on the jacket (formed on the inner space between the concentric tubes).

On Figure 61 (A1) at 0.01 m/s of heating fluid feed flow speed, it is possible to see that the adsorbent beads that were in contact with the column wall reach 55ºC (A2), and the first layer of adsorbent reaches a temperature about 50ºC. The rest of the adsorbent shows gradual a heat profile from 38ºC for the beads of the second layer to 20 ºC at the last adsorbent layer. In Figure 61 (B1) at 0.25 m/s the temperature change from 60ºC to

33ºC for the adsorbent in contact with column wall (B2). At 0.10 m/s in experiment C1 the variation of temperature is from 60ºC to 50º (C2), wile for 0.50 m/s in the experiment D1 is almost a homogeneous temperature of 60ºC (D2).

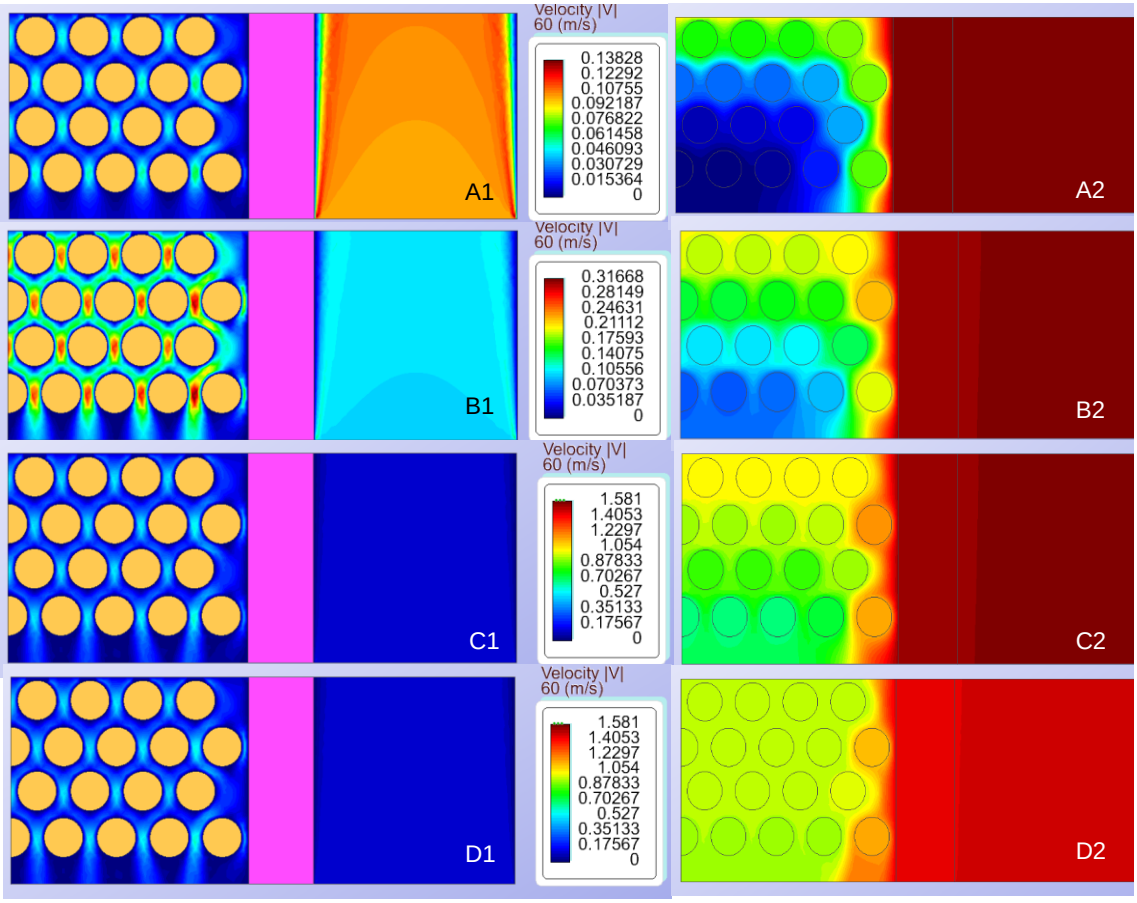

Figure 61: Simulated velocity profile at different gas inlet velocities: A1) 0.01 m/s, B1) 0.25 m/s, C1) 0.10 m/s, D1) 0.50 m/s. Simulated heat flow at different gas inlet velocities: A2) 0.01 m/s, B2) 0.05 m/s, C2) 0.10 m/s, D2) 0.50 m/s.

Figure 62 plots the average temperature profile of the beads at different heating fluid feed flow speeds (from 0.01 m/s to 0.50 m/s) over 60 seconds of simulation time. The plotted temperature profiles were the temperatures of the beads in contact with the column wall. The results obtained were quite like those obtained by heating the beads with the hot gas feed. Increasing the feed flow speed to 0.1 m/s the temperature is about 64ºC and doing it to 0.5 m/s the temperature only increases at 68ºC.

Therefore, the temperature profiles were compared for each strategy. In all cases, the fastest heating was achieved at high CO_2 feed flow speeds (0.5 m/s). Observing the temperature profiles, the best strategy is to heat the filling directly with the hot gas flow, without using the heating fluid in a concentric tube heat exchanger. The conduction heat exchanger strategy is limited by the poor heat flow capacity of the porous adsorbent

beads and the gas. This limitation can be reduced by expanding the effective surface contact by using a finned tube inside the adsorption column. Nevertheless, the design for its application on industrial scale is impractical if it is compared with the recirculation stream of preheated gas feed.

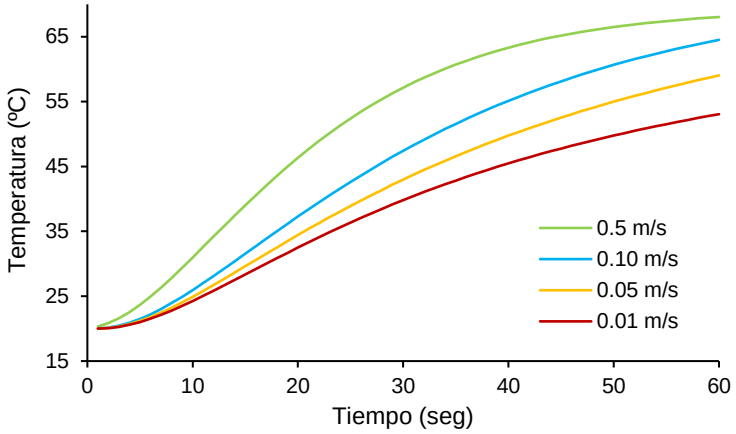

Figure 62: Temperature profile on the second adsorbent layer at different heating fluid speeds.

A critical factor in the regeneration of the TSA process is the energy required to heat the adsorbent bed to the specified regeneration temperature. In a practical point of view, the application of the TSA process has the limitation of poor exchanging heat on materials with low heating capacity. Therefore, the recirculation of a hot source of gas is attractive for the efficient heat exchange for the TSA process. However, for the CO_2 capture application, the adsorbate is the desired product; thus, a large volume of purge gas is required to heat the bed (because of the low heat capacity of gases). However, the indirect heating modes are likely to have scale-up issues and are not practical for large scale beds (>2 m diameter) (Tlili et al., 2009). It is noted that the source of energy and the potential energy losses associated with the method of heat exchange with the regeneration gas may impact the total energy consumption. Likewise, using a low CO_2 purity stream can result in significant dilution of the extracted CO_2 product when hot nonadsorbing gas is used for regeneration. Therefore, the application of a recirculation stream of preheated gas feed for desorption process requires a thermodynamic cycle and/or electrical resistance to heat the stream gas and a compressor to recirculate the stream through the adsorbent bed. The simulation results of heating exchange on a TSA column suggest that this process had higher energy consumptions compared with the VPSA, this supposition is confirmed through the energetic consumption values showed on Table 28.

Therefore, a critical factor in the regeneration of the TSA process is the energy required to heat up the adsorbent bed to the specified regeneration temperature. The best strategy is to heat the packed adsorbent directly with the hot gas stream, without using the heating fluid in a concentric tube heat exchanger. Nevertheless, the conduction heat exchanger strategy is limited by the poor heat flow capacity of the porous adsorbent beds and the gas. The simulation results of the heating exchange on a TSA column suggest that this process had higher energy consumptions compared to the VPSA.

Table 28 shows the energetic consumption values of scrubbing with amines versus TSA, TPSA and VPSA processes. Currently, the significant energy penalty and performance limitation of energy consumption are the main technical barriers to the large-scale applications of CO_2 capture (Vaccarelli et al., 2016). However, despite the TSA strategy being a process with more energy consumption (1.0 to 1.3 kWh/kg_{CO2}) than the VPSA process (0.6 kWh/kg_{CO2}) it has lower energy consumption than the typical absorption process with amines (1.1 to 1.7 kWh/kg_{CO2}).

Table 28: Comparison of Performances among different Processes for CO_2 Capture from Flue Gas

Process	Material	$yCO_{2,feed}$ (%)	Purity (%)	Recovery (%)	Power Consumption kWh/kg_{CO2}	Result type	Reference
Absorption	MEA	13	>99.0	90.0	1.1-1.7	Exp.	(Ho et al., 2008)
Absorption	MEA	15	99	98	1.2-1.3	Sim.	(Abu-zahra et al., 2007)
TSA	13X	12	96.0	90.0	1-1.2	Sim	.(Joss et al., 2017)
TSA	NaUSY	15	91.4	83.6	1.3	Sim.	(Ntiamoah et al., 2016)
VPSA	13X-APG	15	95.6	90.2	0.7	Exp.	(Wang et al., 2013a)
TPSA	5A	15	>99.0	84.5	1.0	Sim.	(Zhao et al., 2017)
VPSA	5A	15	>99.0	84.5	0.8	Sim.	(Zhao et al., 2017)
TSA	ZeolumF	5-40	>90.0	70-95.0	1.0	Sim.	(Song et al., 2015)
VPSA	silica gel	15	>99	>99	0.6	Exp.	(Li et al., 2016)

Desorption under vacuum seems to be simpler for large-scale applications (Zhao et al., 2017). Nevertheless, it is found that the actual power consumption of vacuum pump for VPSA, accounts for two thirds of the total power consumption and is greater than the theoretically predicted value by the conventional adiabatic pump-down calculation (Wang et al., 2013a). Because deep vacuum levels (<50 mbara) are not practical on a large scale, there is a strong necessity to develop a VPSA efficient process that can work with vacuum pressures of up to 250 mbara, to reduce the energy consumption.

Therefore, VPSA performance can be enhanced with a good VPSA cyclic design and the appropriate sizing of the vacuum pump.

4.3. Vacuum pressure swing adsorption study approach.

The aim of this section is to evaluate the performance of available commercial zeolites and CMS for CO_2 capture by Vacuum Pressure Swing Adsorption configuration. Adsorption equilibrium measurements of pure gases were performed in a magnetic suspension microbalance (Rubotherm, Germany) operated in a closed system. As described in section 2.4, adsorption equilibrium data of CO_2 and N_2 at 283 K, 298K, 323K and 343 K in the range of 0 to 10 bara for CMS-I, CMS-III, 4ABL, 5ABL and 13XBL were reported. The full set of data was fitted with Toth, Sips and Dual Site Langmuir (DSL) models. Next, an adsorption model based on the DSL for the mass transfer was developed and validated with the breakthrough experimental data, considering the energy and momentum balances.

The adsorption equilibrium and the adsorption kinetics are the essential set of data required for the process design. Binary equilibrium data was compiled for CO_2 and N_2 over the different adsorbents, as described in section 2.4.3 in a temperature of 293 K and a pressure range from 1 bara to 8 bara on a fixed-bed configuration. Subsequently, the adsorption equilibrium and kinetics of CO_2 or N_2 on zeolite 5ABL and 13XBL were studied at different temperatures. The experimental work was compared with numerical simulations through the Aspen Adsorption® modeling software. The comparison between these materials was made based on the following criteria: adsorption capacity and selectivity.

4.3.1. Monocomponent adsorption isotherms of CO_2 and N_2.

The adsorption isotherms were determined using the high-pressure magnetic suspension balance (see section 2.4) in a temperature range of 293 K to 363 K and a pressure range of 0.1 bara to 10 bara. The experimental values are shown as symbols in Figure 63 shows for CO_2 and Figure 63 for N_2. All isotherms were completely reversible at all pressures. It can be observed that CO_2 always adsorbed more strongly than N_2 on all the adsorbents at all temperatures. In all cases, the CO_2 adsorbed increases with pressure and a gradual flattening is observed when pressure is higher than 5 bara for CMS and 3 bara for zeolites.

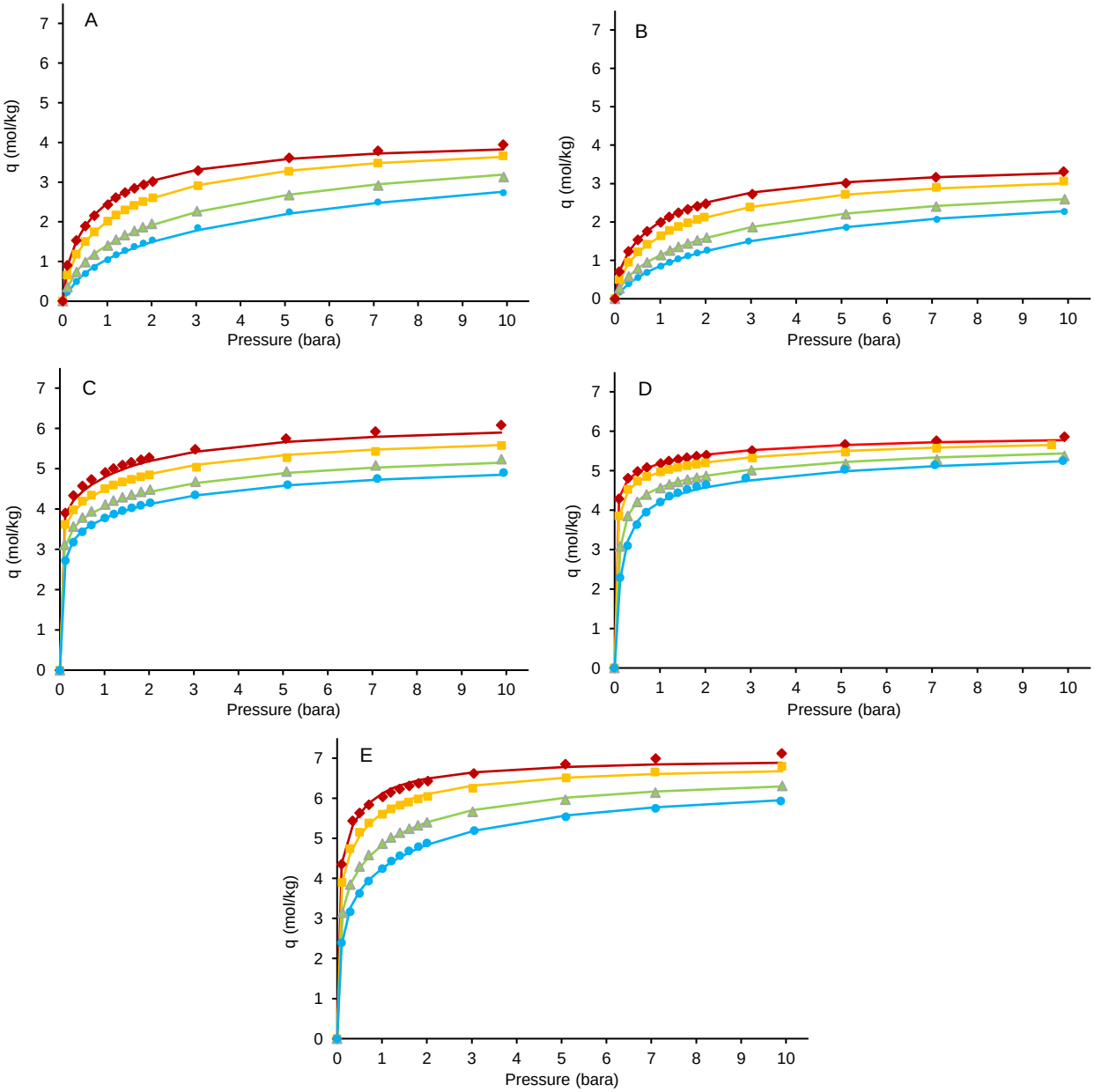

Figure 63: Single-gas adsorption equilibrium isotherms with CO_2 for (A) CMS-I, (B) CMS-II, (C) 4ABL, (D) 5ABL, (E) 13XBL at different temperatures (symbols: absolute experimental loading; lines: fitted DSL equation): ♦, T=283 K; ■, T=298 K; ▲, T=323 K; ●, T=343 K.

The steeper shape of the isotherm in the low-pressure range evidences the higher working capacity of zeolites (6.03 mol/kg at 1 bar and 283 K) compared with CMS (1.98 mol/kg at 1 bar and 283 K). Concerning the N_2 isotherms (Figure 63) the N_2 adsorbed increases almost linearly with pressure for all the adsorbents. Therefore, the materials with higher CO_2 adsorption capacity have the following order 13XBL > 4 ABL > 5ABL > CMS-I > CMS-II.

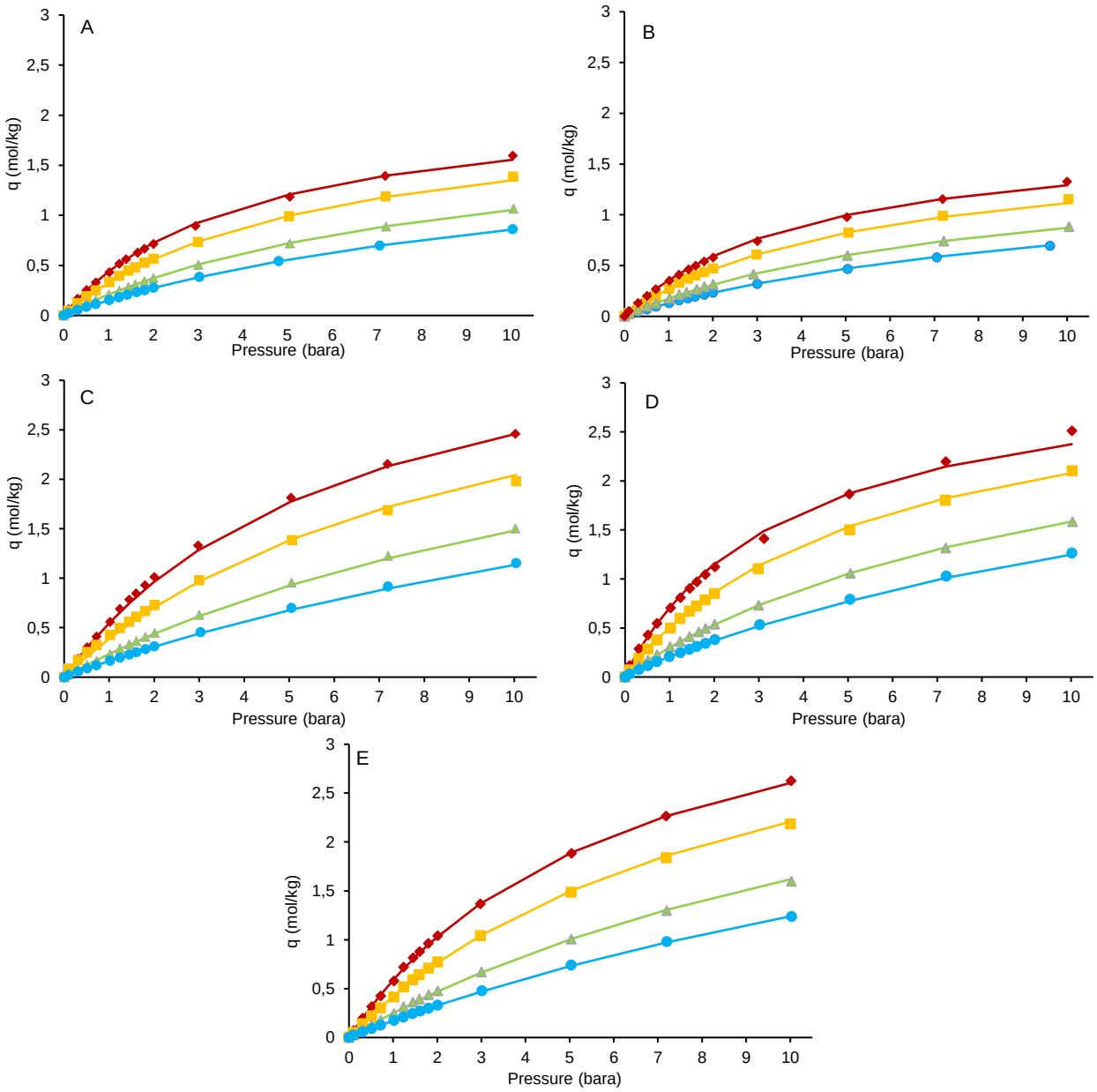

Figure 64: Single-gas adsorption equilibrium isotherms with N_2 for (A) CMS-I, (B) CMS-II, (C) 4ABL, (D) 5ABL, (E) 13XBL at different temperatures (symbols: absolute experimental loading; lines: fitted DSL equation): ♦, T=283 K; ■ , T=298 K; ▲, T=323 K; ●, T=343 K.

4.3.2. Modeling the adsorption isotherms of CO_2 and N_2

The experimental data of adsorption equilibria (absolute amounts adsorbed) of the pure gases on CMS-I, CMS-II, 13XBL, 5ABL and 4ABL were correlated with Toth, Sips, and Dual-Site Langmuir (DSL) isotherm models. A nonlinear regression procedure was carried out using the Excel tool solver. In particular, the values of the different fitting parameters were found by minimizing the sum of the squared relative errors (SSE)

(Garcia et al., 2013), by minimizing the relative differences between the predicted and experimental amounts adsorbed at all temperatures for a particular adsorbate-adsorbent system. The objective function that was used in Solver is given by equation (35).

$$SSE(\%) = \sqrt{\frac{\left[\left(q_{exp,i} - q_{mod,i}\right)/q_{exp,i}\right]^2}{N-1}} \times 100 \quad (35)$$

where $q_{exp,i}$ and $q_{mod,i}$ are the experimental and predicted amounts adsorbed, respectively, and N is the number of data points. The experimental data of CO_2 and N_2 of the studied adsorbents are presented in the appendix 7.1. The best fit among the different models will correspond to the minimum SSE. The fitted parameters from the Toth, Sips, and DSL isotherm models, as well as the SSEs are tabulated in Table 29 for CMSs and Table 30 for binderless zeolites.

Table 29: DSL, Sips and Toth model parameters for single-component adsorption of CO_2 and N_2 on CMSs.

	DSL	**q_{s1} [mol/kg]**	**b_1 [-bar]**	**$-\Delta H_{1,1}$ [kJ/mol)]**	**$-\Delta H_{1,2}$ [kJ/mol]**	**q_{s2} [mol/kg]**	**b_2 [-bar]**	**$-\Delta H_{2,1}$ [kJ/mol]**	**$-\Delta H_{2,2}$ [kJ/mol]**
CMS-I	*CO_2*	2.363	5.59E-05	27.593	29.767	2.473	0.000	27.593	26.996
	N_2	0.001	0.532	16.160	10.543	0.935	0.001	16.160	14.163
	SIPS	**q_s [mol/kg]**	**b_0 [-bar]**	**$-\Delta H$ [kJ/mol]**	**n_0**	**$\alpha(1-T_0)$ [K]**			
	CO_2	4.345	3.61E-04	19.398	1.349	0.000			
	N_2	2.486	2.88E-04	15.553	1.090	1.30E-07			
	Toth	**q_s [mol/kg]**	**b_0 [-bar]**	**$-\Delta H$ [kJ/mol]**	**t**				
	CO_2	5.206	6.68E-05	26.354	0.503				
	N_2	89.430	5.03E-06	19.053	0.254				
	DSL	**q_{s1} [mol/kg]**	**b_1 [-bar]**	**$-\Delta H_{1,1}$ [kJ/mol)]**	**$-\Delta H_{1,2}$ [kJ/mol]**	**q_{s2} [mol/kg]**	**b_2 [-bar]**	**$-\Delta H_{2,1}$ [kJ/mol]**	**$-\Delta H_{2,2}$ [kJ/mol]**
CMS-II	*CO_2*	4.36E-02	7.04E-04	30.701	23.746	1.951	7.79E-04	17.161	16.349
	N_2	1.26E-04	3.090	16.239	6.363	0.600	1.11E-03	15.246	12.613
	SIPS	**q_s [mol/kg]**	**b_0 [-bar]**	**$-\Delta H$ [kJ/mol]**	**n_0**	**$\alpha(1-T_0)$ [K]**			
	CO_2	3.627	3.56E-04	19.323	1.324	0.000			
	N_2	1.994	3.50E-04	15.140	1.072	1.88E-07			
	Toth	**q_s [mol/kg]**	**b_0 [-bar]**	**$-\Delta H$ [kJ/mol]**	**t**				
	CO_2	4.399	7.25E-05	25.823	0.509				
	N_2	1.740	6.64E-04	14.057	0.916				

Although the Toth parameter fitting shows a correct behavior for CO_2 with the different adsorbents, it fails to describe the experimental values for N_2 adsorption at high pressures (4 to10 Bara) reflected in high SSE values as can be seen in Table 31 (CMS- I=7.4%, CMS-III=5.6%, 4ABL=12.3%, 5ABL=5.4% and 13XBL=11.8%). In this

case, experimental data differ considerably from the values predicted by the fitted equation, because the data approaches the behavior of Henry's law in the low-concentration region (the amount adsorbed increases linearly with pressure), and to the saturation limit q_s at high concentrations. The affinity constant b, for CO_2 is larger than the one for N_2 for zeolites on all models (Table 29 and Table 30).

Table 30: DSL, Sips and Toth model parameters for single-component adsorption of CO_2 and N_2 on zeolites.

	DSL	**q_{s1} [mol/kg]**	**b_1 [-bar]**	**$-\Delta H_{1,1}$ [kJ/mol)]**	**$-\Delta H_{1,2}$ [kJ/mol]**	**q_{s2} [mol/kg]**	**b_2 [-bar]**	**$-\Delta H_{2,1}$ [kJ/mol]**	**$-\Delta H_{2,2}$ [kJ/mol]**
4ABL	*CO_2*	1.607	3.22E-02	21.776	19.658	0.863	3.19E-02	9.279	6.995
	N_2	2609.599	1.54E-04	17.794	55.597	2.154	1.54E-04	17.794	16.325
	SIPS	**q_s [mol/kg]**	**b_0 [-bar]**	**$-\Delta H$ [kJ/mol]**	**n_0**	**$\alpha(1-T_0)$ [K]**			
	CO_2	9.430	8.23E-02	5.990	4.749	0.000			
	N_2	4.524	1.03E-04	16.919	1.041	1.29E-07			
	Toth	**q_s [mol/kg]**	**b_0 [-bar]**	**$-\Delta H$ [kJ/mol]**	**t**				
	CO_2	7.294	6.84E-02	31.042	0.225				
	N_2	90.189	4.39E-06	19.800	0.260				
5ABL	**DSL**	**q_{s1} [mol/kg]**	**b_1 [-bar]**	**$-\Delta H_{1,1}$ [kJ/mol)]**	**$-\Delta H_{1,2}$ [kJ/mol]**	**q_{s2} [mol/kg]**	**b_2 [-bar]**	**$-\Delta H_{2,1}$ [kJ/mol]**	**$-\Delta H_{2,2}$ [kJ/mol]**
	CO_2	3.588	2.28E-04	30.597	29.896	1.820	2.27E-04	17.404	18.562
	N_2	0.029	6.72E-03	19.739	19.737	3.227	6.14E-05	19.739	19.737
	SIPS	**q_s [mol/kg]**	**b_0 [-bar]**	**$-\Delta H$ [kJ/mol]**	**n_0**	**$\alpha(1-T_0)$ [K]**			
	CO_2	5.680	2.25E-03	20.340	1.585	0.000			
	N_2	4.008	1.20E-04	17.615	1.125	1.29E-07			
	Toth	**q_s [mol/kg]**	**b_0 [-bar]**	**$-\Delta H$ [kJ/mol]**	**t**				
	CO_2	5.747	2.34E-04	32.217	0.560				
	N_2	90.215	5.85E-06	19.832	0.260				
13XBL	**DSL**	**q_{s1} [mol/kg]**	**b_1 [-bar]**	**$-\Delta H_{1,1}$ [kJ/mol)]**	**$-\Delta H_{1,2}$ [kJ/mol]**	**q_{s2} [mol/kg]**	**b_2 [-bar]**	**$-\Delta H_{2,1}$ [kJ/mol]**	**$-\Delta H_{2,2}$ [kJ/mol]**
	CO_2	2.150	1.77E-04	34.216	32.812	2.640	1.44E-04	23.486	23.105
	N_2	2027.165	8.31E-05	17.929	0.000	4.084	8.31E-05	17.929	17.854
	SIPS	**q_s [mol/kg]**	**b_0 [-bar]**	**$-\Delta H$ [kJ/mol]**	**n_0**	**$\alpha(1-T_0)$ [K]**			
	CO_2	7.698	7.81E-03	14.526	2.245	0.000			
	N_2	4.505	9.66E-05	17.291	1.021	2.14E-07			
	Toth	**q_s [mol/kg]**	**b_0 [-bar]**	**$-\Delta H$ [kJ/mol]**	**t**				
	CO_2	8.212	8.31E-04	32.629	0.331				
	N_2	52.239	3.84E-06	19.681	0.406				

This constant is a measure of how strong adsorbate molecules are attracted onto a surface, and it is also directly related to the Henry constant K ($K=b_{qs}$). Hence, it seems obvious that CO_2 is more strongly attracted to the adsorbent surface than N_2. In an exothermic process like adsorption, b decreases with temperature for all the adsorbates,

so at higher temperature the isotherms become less sharply curved (see Figure 63 and Figure 64). The Sips equation fits the experimental data significantly better than the Toth equation, as it can be seen in the SSE values for each adsorbate (Table 31).

Table 31: SSE obtained with the DSL, Sips and Toth models for the monocomponent adsorption of CO_2 and N_2 on CMSs and zeolites.

SSE (%)		CMS-I	CMS-II	4ABL	5ABL	13XBL
DSL	CO_2	1.72	0.91	1.44	0.87	1.20
	N_2	1.28	1.82	13.70	2.71	1.83
SIPS	CO_2	2.05	2.10	1.57	1.65	0.61
	N_2	1.52	2.04	12.52	2.37	2.62
Toth	CO_2	1.58	1.48	2.02	1.50	0.65
	N_2	7.41	5.68	12.32	5.45	11.19

Even though Sips fitting significantly improves, an important feature to note is, again, the high scatter for the N_2 fitting, mainly in the low-pressure region. From the same fitting tables, the parameter *n* is greater than unity for all the adsorbents, suggesting some degree of heterogeneity of the adsorbent structure. The larger this parameter is, the higher the degree of heterogeneity is (Do, 1998). When considering the whole experimental pressure range, the DSL isotherm fits better than the Toth and Sips models. Figure 63 and Figure 64 show the degree of goodness of the fit between experimental values (symbols) and the mathematical model using the DSL equations (solid line), respectively. This agrees with the lower SSE values obtained for the CO_2 and N_2 fitting (Table 31) except for the CO_2 fitting in CMS-I and 13XBL. In particular, the SSE values for the N_2 fitting decrease in the DSL model with respect to the other two models.

Therefore, the DSL parameters are selected for the simulation of the different adsorbents to predict the adsorption behavior. Note that the adsorption is dependent on the temperature. This effect was used to estimate the CO_2 working capacity of the different adsorbents, by using the 283 K isotherm as an adsorption temperature and 343 K isotherm as the desorption temperature at 10 bars. The results revealed that the adsorbents with higher temperature dependence, impacting on their working capacity, are the CMS-I, CMS-II and zeolite 4ABL (1.05, 1.22 and 1.18, respectively). On the other hand, the adsorbents with lower dependence on the temperature are the binderless zeolites 13XBL and 5ABL with 0.02 and 0.61, respectively at same conditions.

Next, an estimation of the w_{CO2} and w_{N2} of the different adsorbents was calculated using the 298 K isotherm with the equation (16) at 5 bara of adsorption pressure and 0.1 bar of desorption pressure. The $S_{eq(CO2)}$ and $S_{kin(CO2)}$ were calculated using equations (17)

and (18) respectively. The results of these estimations, tabulated on Table 32, shows that the w_{CO2} of zeolites were almost double of that of CMS, while for w_{N2} were almost half. On the other side, $S_{kin(CO2)}$ display a smaller difference between the different adsorbents, where the best selectivity values correspond to 13XBL (2.34) and 5ABL (2.29). Unlike the results of w_{CO2}, CMS-I and CMS-II have slightly a higher $S_{kin(CO2)}$ (1.88 and 1.83, respectively) than 4ABL (1.77). This difference is mainly caused due to the high value of w_{N2}. $S_{eq(CO2)}$ values have a similar tendency than w_{CO2} following the order: 13XBL > 5ABL > 4ABL > CMS-I > CMS-III. $S_{eq(CO2)}$ depends on the relative equilibrium quantities of each component adsorbed under the process conditions, whereas $S_{kin(CO2)}$ depends on differences in diffusion rates. Therefore, due to its low temperature dependence and its higher selectivity, the adsorbents with higher potential for VPSA process are the 13XBL and 5ABL.

Table 32: Working capacity and selectivity at a temperature of 298 K and pressures from 5 bara to 0.1bara.

Adsorbent	CO_2		N_2		w_{CO2}	w_{N2}	$S_{kin(CO2)}$	$S_{eq(CO2)}$
	q_{ads}	q_{des}	q_{ads}	q_{des}	(mol/kg)	(mol/kg)		
5ABL	4.87	1.78	1.41	0.07	3.09	1.35	2.29	19.52
13XBL	5.42	2.34	1.36	0.04	3.08	1.32	2.34	22.64
4ABL	4.35	2.19	1.26	0.04	2.16	1.22	1.77	19.54
CMS-III	1.45	0.12	0.76	0.03	1.33	0.73	1.83	10.84
CMS-I	1.80	0.15	0.92	0.04	1.65	0.88	1.88	11.10

4.3.3. Fixed-bed experiments for binary adsorption equilibria.

The binary dynamic adsorption equilibria for both CO_2 and N_2 were obtained using the methodology described in section 2.4.3 with the experimental set-up described on section 3.2.2 to analyze the suitability of the different adsorbents for CO_2 capture with VPSA. Figure 65 shows the CO_2 adsorption dynamic equilibria of the eight selected materials at 293 K. Comparing the results obtained from the binary adsorption equilibria, it was observed that with all tested adsorbents the q_{CO2} increases with increasing CO_2 partial pressures. In general, the results showed that zeolites have a higher q_{CO2} (almost double) than CMS materials.

The two tested CMS materials seem to have a similar CO_2 adsorption capacity, reaching a higher q_{CO2} of 2.0 mmol/g at total pressure of 8 bara, approximately. Contrarily, the CO_2 adsorption capacity in zeolites differs among them. The zeolite with a higher CO_2 adsorption capacity was 13XBL, reaching an q_{CO2} of 4.5 mmol/g at 8 bara, approximately.

All the binary adsorption equilibria of the zeolites 13XBL, 13X, 13X-APG and APG-III have approximately a similar slope, while 5A and 5ABL present a more horizontal slope with higher capacities in the low-pressure range (1 to 2 bara). 13XBL has the highest capacity in the range from 2 till 8 bara. The CO_2 adsorption capacity under dynamic column conditions at high pressures follow the next trend for the tested adsorbents: 13XBL > 5ABL > APG-II I> 13X-APG > 5A > 13X > CM-II > CMS-I. At lower pressures, the trend is quite similar: 5AB L> 13XBL > APG-III > 5A > 13X-APG >13X>CM-I = CMS- II.

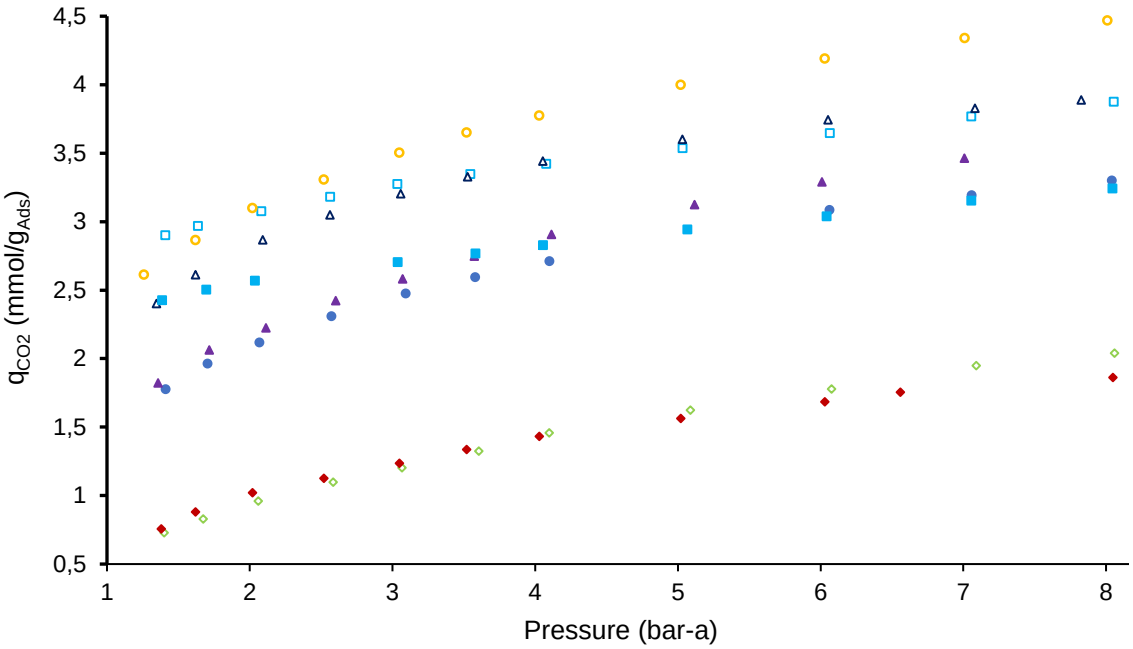

Figure 65: CO_2 binary dynamic adsorption equilibria at 293 K with different CMS and zeolites. ● 13X, ○ 13XBL, ♦ CMS-I, ◊ CMS-II, ■ 5A, □ 5ABL, ▲ 13X-APG, Δ APG-III.

Among them, 13XBL and 5ABL zeolites have the most interesting properties. The 13XBL zeolite adsorbs both components in large amounts at wide ranges of working pressures (2-8 bara). The 5ABL zeolites adsorbs more CO_2 at the low-pressure range (1 to 2 bara) but at higher pressures no great contribution to the CO_2 uptake is observed. The CMS-I and CMS-II are very similar when the CO_2 multicomponent adsorption equilibrium for both are compared. After discussing the differences of the CO_2 adsorption isotherms between CMS and zeolites, 13XBL and 5ABL are considered the most suitable adsorbents to analyze their adsorption capacity under dynamic column conditions.

4.3.4. Column breakthrough and validation of the simulation model.

A simulation model was developed in Aspen Adsorption® to match the experimental binary adsorption data studied on section 4.3.3. The governing equations used in the model were described in section 3.5.2.. Aspen Adsorption® solves the governing model equations for adsorption, consisting on a set of partial differential equations describing the mass, momentum and energy transport between the gas and solid phases, as well as various equilibrium isotherm models. The first-order Upwind Differencing Scheme (UDS1) was selected (with 150 nodes) as the method for spatial discretization, with the integration of the resulting ordinary differential equations performed by the Implicit Euler integrator

Several specifications and assumptions were made (section 3.5.2) in modelling the process in order to match the stream experimental system. The global heat transfer coefficient and the film heat transfer coefficient between the gas phase and the column wall were obtained by fitting the temperature profiles. These estimations were performed with the Aspen Adsorption® software based on the conditions of the experimental column. For this purpose, an initial calculated set of values of the transfer coefficients were proposed and used to calculate the breakthrough curve, which was compared to the experimental one. The deviations were then minimized by fitting the transfer coefficients until a good match was achieved between predicted and experimental breakthrough curves.

Figure 66 (A) shows the good match between predicted breakthrough and the experimental results at inlet feed gas concentrations of 15%/85% CO_2/N_2 (resembling the composition of post-combustion flue gases of power stations), absolute pressure of 2 bar, feed gas velocity of 0.42 m/s and 294K of initial temperature on 13XBL. The movement of the temperature front during the breakthrough run is also shown in Figure **66** (B), is evident that the temperature increase is generated by the adsorption process, where this effect is showed first at the entrance of the column and after 210 seconds at the exit of the column . As can be seen, the bed has not yet been saturated with CO_2 (i.e., C_o/C <1.0) and hence the temperature has not cooled to the feed value. Simulated and experimental breakthrough curves form similar pattern fronts in (Figure 66 A), with the center of the waves matching very well until the feed composition is approached, while the experimental curve shows a more dispersed front. CO_2 breakthrough occurred earlier at the 565th second in the simulation, while in the experiment it happened at the 608th. A possible explanation for the discrepancy is the presence of dead volume in the

experimental system between the end of the column and the CO_2 analyzer, that contributes to delay breakthrough in the experimental system.

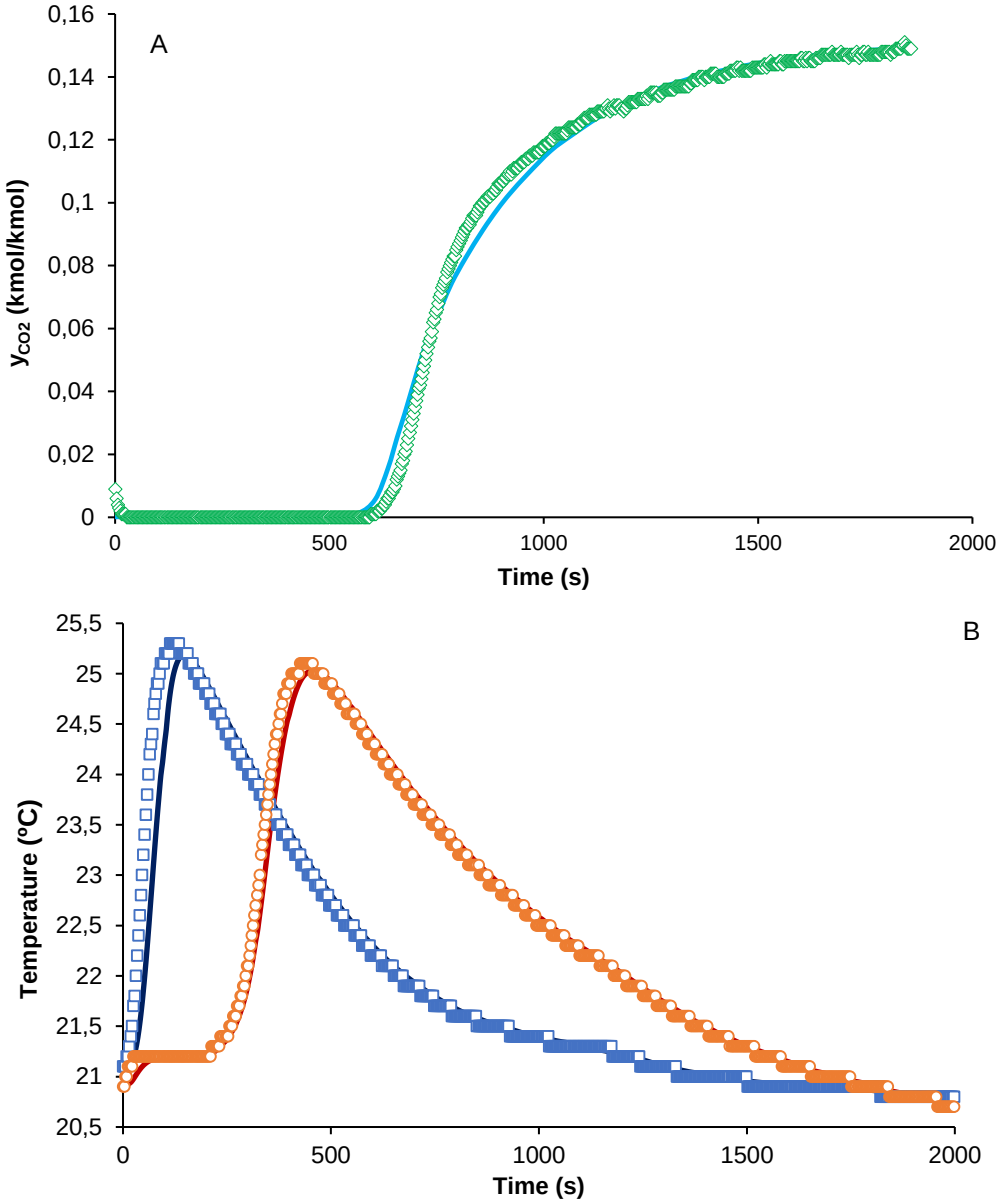

Figure 66: (A) Breakthrough curve for CO_2 and (B) temperature profiles from experiment and simulation. (symbols are the experimental data: ◊ CO_2 mole fraction, ○ temperature at 5 cm, □ temperature at 33 cm; lines: simulation).

4.3.5. Binary dynamic adsorption equilibria experiments and simulation.

Based on the study done in section 4.3.3 of the adsorption kinetics of CO_2/N_2 and the DSL model developed, a set of experiments were performed with the zeolites 5ABL and

13XBL to study their q_{CO2} at different temperatures (see Figure 65). Simulations were performed for up to 8 bara using the commercial Aspen Adsorption® simulator. The equilibrium data were calculated through the breakthrough experiments according to the procedure previously described in Section 2.4.3. Figure 67 shows the predictions of mixed-gas adsorption equilibria for CO_2/N_2, where the symbols represent the experimental data and the dotted lines represent DSL model predictions.

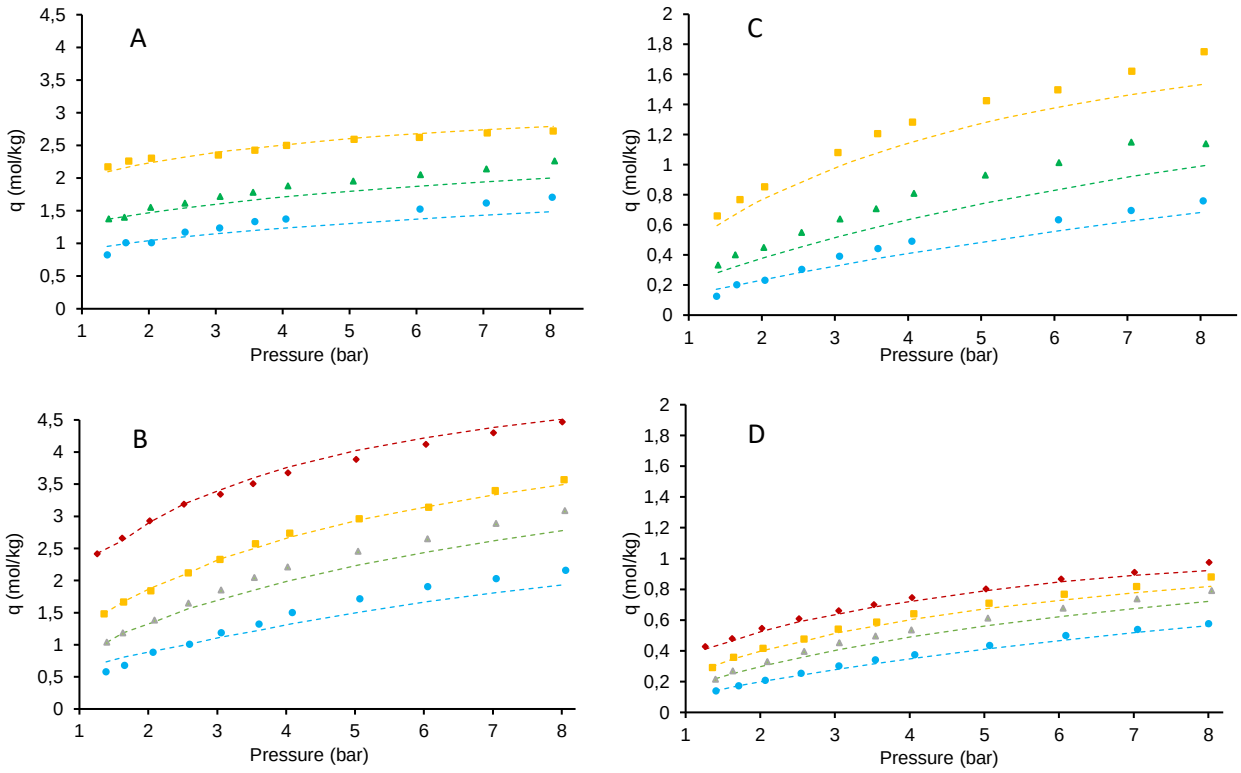

Figure 67: CO_2 adsorption of binary equilibria on (A) 5ABL; (B) 13XBL and. N_2 adsorption of binary equilibria on (C) 5ABL and (D) 13XBL. (symbols: absolute experimental loading; dotted lines: fitted DSL model simulation); ♦, T=293 K; ■, T=313 K; ▲, T=333 K; ●, T=363 K.

The experiments were used to verify the accuracy of the mathematical model and the transport parameters. Table 33 shows the %SSE calculated as the difference between the DSL model predictions and the experimental data for the different temperatures. In general, the model has a close representation of CO_2 and N_2 equilibrium versus the experiments, although the %SSE increases slightly with the temperature. Thereby, and according to the results presented herein, the DSL model with the binary adsorption CO_2/N_2 predicts the gas-mixture behavior of this adsorbate−adsorbent system with an average accuracy of 10.98% for 5ABL and 5.75% for 13XBL keeping in mind that the better results are temperatures lower than 333 K.

Table 33: SSE (%) of the DSL model parameters for binary adsorption of CO_2 and N_2 in 5ABL and 13XBL.

SSE (%)	293 K		313 K		333 K		363 K	
	CO_2	N_2	CO_2	N_2	CO_2	N_2	CO_2	N_2
5ABL	-	-	2.5	10.6	7.3	18.6	10.2	16.7
13XBL	2.1	3.3	1.6	4.7	7.7	8.1	13.5	5.0

In Figure 67, it is observed how the CO_2 adsorption capacity of 5ABL is slightly higher than that of 13XBL in the absolute pressure range from 1.4 to 2.0 bars and in the temperature range of 313 to 363 K. Nevertheless, at pressures higher than 2 bara and at low temperature range (293 to 333 K), 13XBL has a higher CO_2 adsorption capacity than the 5ABL. Meanwhile, N_2 adsorption capacity in 5ABL is higher than in 13XBL at all temperature and pressure ranges. The above discussion suggests a better CO_2 selectivity of 13XBL due to its higher uptake in combination with its lower N_2 uptake. As it can be seen from the equilibrium isotherms (Figure 64), the adsorbents are very selective to CO_2.

A preferential adsorption of CO_2 over N_2 indicates that the adsorbent can be used for the separation of CO_2 from flue gases. The influence of temperature and pressure on the equilibrium $S_{eq(CO2)}$ with a mixture of 15/85% v/v CO_2/N_2 of 5ABL and 13XBL at different temperatures was calculated with equation (17), and the results are shown in Figure 68. It is evident that the $S_{eq(CO2)}$ decreases with increasing pressure. Nevertheless, the effect on the equilibrium $S_{eq(CO2)}$ is more remarkable on 5ABL (Figure 68 A), having high values on the low-pressure range (25-35) and low values in pressure values greater than 3 bar (10-15). On the opposite side, the pressure has a low influence on the $S_{eq(CO2)}$ of 13XBL (Figure 68 B) of a 20-35 in the whole pressure range. Concerning the temperature, it has a lower dependence on the $S_{eq(CO2)}$ of 13XBL (0.25 units per K) than 5ABL (0.38 units per K). Based on this estimation, the 13XBL zeolite shows a better $S_{eq(CO2)}$ over the different pressure values, demonstrating higher values at low pressures and low temperatures. These results show that the 13XBL can be considered as the benchmark adsorbent material for CO_2/N_2 separations.

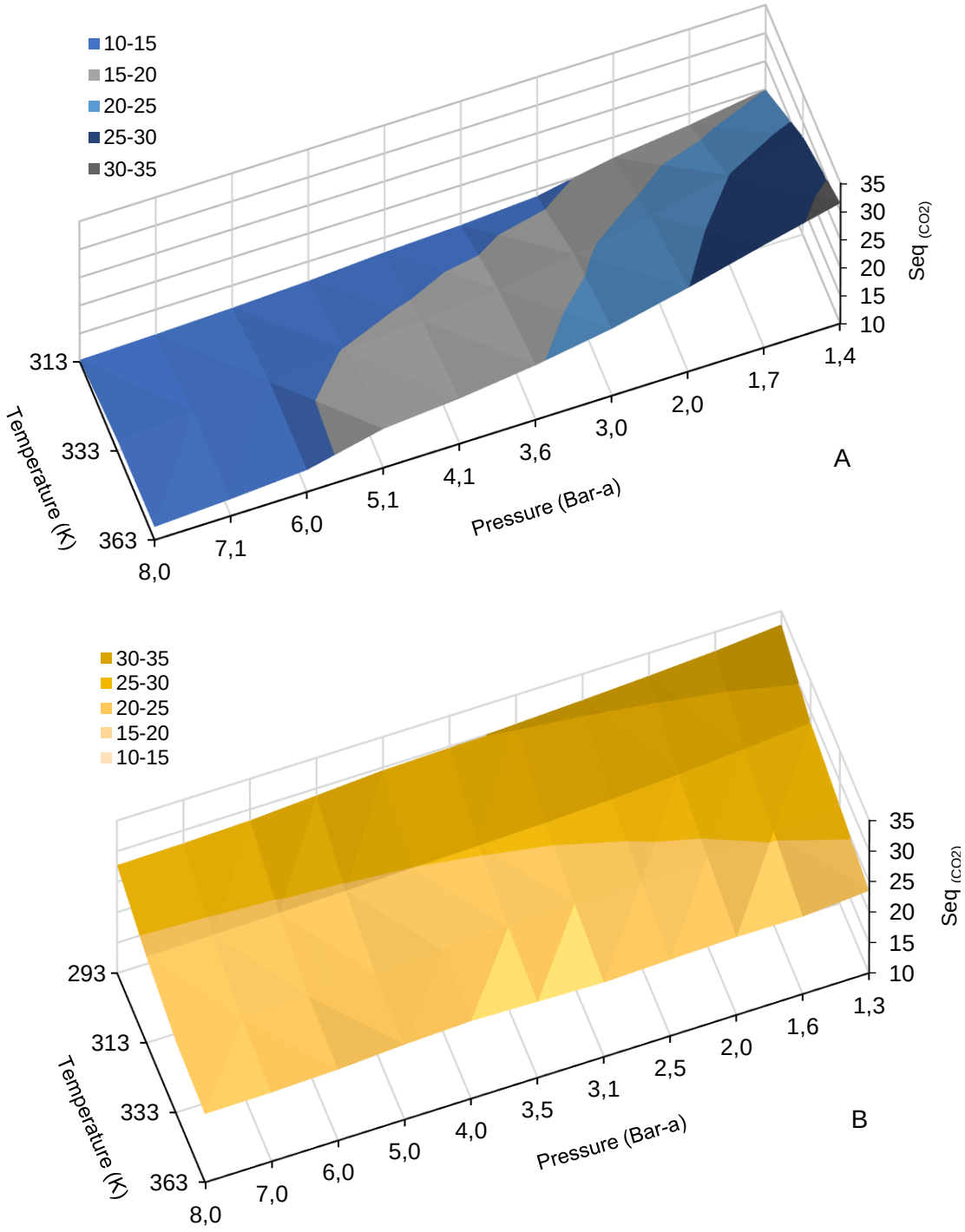

Figure 68: Influence of the pressure and temperature on the CO_2 equilibrium selectivity for zeolites (A) 5ABL, (B) 13XBL.

4.4. VPSA process studies for CO_2 separation

The choice of the sequence of steps is then defined as a function of separation and the target mixture. The selective adsorption of CO_2 is normally carried out at the highest pressure of the system and then it is desorbed at lower pressure, involving the use of a vacuum. Desorption under vacuum seems to be simpler for large-scale applications (Zhao et al., 2017). Nevertheless, using a vacuum instead of heating as a regeneration strategy leads to a residual amount of CO_2 retained in the adsorbent, and this amount will depend on the limit vacuum pressure of the pump and in the different conditions of the cyclic process. Therefore, through the efficient design of the VPSA cycle and the appropriate definition of the control process, it is possible to improve the process performance and make it economically and environmentally viable.

Based on the fixed-bed results obtained in a batch configuration in the previous section, a set of laboratory-scale experiments were performed in a cyclic configuration, using the control system developed in section 3.4.1. The experimental work was divided into two main parts: Single column batch and three-column cyclic experiments for VPSA continuous operation. Subsequently, the experimental work was compared with numerical simulations through VPSA simulations with Aspen Adsorption software® (validated on section 4.3.4), where the energy consumption and cycle productivity were studied during the separation process as performance indicators.

Additionally, a VPSA process for industrial-scale CO_2 capture including rinse and pressure equalization steps was built and tested in an industrial flue gas. Before the VPSA process, H_2O, SO_X, and NO_X were removed in a pretreatment process. Later, the recovered CO_2 was used to replace the use of mineral acids in the pH regulation stage and reduce the CO_2 emissions in the atmosphere. This allowed for the use of a compound that in many cases is a by-product in alkaline water and is an effective, reliable, self-buffering and economical method of controlling pH levels. Finally, the feasibility of concentration, capture and utilization of CO_2 was discussed for industrial applications.

4.4.1. Design of experiments.

To reach the knowledge of a complex process affected by multiple variables with the minimum number of experiments a fractional factorial design was applied. This statistically method involves simultaneous adjustment of experimental factors at two levels. By restricting the tests to only two levels (2^{k-p}), the number of experiments is minimized (Box et al., 2005; Box and Hunter, 2016; Montgomery, 2013). The contrast between levels gives necessary information for process improvement at the beginning of the investigation where many factors must be considered. There is also the possibility to include a third level for every factor, but this would produce a prohibitively large number of runs. Consequently, three levels of a factor are only considered when you get close to the optimum.

To investigate a VPSA process for CO_2 separation with a target purity of 95%, is described next: Use two-level factorial designs as screening tools to separate the key impacting factors (including interactions) from the those that have no significant impact for zeolites 13XBL and 5ABL. Follow up by doing an in-depth investigation of the surviving factors. Generate a full factorial design 2^k using simulation tools from an engineering perspective, with emphasis on the practical aspects.

In a first approximation, up to 7 different factors, have been identified. The studied parameters where the three-output stop point variables S_{FD}, S_{PR} and S_{RN}, the vacuum pressure on the regeneration step (P_V) and the flowrates on the feed (Q_{FD}), rinse (Q_{RN}) and the vacuum (Q_V) streams. As a result, the number of experiments of a full factorial experiment design with seven factors and two discrete possible values or "levels" (2^7) is 128. This amount of experiences is excessive, considering that each experiment takes approximately 8-10 hours. However, when screening factors, it is not necessary to run the full combination of high and low levels; often a fraction is enough. To obtain the maximum amount of information with the minimum experiments seven factors in sixteen experiments, which can be symbolized mathematically as 2^{7-3}, where studied. The levels of each variable were designated in Table 34 in accordance to previous studies done in the researching group (Serracan, 2017). Even if this design is not a two-level fractional factorial high resolution (represented by 2^{7-2} with 32 experimental runs), it provides sound estimates of the main effects and two factor interactions, assuming that three-factor and higher interactions will not be significant. Generally, this is a safe assumption, but there should always be confirmation runs to verify experimental findings.

To know which effect is confounded with the main effect, the definition relations were stablished as $I_1 = Q_F \cdot Q_R \cdot Q_V \cdot S_{RN}$, $I_2 = Q_R \cdot Q_V \cdot P_V \cdot S_{FD}$ and $I_3 = Q_F \cdot Q_V \cdot P_V \cdot S_{PR}$ (Box and Hunter, 1961). The codified matrix or experimental matrix (2^{7-3}) is shown at Table 35.

Table 34: High and low levels of studied variables in fixed column.

	Q_{FD} (g/min)	Q_{RN} (g/min)	Q_V (g/min)	P_V (bar)	S_{RN} (%)	S_{FD} (%)	S_{PR} (%)
Low level (-)	9	9	9	-0.75	110	10	30
High level (+)	11	11	11	-0.95	130	50	70

Table 35: Codify matrix for the fractioned factorial design 2^{7-3}.

Exp. nº	Q_{FD}	Q_{RN}	Q_V	P_V	S_{RN}	S_{FD}	S_{PR}
1	-	-	-	-	-	-	-
2	+	-	-	-	+	-	+
3	-	+	-	-	+	+	-
4	+	+	-	-	-	+	+
5	-	-	+	-	+	+	+
6	+	-	+	-	-	+	-
7	-	+	+	-	-	-	+
8	+	+	+	-	+	-	-
9	-	-	-	+	-	+	+
10	+	-	-	+	+	+	-
11	-	+	-	+	+	-	+
12	+	+	-	+	-	-	-
13	-	-	+	+	+	-	-
14	+	-	+	+	-	-	+
15	-	+	+	+	-	+	-
16	+	+	+	+	+	+	+

The experimental apparatus employed to perform the study was the same employed to measure the dynamic adsorption equilibrium, described on section 3 using the automatization control system developed on section 3.4.1. 5ABL and 13XBL were studied as the benchmark adsorbents for CO_2 capture from a gas mixture of 15% CO_2 and 85% N_2. The experiments were performed during 20 cycles with the column jacket at 293 K of temperature (T_T), keeping a constant adsorption pressure (P_T) of 4 barg and a desorption time of 420 seconds (t_V) once the vacuum pressure was reached. Rinse

and purge steps were carried out with fresh CO_2 and N_2 (purity greater than 99.995% and 99.999%, respectively).

It is important to note that the results of this approach will only become an approximation, as the real process uses recycled feed streams with lower purity. However, this analysis is useful to understand the basic effects of the process unit. The purpose here is to focus on the effects of cyclic design and operation parameters on the process performance, therefore a continuous feed was not employed.

The experimental matrix conditions are summarized in Table 36. The Q_{FD} stream flowrate and stop points were controlled by the automated control system. Q_{RN}, Q_V were calibrated prior to each experiment by the percentage opening of the flow control valves at the operating pressure. Since the effluent of the product rinse step was recycled, it can be considered as an internal recycle process and therefore its effect is not discussed here. Note the balanced array of plus (high) and minus (low) levels in the test matrix (Table 35). Each column contains eight pluses and eight minuses. The matrix offers a very important statistical property called “orthogonality”, which means that factors are not correlated. As factors become more and more correlated, the error in estimation of their effects becomes larger and larger. Orthogonal test matrices make effect estimation neat and easy.

Table 36: Operating conditions of the fractioned factorial design 2^{7-3}.

Exp.nº	Q_{FD} (g/min)	Q_R (g/min)	Q_V (g/min)	Pv (barg)	S_{RN} (%)	S_{FD} (%)	S_{PR} (%)
1	9	9	9	-0.75	110	10	30
2	11	9	9	-0.75	130	10	70
3	9	11	9	-0.75	130	50	30
4	11	11	9	-0.75	110	50	70
5	9	9	11	-0.75	130	50	70
6	11	9	11	-0.75	110	50	30
7	9	11	11	-0.75	110	10	70
8	11	11	11	-0.75	130	10	30
9	9	9	9	-0.95	110	50	70
10	11	9	9	-0.95	130	50	30
11	9	11	9	-0.95	130	10	70
12	11	11	9	-0.95	110	10	30
13	9	9	11	-0.95	130	10	30
14	11	9	11	-0.95	110	10	70
15	9	11	11	-0.95	110	50	30
16	11	11	11	-0.95	130	50	70

4.4.2. VPSA fixed-bed experiments for Zeolite 5ABL.

The cyclic performance of the different adsorbents for CO_2 capture with VPSA was first studied for the 5ABL zeolite doing a total of 16 experiments. Purity and Recovery were selected as response variables, and the experimental results obtained are summarized in Figure 69 . In this Figure, the CO_2 purity ranges between 68% to 94% and the recovery ranges between 45 to 65 %. The highest values are 98% and 81%, respectively, reached at the experiment number 13. Purity and recovery averages are 87.8% and 59.3%, respectively, with experiments from 10 to 16 presenting high purity values in the range of 94% to 98%. On the other hand, experiments from 9 to 16 present the highest CO_2 recovery values, in the range of 69% to 81%. These experiments have in common the high-level vacuum pressure factor (-0.95 barg).

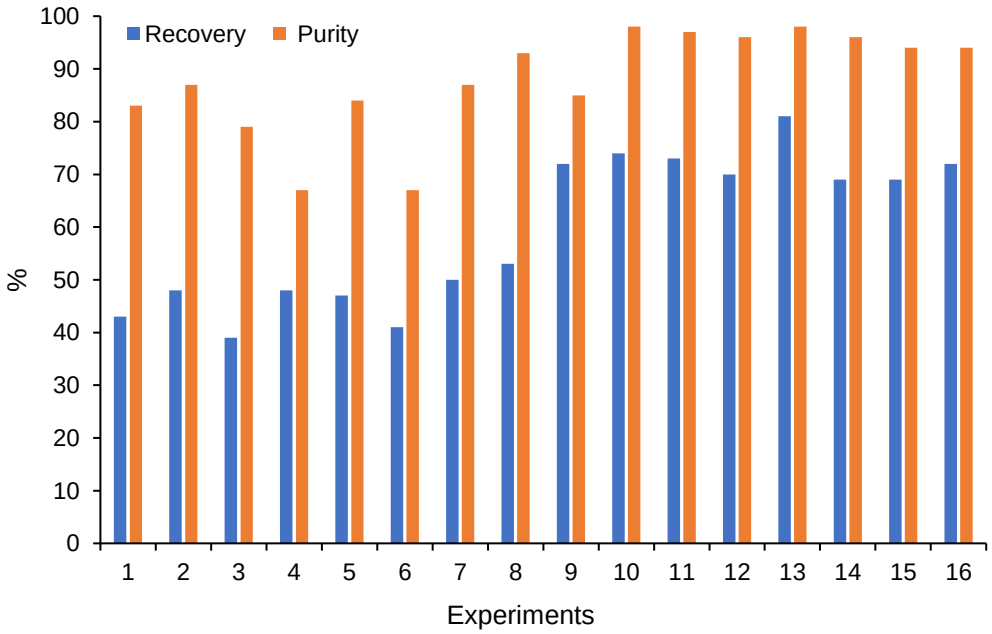

Figure 69: CO_2 purity and recovery performance for 5ABL on fixed column experiments.

Productivity and electrical consumption were calculated as cyclic performance indicators. Figure 70 shows the experimental results for the 16 experiments: the productivity ranges between 0.16 and 0.26 $g_{CO2}/(g_{Ads}\cdot h)$, while the electrical consumption oscillates from 1.4 to 8.7 kWh/kg_{CO2}. Checking the Figure in more detail, it is seen that the series of experiments 9 to 16 provide a higher productivity than experiments 1 to 8, whose productivity was in the range 0.09 to 0.17 $g_{CO2}/(g_{Ads}\cdot h)$. The main difference between these two groups of experiments is the vacuum pressure. In addition, it can be deduced that the productivity has an inverse relation with the electrical consumption

value (the productivity is high when the electrical consumption is low). As an example, experiment 13 have a high productivity 0.26 $g_{CO2}/(g_{Ads}\cdot h)$ and a low energy consumption 1.4 kWh/kg_{CO2}.

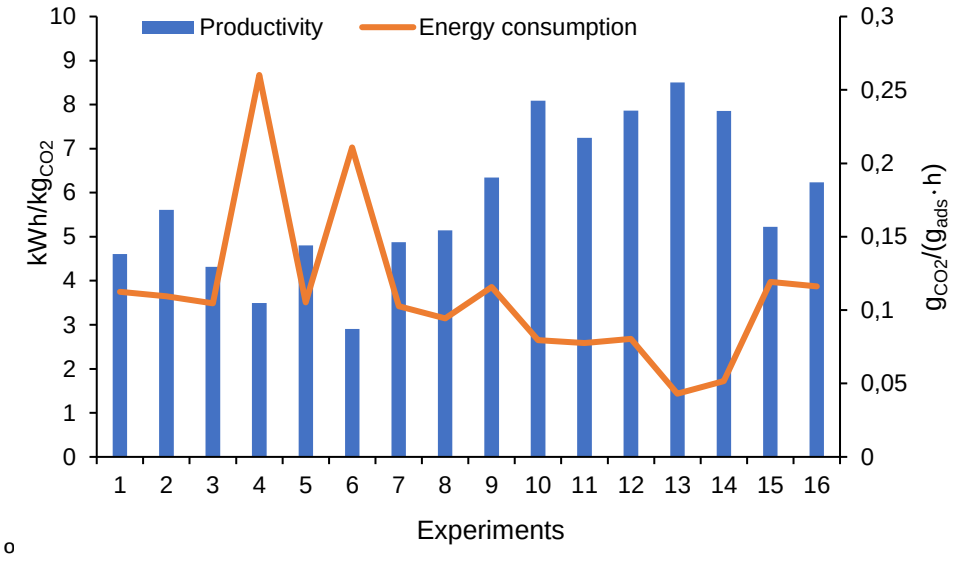

Figure 70: CO_2 productivity and electric consumption performance for 5ABL on fixed column experiments.

With the results obtained (see appendix 7.2), a statistical ANOVA analysis (Box et al., 2005) was performed to determine the influence of the different factors on each performance indicator. The effect of the different factors on the performance is plotted in Figure 71. Each point represents a contrast between the response averages at low versus high factor levels. The steeper is the factor representation line, the more significant the effect is. When the lines do not intersect, they are not part of a significant interaction. On the other side, the crossing lines indicate that the effects interact or can be enhanced. Through the analysis of the effect plots (Figure 71), it is possible to differentiate the significant parameter with higher impact in the measured key performance responses. Clearly, factor P_V needs to be set at its high level (-0.95 barg) to get maximum recovery, purity and productivity on the CO_2 separation cyclic process. At the high level, the purity average is 95%, while at low level, the average purity drops nearly by 15% up to 81%. Unfortunately, a high P_V level also has strong impact on the process energy consumption. This effect is related to the fact that the vacuum pump is the component with the highest energy requirements on the VPSA experimental apparatus; hence, high levels of vacuum represent an extended use of the vacuum pump, which is reflected in a higher energy consumption. Besides the importance of P_V, it is difficult to pick out the factors with more importance on the process, since they seem to have interaction between each other and not all factors have the same importance.

An ANOVA Pareto chart analysis represents in columns the percentage of contribution of the total variability of the matrix data. This analysis includes the possible effects caused for the interaction of the different parameters. Figure 72 shows that the parameters S_{FD} and S_{RN} have also influence, after P_V in the purity and productivity.

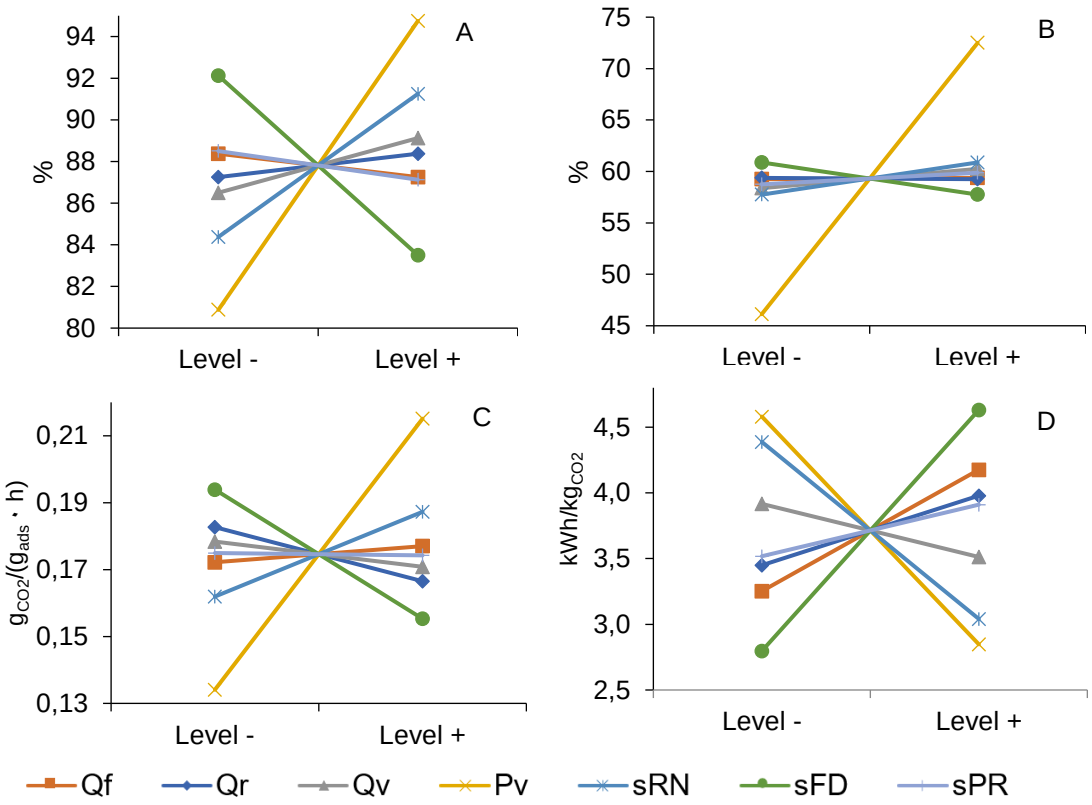

Figure 71: Effect plots for 5ABL CO_2 cyclic adsorption experiments. (A) Purity, (B) Recovery, (C) Productivity, D) Energy consumption in CO_2 separation.

Parameters S_{FD} (feed stop point) and S_{RN} (rinse stop point) are in the second position of importance, with impact mainly in the purity and productivity. Through Figure 73, it is possible to differentiate the kind of effect over the response. S_{FD} has a positive effect for purity, recovery and productivity, but it had a negative effect on the energy consumption. On the other hand, S_{RN} has the opposite effect, with a negative effect for purity, recovery and productivity but a positive effect on the energy consumption. The negative effect means that the results with greater performance will be those that keep these parameter values at low levels. After S_{FD} and S_{RN}, we have Q_R, Q_F and two possible interactions of second order $It_1=Q_{FD} \cdot S_{RN}+Q_R \cdot Q_V+P_V \cdot S_{FD}$ and $It_2=Q_F \cdot P_V +Q_V \cdot S_{PR}+S_{RN} \cdot S_{FD}$. Finally, the parameters with a lower impact on the results are Q_V and S_{PR}. Nevertheless, no parameter can be 100% discarded since its importance can be confused with some second-order interaction.

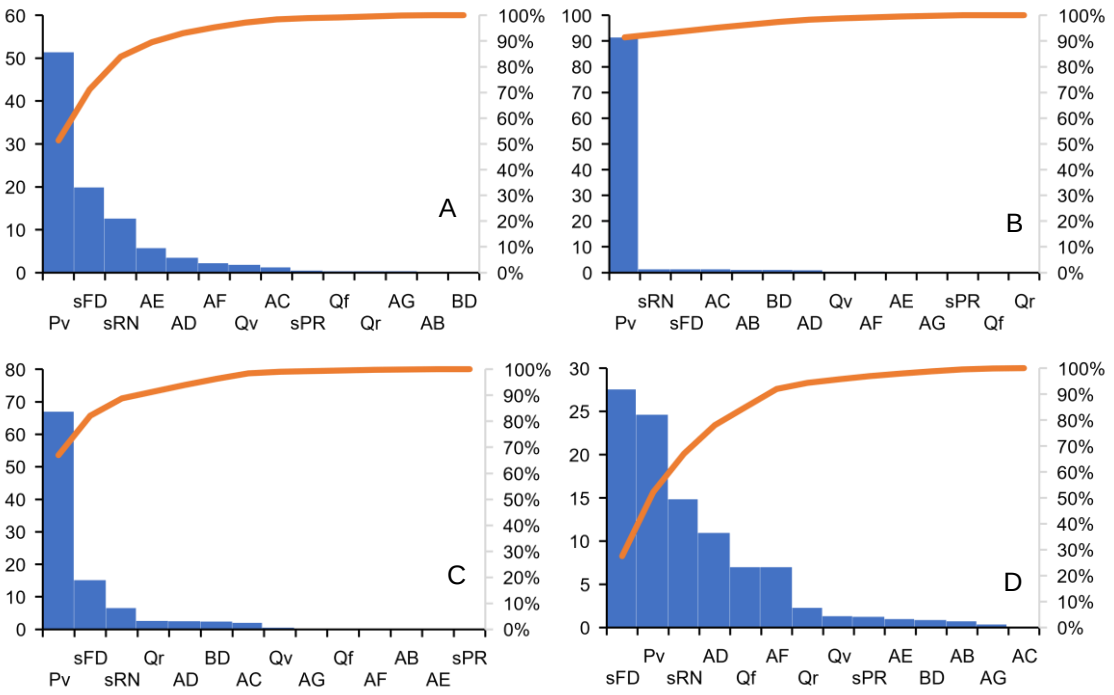

Figure 72: 5ABL Pareto chart for CO_2 cyclic adsorption experiments. (A) Purity, (B) Recovery, (C) Productivity, D) Energy consumption.

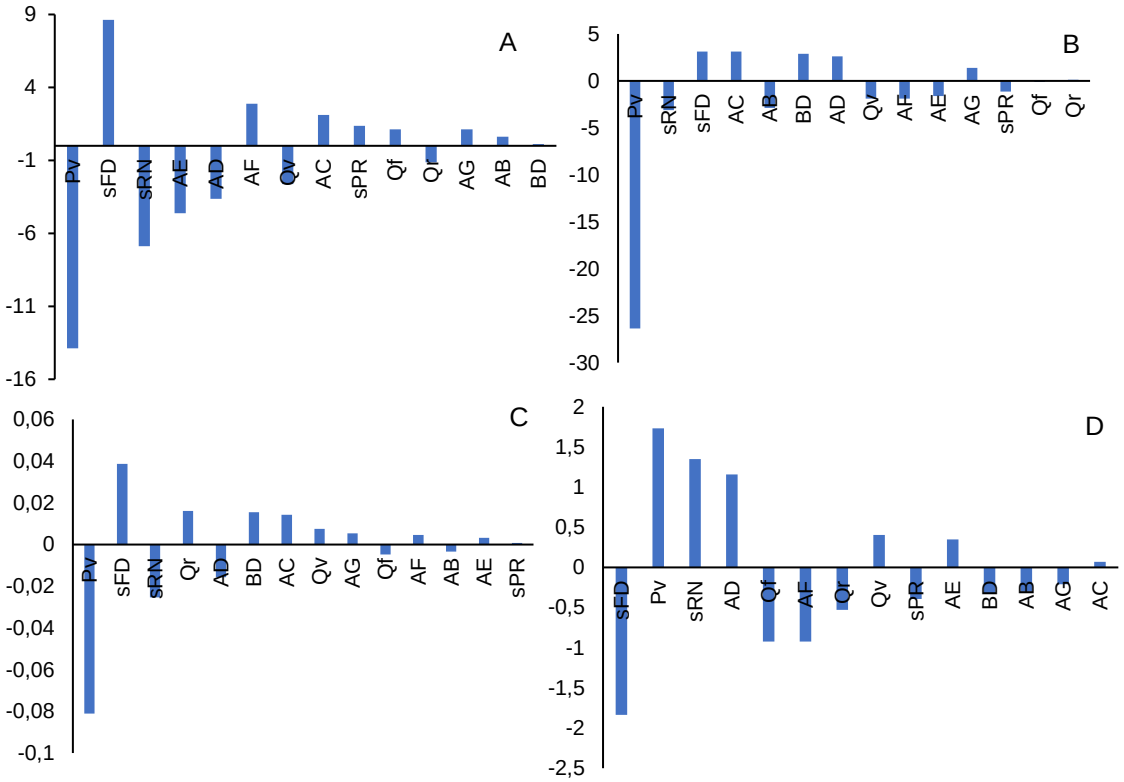

Figure 73: 5ABL Effect representation chart CO_2 cyclic adsorption experiments. (A) Purity, (B) Recovery, (C) Productivity, D) Energy consumption.

The half-normal graph (Montgomery, 2013) plot is used to differentiate if the effects are significant or can be considered insignificant and can be associated as a part of experimental error. In this representation, the effects are set with their assigned probability, a line is draw through the group near-zero effects, and anything significant will fall off to the right of the line. Figure 74 shows the half-normal plot of effects, where the significant effects are labelled. The near-zero effects fall on a straight line exhibiting normal dispersion.

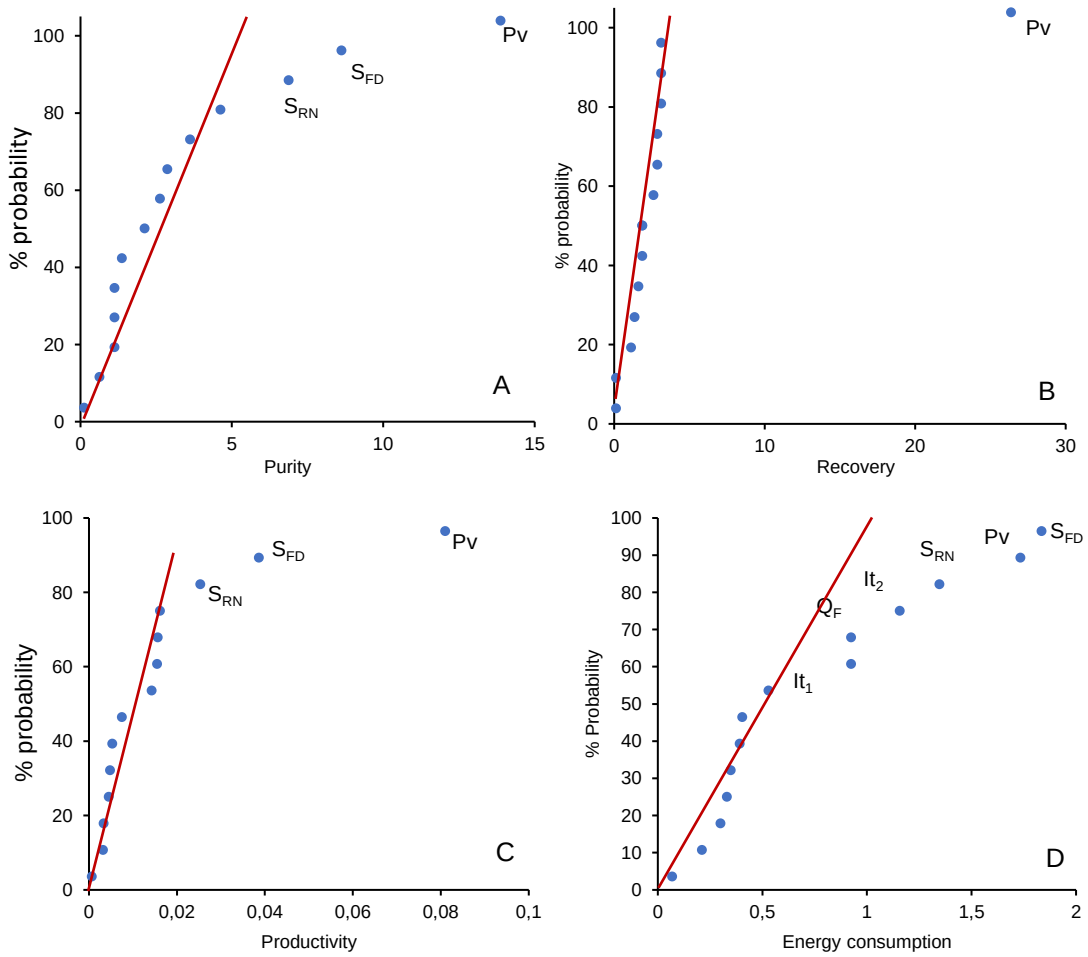

Figure 74: 5ABL CO_2 cyclic adsorption experiments half normal probability plot. (A) Purity, (B) Recovery, (C) Productivity, D) Energy consumption.

Figure 74 shows the effects with more weight on the process performance. Nevertheless, the interaction It_1 and It_2 shows a significant contribution on the energy consumption. To disentangle the interactions, the analysis was performed representing the possible interactions between Q_{FD} and P_V, Q_V and S_{PR} or S_{RN} and S_{FD}, and the respective separate representation for It_2. The main effects are represented on Figure 75, where it can be noticed that the factor Q_V in its low level and S_{PR} in its high level have more energy consumption. This low interaction and the low effect on the global contribution suggest

that the parameter Q_V must be kept at the high level, as the effect is expressed by the weak interaction with the parameter S_{PR}. On the other side, the parameters Q_R and S_{PR} at their high level have a certain impact on the energy consumption, but the effect is drastically changed to lower values of energy consumption when the S_{PR} changes to its low value.

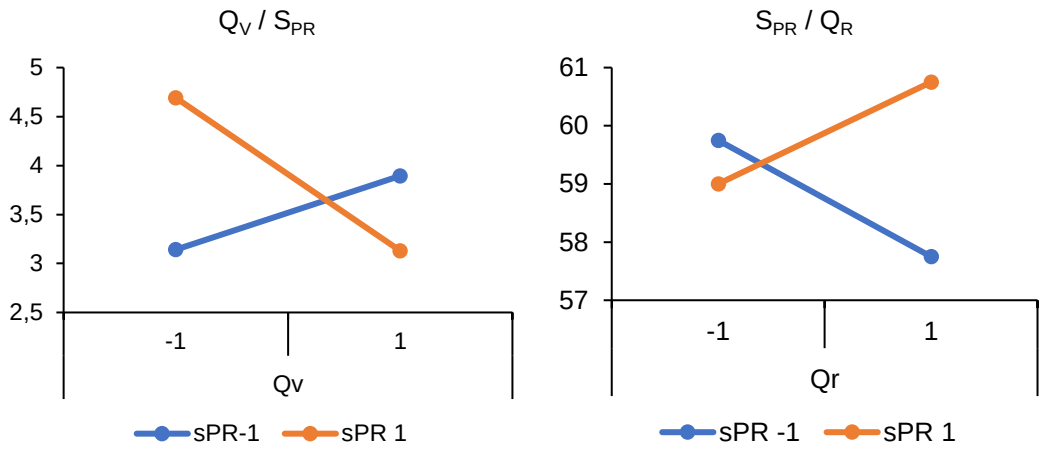

Figure 75: The main possible effects interaction representation for 5ABL experiments.

Table 37 summarises the results for 5ABL cyclic experiments and suggests the experimental matrix design that leads to find the optimal working conditions. The vacuum is the critical parameter for high purity, recovery and productivity. However, using the vacuum at high values leads to higher energetic consumption. S_{PR}, Q_F and Q_R are the following factors on importance.

Table 37: Results from the analysis of overall analysis criteria and variables for the Zeolite 5ABL. (E) Energy consumption; (R) Recuperation; (P) Purity, (T) Productivity.

Factor	Low level -	High level +	Impact	Response effect
Q_F	6	9	low	E
Q_R	6	9	by interaction	E
Q_V		11	negligible	E
P_V		-0.95	High	R, P, T, E
S_{RN}	80	110	medium	R, T
S_{FD}	8	16	medium	E, P, T
S_{PR}	20	40	medium	P

As a first approach to the process, the design of experiements brings an idea of the factors with greater importance, but nevertheless more experiments are needed to clarify the real impact of the rest of the factors and to resolve the interaction confusion. In the following set of experiments, the effect of Q_V is not considered due to its low influence on the response, while P_V must be studied at its highest value to better differentiate the influence of the other parameters. Likewise, the range of factors must move towards the levels that show better results, as is recommended in Table 37.

4.4.3. VPSA fixed-bed experiments for Zeolite 13XBL.

The same design of 2^{7-3} experiments procedure (section 4.4.1) was done for the VPSA fixed-bed experiments for zeolite 13XBL as adsorbent. 16 experiments were performed obtaining their respective responses. In Figure 76, the CO_2 purity and recovery ranges are plotted for all experiments. The results range between 63 to 99.5% for the purity and 35 to 89% for the recovery, with an average of 92% and 62%, respectively. The highest value of purity was 99.5% (at experiment 11), while the highest CO_2 recovery value was 89% (at experiment 9).

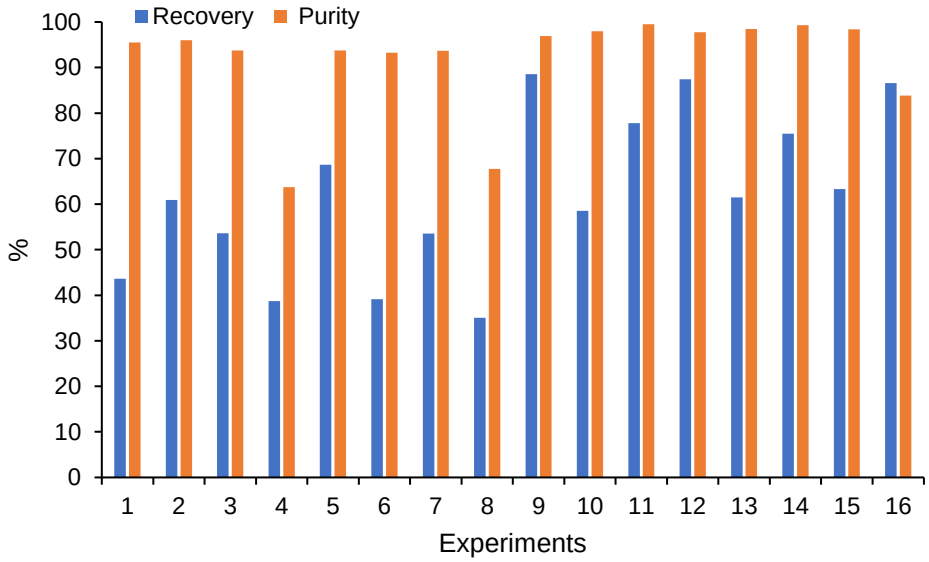

Figure 76: CO_2 purity and recovery cyclic performance for 13XBL on fixed column experiments.

Productivity and electrical consumption experimental results for 13XBL are shown in Figure 77. From the figure, it can be seen the productivity is in a range of 0.06 to 0.35 $g_{CO2}/(g_{Ads} \cdot h)$ and the electrical consumption oscillates from 0.37 till 8.05 (kWh/kg_{CO2}).

Their respective averages are 0.19 $g_{CO2}/(g_{Ads}\cdot h)$ and 3.09 (kWh/kg_{CO2}). Experiment 9 has a high productivity, 0.35 $g_{CO2}/(g_{Ads}\cdot h)$ and it is observed that when the productivity is at its maximum value, the electrical consumption is in a low value of 3.2 kWh/kg_{CO2}. On the other hand, the lower energy consumption is on experiment 10 with 0.35 $kWh/kgCO_2$.

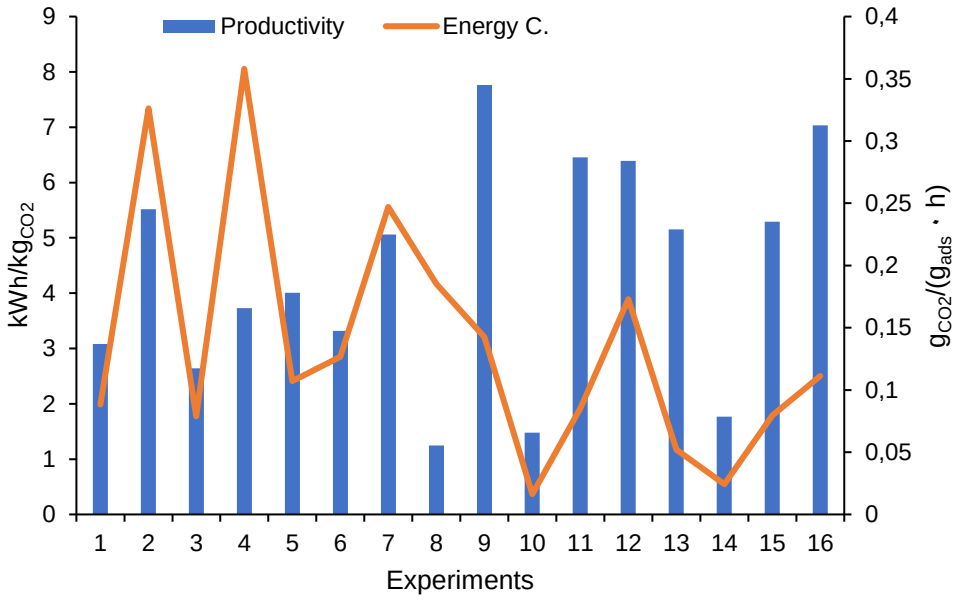

Figure 77: CO_2 purity and recovery among the proposed experiences for fixed column with Zeolite 13XBL

A statistical ANOVA analysis was also performed with the obtained results (see appendix 7.2) to determine the influence of the different factors on each performance indicator objectively. Figure 78 shows that the factor with more impact in all the responses is P_V, where the high level of vacuum pressure leads to high purity, recovery and productivity values, although it also results on high energy consumption values. Q_F and Q_R provide better purity results (Figure 78 A) when these factors are on their low level, having a similar impact than P_V. The high level of S_{PR} is the second parameter with stronger influence over the recovery (Figure 78 B). From Figure 78 (C), it is observed that Q_F on its low value and S_{PR} on its high value are the second and third parameters with more influence in high productivity values, respectively. Finally, S_{PR}, Q_F and Q_R on their high levels have a similar impact achieving high energy consumption values (Figure **78** D).

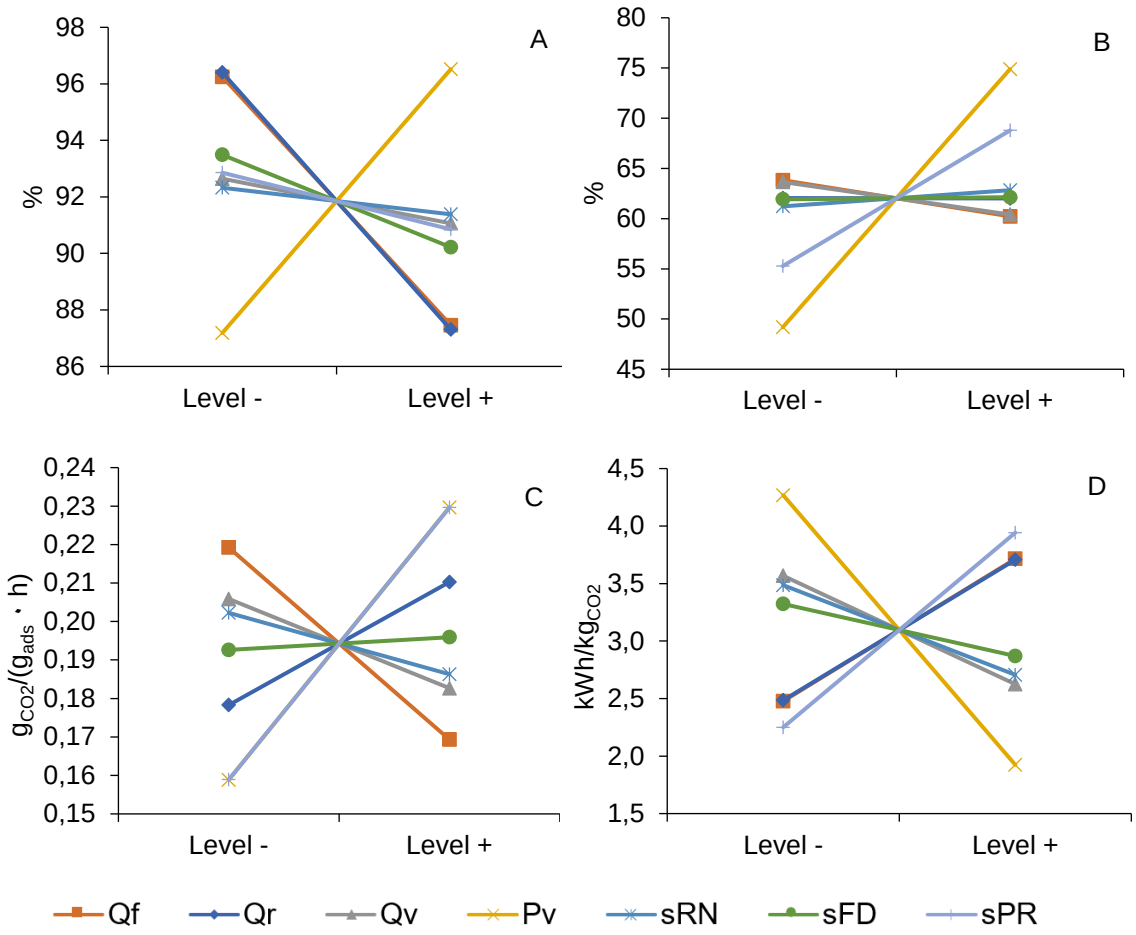

Figure 78: Effect plots for 13XBL CO_2 cyclic adsorption experiments. (A) Purity, (B) Recovery, (C) Productivity, D) Energy consumption in CO_2 separation.

The plot of the contributions Figure 79, reveals that besides the individual importance of the parameters, some interactions between them have a significant impact over the response. For purity, an important interaction $It_3=Q_{FD} \cdot Q_R + Q_V \cdot S_{RN} + S_{PR} \cdot S_{FD}$ is detected with almost the same impact (20%) on the total contribution than P_V (21%), Q_R (20%) and Q_F (18%). For CO_2 recovery, a weak interaction ($It_4=Q_F \cdot S_{FD} + P_V \cdot S_{RN} + Q_R \cdot S_{PR}$) represents the 7.7 % of the contribution when P_V (60%) and S_{PR} (17%) clearly shows more relevance. For the productivity, the interaction $It_5=Q_R \cdot P_V + Q_V \cdot S_{FD} + S_{RN}\ S_{PR}$ shows the third position on relevance after P_V (22%) and before S_{PR} (22%) and Q_F (11%).

Finally, for the energy consumption, the contribution is distributed quite equally over different parameters, but P_V (21%) has the most noticeable impact over the rest. Additionally, a half-normal probability plot (Figure 80 D) was made for the rest of the parameters to confirm that the results of the analysis are relevant. From the qualitative evaluation of the plot, it can be concluded that the point for P_V does not follow a normal distribution, confirming its relevance. The graphic representation also confirmed that the other parameters do not represent a significant effect, as those points follow the normal

distribution. Therefore, these factors can be discriminated since they are considered part of the experimental error.

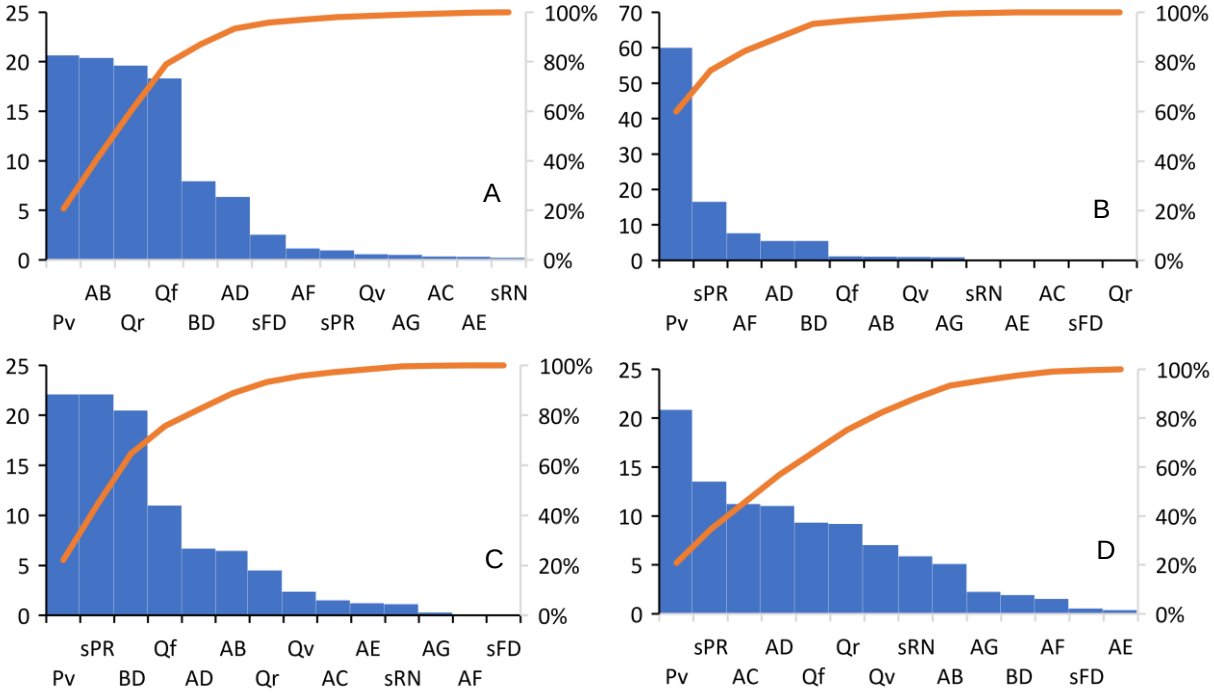

Figure 79: 13XBL Pareto contribution chart of CO_2 cyclic adsorption experiments. (A) Purity, (B) Recovery, (C) Productivity, D) Energy consumption.

For purity (Figure 80 A) the relevance of the factors P_V, Q_R, Q_F is confirmed, as well as and the interaction It_3 is confirmed. Besides, the interactions It_5 and It_4 do not follow a normal distribution, showing their relevance but with low impact on their contributions (7.9% and 6.3% respectively). Likewise, it is confirmed from Figure 80 B that P_V and S_{PR} are the parameters with more importance, although the interactions It_3, It_4 and It_5 can also be considered but with lower impact on their contribution (7.7, 5.6 and 5.5 respectively). Finally, on Figure 80 (C), P_V, S_{PR} and the interaction It_5 confirms that are the relevant values on the productivity because they do not follow the normal distribution.

Figure 81 summarizes the impact (in terms of weight) of the different effects over the response and the process performance. Overall, S_{PR} is the second parameter in relevance with negative effects on the purity and productivity, which means that the results with better performance will be those that keep this parameter at low levels. Q_R and Q_F have a positive effect for purity. On the third position, we have two possible confused interactions of second order It_4 and It_3. The lowest impact on the results correspond to Q_V and S_{FD}; nevertheless, no parameter can be discarded, since its importance can be confused with some second-order interaction.

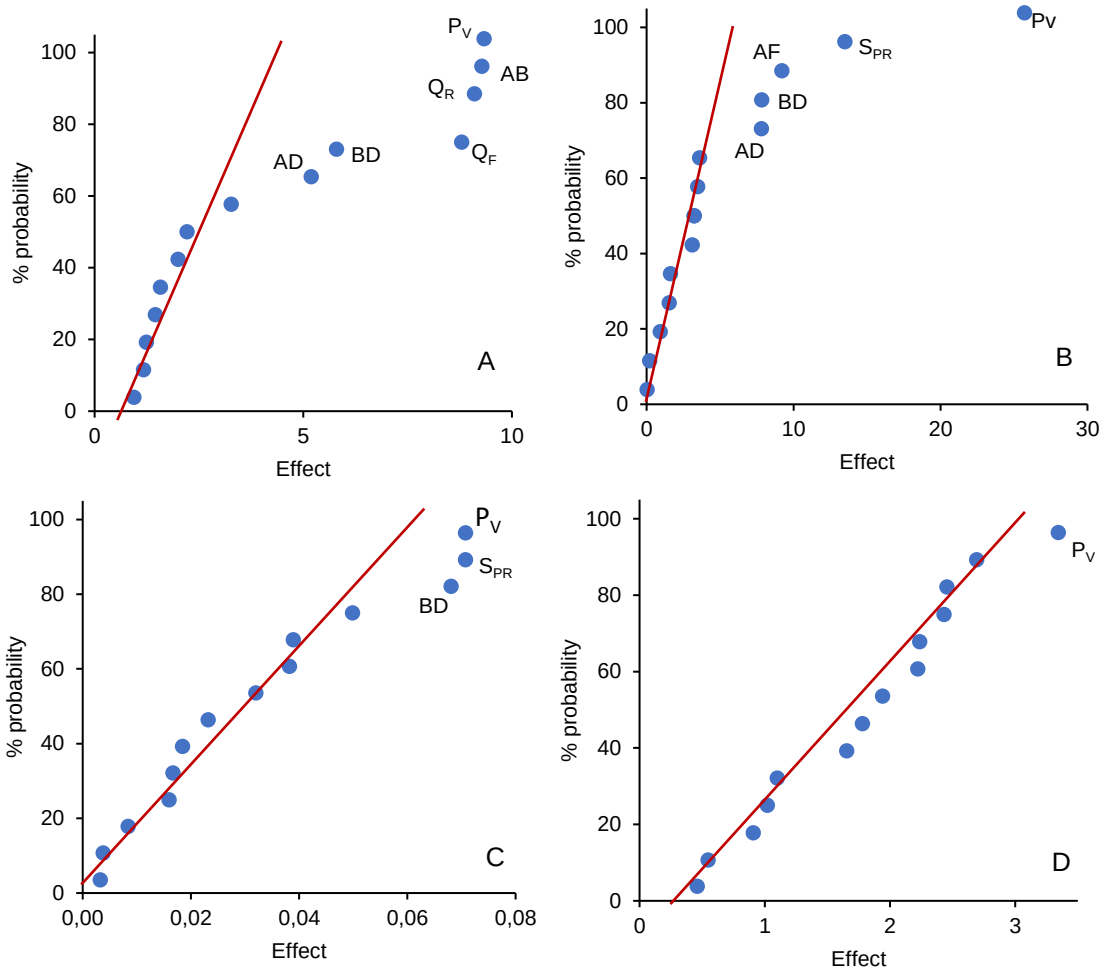

Figure 80: 13XBL CO_2 cyclic adsorption experiments half normal probability chart. (A) Purity, (B) Recovery, (C) Productivity, D) Energy consumption.

This analysis is finally concluded with the factor interaction charts plotted in Figure 81 and showing the representation of the main second order interactions. It can be observed that S_{RN} and S_{FD} (Figure 82 A) have a similar impact on the purity through their interaction: when S_{FD} is at the high level, a change on S_{RN} represents 13% of purity decrease. The interaction of S_{PR} and S_{RN} (Figure 82 B) shows a direct impact on purity, with better values achieved when both factors are either on their high or low levels.

The interaction between P_V and Q_R represents a significant impact on the recovery of 33% when Q_R is at high value and P_V is at low value. Likewise, the productivity is also affected by this interaction, as higher levels of productivity are achieved at higher values of P_V and Q_R.

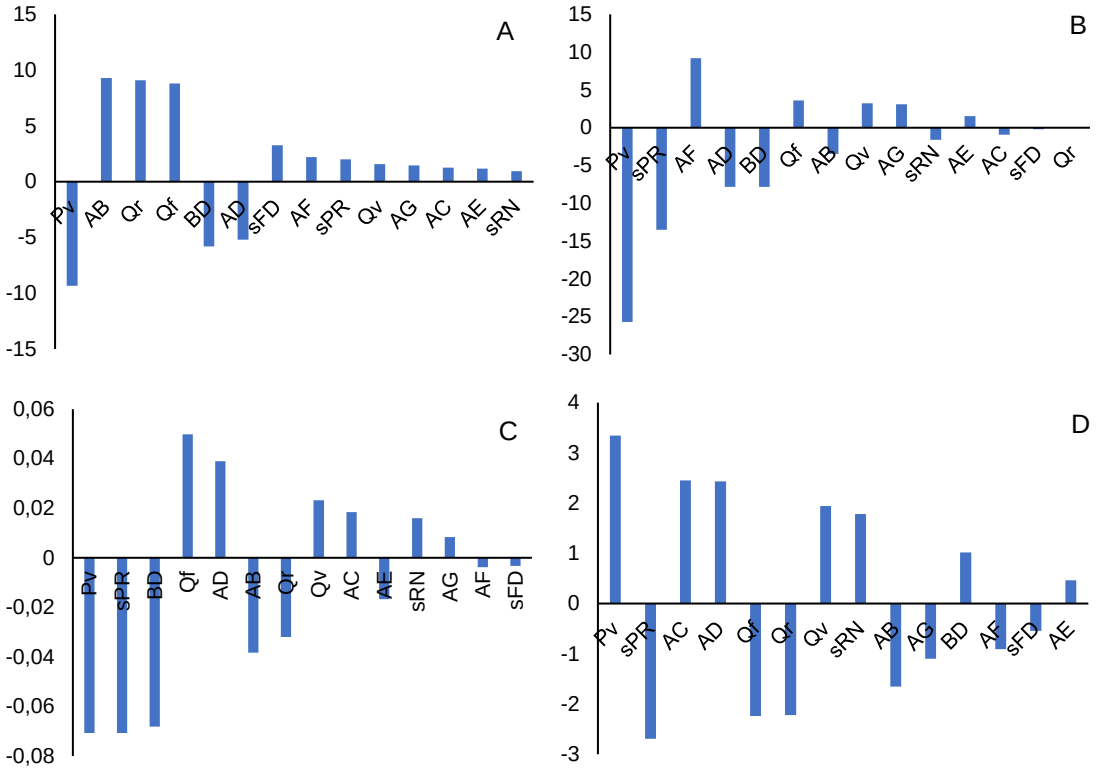

Figure 81: 13XBL Effect representation chart CO_2 cyclic adsorption experiments. (A) Purity, (B) Recovery, (C) Productivity, D) Energy consumption.

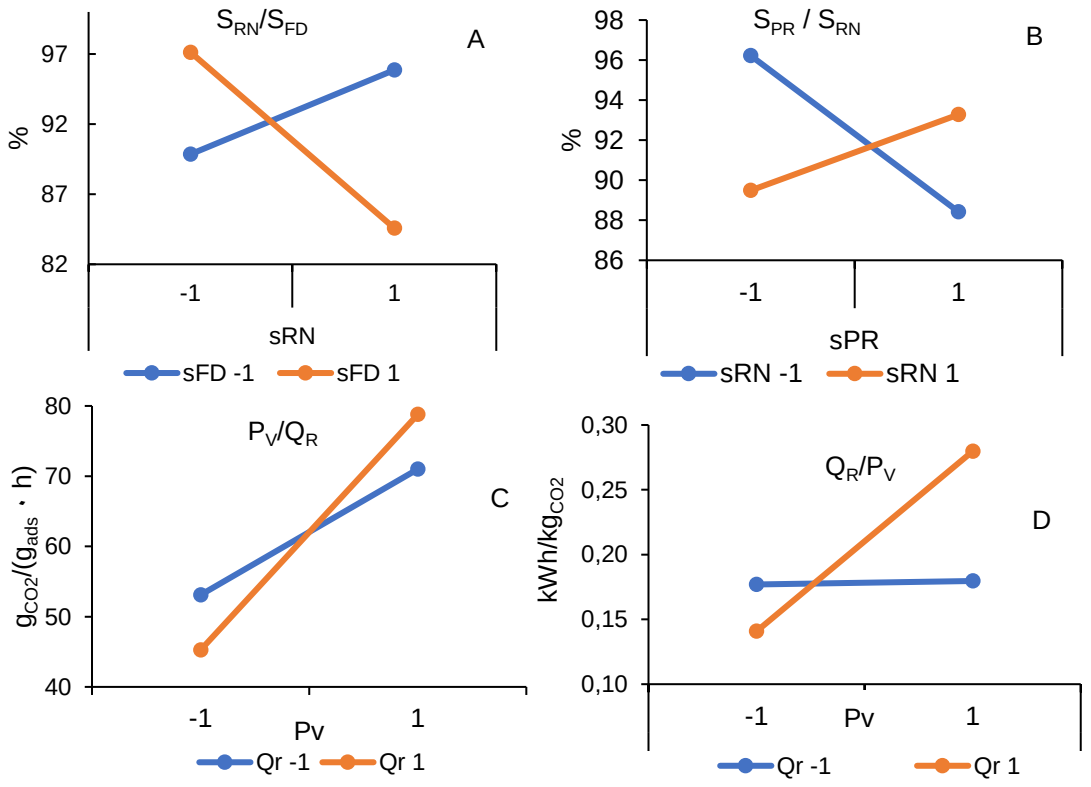

Figure 82: The main possible effects interaction representation for 13XBL experiments.

In summary, the parameter that has a more important impact on the VPSA process using 13XBL is the P_V at its high value, followed by S_{PR}, where better results on the recovery, the productivity and the energy consumption are achieved when this parameter is at the low level. The possible interaction with S_{RN} suggests further studies to understand how the dependence works. The third parameter on importance is Q_F, and the study reveals that high levels lead to a better result on purity and productivity. Finally, the factor Q_R represents an important contribution to the productivity and recuperation through the possible interaction with P_V. Table 38 summarises the results for the 13XBL cyclic experiments and suggests the experimental matrix design that leads to find the optimal working conditions. It is important to remark that this design of experiences brings an idea of the factors with more importance, but more experiments are needed to clarify the real importance and impact of the rest of the factors and to resolve the interaction confusion.

Based on the conclusions of this section, the following set of experiments will not consider the variable Q_V due to its low influence on the response. Moreover, P_V will be fixed at its highest value to better differentiate the influence of the other parameters. The range of factors with the recommended levels for an optimal performance is given in Table 38.

Table 38: Results from the analysis of the overall analysis criteria and variables for the Zeolite 13XBL. (E): Energy consumption; (R) Recuperation; (P) Purity, (T) Productivity.

Factor	Low level -	High level +	Impact	Response effect
Q_F (g/min)	10	15	medium	P, E
Q_R (g/min)	10	15	medium	P
Q_V (g/min)		11	negligible	P, E
P_V (barg)		-0.95	High	R, P, T, E
S_{RN} (%)	130	180	medium	E
S_{FD} (%)	8	16	by interaction	P
S_{PR} (%)	20	40	medium	R, T

4.4.4. Adsorbent comparison for VPSA fixed-bed experiments.

Table 39 compares the effects of the different VPSA process performance indicators in zeolites 13XBL and 5ABL under the same conditions. Zeolite 13XBL has better performance than 5ABL in all indicators achieving higher average values on their purity and recovery. The highest values of purity and recovery for zeolite 13X are 99.5% and 88.5% respectively, representing a 1.4% and 9.5% more compared to the highest CO_2 values obtained with 5ABL. Concerning the productivity and the energy consumptions, they depend on the impact of the different factors over the total cycle time. This means that, if the total cycle time is too high, the productivity will be low even with high purity and recovery values.

Table 39: Zeolites 13XBL and 5ABL VPSA average performance comparison for CO_2 capture.

Adsorbent	Recovery %	Purity %	Productivity $g_{CO2}/(g_{ads} \cdot min)$	Energy C. kWh/kg_{CO2}
13X	62.03	91.85	0.19	3.10
5A	59.31	87.81	0.17	3.71

Figure 83 shows the average response of the parameters for 5ABL and 13XBL adsorbents. Despite the high impact of P_V in both adsorbents, this parameter has more importance for the 5ABL performance (58.6% of contribution) than for 13XBL (30.9% of contribution). This difference can be attributed to their different isotherm shapes (see Figure 63 D and F). For 13XBL, the stepper slope is reflected in a higher working capacity, due to its capacity to desorb more quantity of adsorbed material. Although zeolite 5ABL has similar q_{CO2} at the working pressure (see Figure 67 B and D), it desorbs less at the same pressure level, so the impact of the other parameters is much lower.

The regeneration of adsorbents is always an energy-intensive procedure in all the adsorption processes. For the VPSA process, the evacuation of adsorbed gas from adsorbents consumes more than 70% of the total power consumed by the VPSA process. The vacuum pressure level is therefore the most important parameter related to the CO_2 operating cost and VPSA performance. In previous reports from various research groups (Ling et al., 2015; Liu et al., 2011a; Webley et al., 2017; Xiao et al., 2008), high CO_2 purity (>90%) and high recovery (>70%) were achieved only at deep vacuum pressure (-0.95 barg). However, deeper vacuum levels usually require multistage vacuum units and large vacuum lines and valves, which are not always

economically practical. In general, the vacuum or regeneration step is longer because the vacuum pump takes much longer to reach the required pressure.

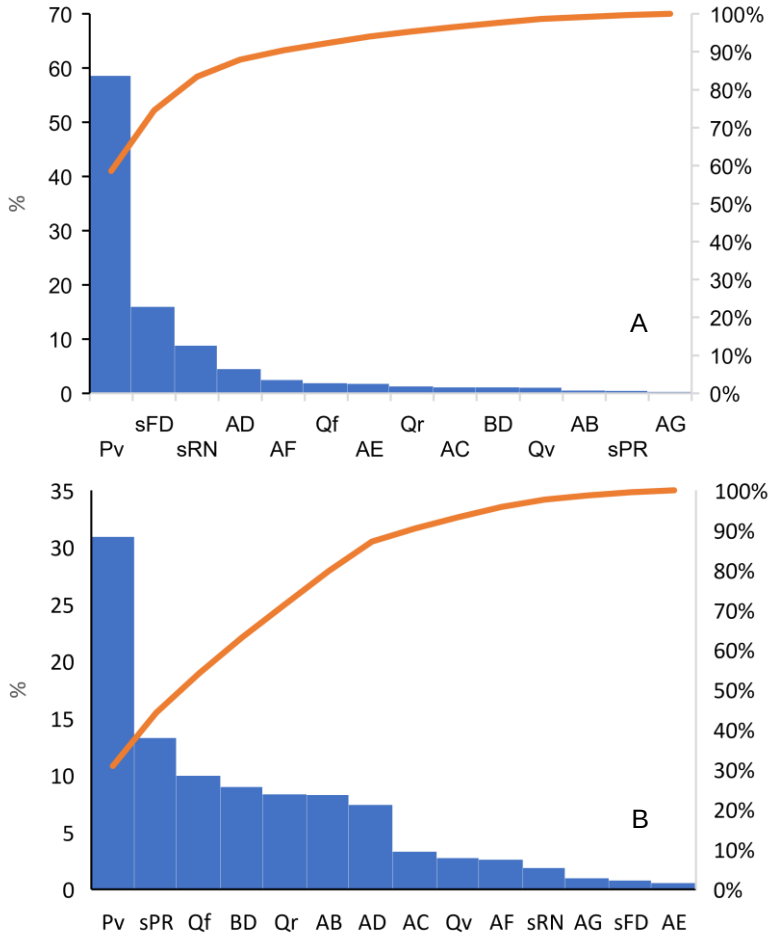

Figure 83: VPSA average parameter contribution. (A) 5ABL, (B) 13XBL.

On the 5ABL experiments, S_{FD} and S_{RN} are the second and third most relevant parameters, representing a 24% of the global contribution. On the other side, 13XBL results reveal that the second important factor is S_{PR} (13% of contribution) in its low level. The purge flow is a flow of high pure inert gas (N_2) fed counter-current to regenerate the column after the vacuum stage. When the gas is introduced to the column, the partial pressure of the of the adsorbate is decreased. This causes a desorption of the adsorbate, cleaning the column for the next cycle of operation. Lower levels of this stop point allow a better bed regeneration and, consequently, a greater CO_2 adsorption.

Q_F is the third importance factor (10%) for 13XBL and better results are achieved at high values, as the total cycle time is decreased. The flowrate of the feed influences on the superficial velocity of the gas throughout the column. This is determinant for the kinetics

of the adsorption process and for the stop point of S_{FD}. The feed stage time will increase if Q_F is decreased. The adsorption time is generally shorter than the breakthrough time in the case of the PSA process recovering a light component. In the case of recovering a heavy component (CO_2), the adsorption time is longer than the breakthrough time to minimize the fraction of light component (N_2) inside the column. However, at high level values of S_{FD} low recovery results were observed since some significant amounts of CO_2 were lost at the outlet of the column. An optimization must to be done to determine the optimal S_{FD}. Results obtained in the 5ABL experiments at the low level of the S_{FD} (10%) resulting in all the performance parameters improving with exception for the energy consumption. The impact was an increase in purity (10%), recuperation (5%) and productivity (18%), and a decrease of the electrical increased (40%). However, the effect of this variable was different for the 13XBL results, performed at the high level of S_{FD} (50%). In this case, the purity, productivity and electrical consumption increased by 4%, 1.6% and 18% respectively, while the recuperation decreased by 0.3%.

There is an important contribution from Q_R (rinse flow) through its interactions with the stop points S_{FD}, S_{RN} and S_{PR} which sums up to 33% of the contribution. The rinse flow is a flow of highly pure CO_2 fed co-current through the column to increase the heavy component (CO_2) fraction inside the column and displace the light fraction (N_2) to the outlet after the feed of the mix. In 5ABL experiments, a low Q_R (9 g/min) increases the recuperation and productivity by 0.2% and 5.9%, respectively. But this also resulted in an increase in the electrical consumption by 14%. On the other side, purity is increased by 1.3% with Q_R (11 g/min). With zeolite 13XBL, a low Q_R (9 g/min) provides and increment of 10% purity respect to the high Q_R (11 g/min). Moreover, high Q_R produces an increase of the productivity and electric consumption by 17% and 88%, respectively.

In summary, based on the above discussion, the more suitable adsorbent for the VPSA process is zeolite 13XBL. However, more experiments are needed to understand the interdependencies of some parameters and to refine the optimal conditions on the proposed cyclic process. In addition, the study must be proved in a cyclic process, since pure recirculation streams in the purge and rinse flows were used on the single column approach, hence the results do not strictly represent thoroughly the real process.

4.4.5. VPSA process simulations in Aspen Adsorption.

In this section, Aspen Adsorption software was used to simulate the cycles studied experimentally on section 4.4.3, in order to better understand the dynamic behavior and the importance of the process parameters. By using the pure component isotherm fitting parameters, the adsorption equilibrium was then predicted for binary gas mixtures using the DSL models. The simulation model was previously described on section 3.5.2 and the methodology for VPSA cyclic simulations was already explained on section 0. The equilibrium data was calculated through the breakthrough experiments and validated through the column binary dynamic experiments at different absolute pressure and temperature values as previously discussed in Section 4.3.3.

As deep vacuum levels (<50 mbar) are not practical at the large scale, vacuum pressures of up to 50 mbar were tested in simulation experiments. An Inlet CO_2 concentration of 15% with a fixed operation temperature of 20°C was studied to represent the concentration and temperatures expected in industry. The study was conducted using a single bed system to match the experimental data of section 4.4.3. The bed is assumed to be initially saturated with N_2 at 1.1 bara and at the designed temperature of 20ºC. All the results such as recovery, purity, profiles of pressure and temperature can be collected after the VPSA system reaches continuous steady state (CSS). The running conditions in the simulation are adjusted to exactly those used in the real experiments. The performance of one cycle at CSS is calculated with following expressions:

$$\text{Purity}_{CO2} = \frac{\sum y_{CO2} Q_{vac} \Delta t}{\sum Q_{vac} \Delta t} \tag{36}$$

$$\text{Recovery}_{CO2} = \frac{\sum y_{CO2} Q_{vac} \Delta t}{15\%(\sum Q_F \Delta t + \sum Q_{rinse} \Delta t)} \tag{37}$$

where Q_F, Q_V and Q_R are the instantaneous flue gas flow rate of adsorption step, vacuum expulsion and rinse step (g/min), respectively, y_{CO2} is the instantaneous mole fraction of CO_2 (%) and Δt is the time interval (min).

In this simulation, a seven-step Skarstrom-type VPSA cycle has been considered to understand the CO_2 capture process from flue gas by 13XBL. Before executing the design of experiments, the model was compared with an experiment to verify the representativity of the simulation. The uptake results after CSS are shown in Figure **84** (A), where each step is represented with a colored area along the graph. It is observed that the CO_2 uptake is adsorbed earlier in the feed step, and later for the desorption on

the regeneration and purge simulation. This kinetic issue is similar to the effect of the breakthrough adjustments on section 4.3.4, where it was found that the model estimations were predicting less capacity than in the experiments. The dead volume existing in the experimental system between the end of the column and the CO_2 analyzer could also contribute to the later breakthrough in the experimental system. The SSE vale estimation of the simulated model is of 3.73%, confirming that the approximations done are acceptable.

Another interesting observation is the fact that the regeneration is the step (light blue) that takes longer time on the process. At the beginning of the regeneration step (in the range of 160 to 400 seconds), the ratio of desorption is 1.75 mol/h, desorbing the 67% of the total CO_2 uptake. From 400 to 1050 seconds, the desorption ratio decreases to 0.15 mol/h with a low variation of the CO_2 uptake (15% of the total). This fact could indicate that the regeneration time of CO_2 is not highly efficient. The steeper CO_2 isotherm of 13XBL facilitates a faster desorption at the beginning of the step; nevertheless, after this fast rate of desorption, 73% of the regeneration time is used to recover 15% of the total CO_2 uptake. Taking in consideration this effect, once the vacuum pressure is reached, the desorption time (t_V) was decreased from 420 to 60 seconds to study its impact on the cyclic performance.

Figure 84 (B) shows the CO_2 load column profile on the different steps of the VPSA cycle. In this graph, the different steps and their impact on the accumulation of CO_2 at the adsorption column are plotted. The feed stage is represented with the green area Figure **84** (A), from where the beginning of the column is clearly saturated with CO_2, but after 40% of the total length of the column, the CO_2 saturation profile starts to decrease gradually. It can be appreciated how at the end of the feed step the adsorbent has not become saturated due to the low stop condition used and how impactful the rinse step is to purify the adsorbed gas.

In the depressurization (represented by the orange line) the load of the column decreases as material is allowed to escape to equalize the pressure with the atmosphere. On the rinse step, the loading of the column increases since CO_2 is injected from the entrance of the column, and in consequence the N_2 is displaced to the end of the column where the profile almost reaches the same level obtained on the feed step. On the regeneration step (blue line) the CO_2 load is desorbed because of the decreases in the pressure. In the purge step (black line) a N_2 flow is circulated counter-current displacing the CO_2 form the end of the column to the beginning on the flow direction.

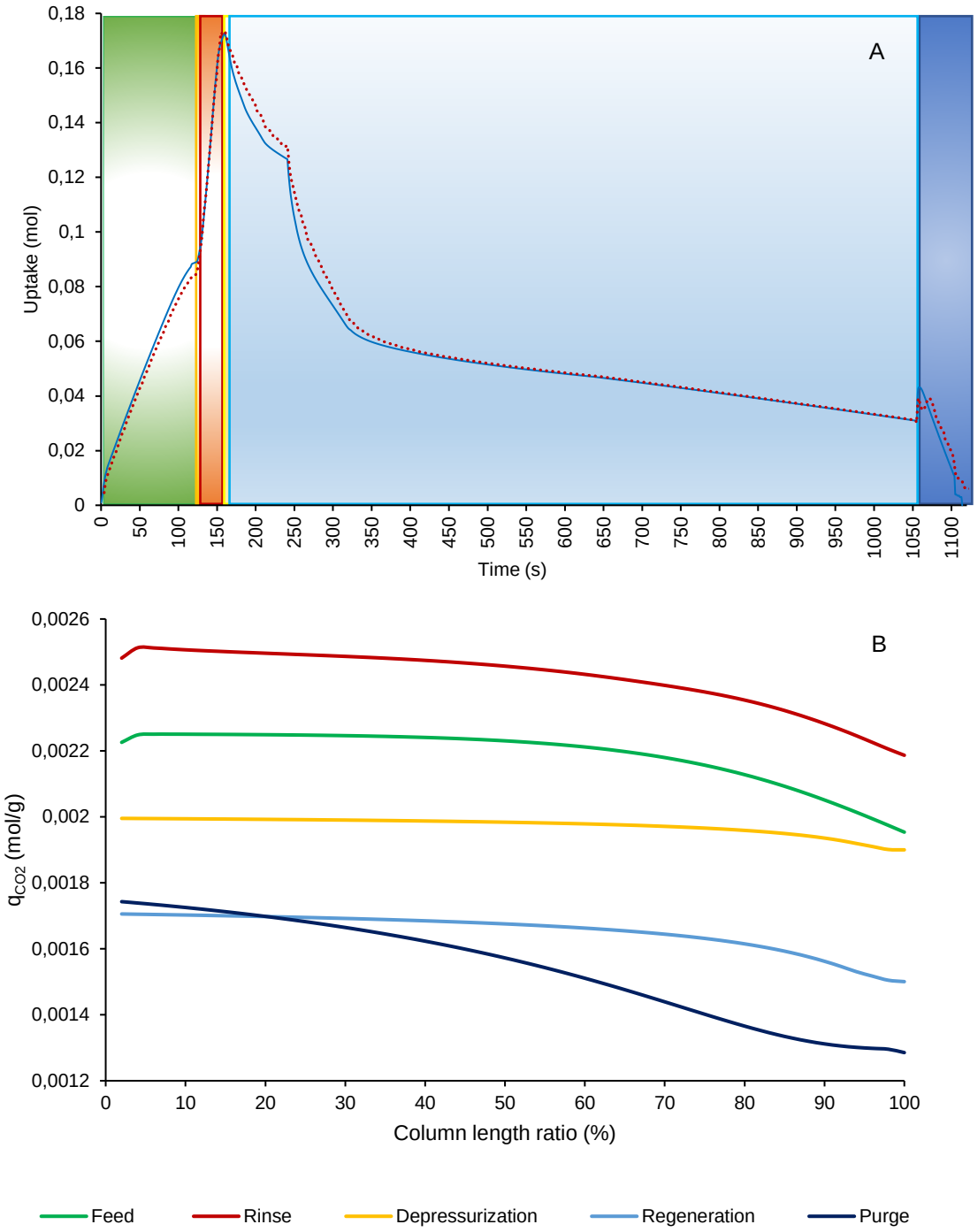

Figure 84: Cyclic simulation results for a single column after CSS was reached (A) Experimental and simulated results of CO2 uptake; (B) CO2 load column profile on the different cyclic steps. Simulation results (solid line), experimental results (dotted line).

4.4.6. Analysis of cycle performance

The cycle configuration was set using the control methodology proposed in section 3.4.1 utilizing the stop points of S_{FD}, S_{PR} and S_{RN}. The Q_V flowrate was set at the maximum possible value and P_V was set constant to -0.95 barg during the cycle step. The purge flowrate (Q_{PR}) was set at the same level value as Q_F. The levels of each factor were fixed based on the results of the ANOVA analysis of section 4.4.3. Dead volumes at both ends of the experimental system were estimated and considered in the simulations. The equalization step was handled in the simulation by specifying the pressure levels reached at the end of each equalization in the cycle organizer, which were based on the values achieved in the experiments. In this study, the working pressure (P_T) is included to study the interaction of the selectivity with the rest of parameters. Table 40 summarizes the levels of the studied parameters for the design of simulations experiments.

Table 40: High and low levels of studied variables in fixed column simulations for 13XBL.

	Q_{FD} (g/min)	Q_{RN} (g/min)	P_T (barg)	S_{RN} (%)	S_{FD} (%)	S_{PR} (%)
Low level	5	5	2	130	5	50
High level	9	9	4	180	10	80

The experiments were performed to study the cyclic VPSA performance of 13XBL during 20 cycles at a temperature of 20ºC. The dimensions and properties of the column are the same as that used in the fixed bed experiments (see Table 8). Using the simulation, a full factorial design can be used since no extra resources are needed to perform the experiments and the time is reduced considerably from 8 hours (time to perform a real experiment) to 30 minutes (time of the simulation run). A full factorial experiment design with six factors and two levels (2^6) was realized with 64 simulated experiments. Productivity, purity and recovery were selected as the response variables. The experimental matrix with the simulated conditions is summarized in Table 41. The process sequence is the same as illustrated in Figure 22.

A summary of the results obtained is plotted in Figure 85. The CO_2 purity range is found in all cases between 93% and 96.5%, while the recovery range is wider (72 to 90%). The highest values are 96.8% and 91%, respectively, both reached at experiment number 43. The purity and recovery averages are 94.8% and 77.5%, respectively. These averages are better than those obtained on the experiments of the section 4.4.3

However, any experiment was capable to reach the maximum purity value found in the previous experiments (99.5%). Cyclic steady state was reached in all the experiments and simulations after approximately 15 cycles.

Table 41: Operating conditions of the full factorial design 2^6

Exp	Q_{FD} g/min	Q_{RN} g/min	S_{RN}	S_{FD}	S_{PR}	P_{FD} barg	Exp	Q_{FD} g/min	Q_{RN} g/min	S_{RN}	S_{FD}	S_{PR}	P_{FD} barg
1	5	5	130	5	50	2	33	5	5	130	5	50	4
2	9	5	130	5	50	2	34	9	5	130	5	50	4
3	5	9	130	5	50	2	35	5	9	130	5	50	4
4	9	9	130	5	50	2	36	9	9	130	5	50	4
5	5	5	180	5	50	2	37	5	5	180	5	50	4
6	9	5	180	5	50	2	38	9	5	180	5	50	4
7	5	9	180	5	50	2	39	5	9	180	5	50	4
8	9	9	180	5	50	2	40	9	9	180	5	50	4
9	5	5	130	10	50	2	41	5	5	130	10	50	4
10	9	5	130	10	50	2	42	9	5	130	10	50	4
11	5	9	130	10	50	2	43	5	9	130	10	50	4
12	9	9	130	10	50	2	44	9	9	130	10	50	4
13	5	5	180	10	50	2	45	5	5	180	10	50	4
14	9	5	180	10	50	2	46	9	5	180	10	50	4
15	5	9	180	10	50	2	47	5	9	180	10	50	4
16	9	9	180	10	50	2	48	9	9	180	10	50	4
17	5	5	130	5	80	2	49	5	5	130	5	80	4
18	9	5	130	5	80	2	50	9	5	130	5	80	4
19	5	9	130	5	80	2	51	5	9	130	5	80	4
20	9	9	130	5	80	2	52	9	9	130	5	80	4
21	5	5	180	5	80	2	53	5	5	180	5	80	4
22	9	5	180	5	80	2	54	9	5	180	5	80	4
23	5	9	180	5	80	2	55	5	9	180	5	80	4
24	9	9	180	5	80	2	56	9	9	180	5	80	4
25	5	5	130	10	80	2	57	5	5	130	10	80	4
26	9	5	130	10	80	2	58	9	5	130	10	80	4
27	5	9	130	10	80	2	59	5	9	130	10	80	4
28	9	9	130	10	80	2	60	9	9	130	10	80	4
29	5	5	180	10	80	2	61	5	5	180	10	80	4
30	9	5	180	10	80	2	62	9	5	180	10	80	4
31	5	9	180	10	80	2	63	5	9	180	10	80	4
32	9	9	180	10	80	2	64	9	9	180	10	80	4

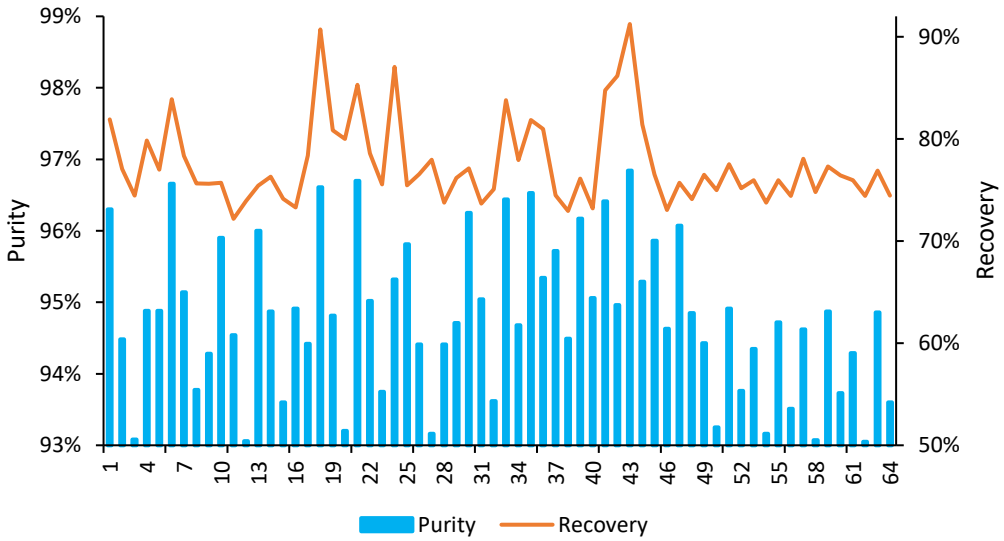

Figure 85: CO_2 purity and recovery performance for 13XBL fixed column simulation experiments.

Productivity was calculated as cyclic performance indicator. Figure 86 shows the experimental results, where the productivity range is 0.10 to 0.36 $g_{CO2}/(g_{Ads} \cdot h)$. The average productivity is 0.23 $g_{CO2}/(g_{Ads} \cdot h)$, representing an increment of 21% in comparison to the experiments performed on section 4.4.3. The new range of the level parameters represent an important improvement on the performance indicator, expressed mainly in the recuperation and reflected in the productivity.

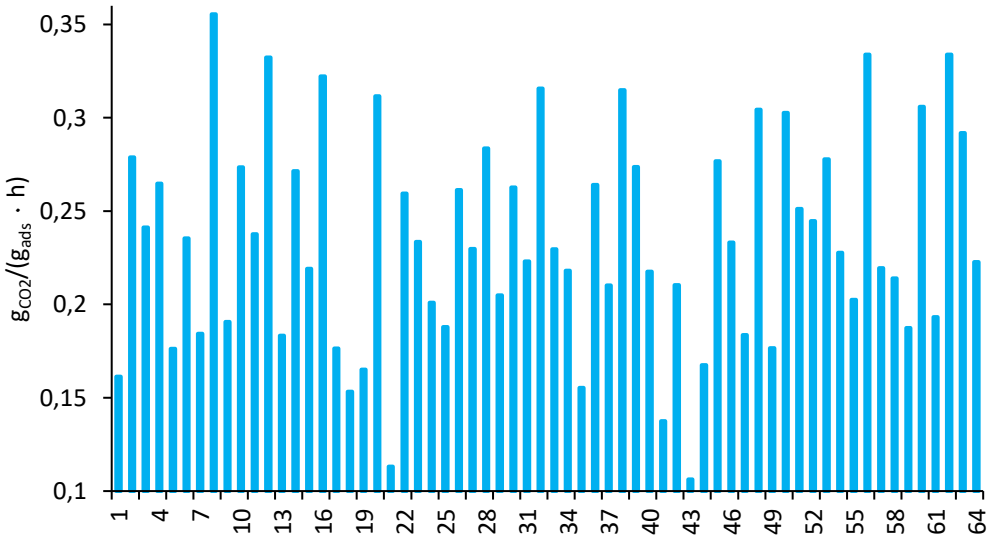

Figure 86: Figure 72: CO_2 productivity for 5ABL on fixed column experiments.

A statistical ANOVA analysis was performed to determine the influence of the different factors on the design of experiments (see appendix 7.3). The effects on the performance indicators by the parameters of the simulations are represented in Figure 87 The factors with more influence are P_T and Q_{RN} in their low level for the purity (Figure 87 A) S_{FD}, P_T and Q_{RN} in their low level for the recovery (Figure 87 B), and Q_F followed by a similar impact of Q_R, S_{FD} and P_T, all of them at their high level, for the productivity (Figure 87 C).

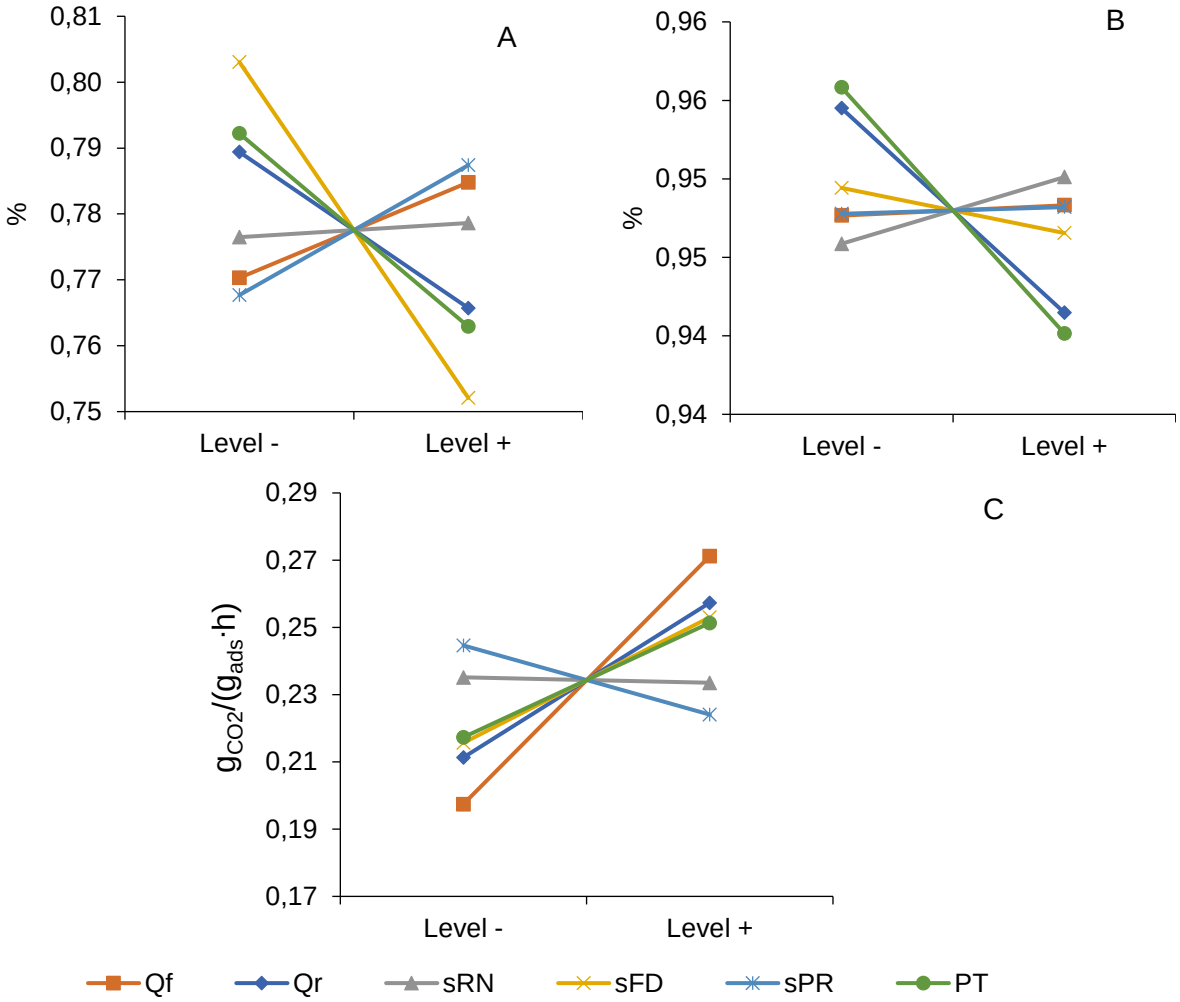

Figure 87: Effect plots for 13XBL CO_2 simulated cyclic adsorption from a full factorial design 2^6. (A) Recovery, (B) Purity and (C) Productivity in CO_2 separation.

The results illustrate that, when P_T decreases, better recovery and purity results are reached. This can be explained based on the higher CO2 selectivity for 13XBL (see section 4.3.5) and the steeper slope of its isotherm at low pressure (Figure 67). On the other side S_{FD} has a strong impact on the recovery but a relatively low effect on the purity.

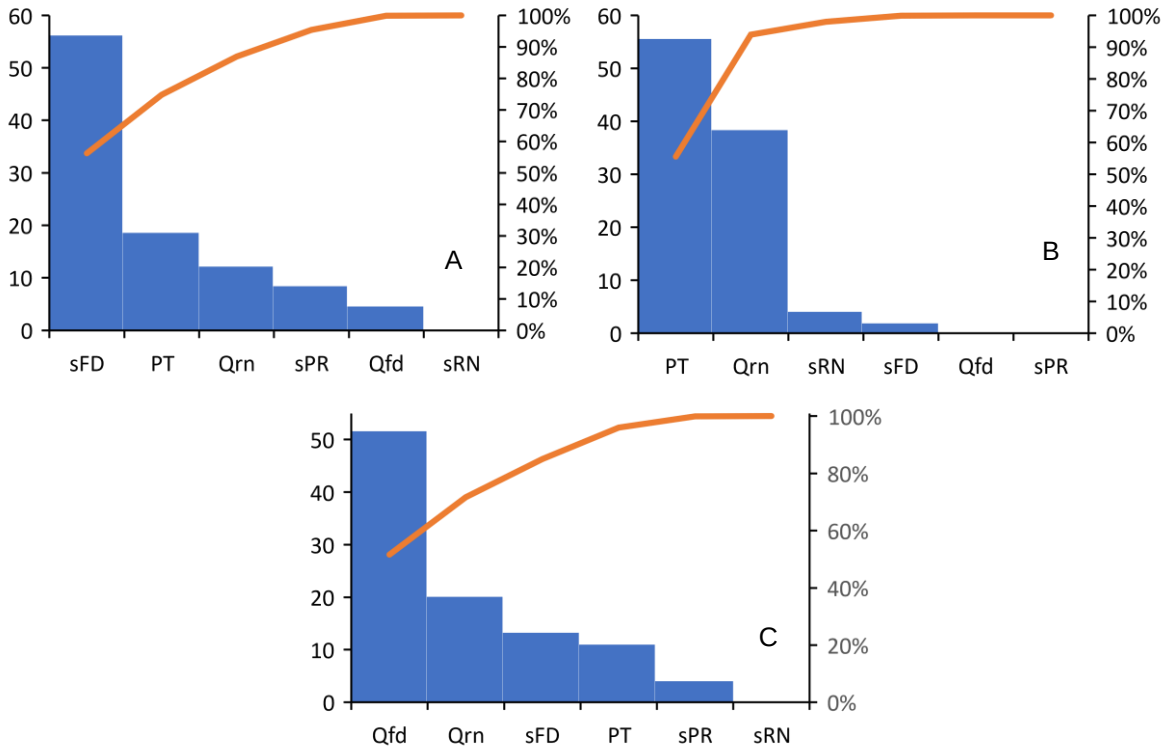

Figure 88: 13XBL Pareto contribution chart of CO_2 cyclic adsorption experiments. (A) Purity, (B) Recuperation, (C) Productivity.

Figure 88 (A) represents the total contribution of the parameters over the response. For the purity, the most relevant parameter is S_{FD} with a 56% of the contribution. The relevance of this parameter is confirmed in Figure 89(A) through the half-normal probability plot. In addition, from a qualitative evaluation, it can be concluded that the point S_{FD} do not follow a normal distribution confirming its relevance. For the recovery, P_T has a contribution of 55.6% and of Q_{RN} 38.4% (Figure 88 B) confirming their relevance through Figure 89(B). Finally, for the productivity, the effect of the parameters is more spread out, but there is a clear contribution from Q_{FD} of 51% of the contribution (Figure **88** C).

These simulations have provided a better understanding of the process. The results confirm the inverse proportionality of some parameters on their response. For example, a low level of S_{FD} contributes to higher purity values, but also leads to low recovery values and therefore a low productivity result. Furthermore, a low value on the S_{FD} stop point represents a shorter cycle time, so the amount of CO_2 recuperated on the same time is lower too, decreasing the productivity. These results suggest that the process can be adapted to increase the purity by a decrease on the recovery or vice versa. On the other hand, S_{RN} had a low relevance in the response, but Q_{RN} seems to represent a high impact on the response.

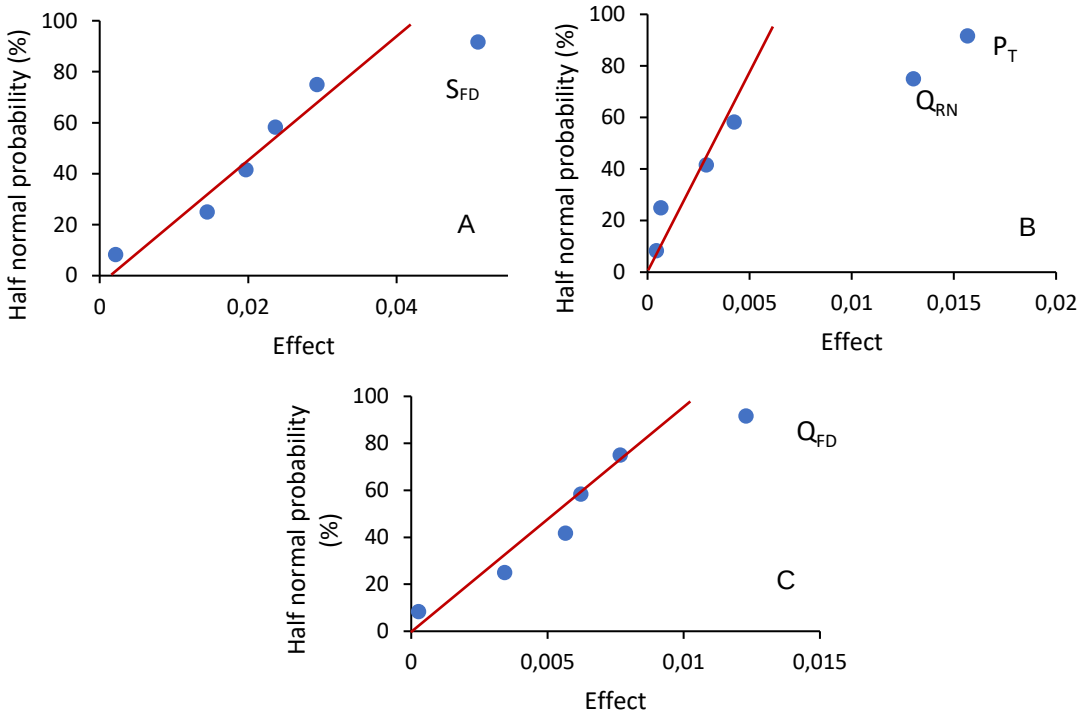

Figure 89: 13XBL CO_2 cyclic adsorption experiments half normal probability chart. (A) Purity, (B) Recuperation, (C) Productivity.

Even if this design of experiences brings an idea of the most significant factors, a setup with the complete process is needed to clarify the real importance and impact of the rest of the factors. In any case, the understanding of the effects of the parameters over the process shows the importance of P_V and P_T on the overall process performance. Therefore, a maximum P_V of -0.95 barg, a maximum Q_V and a low-pressure value of 2 barg are recommended for process experiments with the reflux streams of purge and rinse on three columns. Q_F, Q_R and the stop points S_{FD}, S_{PR} and S_{RN} will be analysed in the continuous process.

4.5. Three column VPSA experiments for CO_2 capture.

4.5.1. VPSA process parameters controlled by a S_{FD} of 5%.

The design of a continuous process for CO_2 capture from flue gas streams was done using a three-column equipment, as described on section 3.2.3, performing the process detailed on section 0. Continuous experiments were carried out to study the CO_2 adsorption from a gas mixture of 15% CO_2 and 85% N_2 using 13XBL in cyclic configuration. The reflux of nitrogen in the process was included to perform the purge stage and a CO_2 recirculation was also done to perform the rinse stage. An eight-step Skarstrom-type VPSA cycle in a three column arrangement was used to achieve a continuous CO_2 separation from flue gases. Figure 23 shows the different interconnections between the three column VPSA process stages. The column streams interconnections allow to recycle both gases (N_2 and CO_2) and to transfer the pressurization energy after rinse stage to another column in the equalization.

The set of three columns with an internal diameter of 5.0 cm described on section 3.2.3 was selected on these experiments, using the equipment to produce gas mixtures shown in section 3.2.1. The experimental process parameters were based on the results obtained from section 4.4.5 to validate the cyclic performance and functionality in a continuous separation process. As discussed before, the purity and the recovery provide inversely proportional responses (higher purity values lead to a lower recovery and productivity). On this experiment, the factors were chosen to achieve high purity results based on the results of the previous sections (4.4.3 and 4.4.5) . The power consumption was measured by a power meter installed on the electrical connection. The execution of the 8 steps on each column is considered one cycle on the process based on the representative scheduling table of Figure 23. Table 42 shows the process parameters selected for the cyclic experiment, from now named as process controlled by a S_{FD} of 5%.

Figure 90 shows the column temperature and pressure of the 5% S_{FD} controlled VPSA experiment on the adsorbent bed. Because the variation of the different parameter evolution during each cycle was quite small, the parameter history is shown only in part to be more easily identified. Figure 90 (A) show the pressure profile of one column is shown over the different steps, where the pressure changes on the process from 2 barg to -0.9 barg are clearly visible. The graph reveals a problem on the control of the pressure in the feed stage, as the pressure increases slowly from 1.91 to 1.98 barg. On the other side, the vacuum pressure of each cycle does not reach the desired value of - 0.95 barg,

due to the mass transference resistance of the column, as it was discussed on section 4.4.5. To avoid longer times of regeneration, a maximum regeneration time was set on the PLC in case the desired vacuum pressure was not reached on the column.

Table 42: VPSA process parameters for CO_2 separation controlled by a S_{FD} of 5%.

Process Parameter	Value	Unit
P_T	2.00	Barg
P_V	-0.95	Barg
Q_F	10.00	L/min
Q_R	5.00	L/min
Q_P	10.00	L/min
S_{RN}	120.00	%
S_{FD}	5.00	%
S_{PR}	50.00	%

A total of 20 cycles were performed in the experiment, and the cyclic steady state (CSS) was considered achieved once the difference between the temperature profiles of the last two cycles were less than 0.1%. As observed in Figure 90 (B), CSS was achieved in the VPSA process after about 17 cycles (at 8500 sec.). Another interesting feature is the fact that the variation of the temperature in the column inlet (T_{top1}, blue line) was 2ºC less than at the outlet ($T_{bottom1}$, orange line), indicating that the regeneration was not highly efficient during the VPSA cycles. In addition, S_{FD}, S_{RN} and S_{PR} stop points can be easily differentiated. The temperature profile of each cycle, depicted in Figure 90 (B), is identified with the different steps of the cycle. A first increment on the temperature from 19 to 21ºC is detected in the bottom temperature sensor, and from 19 to 22ºC in the top temperature sensor. This is followed by a flat zone, observed on the top temperature sensor, corresponding to the depressurization step. A second steeper increment from 22 to 28ºC in the bottom temperature sensor, and from 22 to 30ºC in the top temperature sensor corresponds to the rinse step. Finally, the regeneration step is represented by the fast decrease on the temperature in both sensors, while the purge step is only detected in the bottom temperature sensor, where a change on the temperature decrease rate is observed at 23ºC. Once the purge step is finished, the stream temperature is around 20ºC.

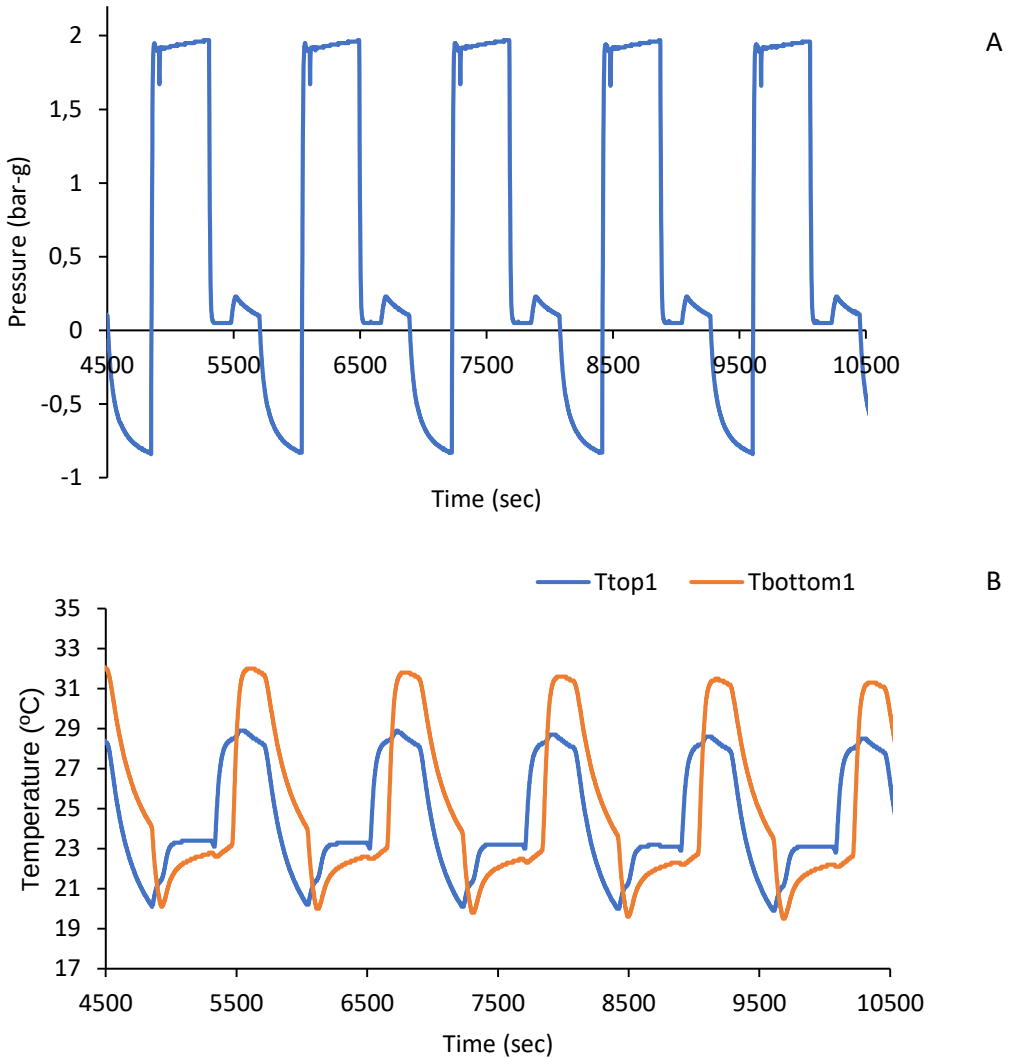

Figure 90: (A) Pressure and (B) Temperature profiles of one column on the VPSA process controlled by a S_{FD} of 5%.

Table 43 shows the numerical results of the capture process with the parameters shown in Table 42. The results illustrate a low productivity value of 0.028 $g_{CO2}/(g_{ads} \cdot h)$ compared to the results obtained on section 4.4.3 (average productivity of 0.19 $g_{CO2}/(g_{ads} \cdot h)$) or the simulated values obtained from section 4.4.5 (0.23 $g_{CO2}/(g_{ads} \cdot h)$). This low productivity is the consequence of the low recuperation of CO_2 (yield of 22%) and the long stand-by time. Stand-by stages mean that the column is waiting for the other columns to finish some parallel steps so as to synchronize the VPSA cycle. On the other hand, the purity result had a high value of 83%, although this value is 10% lower than those from the previous experiments.

Table 43: Results of the VPSA process controlled by a S_{FD} of 5%.

Performance indicator	Value	Unit
Purity	83.	%
Productivity	0.028	$g_{CO2}/(g_{ads} \cdot h)$
Power consumption	6.44	$kWh/(kg_{CO2})$
Yield	9.24	$\%CO_2$
Stand-by time	43.2	%
Cycle time	1198	sec

The time scheduling of the column process is shown in Figure 91, where each step of the VPSA process is represented by a bar of different color. The white bars represent the “stand-by” mode, and therefore it is evident that each column is waiting for 43% of the total cycle time as indicated in Table 43. The regeneration step (blue) is the process that takes longest time, making it the “bottle neck”. These long regeneration times can lead to a longer operation time on the vacuum pump. The combination of long regeneration times and low yield is reflected on a high energy consumption of 6.4 $kWh/(kg_{CO2})$ (see Table 43). On the other hand, the rinse step (red) is the second step with a longer cycle time. The rest of the process steps are quite small compared with those two steps.

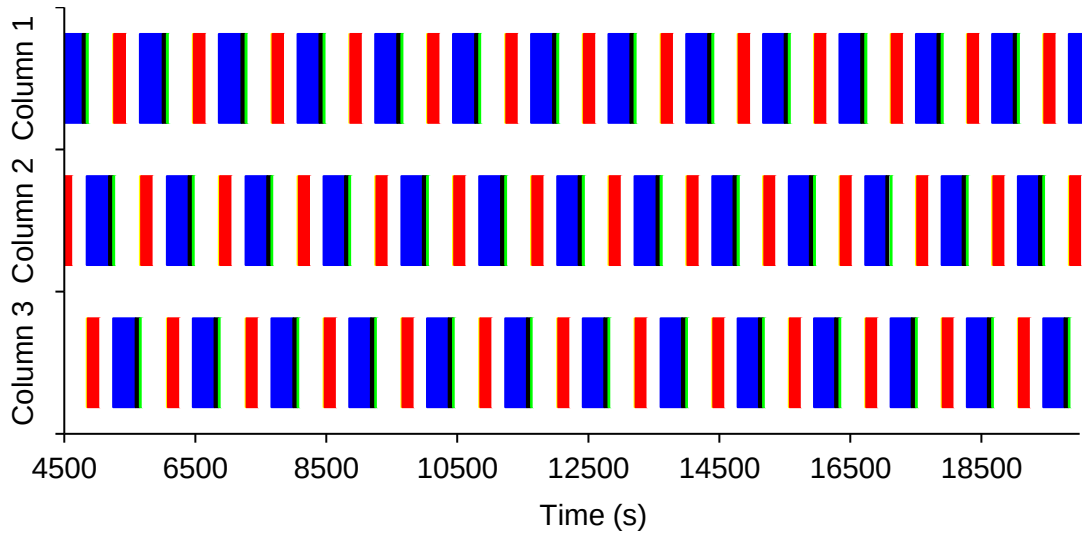

Figure 91: Cycle time for a three column VPSA process for CO_2 / N_2 separation controlled by a S_{FD} of 5%. Pressurization and feed (green), Depressurization (yellow), Rinse (rinse), Equalization (orange), Regeneration (Blue), Purge (black).

Figure 92 shows the CO_2 uptake of one adsorption column. The different process steps are differentiated in a similar way as in Figure 90 (B). The first increment corresponds to the CO_2 load contributed by the feeding stage. The second increment with a slow rate of adsorption corresponds to the CO_2 uptake during the stand-by step before the rinse stage. The third increment corresponds to the rinse step, where the main increment on the load is obtained, corresponding approximately to 91% of the total CO_2 uptake. Unlike the last experiment and the simulations of the previous sections, the CO_2 is recycled from the product recuperated from the process, so the purity of CO_2 depends on the purity of the CO_2 recovered. This unbalanced uptake proportion is the main reason of the low yield results, since just a small part of the feed is processed in each cycle.

After the rinse step, two uptake decrements are shown on the cyclic graph. The first decrement represents the CO_2 recovered by effect of the reduction on the pressure in the regeneration step, desorbing approximately 75% of the total CO_2 adsorbed. The second decrement corresponds to the desorption of CO_2 by the countercurrent flow of N_2 on the purge stage. This means that the CO_2 recovered stream is diluted with the N_2, causing a decrease in global purity.

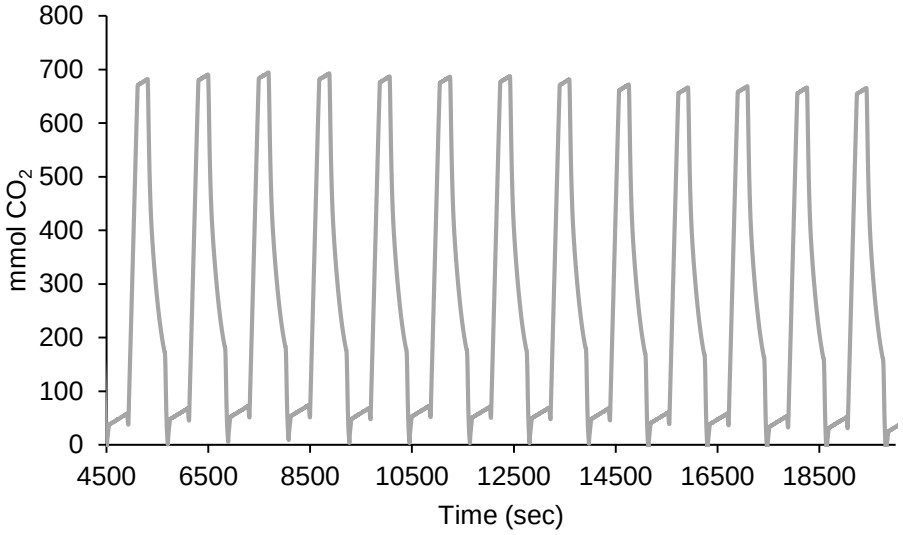

Figure 92: CO_2 molar balance of one column on the VPSA process controlled by a S_{FD} of 5%.

The low proportion of CO_2 recovered suggests a change in the experimental operating conditions. The initial hypothesis was based on a low S_{FD} stop point value, in order to avoid the loss of CO_2 in the partial breakthrough of the outlet column. However, this front creates a waste rate during the feed step and reduces the CO_2 recovery. In order to overcome this issue, a higher S_{FD} value of 40% has been set, while an increment of Q_F to 15 L/min has been chosen to avoid a long feed step time.

In addition, 25% of the CO_2 was being desorbed in the purge step, lowering the overall purity. Therefore, a higher S_{PR} of 80% is proposed to avoid the dilution of the CO_2 recovered. The rest of the conditions has been kept on the same values then the previous experiment.

4.5.2. VPSA process parameters controlled by a S_{FD} of 40%.

The operating VPSA process conditions of the experiment controlled with a 40% of S_{FD} are reported in Table 44.

Table 44: VPSA process parameters for CO_2 separation controlled by a S_{FD} of 5%.

Process Parameter	Value	Unit
P_T	2.00	barg
P_V	-0.95	barg
Q_F	15.00	L/min
Q_R	5.00	L/min
Q_P	15.00	L/min
S_{RN}	120.00	%
S_{FD}	40.00	%
S_{PR}	80.00	%

Figure 93 shows the pressure and temperature profiles of the 40% S_{DF} controlled experiment. As in the previous experiment, a total of 20 cycles were performed, while only a part of the parameter history is shown in the graphs to better identify the variables changes. The homogeneous control over the S_{FD} stop point is shown in Figure 93 (A) is shows the pressure profile of one column over the cyclic process. The main difference of this graph respect with respect to the previous experiments is the enhanced pressure control at the feed step. For this stream experiment, the PLC control pressure block was reprogramed to keep the inlet flow and the column pressure constant. In the previous experiment, the PID control was affected by the noise created by the adsorption capacity of the column adsorbent, despite the algorithm being programmed to keep the pressure constant controlling the outlet flowrate with I-319 as a back pressure controller (see Figure 30 on page 56). However, the controller actions of the inlet pressure performed by the instrument by I-302 were in conflict with the feed flowrate. The non-linearity of the

system and the noise created by the changing rate of adsorption impacted directly on the proportional and integral PID constants. To solve the problem, a cascade PID control was included, connecting the two PID controllers together to yield better dynamic performance, as it can be seen in the graph, where the pressure remains constant over the feed step in a value of 1.95 barg.

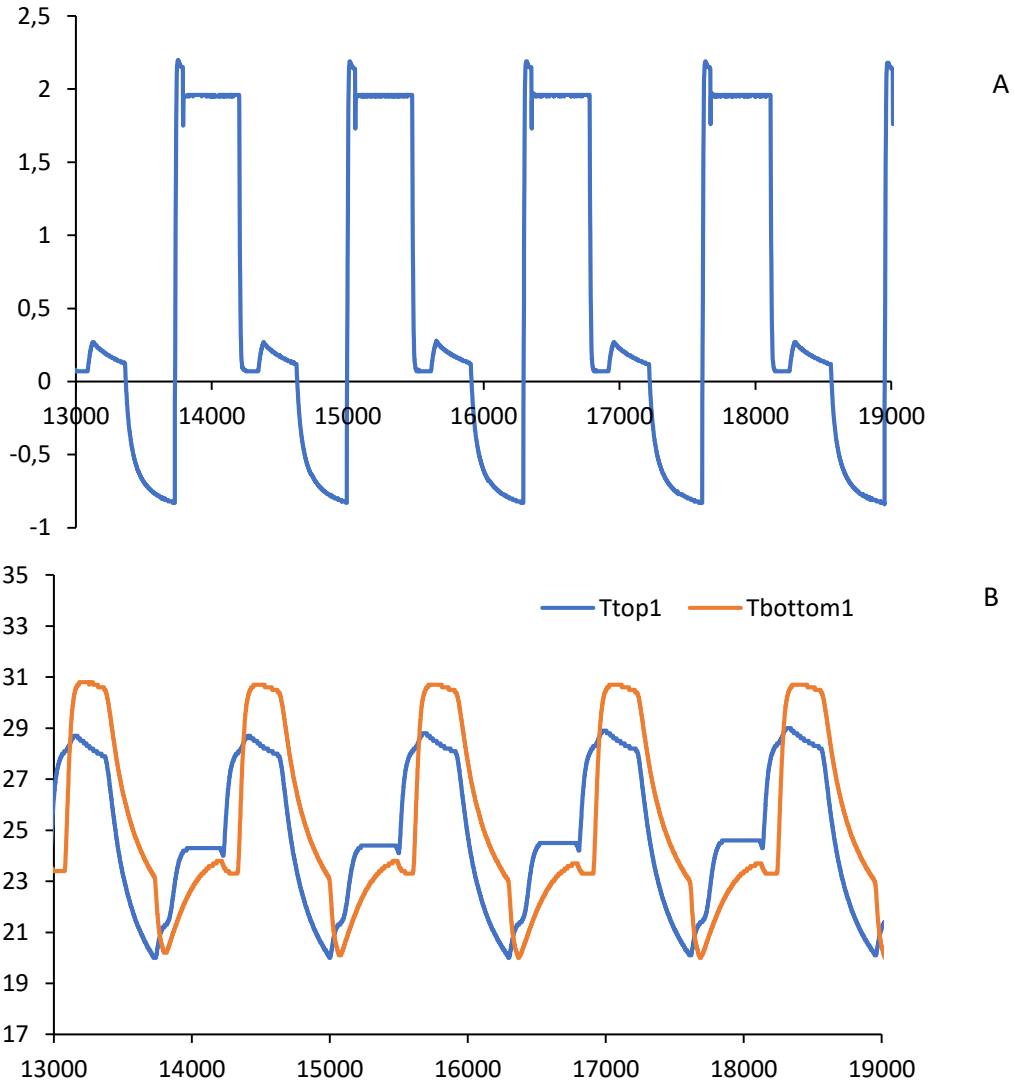

Figure 93: (A) CO_2 molar balance, (B) pressure and (C) temperature profiles of one column on the VPSA process controlled by a S_{FD} of 40%.

In Figure 93 (B), the temperature profile is depicted. The main difference respect to the previous experiment is the first increment of temperature, going approximately from 20 to 24ºC in the bottom temperature sensor, and from 20 to 25ºC in the top temperature sensor. These temperature increments along the column are 2ºC more in each position with respect to the previous experiment and mean that a greater CO_2 adsorption takes place during the feed stage.

Table 43 shows the performance of the VPSA process with the process controlled with an S_{FD} of 40%. The results show an improvement of the productivity and the purity compared to the previous experiment. This result is a consequence of the increment on the yield and the decrement of the stand-by times. On the other hand, the power consumption has decreased as well with the modification of the feed step parameters. Nevertheless, while the overall results are better than in the previous case, the process productivity still remains too low when compared to the results obtained on section 4.4.3 (0.19 $g_{CO2}/(g_{ads} \cdot h)$.

Table 45: Results of the VPSA process controlled by a S_{FD} of 40%.

Performance indicator	Value	Unit
Purity	89.8	%
Productivity	0.035	$g_{CO2}/(g_{ads} \cdot h)$
Power consumption	5.63	$kWh/(kg_{CO2})$
Yield	22.31	$\%CO_2$
Stand-by time	27.3	%
Cycle time	1355	sec

Figure 94 shows the time scheduling of the column process as controlled in the case of 40% of S_{FD}. Compared to the previous case, a better synchrony is shown, with a reduction of 15% of the total stand-by step duration. Therefore, each column is capturing more CO_2 from the feed step and more time of the total cycle is employed in the process. In the time-lapse between 12 000 and 15 000 sec., a difference on the feed steps between the three columns time is observed. This difference is stabilized throughout the cycles until reaching the CSS from 27 000 sec. This column synchronization is the result of the S_{FD} stop points being designed to achieve the time synchrony, regardless of the CO_2 concentration and variation in the stream feed.

In general, the steps with longer process time are the feed and regeneration steps, using approximately the 60% of the cycle time (30% each). The stand-by time accounts for 27.3% and the rinse step represents only the 12%. The time occupied by the depressurization and purge steps is residual, being only 1 and 4%, respectively. The equalization was not executed in the two performed cyclic experiments.

As it shown in Figure 93 (A), the pressure decreases from 1.95 to 0.07 barg in the depressurization step, while during the rinse step the pressure increases until 0.22 barg.

However, the long stand-by before the equalization steps produces a gradual decrease of the pressure inside the column until 0.1 barg.

This pressure drop occurs despite the fact that the column output is closed, and the cause is a continued CO_2 adsorption effect towards the equilibrium, where this kinetic effect is normally limited by the mass transference coefficient of the adsorbent. Therefore, the remaining pressure is not enough to satisfy the requirements for the equalization stage and is automatically skipped by the PLC program.

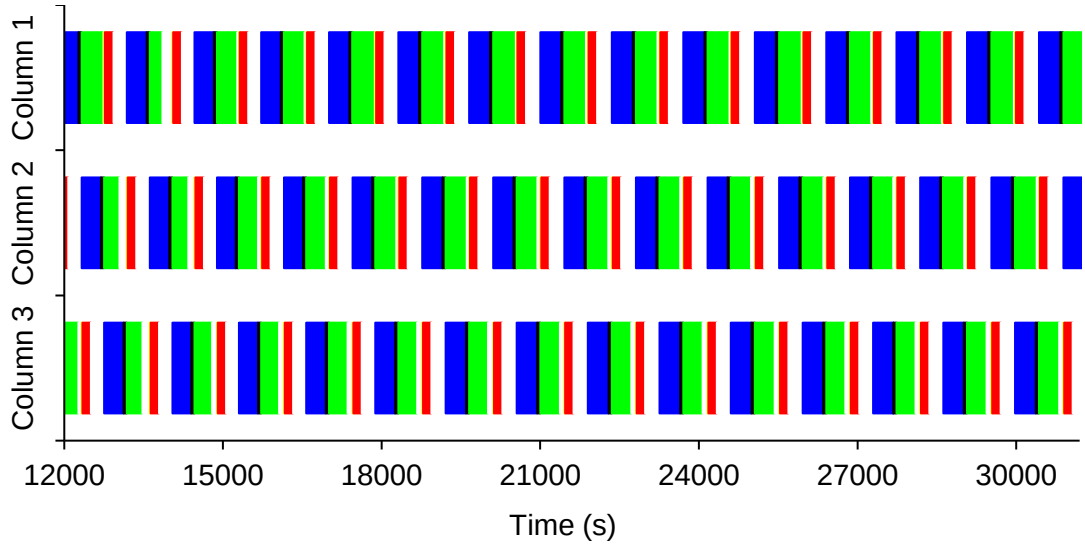

Figure 94: Cycle time for a three column VPSA process for CO_2 / N_2 separation controlled by a S_{FD} of 40%. Pressurization and feed (green), Depressurization (yellow), Rinse (rinse), Equalization (orange), Regeneration (Blue), Purge (black).

The CO_2 molar uptake profile of one adsorption column is shown in Figure 95 The molar uptake in the feed step is 22%, being 13% more compared to the previous experiment (5% S_{FD} controlled). Despite the improvement in the feed step, 78% of the CO_2 uptake is adsorbed during the rinse step, which means that most of the energy consumed is used to recirculate the CO_2 recovered in the previous cycles (as it was previously discussed, higher S_{RN} values increase the average purity). These results are very different than what was obtained in section 4.4.3, where the study was performed in one column without the stream interactions and using pure gas on the recirculation of CO_2 and N_2 for the rinse and purge steps. This fact suggests that the purity of CO_2 has an important effect on the adsorption dynamics. In fact, in the cyclic experiment the CO_2 purity on the rinse stage depends on the product purity achieved on the previous column cycle. This low CO_2 purity leads to a longer rinse step due to the competitive adsorption between CO_2 and N_2. Therefore, more time is needed to reach the desired stop point, promoting higher rinse recirculation rates.

The CO_2 recovered in the purge stage is 12.5%, being a lower fraction compared to the previous experiment, which had a value of 24%. This difference implies a lower amount of N_2 in the product stream, which was reflected in the increase of the overall purity up to 90%.

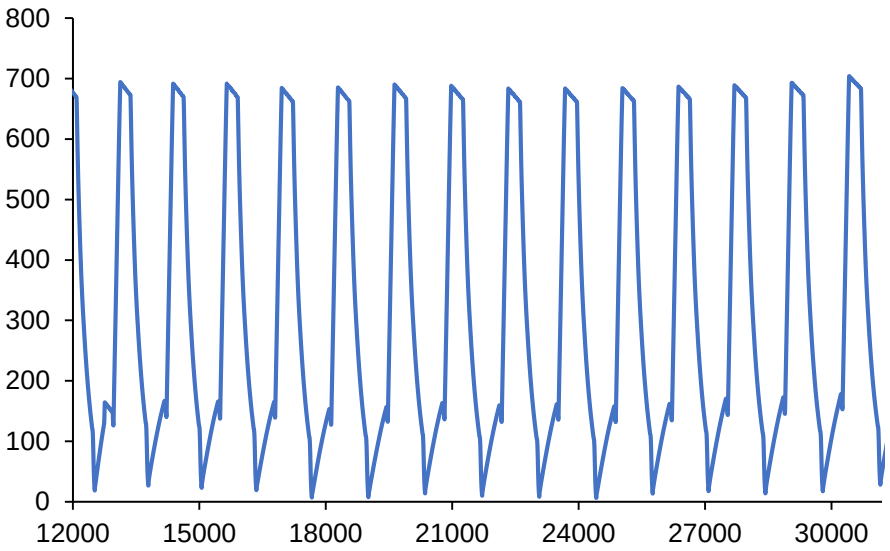

Figure 95: CO_2 molar balance of one column on the VPSA process controlled by a S_{FD} of 40%.

Overall, these results indicate that there is still room for the reduction of the energy consumption. Hence, a third test with a higher S_{FD} of 95% is set to decrease the rinse step time. If the column is saturated with CO_2 from the feed stage, a lower quantity of CO_2 recycled will be expected to achieve the stop point S_{RN}. The main source of electric consumption is the vacuum pump. As discussed in section 4.4.5, at the beginning of the regeneration step, 67% of the total CO_2 uptake was desorbed in 240 seconds, and to desorb 15% more the regeneration stage requires 650 seconds more. Therefore, a new control over the regeneration step was designed based on the regeneration flow. The stop point is the minimum flowrate at expulsion (Q_{EX}) on the vacuum pump, while the vacuum pump operates at its maximum vacuum capacity of P_V= -0.95 barg. The rest of the conditions are kept on the same values than the previous experiments.

4.5.3. VPSA process parameters controlled by a S_{FD} of 95%.

The operating VPSA processes conditions of the experiment controlled with a 95% of S_{FD} are reported in Table 46.

Table 46: VPSA process parameters for CO_2 separation controlled by a S_{FD} of 95%.

Process Parameter	Value	Unit
P_T	2.00	Barg
P_V	-0.95	Barg
Q_F	15.00	L/min
Q_R	5.00	L/min
Q_P	15.00	L/min
Q_{EX}	0.5	L/min
S_{RN}	120.00	%
S_{FD}	95.00	%
S_{PR}	80.00	%

The impact on process performance with the changes made on the process conditions is analyzed in Figure 96. Figure 96 (A) it is shown how the feed step lasts longer compared to the previous cyclic experiments, which is expected from the extension of the value of the S_{FD} parameter used in this experiment. However, the vacuum pressure reaches a maximum value of -0.82 barg, slightly higher than in the previous experiments (-0.84 barg). This change on the vacuum pressure is caused by the Q_{EX} stop point. Finally, the temperature profile is plotted in Figure 96 (B). Now, the height of the peaks of the first increment of both sensors reaches higher values than in previous experiments, moving from 20 to 28ºC in the bottom temperature sensor, and from 20 to 25ºC in the top temperature sensor. Nevertheless, in the second increment the bottom temperature sensor shows a lower value of 25.9ºC, while the top sensor shows a similar behavior, reaching 29ºC. These differences in the shape of the peaks suggest a higher amount of CO_2 adsorbed during the feed step than the one adsorbed on the rinse step.

The main effects of the scheduling of the different process steps with the changes made on the process parameters are shown in Figure 97. The scale of the graphs was reduced in order to distinguish the size of the rinse step. Compared to the previous experiments, the duration of the rinse step was reduced from 247 to 143 seconds, representing only 9% of the total cycle time. The feed step, with 36%, and the regeneration step, with 29%,

represent the steps with longer process times, while the stand-by time remains in a similar level as before (25%).

The results obtained on the process are listed in Table 47 First, it is important to note an increment on the CO_2 purity up to 93.44% of CO_2. This is almost 10% more than the process controlled with a S_{FD} of 40%. Nevertheless, the main improvement was found in the productivity with a value of 0.278 $g_{CO2}/(g_{ads} \cdot h)$ being even a better value than, not only the previous two experiments, but also the results achieved in section 4.4.5 of 0.230 $g_{CO2}/(g_{ads} \cdot h)$.

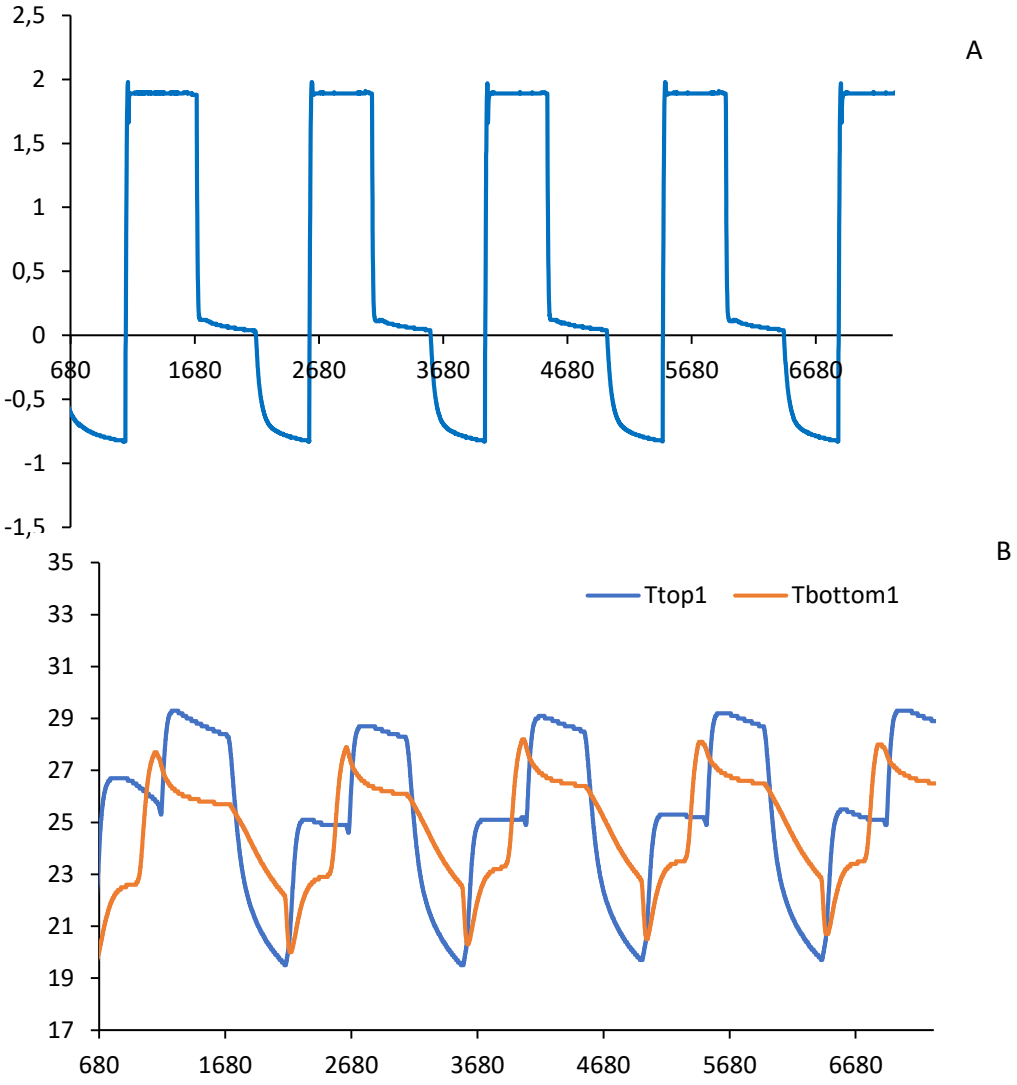

Figure 96: (A) CO_2 molar balance, (B) pressure and (C) temperature profiles of one column on the VPSA process controlled by a S_{FD} of 95%.

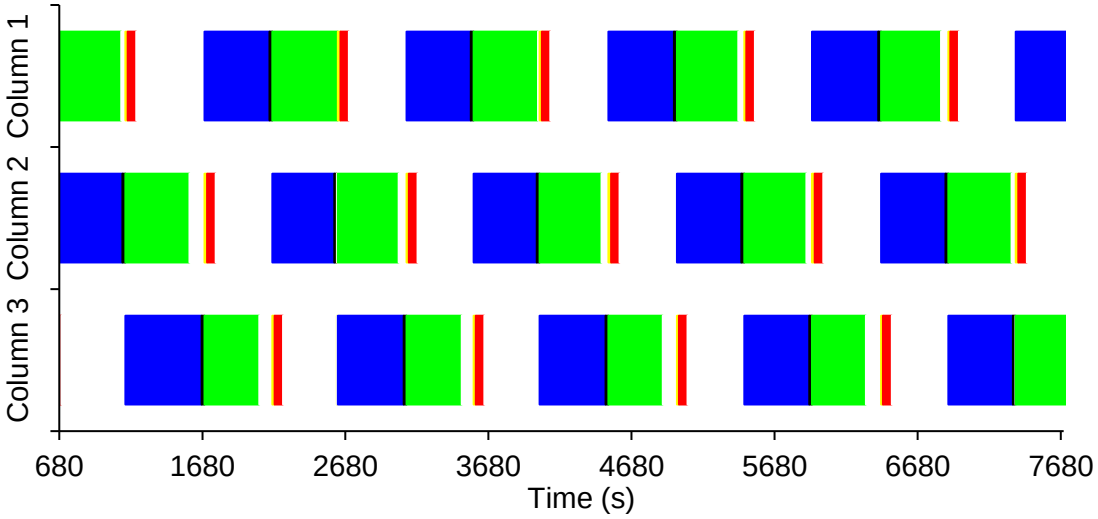

Figure 97: Cycle time for a three column VPSA process for CO_2 / N_2 separation controlled by a S_{FD} of 95%. Pressurization and feed (green), Depressurization (orange), Rinse (rinse), Equalization (yellow), Regeneration (Blue), Purge (black).

This higher productivity confirms the previous assumption that the higher value on the S_{FD} stop point allows to compute more CO_2 from the feed stage. This is also confirmed through the CO_2 uptake profile on one column, which is shown in Figure 98. It can be observed that 70% of CO_2 uptake was adsorbed during the feed stage, while the remaining 30% was absorbed during the rinse stage. Additionally, an important reduction on the power consumption up to 2.67 $kWh/(kg_{CO2})$ was obtained, due to the reduction on the operation of the vacuum pump, as a consequence of the higher amount of CO_2 recovered from the inlet mixture.

Table 47: Results of the VPSA process controlled by a S_{FD} of 95%.

Performance indicator	Value	Unit
Purity	93.4	%
Productivity	0.278	$g_{CO2}/(g_{ads} \cdot h)$
Power consumption	2.67	$kWh/(kg_{CO2})$
Yield	47.86.	$\%CO_2$
Stand-by time	27.3	%
Cycle time	1420	sec

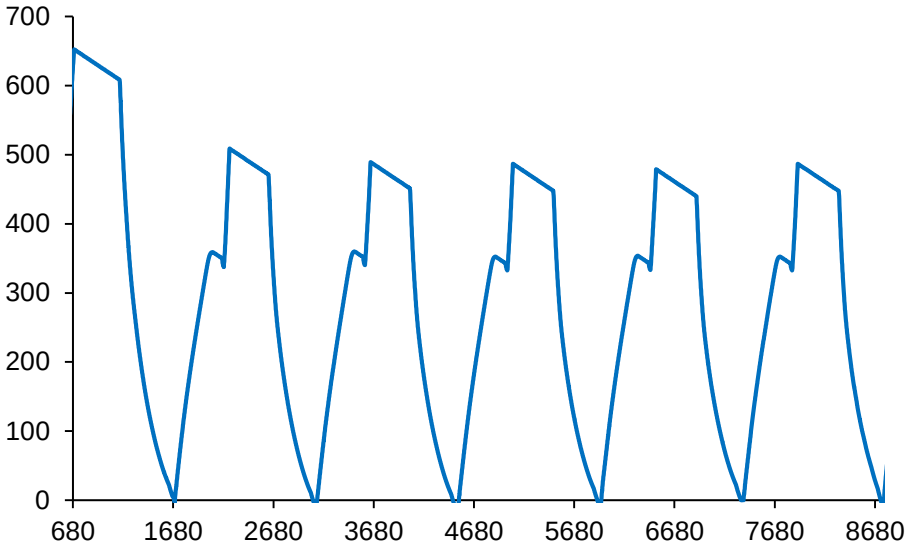

Figure 98: CO_2 molar balance of one column on the VPSA process controlled by a S_{FD} of 95%.

Therefore, the CO_2 recovery efficiency increases with an increasing S_{FD} stop point. This behavior suggests that the duration of the feed step might be a useful operating parameter for controlling product purity and recovery. As is detailed in this Table 47, with an increase in the S_{FD}, the experimental energy consumption decreased. The purity of the CO_2 obtained as a product was still low compared to the requirements for CO_2 storage (purity higher than 95%). One proposed solution to increase the purity of the CO_2 recovered is to optimize the rinse and purge stages.

4.6. Industrial VPSA experiments for CO_2 capture.

The results of the industrial plant set-up for CO_2 capture and the in-site utilization are divided in three stages: Flue gase pre-treatment, CO_2 capture and storage and CO_2 utilization application.

4.6.1. Flue gases pretreatment.

Previous to the VPSA process, a pre-treatment stage is requiered to cool down the flue gases and to remove the impurities using the system designed on section 3.3.1. The pre-treatment set-up was installed in an industrial boiler chimney of 11000 kW that burns from 126 to 966 Nm^3/h of CH_4. An analysis of the flue gase composition was performed using a KIMO KIGAZ 310 analyser. The instrument has electrochemical sensors to measure the concentration of O_2, CO_2, CO, NO_x, CH_4 and SO_x. It also has sensors to measure the temperature and the dew temperature of the combustion gas. The results of the flue gas analysis are shown in Table 48.

Table 48: Results from flue gases of the chimney with KIMO KIGAZ 310 analyzer.

Parameter	Result
Temperature	65 – 75 °C
O_2	2.5 – 3.5 %
CO	ND
SO_X	ND
CO_2	10.4 – 12 %
NO_X	76 – 96 ppm
Dew Point	45ºC – 55ºC

Due to the previous CH_4 desulfuration stage, SO_x compounds were not found in the flue gas. However, a level of 96 ppm of NO_X was detected, produced by the oxidation of CH_4 with excess air (Xu et al., 2005). This can negatively impact on the CO_2 separation processes, as NO can be oxidized to NO_2, N_2O_3, N_2O_5 and eventually react with the adsorbent (Zhang et al., 2009).Therefore, the pre-treatment was designed to cool down the flue gas stream and to eliminate the NO_X impurities without decreasing the concentration of CO_2.

The major NO_X components generated by fuel combustion are NO and NO_2, although equilibrium small amounts of N_2O_4 and N_2O_3 exist. The quite complex mechanism of absorption of these nitrogen oxides into water results in the formation of nitric and nitrous acids, through the following reactions occurring in the gas phase (Liémans et al., 2011).

$$2\,NO_{(g)} + O_{2(g)} \rightarrow 2\,NO_{2(g)} \quad (38)$$

$$2\,NO_{2(g)} \rightleftarrows N_2O_{4(g)} \quad (39)$$

$$NO_{(g)} + NO_{2(g)} \rightleftarrows N_2O_{3(g)} \quad (40)$$

$$NO_{(g)} + NO_{2(g)} + H_2O_{(g)} \rightleftarrows 2HNO_{2(g)} \quad (41)$$

The adiabatic cooling unit E-401 (see Figure 31) cools down the flue gas from 70ºC to 30ºC using water sprays. Small liquid droplets cool the exhaust stream more quickly than large droplets because they evaporate more easily. Therefore, less liquid is required. The E-401 unit also removes a fraction of the NO_x. The process for NO_X absorption into water involves several multiple reversible reactions in both the gas and the liquid phase. The gases NO_2, N_2O_4 and N_2O_3 are absorbed in the aqueous phase and react with water as follows:

$$NO_{2(g)} \rightarrow NO_{2(l)} \quad (42)$$

$$N_2O_{4(g)} \rightarrow N_2O_{4(l)} \quad (43)$$

$$N_2O_{3(g)} \rightarrow N_2O_{3(l)} \quad (44)$$

$$2NO_{2(l)} + H_2O_{(l)} \rightleftarrows HNO_{3(l)} + HNO_{2(l)} \quad (45)$$

$$N_2O_{4(l)} + H_2O_{(l)} \rightleftarrows HNO_{3(l)} + HNO_{2(l)} \quad (46)$$

$$N_2O_{3(l)} + H_2O_{(l)} \rightleftarrows 2HNO_{2(l)} \quad (47)$$

It is usually assumed that the equilibrium between NO_2 and N_2O_4, (equation (39) is instantaneously established. The reactions (45) and (46) are competing and it is known that reaction (45) makes a major contribution to the absorption of tetravalent oxide (NO_2+N_2O_4) when their concentration is relatively large (higher than 1000 ppm). At low concentrations the major absorption occurs via reaction (45). Reactions (45) and (46) can also occur in the gas phase. Nitrous acid produced by reactions (45) to (47) decomposes in the liquid phase according to the following equations: (Joshi et al., 1985)

$$3HNO_{2(l)} \rightleftarrows HNO_{3(l)} + 2NO_{(l)} + H_2O_{(l)} \quad (48)$$

$$2HNO_{2(l)} \rightleftarrows NO_{(l)} + H_2O_{(l)} + NO_{2(l)} \quad (49)$$

The absorption of NO_X gas into water results into two oxyacids namely nitric acid and nitrous acid. Several equilibria exist between NO_X and oxyacids, both in the gas and liquid phases. Absorption and desorption operations occur simultaneously. Further, the absorption is accompanied by a chemical reaction and the desorption is also preceded by a chemical reaction. E-401 has an efficient defogger, which solve the problem of water removal from the absorbent solution by the gas. In addition, the liquid absorption solution can be recycled or reutilized.

The low solubility of NO that accounts for more than 90% of all NO_X and NO_2 in water compared with other waste gases, such as CO_2, SO_2 and NH_3 is a problem because low solubility results in a high mass transfer resistance of water (Joshi et al., 1985). Therefore, a gas absorption system using alkaline solution or oxidants is usually adopted to decrease NO_X concentration in waste gases. However, using alkaline solutions such as NaOH can react with CO_2 to form Na_2CO_3, removing this substance from the flue gas stream and leading into high operations cost and a high level of residual coproducts. Liquid oxidants are used as absorbents, such as HNO_3, sodium chlorite, hydrogen peroxide and potassium permanganate ($KMnO_4$).

For the complete NO_x removal, a chemical absorption with $KMnO_4$ was employed on the unit E-406 (see Figure 31). Alphasorb 8 adsorbent is a spherical alumina impregned in $KMnO_4$. This is a commercial and common solution to remove a large spectrum of pollutants. The reactions utilized for the NO_x removal were the following:

$$KMnO_4 + NO \rightarrow KNO_3 + MnO_2 \quad (50)$$

$$5NO_2 + KMnO_4 + H_2O \rightarrow 2HNO_3 + Mn(NO_3)_2 + KNO_3 \quad (51)$$

The E-405 (see Figure 31) unit avoids that the saturated flue gas JOSHI the impregnated $KMnO_4$ from the alumina by taking advantage of the excess of water present in the flue gases. Thus, E-405 works as an adsorption dryer to remove water vapor from the gas by passing it through an adsorbent desiccant material based on the principle that moisture always migrates to the driest possible medium. Upon entering in contact with the adsorbent material, the water vapor is transferred from the gas to the dry desiccant. The flue gas flows through a vessel containing the desiccant and stays into intensive contact with the desiccant.

On the other hand, the unit E-406 (see Figure 31) protects the compressor unit E-403 from particles between 3.0 to 10 μm in size. Once the flue gas was denitrified and filtered, the gas is compressed until 8 bars in the unit E-403. The E-407 unit separates the water

condensed from the compression work by a centrifugal effect. Table 49 shows the average results of the monitorization on different points of the pre-treatment stage during two weeks of operation.

Table 49: Pre-treatment results from flue gases with KIMO KIGAZ 310 analyser.

Parameter	Chimney	Before E-401	After E-401	After E-405	After E-406	E-404
Gases temperature (ºC)	70.7	69.4	30.2	26.2	26.4	25.3
O_2 (%)	5.4	5.1	5.1	5.1	5.2	5.2
NO (%)	74.0	74.0	54.0	49.0	0.0	0.0
SO_2 (%)	0.0	0.0	0.0	0.0	0.0	0.0
CO_2 (%)	11.1	11.0	11.1	11.2	11.2	11.0
NO_X (ppmv)	77.0	77.0	55.0	51.0	0.0	0.0
Relative humidity (%)	36.9	42.5	100	28.93	26.5	37.7

As it can be seen on Table 49, NO_x were totally removed without affecting the CO_2 content. The removal efficiency in E-401 was 29% of the NO_x inlet concentration, removing mainly the gases NO_2, N_2O_4 and N_2O_3. E-405 removed 6.5% and the E-406 completely removed the remaining NO_X from the flue gases. As it can be seen the O_2 present because of the excess of air during the combustion was not removed. This gas is separated in later stages.

4.6.2. CO_2 capture and storage pilot plant

The CO_2 removal capability can be dramatically affected by the presence of water in the flue gases by the formation of carbonates or bicarbonates on zeolites. A relative humidity (RH) below 0.5 % is needed to avoid affecting the CO_2 removal capability (Wang and LeVan, 2010). The drying unit E-505 of the VPSA pilot plant (see Figure 35) operates by a reversible adsorption process with molecular alumina as desiccant. The desiccant removes moisture from the compressed flue gases and stores it in its internal structure. The dryer can additionally capture small amounts of SO_x and NO_x present in the flue gas, which are easily adsorbed on and difficult to desorb from zeolites (Ishibashi et al., 1996). With continuous moisture loading of the desiccant, the dryer performance is reduced until the desiccant is saturated with moisture. Therefore, when an adsorption column was used for drying the compressed flue gas, the other column performed the regeneration phase. The continuous operation of the drying unit E-505 was achieved with two

adsorption columns that are operated alternately in a three-process cycle described follows:

1. The moist compressed flue gas is supplied via a prefilter to the drying unit E-505. The main valve (V-441/V-552) forwards the compressed flue gas to the vessel which is in adsorption mode (e.g. CS-01 see Figure 99). In the lower part of the vessel the compressed flue gas is decelerated and distributed over the vessel cross-section and slowly flows through the desiccant bed. The compressed flue gas exits the vessel via the exit valves (V-444/V-554), and the dew point sensor (I-502 see Figure 35) checks the dryer performance at the compressed air outlet. During this time the second vessel (e.g. CS-02 see Figure 99) is in regeneration mode and waits for operation.
2. The switch-over of the vessel is carried out by turning the main valve (V-441/V-552) form vessel (CS-01 see Figure 99) from vessel (CS-02). The compressed flue gas flow changes from one vessel to the other. A free flow path through the dryer is available at any time during switchover. As a result, the task of drying is passed on to the other vessel without interruption.

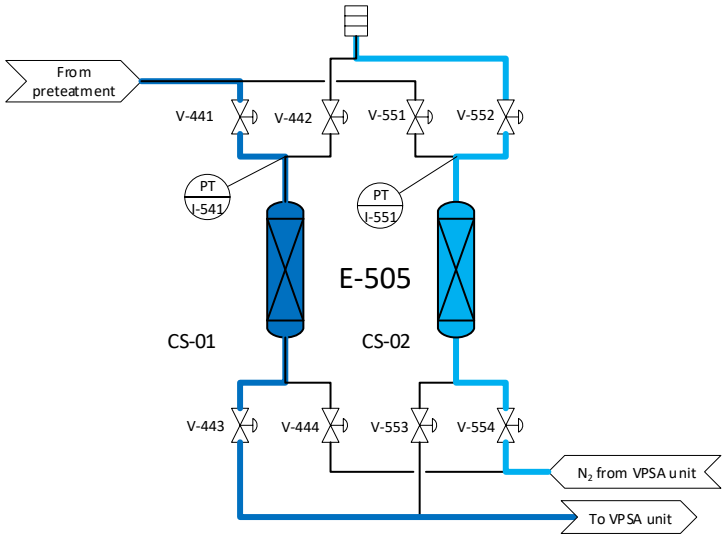

Figure 99: Dryer adsorption phase.

3. After the wet vessel (e.g. CS-01 see Figure 99) has completed the adsorption phase and passed on the tank to the second vessel (e.g. CS-02 see Figure 99), the first vessel (offline vessel) runs the regeneration phase. After the vessel switch-over the expansion valve (V442/V552) is opened and the wet vessel is depressurised. The compressed air flows to the outside via the silencer. After the vessel pressure has almost reached atmospheric pressure, dry N_2 from the VPSA unit (regeneration gas) flows into the column (e.g. CS-01 see Figure 99) to

regenerate the desiccant. The dry and pressure-less regeneration gas is distributed throughout the vessel cross-section and passed through the desiccant. The dry regeneration N_2 vaporises the water stored in the desiccant. In the form of steam, the water together with the regeneration N_2 flow, is then sent via valve (V-442/V-552) to the regeneration outlet.

4. After the regeneration phase has expired, the pressurization phase begins. The pressurisation phase ensures that the two drying columns have the same pressure prior to the column switch-over. The regeneration N_2 valve (V-442/V-552) was closed and dry compressed N_2 continues to flow into vessel (e.g. C-01 see Figure 99) gradually equalising the pressure in both vessels. The next phase begins when the vessel pressure is almost the same in both vessels.

Figure 104 shows the experimental CO_2 concentration and humidity (RH) monitoring results on one cycle of a dryer column. The dry flue gas CO_2 concentration oscillates between 10.3 to 10.8%, while the RH moves from 0.24 to 0.70% with an average value of 0.37%. On one side, a competitive physical adsorption is produced between H_2O and the CO_2. On the other side, the RH increases over the time taking 333 minutes to achieve a value above 0.5%. In any case, the time of the cycle is fixed in 3 hours to ensure a RH lower than 0.3% to ensure the adequate operation of the equipment.

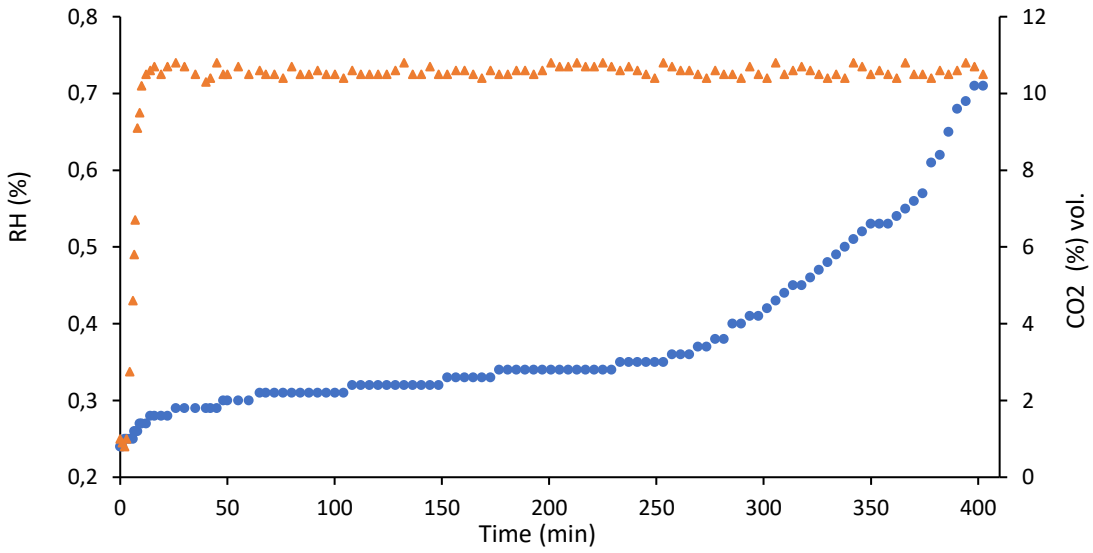

Figure 100: Characterization of the outlet dry flue gas of the adsorption dryer E-505 with a constant flowrate of 3000 L/min at 2 barg. (Δ) CO_2 concentration, (●) % RH.

Once the flue gas is dried to a RH below 0.5%, it enters the CO_2 VPSA separation unit. Based on the results achieved in section 4.5 the design conditions to carry out a CO_2 separation with zeolite 13XBL were set to scale the process up. In the stream process, the length of unused bed (LUB) method was applied for the scaling-up. The variables were scaled from the process controlled with a S_{FD} of 95% from the section 4.5, the process conditions for the CO_2 separation with zeolite 13XBL was selected for the industrial set-up.The variables are scaled from the process controlled with a S_{FD} of 95% from the section 4.5 obtained with cyclic laboratory equipment. The parameters P_T, P_V, S_{RN}, S_{FD} and S_{PR} are directly applicable since these do not dependent on the equipment scale. The flowrates Q_F, Q_R, Q_P and Q_{EX} were scaled respecting the same superficial velocity through the pilot experiments.

The LUB can therefore be measured at the design velocity in a small-scale laboratory column packed with the selected adsorbent. The design of the full-scale adsorption column was obtained by simply adding the LUB to the length of bed needed to achieve the required stoichiometric capacity (LES). The Table 50 shows the process parameters applied to the industrial cyclic experiment.

Table 50: Conditions for the VPSA industrial plant for CO_2 separation.

Process Parameter	Value	Unit
P_T	2.00	Barg
P_V	-0.95	Barg
Q_F	2000	L/min
Q_R	600	L/min
Q_P	2000	L/min
Q_{EX}	60	L/min
S_{RN}	120.00	%
S_{FD}	95.00	%
S_{PR}	80.00	%

The denitrified flue gas passes through the dehumidifier with a relative humidity less than 0.5% as needes for the carbon capture unit. The concentration of CO_2 in the dry flue gas is 9.5-11.0%, while the temperature of the dry flue gas is about 18ºC. Figure 101 shows the pressure evolution profiles during the three-bed eight-step VPSA operation for CO_2 capture from flue gas. The industrial set-up was designed to obtain a robust commercial product by reducing the costs and the complexity of the operational and production

processes. The pressure control system was designed just with one regulator valve in a PID control system, simplifying the laboratory set-up, which had two control valves in a PID cascade control configuration. From the figure, it is possible to observe that the pressure control on the feed step presents some variations from the pressure set-point, mainly caused by the sensitivity of 0.1 bar of the pneumatic regulation valve used. Although it presents a lower precision compared to the lab control configuration (caused by the dispersion of the values), the pressure values are spread over the set-point in a narrow range, becoming acceptable for operational purposes.

Figure 101 shows the scheduling of the three columns on the industrial process. In general, the synchronization of the step process times was similar to the one obtained in the laboratory and plotted on Figure 97. The main contribution on the cycle times are the feed and regeneration steps forming 31% and 33% of the total respectively. On the other hand, the regeneration step represents only a 4% of the cycle time but, unlike the previous results, the pressure after the rinse was kept at 0.5 barg (see Figure 101). Therefore, the equalization step was executed occupying an 9% of the cycle time. The pressure equalization steps were performed from a pressure of 0.5 barg on the equalization provided pressures to a 0.15 barg of on the equalization received pressure.

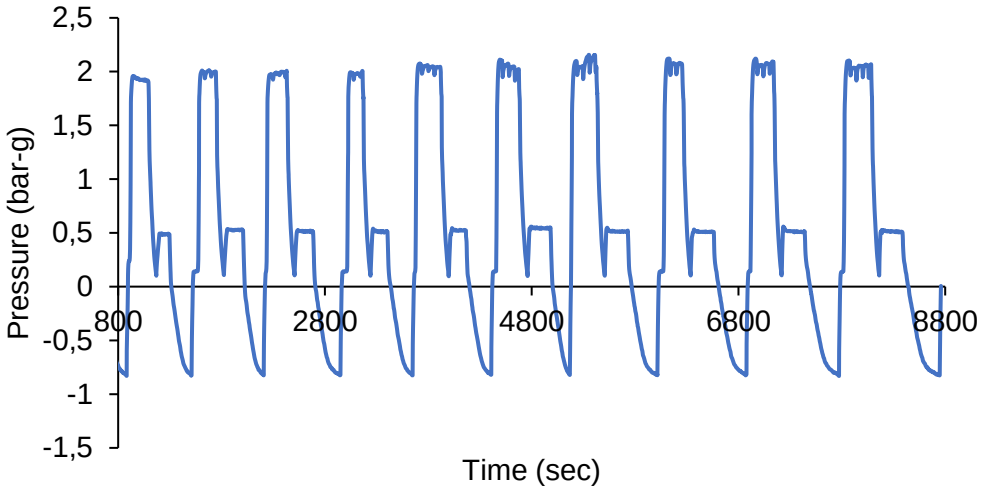

Figure 101: Pressure profiles measured for the industrial three-bed eight step VPSA process.

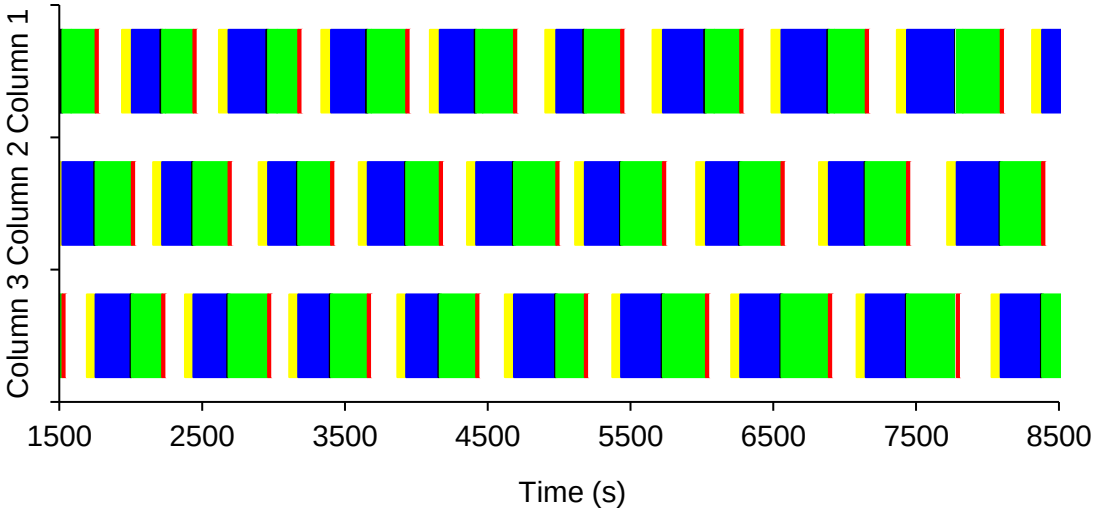

Figure 102: Cycle time for the industrial VPSA process for CO_2/N_2 separation controlled. Pressurization and feed (green), Depressurization (orange), Rinse (rinse), Equalization (yellow), Regeneration (Blue), Purge (black).

The experiment was performed continuously during 7 h, executing 28 cycles. The Figure **103** shows the purity profile of the CO_2 captured from flue gas by the three-bed eight-step VPSA process. As showed in the graph, the purity varies from 84.9% to 94.7 % of CO_2 v/v with an average of 88.9%. It can be observed that the purity gradually increases until it apparently stabilizes around 90% after 13 cycles.

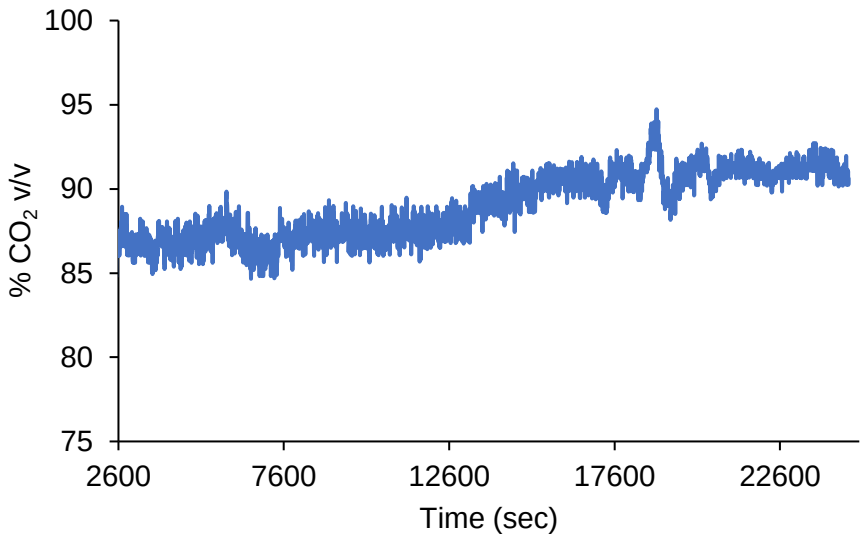

Figure 103: CO_2 product purity obtained the VPSA industrial plant.

The experimental results are summarized in Table 51 for the CO_2 capture unit packed with 13XBL. With a controlled flow rate of 2000 L/min, 48.06 to 56.12 % of CO_2 can be recovered from the real flue gas with 84-95% purity in product gas. The power consumption of the pre-treatment measured on site was 1.154 kWh/(kg_{CO2}), and the

power consumption for the CO_2 industrial separation unit was 0.326 kWh/(kg_{CO2}). The energy consumption on the industrial process was higher than the results obtained in the laboratory (section 4.5). This is because the power consumption measured in the lab did not include the power for the CO_2 compression, the energy to increase the pressure on the feed gas related to the purge, and the energy to increase the CO_2 product for the rinse steps. Also, the pressure and heat losses throughout the setup contribute significantly to the energy and should be included for the real power consumption.

Table 51: Results of the industrial VPSA process.

Performance indicator	Value	Unit
Purity	85- 95	%
Productivity	0.21 - 0.25	$g_{CO2}/(g_{ads} \cdot h)$
Power consumption	1.48	kWh/(kg_{CO2})
Yield	48 - 56.	$\%CO_2$
Stand-by time	21	%
Cycle time	973	sec
CO_2 product capacity	9 - 10	m^3/h
Energy cost	0.1	€/kWh
CO_2 recuperation cost	0.29	€/Nm^3_{CO2}

The pressure drop of the flow from the outlet of the compressor E-403 (see Figure 31 on page 58) to the feed entrance of the drying unit E-505 (see Figure 35 on page 61) was about 0.2 bar, and the pressure drop from the drying unit to the feed end of the column was 0.3 bar. This second pressure drop was significantly affected by the outlet pressure, being even slightly higher than that for the vacuum pump E-501 (see Figure 35).

These results indicate that there is more room for the reduction of the energy consumption by the compressing stage than the vacuum pump. To further reduce the power consumption, the quite large pressure drop should be avoided. Therefore, the separation performance for CO_2 capture from flue gas by adsorption technology does not simply depend on the CO_2 adsorption capacity of adsorbent, and other properties such as adsorption/desorption kinetics and fluid dynamics should be considered simultaneously.

On the other hand, The performance parameters of the VPSA process for capturing CO_2 using zeolite 13XBL, such as CO_2 purity, CO_2 recovery, and specific power consumption, were compared with those of other adsorption processes for CO_2 capture reported previously in the literature, as summarized in Table 1 and Table 28. It can be observed

that most of the studies used the zeolites 13X or 5A as the adsorbent, which have the highest CO_2 capacities and selectivity among the commercial adsorbents. The energy consumption varied from 0.5 to 1.3 kWh/kg_{CO2} because of the different processes employed and different amounts of flue gas processed. However, in all cases, yields, purities, energy consumption and productivity are published using a desulfurized and dehumidified combustion gas. In addition, the data published on most occasions has been obtained from numerical simulations or experimental prototypes on a laboratory scale. Only a minimum number of articles (3) present data from real installations at pilot scale, but processing previously treated combustion gases, by unspecified methods. Another major obstacle presented in the bibliographic comparison was that all publications are focused on petroleum or coal combustion fuels with a higher concentration of carbon dioxide of 12 to 16%, while for the installation of gas capture the combustion used in this thesis is natural gas and the CO_2 concentration is always lower than 11%. As is well known, the concentration of CO_2 in the gases entering the capture system is very critical when the concentration is low.

Therefore, the specific power consumption required in this study is not comparable to other reports, but it can be observed that the capture power consumption for the VPSA process was lower than that of the amine scrubbing process of 1.76 kWh/(kg_{CO2}) (Ho et al., 2008). Moreover, compared with the VPSA system, the amine scrubbing process usually needs large areas for its installation, which makes it difficult to use existing power plants. As an example, a 500 MW coal-fired power station of 670 Nm^3/s flue gas flow rate (Ho et al., 2008) where the amine scrubbing is used, is a process with two columns of 35 m length and 12 m diameter (total volume of 7913 m^3) plus two regenerators and heat exchangers.

Productivity is one of the performance indicators with more relevance over the process, a process with high purity and high recovery is not necessarily the best option if the process cycle time is too long. Despite the lack of publications that consider this indicator and the fact that the results cannot be compared objectively, the present process shows very encouraging results of 0.21 to 0.25 $g_{CO2}/g_{Ads}\cdot h$, while the values of the publications range between 0.02 and 0.044 $g_{CO2}/g_{Ads}\cdot h$ with similar results in the yield, and the purity.

Consequently, it can be confirmed that the capture of CO_2 from a real industrial flue gas was demonstrated on a pilot plant scale processing 2000 L/min ($120m^3/h$) of flue gas represents an opportunity to apply this technology in an economically and environmentally sustainable way. The flue gas containing 9 to 11% of CO_2 was denitrified and dehumidified to a water content lower than 0.5% of relative humidity. Using an eight-

step VPSA, 48 to 56% CO_2 is recovered from the flue gas with 85 to 95% purity in product gas with a power consumption of 1.48 $kW \cdot h/(kg_{CO2})$, with a productivity of 1.18 $g_{CO2}/(g_{Ads} \cdot min)$.

4.6.1. CO_2 utilization application

The recovered CO_2 was used to replace the use of mineral acids in the pH regulation stage in an existent wastewater plant. Replacing mineral acid with CO_2 in alkaline water is an effective, reliable, self-buffering and economical method of controlling pH levels (Gaur et al., 2009; Gelb and Palley, 2014). CO_2 is a safer alternative than mineral acids and an effective chemical for lowering the pH of various kinds of alkaline waters. For several years, sulfuric acid was used in water treatment facilities to control alkalinity. However, this acid is hard to handle because of its poisonous nature, storage problem, secondary contaminant availability, and salt formation in water can affect the pump selection and increase the maintenance cost.

The system for the pH regulation described on Figure 38 was installed into the pipe of 8" which transports the waste water from the factory to the homogenization tank. Figure **104** shows the industrial wastewater plant set-up, where the wastewater of the plant was pumped to a homogenization tank through a battery of centrifugal pumps. The water flow was controlled depending on the wastewater production and the level of the homogenization tank. After the homogenization tank, the water is transported to a second tank where the pH is regulated with a mineral acid (H_2SO_4). Once the pH is regulated, a biological treatment is used to minimize the organic matter with an aerobic digestion. Finally, the mud (product of the aerobic digestion) is separated in a decanter from the clean water to return the treated water to a river.

The pH of the water is measured upstream before the pH regulation and after the CO_2 is injected in the wastewater. CO_2 gas is highly soluble in water. For pure water in equilibrium with a partial pressure of one atmosphere of CO_2, the solubility is about 1.5g/L at 25°C. Initially, dissolved CO_2 forms carbonic acid, which subsequently dissociates into bicarbonates, carbonates and hydrogen ions. The hydrogen ions in turn reduce the pH. (Norwater - Nordic Road Water, 2014). The following reactions are relevant for describing the process where CO_2 gas dissolves in water.

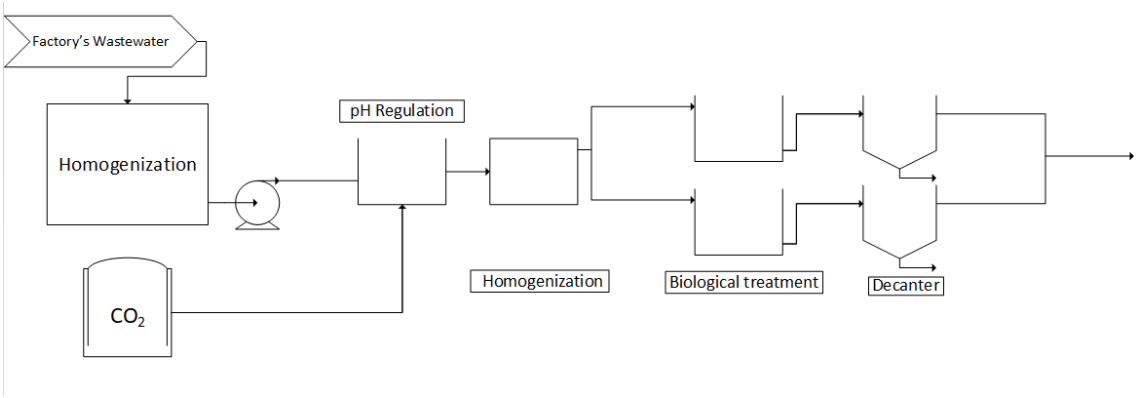

Figure 104: Flowsheet diagram of the wastewater treatment plant

$$CO_{2(g)} + H_2O \rightleftarrows H_2CO_3^* \quad (52)$$

$$H_2CO_3^* \rightleftarrows H^+ + HCO_3^- \quad (53)$$

$$HCO_3^- \rightleftarrows H^+ + CO_3^{2-} \quad (54)$$

$$H_2O \rightleftarrows H^+ + OH^- \quad (55)$$

With the configuration described in Figure 38, a volumetric gas flow from 6 to 12 Nm^3/h of CO_2 is injected to keep the pH of the wastewater between in the homogenization tank between 7.0 to 8.0. Gas-liquid mixing was carried out by two gas in line injectors, where the first is separated by 20 m from the second, and the second injector is 15 m prior to the homogenization tank. CO_2 is introduced into the high pH water by means of a diffuser, which is typically installed in the existing pressurized pipe. Small CO_2 bubbles are then released by the diffusers into the high pH water. Two pH probes are installed upstream on each gas injection point, thus measuring pH in the water before absorption and CO_2 reaction. The first pH meter (I-605 see Figure 38) measure the pH value and act over the first CO_2 injection point to regulate the pH value. The second inline pH meter (I-606) confirms the value after the first injection point and injects more CO_2 if the pH was out of the desirable range. On the other side the pH of the homogenization tank was continuously monitored with pH meter I-607. Figure 105 shows the pH profiles on CO_2 injection process for the pH stabilization. The red line represents the first injection point the with the initial pH on the wastewater, the blue line represents the pH of the adjusted wastewater after the first injection point and the gray line shows the pH on the homogenization tank.

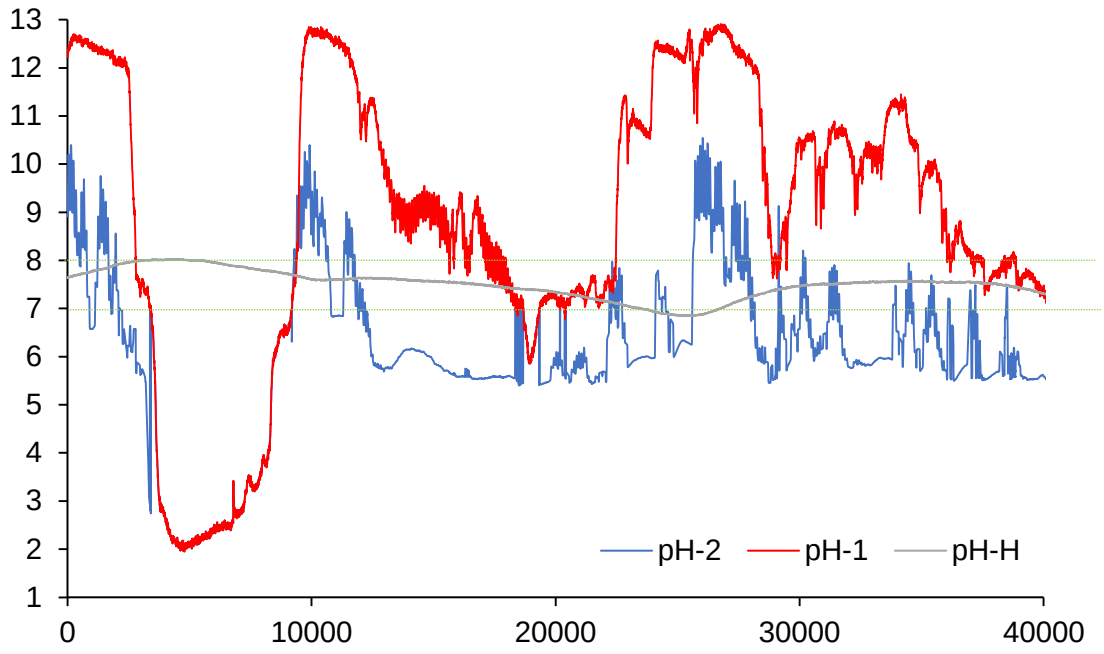

Figure 105: pH profiles on CO_2 injection for the pH stabilization. pH-1: first injection point; pH- 2: second injection point; pH-H: homogenization tank

Even though the wastewater is usually alkaline, it had a range of pH values from 2 to 12.8. This was caused by the cleaning agent used at that time on the process. The low pH was caused by the usage of HNO_3 and the high pH was caused by NaOH. Therefore, the control system must evaluate the difference on pH between the inlet and the mixed wastewater in the homogenization tank to regulate the CO_2 injected, and to avoid to wasting CO_2 in acid pH values. As is shown Figure 105 the grey line was in the desired regulation range (marked by green dotted lines).

CO_2 is a gas, which once dissolved into water produces as weak acid: carbonic acid. This substance reacts immediately with alkalis such as NaOH, Na_2CO_3 and $Ca(OH)_2$ turning them into neutral carbonates and bicarbonate salts. Carbonic acid is a mild acid present in water as ions H^+ and HCO_3, which are highly reactive. They will immediately react with ions responsible for alkalinity of water.

$$CO_{2(g)} + H_2O \rightleftarrows H_2CO_3 \quad (56)$$

$$H_2CO_3 + 2NaOH \rightarrow Na_2CO_3 + 2H_2O \quad (57)$$

$$H_2CO_3 + Na_2CO_3 \rightarrow 2Na_2HCO_3 \quad (58)$$

There is no secondary pollution introduced into the treated water by salts such as chlorides (from HCl) or sulphates (from (H_2SO_4). The introduction of CO_2 will contribute

to the chemical equilibrium of water by forming neutral carbonates and bicarbonates. Therefore, CO_2 is better than strong acids for controlling pH because it forms a mild but highly reactive acid which minimizes risks of overt acidification and rapidly responds to any variations of the incoming pH or water flowrate. Over or under treatment with mineral acids will often result in a pH, which rapidly deviates from the compliance range. Figure **106** shows the comparative curves of H_2SO_4 and CO_2 for the neutralization of an industrial effluent.

The past few years have seen prices spike for both HCl and H_2SO_4. Transportation is a significant part of the cost of mineral acids (on the order of 50% for HCl), and costs for diesel and other fuels are trending upward (this exerts greater pressure on distributor pricing). Beyond raw material costs are storage, safety and handling issues. The highly corrosive acids can take a toll on storage and processing equipment. Worker safety and maintenance procedures are constant concerns. Unexpected pipe or equipment failures can cause injuries and quickly drive up operating costs and worker compensation claims.

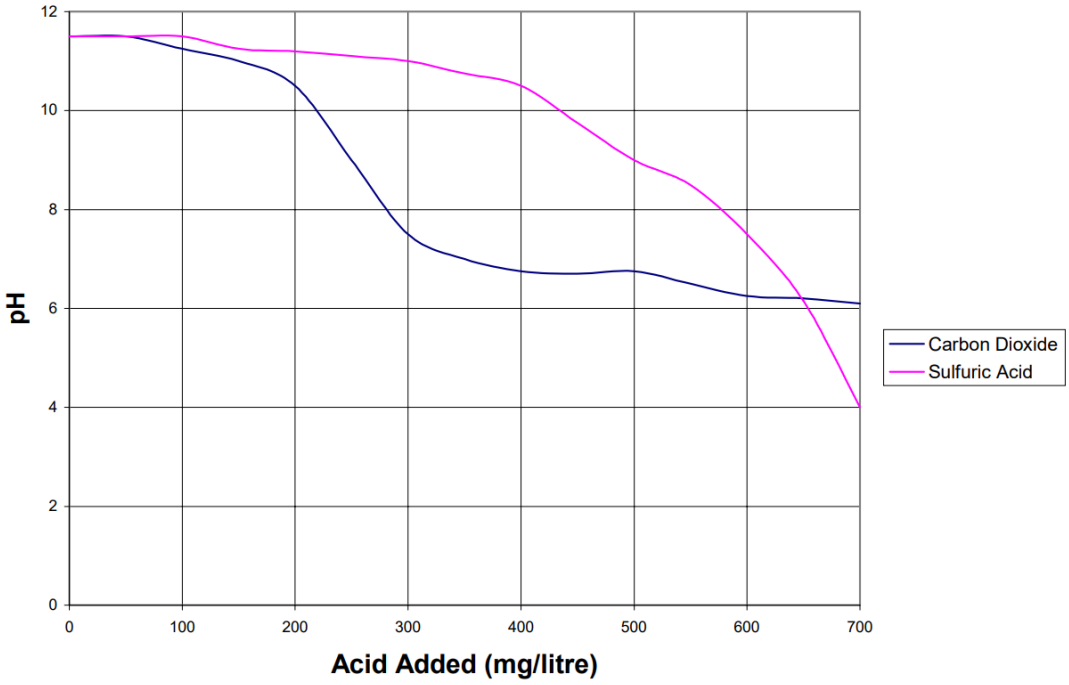

Figure 106: Comparative Neutralization Curves of an Industrial Effluent (Gregg, 2013).

Due to increasing raw material and environmental costs for mineral acids, CO_2 wastewater treatment systems are highly competitive. In many cases, capital and operating costs may in fact be lower for an equivalent system, especially when “soft costs” are considered. CO_2 neutralization does not produce acid-reaction by-products

that can foul or corrode equipment internals and create other downstream control concerns. The use of CO_2 captured in these emission sources has two clear advantages. On the one hand, it reduces the CO_2 emissions in the atmosphere, and it allows to use a compound that in many cases is a by-product of different reactions, or that can even be considered as a waste. In addition, as it is a non-toxic, non-flammable and abundant compound in nature, it is considered a "green" solvent, that is, environmentally benign, compared to other compounds that it replaces in numerous applications (as is the case).

Another potential to decrease the CO_2 cost and to increase the added value is related to the carbon credit market. Carbon pricing and the credits system provide incentives for businesses to invest in sustainable products and reduce their carbon footprint, thus benefiting them financially. The price of carbon credits depends on several factors, including its market and economic value, supply and demand, size and type of project and more. In this industry, costs fluctuate over small intervals and over continents. However, a trend towards higher values of the carbon credit is evident. One substantial change was the growth in the European Union Allowance price from €5/tCO_2 emitted to €13/tCO_2 emitted. Future regulations of the European Union ETS in the post-2020 period will also increase this values (Pfahler et al., 2018). On October 1, 2018, for example, one ton of carbon dioxide equivalent was worth $24.80.

5. Conclusions

The main outcomes of the work carried out during this thesis are summarized in the following bullets:

- A qualitative fast screening methodology using TGA and DSC analysis was developed to select adsorbents that could be applied in TSA for CO_2 capture in post combustion processes. The performed analysis unveiled the effect of the adsorption and desorption steps and the cyclic performance to show their potential on a continuous TSA process. The CO_2 adsorption capacity, adsorption heat and time to reach adsorption equilibrium for ten commercial adsorbents (3 CMSs and 7 zeolites) were determined using a mixture of 15% CO_2/ 85% N_2. The zeolites 13XBL and 5ABL showed the highest values of CO_2 adsorption capacity and heat of adsorption over the different studied materials. The productivity for CMSs was almost constant in every adsorption-desorption cycle, showing a complete and fast regeneration, even working at low temperatures. Two strategies for energy efficiency were formulated, the first one using low working temperatures in a range of 60ºC for adsorption and 150ºC for desorption, and the second one, at high process temperatures in a range of 90ºC to 350ºC.
  This fast screening methodology through TGA/DSC can be considered a useful tool on the screening stages of the research of different adsorbents for CO_2 capture, better than the classic physical adsorption measurements methodologies of analysis (gravimetric and volumetric adsorption measurements), which require longer analysis times and more resources. As many operating conditions were considered, the obtained results can serve as a basis to guide the cycle design adapted to given separation process targets, adsorbent design, adsorbent modification, or adsorbent optimization as a first rapid approach.

- A simulation of coupled fluid dynamics and heat exchange using Tdyn® to evaluate the potential of the combination of the indirect and direct heat TSA process for CO_2 capture. For this purpose, simulations were carried out at different operating conditions, and the performances were referred to the heat flow velocity. A critical factor in the regeneration of the TSA process is the energy required to heat up the adsorbent bed to the specified regeneration temperature. The best strategy is to heat the packed adsorbent directly with the hot gas stream, without using the heating fluid in a concentric tube heat exchanger. Nevertheless, the conduction heat exchanger strategy is limited by the poor heat flow capacity of the porous adsorbent beds and the gas. The simulation results of the heating

exchange on a TSA column suggest that this process had higher energy consumptions compared to the VPSA.

- A collection of adsorption equilibrium data of several available commercial adsorbents was measured by the gravimetric method. A set of adsorption isotherms for pure CO_2 and N_2 on CMS-I, CMS-II, 4ABL, 5ABL and 13XBL materials for pressures ranging from 0 to 10 bara and for temperatures ranging from 283 to 343 K was presented. The experimental data were described with the Thoth, Sips, and DSL isotherms. The most accurate predictions of the CO_2 loadings in the gas mixture−adsorbent system were attained with the extended DSL model. Adsorption equilibria of CO_2/N_2 mixtures were measured at 293 K, 313 K, 333 K and 363 K at 15/85 %v/v CO_2/N_2 gas phase composition and varying total pressure in a fixed-bed set-up. Experimental data from mixed-gas adsorption were compared to isotherms calculated with the DSL model. According to the results presented herein, the DSL model with the binary adsorption CO_2/N_2 predicted the gas-mixture behavior of this adsorbate−adsorbent system with acceptable accuracy. Zeolite 13XBL showed a better selectivity over the different pressure values having higher values at low pressures and low temperatures. The equilibrium data was used to model and simulate the competitive CO_2/N_2 adsorption and to correctly select an appropriate adsorbent.

- Design, construction and operation of three experimental laboratory units with a single adsorption column for performing VPSA experiments and the development of a Vacuum Swing Adsorption process to obtain enriched CO_2 product from a feed mixture of 15% CO_2/ 85% N_2 are built up. The control and automatization of all the designed units were developed using PLCs. Based on the experimental equilibrium and kinetic data collected for the 13XBL and 5ABL zeolite and the simulations carried out with Aspen adsorption simulator, an eight step VPSA process was designed to obtain high purity CO_2. An average purity of 87% with recovery of 62% and a productivity of 0.19 $g_{CO2}/(g_{Ads} \cdot min)$ was obtained with the 13XBL zeolite. For the 5ABL zeolite using the same VPSA cycle, a purity of 88%, a recovery of 59% with a productivity of 0.17 $g_{CO2}/(g_{Ads} \cdot min)$ was obtained. In general, purity over 95%, recoveries between 20 and 40% with productivity in the range of 0.75-1.2 mol/kg·h are easily obtained with both adsorbents using the VPSA unit.

- Based on the results obtained, cyclic experiments were performed in the three-column laboratory unit. A VPSA process including rinse and pressure equalization steps was studied for CO_2 capture from flue gas to obtain high CO_2 recovery and purity, also checking the power consumption. The CO_2 adsorbent selected was zeolite 13XBL. The composition of the feed flue gas entering the VPSA process was 15.0 vol % CO_2, 85.0 vol % N_2. Three VPSA runs were performed with a feed stop point of 95%. With a three-bed eight-step VPSA process, 93% CO_2 was obtained with a recovery of 48% from flue gas. The measured energy consumption was 2.7 $kW \cdot h/(kg_{CO2})$ with a productivity of 0.27 $g_{CO2}/(g_{Ads} \cdot min)$. The effects of adsorption duration and regeneration step pressures were studied.

- The capture of CO_2 from a real industrial flue gas was demonstrated on a pilot plant scale. In it, 2000 L/min of flue gas were denitrified and dehumidified. Then, the conditioned flue gas containing 9 to 11% of CO_2 with less than 0.5% relative humidity is treated in the VPSA three-columns CO_2 capture unit with zeolite 13XBL designed and developed in this work. 48 to 56% CO_2 is recovered from the flue gas with 85 to 95% purity in product gas. Using an eight-step VPSA, the measured power consumption was 1.48 $kW \cdot h/(kg_{CO2})$, with a productivity of 1.18 $g_{CO2}/(g_{Ads} \cdot min)$.

- The recovered CO_2 was used to replace the use of mineral acids in the pH regulation stage in an existent wastewater plant. The use of CO_2 captured in these emission sources has two clear advantages. On the one hand, it reduces the CO_2 emissions in the atmosphere. On the other hand, it allows to use a compound that in many cases is a by-product of different reactions, or that can even be considered as a waste.

6. Bibliography

Abu-zahra, M.R.M., Feron, P.H.M., Versteeg, G.F., 2007. CO 2 capture from power plants Part I . A parametric study of the technical performance based on monoethanolamine 1, 37–46. https://doi.org/10.1016/S1750-5836(06)00007-7

Ahmad, M.A., Wan Daud, W.M.A., Aroua, M.K., 2008. Adsorption kinetics of various gases in carbon molecular sieves (CMS) produced from palm shell. Colloids Surfaces A Physicochem. Eng. Asp. 312, 131–135. https://doi.org/10.1016/j.colsurfa.2007.06.040

Alper, E., Orhan, O.Y., 2017. CO 2 utilization : Developments in conversion processes. Petroleum 3, 109–126. https://doi.org/10.1016/j.petlm.2016.11.003

Alphonsus, E.R., Abdullah, M.O., 2016. A review on the applications of programmable logic controllers (PLCs). Renew. Sustain. Energy Rev. 60, 1185–1205. https://doi.org/10.1016/j.rser.2016.01.025

Andersen, A., Divekar, S., Dasgupta, S., Hafizovic, J., Blom, R., 2013. On the development of Vacuum Swing adsorption (VSA) technology for post-combustion CO 2 capture. Energy Procedia 37, 33–39. https://doi.org/10.1016/j.egypro.2013.05.082

APEC, 2012. Building Capacity for CO2 Capture and Storage in the APEC Region: A Training Manual for Policy Makers and Practioners 1–235.

Baracos, P., 1992. Reference guide to Grafcet Language.

Ben-Mansour, R., Habib, M.A., Bamidele, O.E., Basha, M., Qasem, N.A.A., Peedikakkal, A., Laoui, T., Ali, M., 2016. Carbon capture by physical adsorption: Materials, experimental investigations and numerical modeling and simulations - A review. Appl. Energy 161, 225–255. https://doi.org/10.1016/j.apenergy.2015.10.011

Bhadra, S.J., Ebner, A.D., Ritter, J.A., 2012. On the use of the dual process Langmuir model for predicting unary and binary isosteric heats of adsorption. Langmuir 28, 6935–6941. https://doi.org/10.1021/la301004e

Bird, R.B., Stewart, W.E., Lightfoot, E.N., 2007. Transport phenomena, Chemistry.

Bolton, W., 2009. Programmable Logic controiles, Fifth. ed. Elsevier.

Box, G., Stuart Hunter, J., Hunter, W.G., 2005. Statistics for Experimenters: Design, Innovation, and Discovery, AMC.

Box, G.E.P., Hunter, J.S., 2016. The 2k-p Fractional Factorial Designs Part I 1706. https://doi.org/10.1080/00401706.2000.10485977

Box, G.E.P., Hunter, J.S., 1961. The 2 k — p Fractional Factorial Designs. Technometrics 3, 311–351. https://doi.org/10.1080/00401706.1961.10489951

Broom, D., 2018. Characterizing adsorbents for gas separations. Chem. Eng. Prog. 114, 30–37.

Brunetti, A., Scura, F., Barbieri, G., Drioli, E., 2010. Membrane technologies for CO2separation. J. Memb. Sci. 359, 115–125. https://doi.org/10.1016/j.memsci.2009.11.040

Cavenati, S., Grande, C.A., Rodrigues, A.E., 2004. Adsorption Equilibrium of Methane, Carbon Dioxide, and Nitrogen on Zeolite 13X at High Pressures. J. Chem. Eng. Data 49, 1095–1101. https://doi.org/10.1021/je0498917

Cheung, O., Hedin, N., 2014. Zeolites and related sorbents with narrow pores for CO2 separation from flue gas. RSC Adv. 4, 14480–14494. https://doi.org/10.1039/c3ra48052f

Choi, S., Drese, J.H., Jones, C.W., 2009. Adsorbent materials for carbon dioxide capture from large anthropogenic point sources. ChemSusChem 2, 796–854. https://doi.org/10.1002/cssc.200900036

Clausse, M., Merel, J., Meunier, F., 2011. Numerical parametric study on CO2 capture by indirect thermal swing adsorption. Int. J. Greenh. Gas Control 5, 1206–1213. https://doi.org/10.1016/j.ijggc.2011.05.036

Cruz, P., Santos, J.C., Magalhães, F.D., Mendes, a., 2003. Cyclic adsorption separation processes: analysis strategy and optimization procedure. Chem. Eng. Sci. 58, 3143–3158. https://doi.org/10.1016/S0009-2509(03)00189-1

Dąbrowski, A., 2001. Adsorption - From theory to practice. Adv. Colloid Interface Sci. 93, 135–224. https://doi.org/10.1016/S0001-8686(00)00082-8

Dai, H.C., Zhang, H. Bin, Wang, W.T., 2017. The impacts of U.S. withdrawal from the Paris Agreement on the carbon emission space and mitigation cost of China, EU, and Japan under the constraints of the global carbon emission space. Adv. Clim. Chang. Res. 8, 226–234. https://doi.org/10.1016/j.accre.2017.09.003

Do, D.D., 1998. Adsorption Analysis: Equilibria and Kinetics. https://doi.org/10.1142/p111

Dreisbach, F., Staudt, R., Keller, J.U., 1999. High Pressure Adsorption Data of Methane , Nitrogen , Carbon Dioxide and their Binary and Ternary Mixtures on Activated Carbon 227, 215–227.

Du, W., Abdulghani, K., Alkebsi, M., 2017. Model Predictive Control and Optimization of Vacuum Pressure Swing Adsorption for Carbon Dioxide Capture.

Erlach, B., Schmidt, M., Tsatsaronis, G., 2011. Comparison of carbon capture IGCC with pre-combustion decarbonisation and with chemical-looping combustion. Energy 36, 3804–3815. https://doi.org/10.1016/j.energy.2010.08.038

European Climate Foundation, 2010. Roadmap 2050 1–100. https://doi.org/10.2833/10759

European Commision, 2018. A Clean Planet for all A European strategic long-term vision for a prosperous, modern, competitive and climate neutral economy. Brussels.

European Union – Mission Innovation [WWW Document], n.d. URL http://mission-innovation.net/participating-countries/european-union/ (accessed 10.9.18).

Feron, P.H.M., 2010. Exploring the potential for improvement of the energy performance of coal fired power plants with post-combustion capture of carbon dioxide. Int. J. Greenh. Gas Control 4, 152–160. https://doi.org/10.1016/j.ijggc.2009.10.018

Fortunato, E., Heuer, R.-D., 2018. Novel carbon capture and utilisation technologies. https://doi.org/10.2777/01532

Fujiki, J., Chowdhury, F.A., Yamada, H., Yogo, K., 2017. Highly efficient post-combustion CO2 capture by low-temperature steam-aided vacuum swing adsorption using a novel polyamine-based solid sorbent. Chem. Eng. J. 307, 273–282. https://doi.org/10.1016/j.cej.2016.08.071

García, J.C., Alonso, R., Casero, P., Cortés, V., 2014. Captura de CO 2 : tecnologías para una captación a gran escala. Plataforma Tecnológica Española CO2 1, 152.

Garcia, S., Rubiera, F., Pevida, C., 2013. Predicting mixed-gas adsorption equilibria on activated carbon for pre-combustion CO2 capture. Langmuir 1–7. https://doi.org/10.1021/la4004998

Gaur, A., Park, J.W., Jang, J.H., Maken, S., Lee, J., Song, H.J., 2009. Characteristics of alkaline wastewater neutralization for CO2 capture from Landfill Gas (LFG). Energy and Fuels 23, 5467–5473. https://doi.org/10.1021/ef900615h

Gelb, J., Palley, M.L., 2014. Using CO2-gas to lower the pH of tunnelling waste water XIII, 182.

Gleichmann, K., Unger, B., Brandt, A., 2016. Industrial Zeolite Molecular Sieves. InTech. https://doi.org/110.5772/intechopen.68549

Gregg, S., 2013. Abandoning Mineral Acid Attractive wastewater treatment alternatives. Ind. water wastes Dig. 18–19.

Hamon, L., Chenoy, L., De Weireld, G., 2014. Determination of absolute gas adsorption isotherms: Simple method based on the potential theory for buoyancy effect correction of pure gas and gas mixtures adsorption. Adsorption 20, 397–408. https://doi.org/10.1007/s10450-013-9579-3

Hedin, N., Andersson, L., Bergström, L., Yan, J., 2013. Adsorbents for the post-combustion capture of CO2 using rapid temperature swing or vacuum swing adsorption. Appl. Energy 104, 418–433. https://doi.org/10.1016/j.apenergy.2012.11.034

Ho, M.T., Allinson, G.W., Wiley, D.E., 2008. Reducing the Cost of CO_2 Capture from Flue Gases Using Pressure Swing Adsorption. Ind. Eng. Chem. Res. 47, 4883–4890. https://doi.org/10.1021/ie070831e

Ho, S.H., Chen, C.Y., Lee, D.J., Chang, J.S., 2011. Perspectives on microalgal CO2-emission mitigation systems - A review. Biotechnol. Adv. 29, 189–198. https://doi.org/10.1016/j.biotechadv.2010.11.001

IPCC, 2014. Climate Change 2014: Synthesis Report. Contribution of Working Groups I, II and III to the Fifth Assessment Report of the Intergovernmental Panel on Climate Change, Core Writing Team, R.K. Pachauri and L.A. Meyer. https://doi.org/10.1017/CBO9781107415324.004

Ishibashi, M., Ota, H., Akutsu, N., Umeda, S., Tajika, M., J., I., Yasutake, A., Kabata, T., 1996. Technology for removing carbon dioxide from power plant flue gas by the physical adsorption method. Energy Convers. Manag. 37, 929–933.

Jarvis, S.M., Samsatli, S., 2018. Technologies and infrastructures underpinning future CO 2 value chains : A comprehensive review and comparative analysis. Renew. Sustain. Energy Rev. 85, 46–68. https://doi.org/10.1016/j.rser.2018.01.007

Joshi, J.B., Mahajani, V.V., Juvekar, V.A., 1985. Invited Review Absorption of Nox Gases, Chemical Engineering Communications. https://doi.org/10.1080/00986448508911161

Joss, L., Gazzani, M., Mazzotti, M., 2017. Rational design of temperature swing adsorption cycles for post-combustion CO2 capture. Chem. Eng. Sci. 158, 381–394. https://doi.org/10.1016/j.ces.2016.10.013

Jüntgen, H., Knoblauch, K., Harder, K., 1981. Carbon molecular sieves: production from coal and application in gas separation. Fuel 60, 817–822. https://doi.org/10.1016/0016-2361(81)90144-7

Kacem, M., Pellerano, M., Delebarre, A., 2015. Pressure swing adsorption for CO 2 / N 2 and CO 2 / CH 4 separation : Comparison between activated carbons and zeolites performances. Fuel Process. Technol. 138, 271–283. https://doi.org/10.1016/j.fuproc.2015.04.032

Kang, D., Lee, M., Lim, H.S., Lee, J.W., 2018. Chemical looping partial oxidation of methane with CO2utilization on the ceria-enhanced mesoporous Fe2O3oxygen carrier. Fuel 215, 787–798. https://doi.org/10.1016/j.fuel.2017.11.106

Kassim, M.A., Meng, T.K., 2017. Carbon dioxide (CO2) biofixation by microalgae and its potential for biorefinery and biofuel production. Sci. Total Environ. 584–585, 1121–1129. https://doi.org/10.1016/j.scitotenv.2017.01.172

Kast, W., 1985. Principles of adsorption and adsorption processes. Chem. Eng. Process. Process Intensif. https://doi.org/10.1016/0255-2701(85)80013-1

Khalilpour, R., Mumford, K., Zhai, H., Abbas, A., Stevens, G., Rubin, E.S., 2015. Membrane-based carbon capture from flue gas: A review. J. Clean. Prod. 103, 286–300. https://doi.org/10.1016/j.jclepro.2014.10.050

Koytsoumpa, E.I., Bergins, C., Kakaras, E., 2018. The Journal of Supercritical Fluids The CO 2 economy : Review of CO 2 capture and reuse technologies 132, 3–16. https://doi.org/10.1016/j.supflu.2017.07.029

Krishna, R., Van Baten, J.M., 2012. A comparison of the CO2capture characteristics of zeolites and metal-organic frameworks. Sep. Purif. Technol. 87, 120–126. https://doi.org/10.1016/j.seppur.2011.11.031

Lee, S.Y., Park, S.J., 2015. A review on solid adsorbents for carbon dioxide capture. J. Ind. Eng. Chem. 23, 1–11. https://doi.org/10.1016/j.jiec.2014.09.001

Leung, D.Y.C.C., Caramanna, G., Maroto-Valer, M.M., 2014. An overview of current status of carbon dioxide capture and storage technologies. Renew. Sustain. Energy Rev. 39, 426–443. https://doi.org/10.1016/j.rser.2014.07.093

Li, D., Zhou, Y., Shen, Y., Sun, W., Fu, Q., Yan, H., Zhang, D., 2016. Experiment and simulation for separating CO2/N2by dual-reflux pressure swing adsorption process. Chem. Eng. J. 297, 315–324. https://doi.org/10.1016/j.cej.2016.03.075

Li, G., Xiao, P., Webley, P., Zhang, J., Singh, R., Marshall, M., 2008. Capture of CO2from high humidity flue gas by vacuum swing adsorption with zeolite 13X. Adsorption 14, 415–422. https://doi.org/10.1007/s10450-007-9100-y

Li, J.R., Ma, Y., McCarthy, M.C., Sculley, J., Yu, J., Jeong, H.K., Balbuena, P.B., Zhou, H.C., 2011. Carbon dioxide capture-related gas adsorption and separation in metal-organic frameworks. Coord. Chem. Rev. 255, 1791–1823. https://doi.org/10.1016/j.ccr.2011.02.012

Liémans, I., Alban, B., Tranier, J.P., Thomas, D., 2011. SOxand NOxabsorption based removal into acidic conditions for the flue gas treatment in oxy-fuel combustion. Energy Procedia 4, 2847–2854. https://doi.org/10.1016/j.egypro.2011.02.190

Linda Shi, C., Hurst, J.E., n.d. Binderless zeolitic adsorbents, methods for producing binderless zeolitic adsorbents, and processes for adsorptive separation of para-xylene from mixed xylenes using the binderless zeolitic adsorbents.

Ling, J., Ntiamoah, A., Xiao, P., Webley, P.A., Zhai, Y., 2015. Effects of feed gas concentration, temperature and process parameters on vacuum swing adsorption performance for CO2 capture. Chem. Eng. J. 265, 47–57. https://doi.org/10.1016/j.cej.2014.11.121

Ling, J., Ntiamoah, A., Xu, D., Webley, P.A., Zhai, Y., 2014. Overview of CO 2 Capture from Flue Gas Streams by Vacuum Pressure Swing Adsorption Technology. Austin J. Chem. Eng. 1, 1–7.

Liu, D., Yi, H., Tang, X., Zhao, S., Wang, Z., Gao, F., Li, Q., Zhao, B., 2016. Adsorption Separation of CO2 /CH4 Gas Mixture on Carbon Molecular Sieves Modified by Potassium Carbonate. J. Chem. Eng. Data 61, 2197–2201. https://doi.org/10.1021/acs.jced.5b00742

Liu, J., Liu, Y., Kayrak Talay, D., Calverley, E., Brayden, M., Martinez, M., 2015. A new carbon molecular sieve for propylene/propane separations. Carbon N. Y. 85, 201–211. https://doi.org/10.1016/j.carbon.2014.12.089

Liu, Z., Grande, C. a., Li, P., Yu, J., Rodrigues, A.E., 2011a. Multi-bed Vacuum Pressure Swing Adsorption for carbon dioxide capture from flue gas. Sep. Purif. Technol. 81, 307–317. https://doi.org/10.1016/j.seppur.2011.07.037

Liu, Z., Grande, C. a., Li, P., Yu, J., Rodrigues, A.E., 2011b. Adsorption and Desorption of Carbon Dioxide and Nitrogen on Zeolite 5A. Sep. Sci. Technol. 46, 434–451. https://doi.org/10.1080/01496395.2010.513360

Liu, Z., Wang, L., Kong, X., Li, P., Yu, J., Rodrigues, A.E., 2012. Onsite CO2 capture from flue gas by an adsorption process in a coal-fired power plant. Ind. Eng. Chem. Res. 51, 7355–7363. https://doi.org/10.1021/ie3005308

Lively, R.P., Chance, R.R., Koros, W.J., 2010. Enabling Low-Cost CO_2 Capture via Heat Integration. Ind. Eng. Chem. Res. 49, 7550–7562. https://doi.org/10.1021/ie100806g

Maring, B.J., Webley, P.A., 2013. A new simplified pressure/vacuum swing adsorption model for rapid adsorbent screening for CO2 capture applications. Int. J. Greenh. Gas Control 15, 16–31. https://doi.org/10.1016/j.ijggc.2013.01.009

Martin-Calvo, A., Parra, J.B., Ania, C.O., Calero, S., 2014. Insights on the anomalous adsorption of carbon dioxide in LTA zeolites. J. Phys. Chem. C 118, 25460–25467. https://doi.org/10.1021/jp507431c

May, E.F., Zhang, Y., Saleman, T.L.H., Xiao, G., Li, G. (Kevin), Young, B.R., 2017. Demonstration and optimisation of the four Dual-Reflux Pressure Swing Adsorption configurations. Sep. Purif. Technol. 177, 161–175. https://doi.org/10.1016/j.seppur.2016.12.007

Mendes, P.A.P., Ribeiro, A.M., Gleichmann, K., Ferreira, A.F.P., Rodrigues, A.E., 2017. Separation of CO 2 / N 2 on binderless 5A zeolite. J. CO2 Util. 20, 224–233. https://doi.org/10.1016/j.jcou.2017.05.003

Mendes, P.A.P., Ribeiro, A.M., Gleichmann, K., Ferreira, A.F.P., Rodrigues, A.E., 2017. Separation of CO2/N2 on binderless 5A zeolite. J. CO2 Util. 20, 224–233. https://doi.org/10.1016/j.jcou.2017.05.003

Merel, J., Clausse, M., Meunier, F., 2008. Experimental investigation on CO2 post-combustion capture by indirect thermal swing adsorption using 13X and 5A zeolites. Ind. Eng. Chem. Res. 47, 209–215. https://doi.org/10.1021/ie071012x

Metz, B., Davidson, O., Coninck, H. De, Loos, M., Meyer, L., 2005. Carbon dioxide capture and storage 266.

Mokhatab, S., Corso, S., 2016. Onsite nitrogen generation via PSA technology. Chem. Eng. (United States) 123.

Molsiv, U.O.P., 2015. Enhanced performance adsorbent for air pre-purification units APG-III can significantly reduce capital a costs and offers greater operational flex [WWW Document]. 2015. URL https://www.uop.com/wp-content/uploads/2015/08/uop-molsiv-apg-III-adsorbent-brochure.pdf

Montgomery, D., 2013. Rushing, Heath; Karl, Andrew; Wisnowski, James. Design and Analysis of Experiments by.

Müller, P., Russell, A., Tomas, J., 2015. Influence of binder and moisture content on the strength of zeolite 4A granules. Chem. Eng. Sci. 126, 204–215. https://doi.org/10.1016/j.ces.2014.12.031

Murata, K., Miyawaki, J., Kaneko, K., 2002. A simple determination method of the absolute adsorbed amount for high pressure gas adsorption. Carbon N. Y. 40, 425–428. https://doi.org/10.1016/S0008-6223(01)00126-9

Na, B.-K., Lee, H., Koo, K.-K., Song, H.K., 2002. Effect of Rinse and Recycle Methods on the Pressure Swing Adsorption Process To Recover CO 2 from Power Plant Flue Gas Using Activated Carbon. Ind. Eng. Chem. Res. 41, 5498–5503. https://doi.org/10.1021/ie0109509

Nabais, J.M.V., Carrott, P.J.M., Carrott, M.M.L.R., Padre-Eterno, A.M., Menéndez, J.A., Dominguez, A., Ortiz, A.L., 2006. New acrylic monolithic carbon molecular sieves for O2/N 2 and CO2/CH4 separations. Carbon N. Y. 44, 1158–1165. https://doi.org/10.1016/j.carbon.2005.11.005

Nakamura, T., Olaizola, M., Masutani, S., 2003. Recovery and Sequestration of CO2 from Stationary Combustion Systems by Photosynthesis of Microalgae. Pittsburgh,.

Nandy, A., Loha, C., Gu, S., Sarkar, P., Karmakar, M.K., Chatterjee, P.K., 2016. Present status and overview of Chemical Looping Combustion technology. Renew. Sustain. Energy Rev. 59, 597–619. https://doi.org/10.1016/j.rser.2016.01.003

Nazir, S.M., Bolland, O., Amini, S., 2017. Full Plant Scale Analysis of Natural Gas Fired Power Plants with Pre-Combustion CO 2 Capture and Chemical Looping Reforming. Energy Procedia 114, 2146–2155. https://doi.org/10.1016/j.egypro.2017.03.1350

Norwater - Nordic Road Water, 2014. Using CO2-gas to lower the pH of tunnelling waste water 16.

Ntiamoah, A., Ling, J., Xiao, P., Webley, P.A., Zhai, Y., 2016. CO 2 Capture by Temperature Swing Adsorption : Use of Hot CO 2 - Rich Gas for Regeneration. https://doi.org/10.1021/acs.iecr.5b01384

Pahinkar, D.G., 2016. Temperature swing adsorption processes for gas separation.

Parra, J.B., Sousa, J.C. De, Bansal, R.C., Pis, J.J., Pajares, J.A., 1995. Characterization of Activated Carbons by the BET Equation — An Alternative Approach. Adsorpt. Sci. Technol. 12, 51–66. https://doi.org/10.1177/026361749501200106

Pfahler, M., Branner, S., Refior, H., 2018. State and trends of Carbon Pricing 2018, World bank group. ECOFYS, Washintong DC. https://doi.org/10.1596/978-1-4648-1218-7

Plaza, M.G., García, S., Rubiera, F., Pis, J.J., Pevida, C., 2010. Post-combustion CO2capture with a commercial activated carbon: Comparison of different regeneration strategies. Chem. Eng. J. 163, 41–47. https://doi.org/10.1016/j.cej.2010.07.030

Poling, B., Prausnitz, J., Paul, O.J., Reid, R., 2001. The properties of gases and liquids, 5th ed. McGraw-Hill International, Boston.

Protasova, L., Snijkers, F., 2016. Recent developments in oxygen carrier materials for hydrogen production via chemical looping processes. Fuel 181, 75–93. https://doi.org/10.1016/j.fuel.2016.04.110

Quadrelli, R., Peterson, S., 2007. The energy-climate challenge: Recent trends in CO2emissions from fuel combustion. Energy Policy 35, 5938–5952. https://doi.org/10.1016/j.enpol.2007.07.001

Rashidi, N.A., Yusup, S., 2016. An overview of activated carbons utilization for the post-combustion carbon dioxide capture. J. CO2 Util. 13, 1–16. https://doi.org/10.1016/j.jcou.2015.11.002

Ravindran, B., Gupta, S.K., Cho, W.M., Kim, J.K., Lee, S.R., Jeong, K.H., Lee, D.J., Choi, H.C., 2016. Microalgae potential and multiple roles-current progress and future prospects-an overview. Sustain. 8, 1–16. https://doi.org/10.3390/su8121215

Riboldi, L., Bolland, O., 2017a. Overview on Pressure Swing Adsorption (PSA) as CO2Capture Technology: State-of-the-Art, Limits and Potentials. Energy Procedia 114, 2390–2400. https://doi.org/10.1016/j.egypro.2017.03.1385

Riboldi, L., Bolland, O., 2017b. Overview on Pressure Swing Adsorption (PSA) as CO2 Capture Technology: State-of-the-Art, Limits and Potentials. Energy Procedia 114, 2390–2400. https://doi.org/10.1016/j.egypro.2017.03.1385

Riboldi, L., Bolland, O., 2015. Evaluating Pressure Swing Adsorption as a CO2 separation technique in coal-fired power plants. Int. J. Greenh. Gas Control 39, 1–16. https://doi.org/10.1016/j.ijggc.2015.02.001

Ritter, J.A., Bhadra, S.J., Ebner, A.D., 2011. On the use of the dual-process langmuir model for correlating unary equilibria and predicting mixed-gas adsorption equilibria. Langmuir 27, 4700–4712. https://doi.org/10.1021/la104965w

Rouquerol, F., Rouquerol, J., Sing, K.S.W., Llewellyn, P., Maurin, G., 2014a. Adsorption by powders and porous solids, Climate Change 2013 - The Physical Science Basis. https://doi.org/10.1017/CBO9781107415324.004

Rouquerol, F., Rouquerol, J., Sing, K.S.W., Llewellyn, P., Maurin, G., Rouquerol, J., Llewellyn, P., Sing, K., 2014b. Adsorption by Powders and Porous Solids, Adsorption by Powders and Porous Solids. https://doi.org/10.1016/B978-0-08-097035-6.00012-7

Rouquerol, J., Llewellyn, P., Rouquerol, F., 2007. Is the BET equation applicable to microporous adsorbents. Stud. Surf. Sci. Catal. 160, 57–62. https://doi.org/10.1016/S0167-2991(07)80008-5

Ruthven, D.M., 2011. Molecular sieve separations. Chemie-Ingenieur-Technik 83, 44–52. https://doi.org/10.1002/cite.201000145

Ruthven, D.M., 2002. Pressure swing adsorption. Ind. Eng. Chem. Res.

Schroter, J., Carbon, P.S. a, 1993. Carbon molecular sieves for gas separation processes. Gas Sep. Purif. 7, 247–251.

Schumann, K., Unger, B., Brandt, A., Scheffler, F., 2012. Investigation on the pore structure of binderless zeolite 13× shapes. Microporous Mesoporous Mater. 154, 119–123. https://doi.org/10.1016/j.micromeso.2011.07.015

Sculley, J.P., Verdegaal, W.M., Lu, W., Wriedt, M., Zhou, H.C., 2013. High-throughput analytical model to evaluate materials for temperature swing adsorption processes. Adv. Mater. 25, 3957–3961. https://doi.org/10.1002/adma.201204695

Serracan, O., 2017. (Chemical Engineering Degree).

Seul-yi, Q., Park, S., 2014. Journal of Industrial and Engineering Chemistry A review on solid adsorbents for carbon dioxide capture. J. Ind. Eng. Chem. https://doi.org/10.1016/j.jiec.2014.09.001

Silva, J.A.C., Cunha, A.F., Schumann, K., Rodrigues, A.E., 2014. Binary adsorption of CO2/CH4 in binderless beads of 13X zeolite. Microporous Mesoporous Mater. 187, 100–107. https://doi.org/10.1016/j.micromeso.2013.12.017

Silva, J.A.C., Schumann, K., Rodrigues, A.E., 2012. Sorption and kinetics of CO2and CH4in binderless beads of 13X zeolite. Microporous Mesoporous Mater. 158, 219–228. https://doi.org/10.1016/j.micromeso.2012.03.042

Siriwardane, R. V., Shen, M.-S., Fisher, E.P., Poston, J.A., 2001. Adsorption of CO_2 on Molecular Sieves and Activated Carbon. Energy & Fuels 15, 279–284. https://doi.org/10.1021/ef000241s

Son, S.-J., Choi, J.-S., Choo, K.-Y., Song, S.-D., Vijayalakshmi, S., Kim, T.-H., 2005. Development of carbon dioxide adsorbents using carbon materials prepared from coconut shell. Korean J. Chem. Eng. 22, 291–297. https://doi.org/10.1007/BF02701500

Song, C., Kansha, Y., Fu, Q., Ishizuka, M., Tsutsumi, A., 2015. Reducing energy consumption of advanced PTSA CO2capture process-Experimental and numerical study. J. Taiwan Inst. Chem. Eng. 64, 69–78. https://doi.org/10.1016/j.jtice.2015.12.006

Song, C., Liu, Q., Ji, N., Deng, S., Zhao, J., Kitamura, Y., 2017a. Advanced cryogenic CO2capture process based on Stirling coolers by heat integration. Appl. Therm. Eng. 114, 887–895. https://doi.org/10.1016/j.applthermaleng.2016.12.049

Song, C., Liu, Q., Ji, N., Deng, S., Zhao, J., Li, Y., Kitamura, Y., 2017b. Reducing the energy consumption of membrane-cryogenic hybrid CO2capture by process optimization. Energy 124, 29–39. https://doi.org/10.1016/j.energy.2017.02.054

Song, C.F., Kitamura, Y., Li, S.H., 2012. Evaluation of Stirling cooler system for cryogenic CO2capture. Appl. Energy 98, 491–501. https://doi.org/10.1016/j.apenergy.2012.04.013

Songolzadeh, M., Ravanchi, M.T., Soleimani, M., 2012. Carbon Dioxide Capture and Storage : A General Review on Adsorbents. World Acad. Sci. Eng. Technol. 6, 213–220.

Songolzadeh, M., Soleimani, M., Ravanchi, M.T., Songolzadeh, R., 2014. Carbon Dioxide Separation From Flue Gases: A Technological, Review Emphasizing Reduction in Greenhouse Gas Emissions Film-Pore-[Concentration-Dependent] Surface Diffusion Model for Heavy Metal Ions Adsorption: Single and Multi-Component Systems View proje. Sci. World J. 2014, 1–34. https://doi.org/10.1155/2014/828131

Sreenivasulu, B., Sreedhar, I., Suresh, P., Raghavan, K.V., 2015. Development Trends in Porous Adsorbents for Carbon Capture. Environ. Sci. Technol. 49, 12641–12661. https://doi.org/10.1021/acs.est.5b03149

Su, F., Lu, C., 2012. CO2 capture from gas stream by zeolite 13X using a dual-column temperature/vacuum swing adsorption. Energy Environ. Sci. 5, 9021. https://doi.org/10.1039/c2ee22647b

Sumida, K., Rogow, D.L., Mason, J.A., Mcdonald, T.M., Bloch, E.D., Herm, Z.R., Bae, T., Long, R., 2012a. Carbon Dioxide Capture in Metal À Organic Frameworks 724–781. https://doi.org/10.1021/cr2003272

Sumida, K., Rogow, D.L., Mason, J.A., McDonald, T.M., Bloch, E.D., Herm, Z.R., Bae, T.H., Long, J.R., 2012b. Carbon dioxide capture in metal-organic frameworks. Chem. Rev. 112, 724–781. https://doi.org/10.1021/cr2003272

Tan, Y., Nookuea, W., Li, H., Thorin, E., Yan, J., 2016. Property impacts on Carbon Capture and Storage (CCS) processes : A review. Energy Convers. Manag. 118, 204–222. https://doi.org/10.1016/j.enconman.2016.03.079

Technologies, I., 2007. Selective Carbon Dioxide Adsorption From N2 - Ch4 -CO2 Mixture on Carbon Molecular Sieves 67.

Thambimuthu, K., Soltanieh, M., Abanades, J.C., Feron, P., Rubin, E., Wilkinson, M., 2005. Capture of CO 2. IPCC Spec. Rep. Carbon dioxide Capture Storage 107–171.

The global status of CCS 2015, 2015. https://doi.org/978-0-9944115-2-5

Tlili, N., Grévillot, G., Vallières, C., 2009. Carbon dioxide capture and recovery by means of TSA and/or VSA. Int. J. Greenh. Gas Control 3, 519–527. https://doi.org/10.1016/j.ijggc.2009.04.005

Torkkeli, A., 2014. CO2 Capture from Dry Flue Gas by Vacuum Swing Adsorption: A Pilot Plant Study. VTT Publ. 60, 3–194. https://doi.org/10.1002/aic

Tuinier, M.J., Hamers, H.P., Van Sint Annaland, M., 2011. Techno-economic evaluation of cryogenic CO2 capture-A comparison with absorption and membrane technology. Int. J. Greenh. Gas Control 5, 1559–1565. https://doi.org/10.1016/j.ijggc.2011.08.013

Tuinier, M.J., van Sint Annaland, M., Kramer, G.J., Kuipers, J.A.M., 2010. Cryogenic CO2capture using dynamically operated packed beds. Chem. Eng. Sci. 65, 114–119. https://doi.org/10.1016/j.ces.2009.01.055

UNFCCC. Conference of the Parties (COP), 2015. Paris Climate Change Conference-November 2015, COP 21. Adopt. Paris Agreement. Propos. by Pres. 21932, 32. https://doi.org/FCCC/CP/2015/L.9/Rev.1

Vaccarelli, M., Sammak, M., Jonshagen, K., Carapellucci, R., Genrup, M., 2016. Combined cycle power plants with post-combustion CO2capture: Energy analysis at part load conditions for different HRSG configurations. Energy 112, 917–925. https://doi.org/10.1016/j.energy.2016.06.115

Vaduva, M., Stanciu, V., 2007. Carbon molecular sieves production and performance assessment in carbon dioxide separation. J. Optoelectron. Adv. Mater. 9, 2296–2301.

Verma, S., Walker, P.L.J., 2015. Preparation of carbon molecular sieve by propilene pyrolisis over microporous carbons 33, 1761–1764.

Vu, D.Q., Koros, W.J., Miller, S.J., 2002. High Pressure CO2 /CH4 Separation Using Carbon Molecular Sieve Hollow Fiber Membranes. Ind. Eng. Chem. Res. 41, 367–380. https://doi.org/10.1021/ie010119w

Wang, L., Liu, Z., Li, P., Yu, J., Rodrigues, A.E., 2012. Experimental and modeling investigation on post-combustion carbon dioxide capture using zeolite 13X-APG by hybrid VTSA process. Chem. Eng. J. 197, 151–161. https://doi.org/10.1016/j.cej.2012.05.017

Wang, L., Yang, Y., Shen, W., Kong, X., Li, P., Yu, J., Rodrigues, A.E., 2013a. Experimental evaluation of adsorption technology for CO2capture from flue gas in an existing coal-fired power plant. Chem. Eng. Sci. 101, 615–619. https://doi.org/10.1016/j.ces.2013.07.028

Wang, L., Yang, Y., Shen, W., Kong, X., Li, P., Yu, J., Rodrigues, A.E., 2013b. CO2 capture from flue gas in an existing coal-fired power plant by pilot-scale two successive VPSA units. Ind. Eng. Chem. Res. 130514043648000. https://doi.org/10.1021/ie4009716

Wang, Y., LeVan, M.D., 2010. Adsorption Equilibrium of Binary Mixtures of Carbon Dioxide and Water Vapor on Zeolites 5A and 13X. J. Chem. Eng. Data 55, 3189–3195. https://doi.org/10.1021/je100053g

Webley, P.A., Qader, A., Ntiamoah, A., Ling, J., Xiao, P., 2017. A new multi-bed vacuum swing adsorption cycle for CO 2 capture from flue gas streams. Energy Procedia 114, 2467–2480. https://doi.org/10.1016/j.egypro.2017.03.1398

Xiao, P., Zhang, J., Webley, P., Li, G., Singh, R., Todd, R., 2008. Capture of CO2 from flue gas streams with zeolite 13X by vacuum-pressure swing adsorption. Adsorption 14, 575–582. https://doi.org/10.1007/s10450-008-9128-7

Xiaowei, L., Ruixue, C., Ling, L., Shufang, W., Wenming, Z., Kezhong, W., Wenyan, L., Mingxing W, 2016. A comparative evaluation of catalytic activities of carbon molecular sieve counter electrode toward different redox couples in dye-sensitized solar cells 200, 168–173. https://doi.org/10.1016/j.electacta.2016.03.173

Xinyan Technology, 2014. Zeolite Molecular Sieve Zeolite - Structure and Properties Zeolite Molecular Sieve [WWW Document]. URL http://www.molecularsieve.org/Zeolite_Molecular_Sieve.htm

Xu, X., Song, C., Miller, B.G., Scaroni, A.W., 2005. Adsorption separation of carbon dioxide from flue gas of natural gas-fired boiler by a novel nanoporous “molecular basket” adsorbent. Fuel Process. Technol. 86, 1457–1472. https://doi.org/10.1016/j.fuproc.2005.01.002

Yang, R.T., 2003. Adsorbents: fundamentals and applications, 1st ed, Chemical Engineering. Johon Wiley, New Jwrsey. https://doi.org/10.1002/047144409X

Yu, C.-H., 2012. A Review of CO2 Capture by Absorption and Adsorption. Aerosol Air Qual. Res. 745–769. https://doi.org/10.4209/aaqr.2012.05.0132

Yu, L., Gong, J., Zeng, C., Zhang, L., 2012. Synthesis of monodisperse zeolite A/chitosan hybrid microspheres and binderless zeolite A microspheres. Ind. Eng.

Chem. Res. 51, 2299–2308. https://doi.org/10.1021/ie202242e

Zenz, K., Harvey, C.F., Aziz, M.J., Daniel, P., 2009. The energy penalty of post-combustion CO2 capture & storage and its implications for retrofitting the U . S . installed base. https://doi.org/10.1039/b811608c

Zhang, J., Xiao, P., Li, G., Webley, P.A., 2009. Effect of flue gas impurities on CO2capture performance from flue gas at coal-fired power stations by vacuum swing adsorption. Energy Procedia 1, 1115–1122. https://doi.org/10.1016/j.egypro.2009.01.147

Zhang, Y., Saleman, T.L.H., Li, G. (Kevin), Xiao, G., Young, B.R., May, E.F., 2016. Non-isothermal numerical simulations of dual reflux pressure swing adsorption cycles for separating N2 + CH4. Chem. Eng. J. 292, 366–381. https://doi.org/10.1016/j.cej.2016.02.018

Zhang, Y.X., Chao, Q.C., Zheng, Q.H., Huang, L., 2017. The withdrawal of the U.S. from the Paris Agreement and its impact on global climate change governance. Adv. Clim. Chang. Res. 8, 213–219. https://doi.org/10.1016/j.accre.2017.08.005

Zhang, Z., Yao, Z.Z., Xiang, S., Chen, B., 2014. Perspective of microporous metal-organic frameworks for CO2 capture and separation. Energy Environ. Sci. 7, 2868–2899. https://doi.org/10.1039/c4ee00143e

Zhao, R., Zhao, L., Deng, S., Song, C., He, J., Shao, Y., Li, S., 2017. A comparative study on CO2capture performance of vacuum-pressure swing adsorption and pressure-temperature swing adsorption based on carbon pump cycle. Energy 137, 495–509. https://doi.org/10.1016/j.energy.2017.01.158

Zhao, Y., Liu, X., Han, Y., 2015. Microporous carbonaceous adsorbents for CO_2 separation via selective adsorption. RSC Adv. 5, 30310–30330. https://doi.org/10.1039/C5RA00569H

Zhou, W., Wang, J., Chen, P., Ji, C., Kang, Q., Lu, B., Li, K., Liu, J., Ruan, R., 2017. Bio-mitigation of carbon dioxide using microalgal systems: Advances and perspectives. Renew. Sustain. Energy Rev. 76, 1163–1175. https://doi.org/10.1016/j.rser.2017.03.065

Zhu, M., Chen, S., Ma, S., Xiang, W., 2017. Carbon formation on iron-based oxygen carriers during CH4reduction period in Chemical Looping Hydrogen Generation process. Chem. Eng. J. 325, 322–331. https://doi.org/10.1016/j.cej.2017.05.027

Zhu, M., Chen, S., Soomro, A., Hu, J., Sun, Z., Ma, S., Xiang, W., 2018. Effects of supports on reduction activity and carbon deposition of iron oxide for methane chemical looping hydrogen generation. Appl. Energy 225, 912–921. https://doi.org/10.1016/j.apenergy.2018.05.082

7. Appendix

7.1. Experimental data of adsorption isotherms of CO_2 and N_2 at 283 K, 298 K, 324 K and 345 K

7.1.1. CMS-I.

N_2					CO_2			
Temp.	Pres.	Absolute weight	Adsorbate weight	q	Pres.	Absolute weight	Adsorbate weight	q
K	Bar	g	g	mol/kg	Bar	g	g	mol/kg
284	0.00	1.193	0.00E+00	0.000	0.00	1.193	0.00E+00	0.000
	0.10	1.195	2.07E-03	0.062	0.10	1.240	4.73E-02	0.901
	0.31	1.198	5.51E-03	0.165	0.30	1.273	8.02E-02	1.529
	0.51	1.201	8.45E-03	0.253	0.50	1.292	9.92E-02	1.891
	0.71	1.204	1.10E-02	0.330	0.71	1.305	1.13E-01	2.148
	1.02	1.207	1.44E-02	0.432	1.01	1.320	1.27E-01	2.426
	1.24	1.210	1.72E-02	0.515	1.19	1.330	1.37E-01	2.609
	1.39	1.211	1.87E-02	0.560	1.40	1.336	1.43E-01	2.732
	1.65	1.214	2.09E-02	0.626	1.61	1.342	1.49E-01	2.841
	1.80	1.215	2.22E-02	0.664	1.82	1.347	1.54E-01	2.934
	2.00	1.217	2.38E-02	0.712	2.02	1.351	1.58E-01	3.012
	2.94	1.223	2.98E-02	0.893	3.05	1.365	1.73E-01	3.288
	5.05	1.232	3.95E-02	1.184	5.10	1.382	1.89E-01	3.605
	7.18	1.239	4.65E-02	1.393	7.10	1.391	1.99E-01	3.784
	10.03	1.246	5.33E-02	1.597	9.92	1.400	2.07E-01	3.944
299	0.00	1.185	0.00E+00	0.000	0.00	1.185	0.00E+00	0.000
	0.10	1.186	1.50E-03	0.045	0.10	1.219	3.40E-02	0.652
	0.31	1.189	3.99E-03	0.120	0.30	1.246	6.14E-02	1.177
	0.51	1.191	6.21E-03	0.187	0.51	1.263	7.83E-02	1.502
	0.71	1.193	8.22E-03	0.248	0.71	1.276	9.08E-02	1.741
	1.02	1.196	1.09E-02	0.330	1.01	1.290	1.05E-01	2.007
	1.24	1.198	1.31E-02	0.396	1.20	1.298	1.13E-01	2.166
	1.44	1.200	1.47E-02	0.444	1.40	1.305	1.20E-01	2.296
	1.59	1.201	1.59E-02	0.479	1.61	1.310	1.26E-01	2.408
	1.81	1.202	1.74E-02	0.523	1.80	1.315	1.31E-01	2.504
	2.01	1.204	1.87E-02	0.564	2.03	1.320	1.35E-01	2.596
	3.00	1.209	2.43E-02	0.731	3.04	1.336	1.51E-01	2.904
	5.03	1.218	3.28E-02	0.988	5.09	1.355	1.70E-01	3.266
	7.20	1.224	3.94E-02	1.187	7.09	1.366	1.81E-01	3.473
	10.04	1.231	4.59E-02	1.383	9.91	1.376	1.91E-01	3.657

N_2					CO_2			
Temp.	Pres.	Absolute weight	Adsorbate weight	q	Pres.	Absolute weight	Adsorbate weight	q
K	Bar	g	g	mol/kg	Bar	g	g	mol/kg
324	0.00	1.193	0.00E+00	0.000	0.00	1.192	0.00E+00	0.000
	0.10	1.193	9.18E-04	0.028	0.10	1.211	1.88E-02	0.358
	0.31	1.195	2.44E-03	0.073	0.31	1.231	3.82E-02	0.728
	0.51	1.196	3.84E-03	0.115	0.51	1.244	5.14E-02	0.979
	0.71	1.198	5.17E-03	0.155	0.71	1.254	6.16E-02	1.175
	1.01	1.199	6.96E-03	0.209	1.01	1.266	7.36E-02	1.403
	1.24	1.201	8.29E-03	0.248	1.20	1.274	8.12E-02	1.547
	1.44	1.202	9.45E-03	0.283	1.40	1.280	8.71E-02	1.661
	1.60	1.203	1.03E-02	0.309	1.61	1.285	9.28E-02	1.768
	1.80	1.204	1.14E-02	0.341	1.80	1.290	9.76E-02	1.859
	2.01	1.205	1.24E-02	0.371	2.00	1.295	1.02E-01	1.946
	3.01	1.209	1.68E-02	0.504	3.02	1.311	1.19E-01	2.268
	5.05	1.217	2.40E-02	0.718	5.10	1.333	1.40E-01	2.671
	7.20	1.222	2.97E-02	0.889	7.10	1.345	1.53E-01	2.909
	10.05	1.228	3.55E-02	1.064	9.93	1.357	1.64E-01	3.127
345	0.00	1.192	0.00E+00	0.000	0.00	1.192	0.00E+00	0.000
	0.10	1.193	7.12E-04	0.021	0.10	1.204	1.15E-02	0.220
	0.31	1.194	1.76E-03	0.053	0.31	1.218	2.57E-02	0.490
	0.51	1.195	2.81E-03	0.084	0.51	1.228	3.61E-02	0.687
	0.71	1.196	3.76E-03	0.113	0.71	1.237	4.44E-02	0.847
	1.02	1.198	5.11E-03	0.153	1.01	1.247	5.45E-02	1.040
	1.23	1.198	6.05E-03	0.181	1.20	1.254	6.11E-02	1.165
	1.42	1.199	6.84E-03	0.205	1.40	1.259	6.67E-02	1.271
	1.63	1.200	7.69E-03	0.230	1.61	1.264	7.18E-02	1.368
	1.81	1.201	8.40E-03	0.252	1.81	1.269	7.65E-02	1.457
	2.01	1.202	9.19E-03	0.275	2.01	1.273	8.05E-02	1.534
	3.03	1.205	1.28E-02	0.383	3.04	1.289	9.67E-02	1.844
	4.80	1.210	1.80E-02	0.540	5.10	1.310	1.18E-01	2.244
	7.06	1.216	2.33E-02	0.697	7.09	1.323	1.31E-01	2.493
	10.03	1.221	2.87E-02	0.858	9.92	1.336	1.43E-01	2.729

7.1.2. CMS-III.

N_2					CO_2			
Temp.	Pres.	Absolute weight	Adsorbate weight	q	Pres.	Absolute weight	Adsorbate weight	q
K	Bar	g	g	mol/kg	Bar	g	g	mol/kg
284	0.00	1.226	0.00E+00	0.000	0.00	1.226	0.00E+00	0.000
	0.10	1.228	1.79E-03	0.052	0.10	1.264	3.83E-02	0.710
	0.31	1.231	4.45E-03	0.130	0.30	1.293	6.68E-02	1.238
	0.51	1.233	6.89E-03	0.201	0.51	1.309	8.30E-02	1.539
	0.71	1.235	9.15E-03	0.267	0.71	1.321	9.47E-02	1.755
	1.01	1.238	1.21E-02	0.352	1.01	1.333	1.07E-01	1.988
	1.23	1.240	1.41E-02	0.410	1.20	1.341	1.15E-01	2.128
	1.45	1.242	1.58E-02	0.461	1.40	1.347	1.21E-01	2.237
	1.61	1.243	1.71E-02	0.498	1.61	1.352	1.26E-01	2.329
	1.80	1.245	1.85E-02	0.539	1.82	1.356	1.30E-01	2.411
	2.00	1.246	1.99E-02	0.579	2.01	1.360	1.34E-01	2.476
	3.01	1.252	2.54E-02	0.739	3.03	1.373	1.47E-01	2.724
	5.03	1.260	3.35E-02	0.975	5.10	1.388	1.62E-01	3.008
	7.19	1.266	3.96E-02	1.155	7.09	1.397	1.71E-01	3.168
	10.00	1.272	4.55E-02	1.325	9.91	1.405	1.79E-01	3.311

	N_2				CO_2			
Temp.	Pres.	Absolute weight	Adsorbate weight	q	Pres.	Absolute weight	Adsorbate weight	q
K	Bar	g	g	mol/kg	Bar	g	g	mol/kg
299	0.00	1.216	0.00E+00	0.000	0.00	1.216	0.00E+00	0.000
	0.10	1.217	1.17E-03	0.034	0.10	1.242	2.67E-02	0.499
	0.31	1.219	3.24E-03	0.095	0.30	1.266	5.08E-02	0.949
	0.51	1.221	5.12E-03	0.151	0.51	1.281	6.52E-02	1.219
	0.71	1.223	6.85E-03	0.201	0.71	1.292	7.59E-02	1.419
	1.02	1.225	9.16E-03	0.269	1.01	1.303	8.78E-02	1.641
	1.24	1.227	1.12E-02	0.329	1.20	1.311	9.50E-02	1.776
	1.45	1.228	1.26E-02	0.370	1.40	1.316	1.01E-01	1.883
	1.60	1.229	1.36E-02	0.400	1.61	1.321	1.06E-01	1.978
	1.80	1.231	1.48E-02	0.435	1.82	1.326	1.10E-01	2.063
	2.00	1.232	1.60E-02	0.469	1.98	1.329	1.13E-01	2.121
	2.99	1.236	2.07E-02	0.607	2.98	1.343	1.28E-01	2.389
	5.06	1.244	2.81E-02	0.824	5.09	1.361	1.45E-01	2.716
	7.19	1.249	3.36E-02	0.987	7.10	1.371	1.55E-01	2.899
	10.03	1.255	3.91E-02	1.150	9.91	1.379	1.64E-01	3.062
324	0.00	1.226	0.00E+00	0.000	0.00	1.226	0.00E+00	0.000
	0.10	1.227	7.96E-04	0.023	0.10	1.241	1.48E-02	0.274
	0.31	1.228	2.10E-03	0.061	0.31	1.257	3.13E-02	0.581
	0.51	1.229	3.40E-03	0.099	0.51	1.268	4.25E-02	0.788
	0.71	1.230	4.52E-03	0.132	0.71	1.277	5.12E-02	0.949
	1.02	1.232	6.10E-03	0.178	1.02	1.287	6.14E-02	1.139
	1.24	1.233	7.35E-03	0.214	1.21	1.294	6.79E-02	1.260
	1.40	1.234	8.11E-03	0.236	1.41	1.299	7.28E-02	1.350
	1.63	1.235	9.18E-03	0.268	1.61	1.303	7.75E-02	1.438
	1.81	1.236	9.99E-03	0.291	1.82	1.308	8.19E-02	1.518
	2.00	1.237	1.08E-02	0.315	2.03	1.312	8.59E-02	1.592
	2.91	1.240	1.42E-02	0.414	3.04	1.326	1.00E-01	1.863
	5.04	1.246	2.05E-02	0.598	5.10	1.345	1.19E-01	2.202
	7.21	1.251	2.54E-02	0.739	7.09	1.355	1.30E-01	2.404
	10.04	1.256	3.02E-02	0.881	9.93	1.366	1.40E-01	2.594
345	0.00	1.216	0.00E+00	0.000	0.00	1.216	0.00E+00	0.000
	0.10	1.216	5.73E-04	0.017	0.10	1.225	9.26E-03	0.173
	0.31	1.217	1.46E-03	0.043	0.31	1.237	2.10E-02	0.392
	0.51	1.218	2.30E-03	0.068	0.51	1.245	2.97E-02	0.556
	0.71	1.219	3.25E-03	0.095	0.71	1.252	3.68E-02	0.687
	1.02	1.220	4.39E-03	0.129	1.02	1.261	4.53E-02	0.847
	1.24	1.221	5.30E-03	0.156	1.21	1.266	5.09E-02	0.951
	1.44	1.222	6.00E-03	0.176	1.40	1.271	5.53E-02	1.035
	1.60	1.222	6.55E-03	0.193	1.61	1.275	5.99E-02	1.119
	1.81	1.223	7.23E-03	0.212	1.82	1.279	6.38E-02	1.193
	2.00	1.223	7.87E-03	0.231	2.04	1.283	6.76E-02	1.263
	3.01	1.226	1.08E-02	0.318	2.95	1.296	8.01E-02	1.497
	5.05	1.231	1.58E-02	0.464	5.11	1.315	9.92E-02	1.855
	7.06	1.235	1.97E-02	0.578	7.11	1.326	1.11E-01	2.066
	9.62	1.239	2.36E-02	0.693	9.92	1.337	1.21E-01	2.268

7.1.3. Zeolite 4ABL.

N_2					CO_2			
Temp.	Pres.	Absolute weight	Adsorbate weight	q	Pres.	Absolute weight	Adsorbate weight	q
K	Bar	g	g	mol/kg	Bar	g	g	mol/kg
284	0.00	1.105	0.00E+00	0.000	0.00	1.104	0.00E+00	0.000
	0.10	1.107	2.07E-03	0.067	0.12	1.294	1.90E-01	3.902
	0.31	1.110	5.82E-03	0.188	0.30	1.315	2.11E-01	4.334
	0.51	1.114	9.35E-03	0.302	0.51	1.327	2.22E-01	4.573
	0.71	1.117	1.27E-02	0.410	0.71	1.335	2.30E-01	4.737
	1.02	1.122	1.73E-02	0.560	1.02	1.343	2.39E-01	4.910
	1.24	1.126	2.13E-02	0.689	1.20	1.348	2.43E-01	5.008
	1.44	1.129	2.42E-02	0.783	1.40	1.352	2.47E-01	5.090
	1.59	1.131	2.62E-02	0.847	1.60	1.355	2.51E-01	5.159
	1.79	1.133	2.88E-02	0.930	1.82	1.358	2.54E-01	5.226
	2.00	1.136	3.13E-02	1.011	2.00	1.361	2.57E-01	5.279
	2.97	1.146	4.12E-02	1.332	3.03	1.371	2.67E-01	5.486
	5.04	1.161	5.61E-02	1.814	5.07	1.384	2.80E-01	5.752
	7.18	1.171	6.66E-02	2.153	7.07	1.392	2.88E-01	5.923
	10.02	1.181	7.60E-02	2.458	9.89	1.400	2.96E-01	6.087
299	0.00	1.171	0.00E+00	0.000	0.00	1.170	0.00E+00	0.000
	0.10	1.172	1.49E-03	0.086	0.12	1.347	1.77E-01	3.614
	0.31	1.175	4.00E-03	0.172	0.30	1.366	1.96E-01	3.976
	0.51	1.177	6.32E-03	0.253	0.51	1.377	2.07E-01	4.194
	0.71	1.179	8.65E-03	0.324	0.71	1.385	2.14E-01	4.344
	1.02	1.183	1.19E-02	0.424	1.01	1.393	2.23E-01	4.503
	1.24	1.185	1.42E-02	0.494	1.20	1.398	2.27E-01	4.597
	1.44	1.187	1.64E-02	0.560	1.41	1.402	2.31E-01	4.672
	1.60	1.189	1.80E-02	0.609	1.60	1.405	2.35E-01	4.736
	1.80	1.191	1.99E-02	0.668	1.82	1.408	2.38E-01	4.795
	2.01	1.193	2.19E-02	0.727	2.01	1.411	2.40E-01	4.844
	3.00	1.201	3.01E-02	0.979	3.07	1.421	2.50E-01	5.037
	5.06	1.214	4.34E-02	1.384	5.09	1.433	2.62E-01	5.273
	7.19	1.224	5.33E-02	1.686	7.08	1.441	2.70E-01	5.425
	10.04	1.234	6.29E-02	1.980	9.90	1.448	2.78E-01	5.574
324	0.00	1.105	0.00E+00	0.000	0.00	1.104	0.00E+00	0.000
	0.10	1.105	8.42E-04	0.027	0.10	1.256	1.51E-01	3.112
	0.31	1.107	2.31E-03	0.075	0.30	1.278	1.73E-01	3.566
	0.51	1.108	3.73E-03	0.121	0.51	1.289	1.84E-01	3.792
	0.71	1.110	5.12E-03	0.166	0.71	1.296	1.92E-01	3.947
	1.02	1.112	7.19E-03	0.232	1.02	1.304	2.00E-01	4.113
	1.24	1.114	8.95E-03	0.290	1.20	1.309	2.05E-01	4.213
	1.44	1.115	1.03E-02	0.333	1.40	1.313	2.08E-01	4.290
	1.60	1.116	1.13E-02	0.365	1.61	1.316	2.12E-01	4.360
	1.80	1.117	1.26E-02	0.407	1.82	1.319	2.15E-01	4.424
	2.01	1.118	1.38E-02	0.447	2.02	1.322	2.18E-01	4.480
	3.00	1.124	1.95E-02	0.630	3.04	1.332	2.27E-01	4.681
	5.05	1.134	2.95E-02	0.955	5.08	1.344	2.40E-01	4.929
	7.20	1.142	3.79E-02	1.226	7.08	1.352	2.47E-01	5.085
	10.02	1.151	4.65E-02	1.502	9.89	1.359	2.54E-01	5.235

N_2					CO_2			
Temp.	Pres.	Absolute weight	Adsorbate weight	q	Pres.	Absolute weight	Adsorbate weight	q
K	Bar	g	g	mol/kg	Bar	g	g	mol/kg
345	0.00	1.105	0.00E+00	0.000	0.00	1.105	0.00E+00	0.000
	0.10	1.106	6.63E-04	0.021	0.12	1.237	1.32E-01	2.719
	0.31	1.107	1.73E-03	0.056	0.30	1.259	1.54E-01	3.171
	0.51	1.108	2.71E-03	0.088	0.51	1.272	1.67E-01	3.433
	0.71	1.109	3.68E-03	0.119	0.71	1.280	1.75E-01	3.600
	1.02	1.110	5.08E-03	0.164	1.01	1.288	1.83E-01	3.772
	1.23	1.111	6.05E-03	0.195	1.21	1.293	1.88E-01	3.877
	1.44	1.112	7.02E-03	0.227	1.40	1.297	1.92E-01	3.956
	1.61	1.113	7.78E-03	0.251	1.61	1.301	1.96E-01	4.029
	1.80	1.114	8.71E-03	0.281	1.82	1.304	1.99E-01	4.094
	2.00	1.114	9.57E-03	0.309	2.03	1.306	2.02E-01	4.151
	3.03	1.119	1.40E-02	0.452	3.03	1.316	2.11E-01	4.350
	5.05	1.126	2.16E-02	0.698	5.11	1.328	2.24E-01	4.600
	7.19	1.133	2.83E-02	0.915	7.11	1.336	2.31E-01	4.755
	10.04	1.141	3.56E-02	1.152	9.94	1.343	2.38E-01	4.904

7.1.4. Zeolite 5ABL.

N_2					CO_2			
Temp.	Pres.	Absolute weight	Adsorbate weight	q	Pres.	Absolute weight	Adsorbate weight	q
K	Bar	g	g	mol/kg	Bar	g	g	mol/kg
284	0.00	1.244	0.00E+00	0.000	0.00	1.244	0.00E+00	0.000
	0.10	1.248	4.16E-03	0.119	0.10	1.479	2.35E-01	4.286
	0.31	1.254	1.00E-02	0.288	0.30	1.507	2.63E-01	4.809
	0.51	1.259	1.49E-02	0.428	0.51	1.516	2.72E-01	4.979
	0.71	1.263	1.91E-02	0.549	0.71	1.522	2.78E-01	5.080
	1.02	1.269	2.46E-02	0.707	1.02	1.528	2.84E-01	5.183
	1.24	1.272	2.82E-02	0.810	1.20	1.531	2.87E-01	5.243
	1.45	1.275	3.15E-02	0.905	1.40	1.533	2.89E-01	5.289
	1.61	1.278	3.38E-02	0.970	1.60	1.536	2.92E-01	5.328
	1.80	1.280	3.64E-02	1.046	1.81	1.537	2.94E-01	5.363
	2.01	1.283	3.91E-02	1.123	2.03	1.539	2.95E-01	5.397
	3.11	1.293	4.91E-02	1.411	3.04	1.546	3.02E-01	5.512
	5.03	1.309	6.51E-02	1.869	5.09	1.554	3.10E-01	5.663
	7.19	1.321	7.66E-02	2.198	7.10	1.559	3.15E-01	5.762
	10.02	1.331	8.75E-02	2.512	9.92	1.565	3.21E-01	5.863

N_2					CO_2			
Temp.	Pres.	Absolute weight	Adsorbate weight	q	Pres.	Absolute weight	Adsorbate weight	q
K	Bar	g	g	mol/kg	Bar	g	g	mol/kg
299	0.00	1.245	0.00E+00	0.000	0.00	1.244	0.00E+00	0.000
	0.10	1.248	2.48E-03	0.071	0.10	1.455	2.11E-01	3.850
	0.31	1.252	6.50E-03	0.187	0.30	1.492	2.48E-01	4.523
	0.51	1.255	1.00E-02	0.287	0.51	1.503	2.59E-01	4.732
	0.71	1.258	1.31E-02	0.377	0.71	1.510	2.65E-01	4.850
	1.02	1.262	1.74E-02	0.498	1.02	1.516	2.72E-01	4.966
	1.24	1.266	2.08E-02	0.598	1.20	1.520	2.75E-01	5.031
	1.44	1.268	2.34E-02	0.671	1.40	1.522	2.78E-01	5.080
	1.60	1.270	2.52E-02	0.722	1.61	1.525	2.80E-01	5.124
	1.79	1.272	2.74E-02	0.786	1.81	1.527	2.83E-01	5.161
	2.01	1.275	2.96E-02	0.849	2.00	1.528	2.84E-01	5.193
	2.99	1.284	3.85E-02	1.104	3.04	1.535	2.91E-01	5.317
	5.04	1.297	5.23E-02	1.501	5.10	1.543	2.99E-01	5.469
	7.19	1.308	6.29E-02	1.805	7.11	1.549	3.05E-01	5.564
	10.02	1.318	7.33E-02	2.104	9.64	1.553	3.09E-01	5.650
324	0.00	1.244	0.00E+00	0.000	0.00	1.244	0.00E+00	0.000
	0.10	1.246	1.55E-03	0.044	0.12	1.413	1.69E-01	3.079
	0.31	1.248	3.88E-03	0.111	0.29	1.455	2.11E-01	3.852
	0.51	1.250	6.02E-03	0.173	0.50	1.474	2.30E-01	4.205
	0.71	1.252	7.99E-03	0.229	0.71	1.485	2.41E-01	4.395
	1.01	1.255	1.07E-02	0.308	1.01	1.494	2.50E-01	4.561
	1.24	1.257	1.27E-02	0.363	1.21	1.499	2.55E-01	4.653
	1.44	1.258	1.44E-02	0.413	1.40	1.502	2.58E-01	4.714
	1.65	1.260	1.61E-02	0.463	1.61	1.505	2.61E-01	4.771
	1.80	1.261	1.73E-02	0.496	1.81	1.508	2.64E-01	4.820
	2.00	1.263	1.88E-02	0.539	2.02	1.510	2.66E-01	4.863
	3.00	1.269	2.55E-02	0.732	3.02	1.518	2.74E-01	5.006
	5.05	1.281	3.68E-02	1.057	5.10	1.528	2.83E-01	5.177
	7.19	1.290	4.58E-02	1.316	7.11	1.533	2.89E-01	5.277
	10.03	1.299	5.52E-02	1.584	9.92	1.538	2.94E-01	5.370
345	0.00	1.236	0.00E+00	0.000	0.00	1.221	0.00E+00	0.000
	0.10	1.237	1.05E-03	0.030	0.12	1.344	1.23E-01	2.289
	0.31	1.239	2.57E-03	0.074	0.29	1.388	1.66E-01	3.096
	0.51	1.240	4.04E-03	0.117	0.50	1.416	1.95E-01	3.632
	0.71	1.242	5.40E-03	0.156	0.70	1.433	2.12E-01	3.941
	0.99	1.243	7.17E-03	0.207	1.01	1.447	2.26E-01	4.203
	1.24	1.245	8.60E-03	0.248	1.21	1.455	2.34E-01	4.350
	1.44	1.246	9.77E-03	0.282	1.40	1.460	2.39E-01	4.441
	1.61	1.247	1.08E-02	0.311	1.60	1.464	2.43E-01	4.522
	1.81	1.248	1.19E-02	0.344	1.82	1.468	2.47E-01	4.592
	2.01	1.249	1.32E-02	0.380	2.02	1.471	2.50E-01	4.647
	3.02	1.255	1.85E-02	0.534	2.90	1.480	2.59E-01	4.811
	5.04	1.264	2.75E-02	0.794	5.08	1.492	2.70E-01	5.030
	7.20	1.272	3.56E-02	1.028	7.07	1.498	2.77E-01	5.146
	10.02	1.280	4.38E-02	1.265	9.89	1.503	2.82E-01	5.252

7.1.5. Zeolite 13XBL

N_2					CO_2			
Temp.	Pres.	Absolute weight	Adsorbate weight	q	Pres.	Absolute weight	Adsorbate weight	q
K	Bar	g	g	mol/kg	Bar	g	g	mol/kg
284	0.00	1.279	0.00E+00	0.000	0.00	1.279	0.00E+00	0.000
	0.10	1.282	2.51E-03	0.070	0.10	1.524	2.45E-01	4.351
	0.31	1.286	7.07E-03	0.197	0.35	1.585	3.06E-01	5.434
	0.51	1.291	1.13E-02	0.315	0.50	1.596	3.17E-01	5.631
	0.71	1.294	1.52E-02	0.425	0.71	1.607	3.28E-01	5.835
	1.02	1.300	2.07E-02	0.579	1.02	1.619	3.40E-01	6.034
	1.23	1.305	2.57E-02	0.718	1.20	1.625	3.46E-01	6.146
	1.45	1.308	2.92E-02	0.814	1.40	1.630	3.51E-01	6.232
	1.60	1.311	3.14E-02	0.878	1.61	1.634	3.55E-01	6.307
	1.80	1.314	3.44E-02	0.961	1.82	1.638	3.59E-01	6.372
	2.01	1.317	3.73E-02	1.041	2.02	1.641	3.62E-01	6.427
	2.97	1.328	4.90E-02	1.367	3.05	1.651	3.72E-01	6.618
	5.04	1.347	6.75E-02	1.883	5.09	1.664	3.85E-01	6.849
	7.18	1.360	8.11E-02	2.263	7.10	1.672	3.93E-01	6.989
	10.02	1.373	9.40E-02	2.625	9.91	1.679	4.00E-01	7.116
299	0.00	1.279	0.00E+00	0.000	0.00	1.279	0.00E+00	0.000
	0.10	1.281	1.78E-03	0.050	0.11	1.498	2.19E-01	3.892
	0.31	1.284	4.93E-03	0.138	0.29	1.546	2.67E-01	4.743
	0.51	1.287	7.91E-03	0.221	0.50	1.569	2.90E-01	5.146
	0.71	1.290	1.08E-02	0.300	0.71	1.582	3.03E-01	5.379
	1.02	1.294	1.48E-02	0.412	1.01	1.594	3.15E-01	5.601
	1.24	1.298	1.86E-02	0.518	1.21	1.602	3.23E-01	5.732
	1.44	1.300	2.11E-02	0.589	1.41	1.607	3.28E-01	5.826
	1.59	1.302	2.29E-02	0.640	1.60	1.611	3.32E-01	5.902
	1.80	1.305	2.53E-02	0.707	1.81	1.615	3.36E-01	5.976
	2.01	1.307	2.76E-02	0.770	2.02	1.619	3.40E-01	6.039
	2.98	1.317	3.73E-02	1.041	3.03	1.631	3.52E-01	6.246
	5.03	1.332	5.32E-02	1.485	5.11	1.645	3.66E-01	6.505
	7.19	1.345	6.58E-02	1.837	7.09	1.654	3.75E-01	6.657
	10.00	1.357	7.82E-02	2.183	9.91	1.662	3.83E-01	6.798
324	0.00	1.279	0.00E+00	0.000	0.00	1.279	0.00E+00	0.000
	0.10	1.280	9.61E-04	0.027	0.13	1.456	1.77E-01	3.143
	0.31	1.282	2.80E-03	0.078	0.30	1.496	2.17E-01	3.850
	0.51	1.284	4.57E-03	0.128	0.50	1.521	2.42E-01	4.298
	0.71	1.285	6.29E-03	0.176	0.71	1.537	2.58E-01	4.588
	1.02	1.288	8.79E-03	0.245	1.01	1.553	2.74E-01	4.864
	1.24	1.290	1.12E-02	0.314	1.20	1.562	2.83E-01	5.025
	1.45	1.292	1.29E-02	0.360	1.40	1.568	2.89E-01	5.139
	1.59	1.293	1.40E-02	0.392	1.61	1.574	2.95E-01	5.239
	1.80	1.295	1.56E-02	0.436	1.80	1.578	3.00E-01	5.323
	2.01	1.296	1.71E-02	0.478	2.00	1.583	3.04E-01	5.400
	3.00	1.303	2.40E-02	0.669	3.02	1.597	3.19E-01	5.660
	5.04	1.315	3.60E-02	1.006	5.09	1.615	3.36E-01	5.964
	7.20	1.325	4.64E-02	1.296	7.09	1.625	3.46E-01	6.143
	10.02	1.336	5.72E-02	1.597	9.92	1.634	3.55E-01	6.309

N_2					CO_2			
Temp.	Pres.	Absolute weight	Adsorbate weight	q	Pres.	Absolute weight	Adsorbate weight	q
K	Bar	g	g	mol/kg	Bar	g	g	mol/kg
345	0.00	1.273	0.00E+00	0.000	0.00	1.279	0.00E+00	0.000
	0.10	1.274	7.71E-04	0.022	0.10	1.413	1.34E-01	2.388
	0.31	1.276	2.02E-03	0.057	0.30	1.457	1.78E-01	3.165
	0.51	1.277	3.23E-03	0.091	0.50	1.483	2.04E-01	3.620
	0.71	1.278	4.42E-03	0.124	0.71	1.500	2.21E-01	3.931
	1.02	1.280	6.22E-03	0.174	1.01	1.518	2.39E-01	4.242
	1.24	1.281	7.45E-03	0.209	1.21	1.528	2.49E-01	4.431
	1.44	1.282	8.64E-03	0.242	1.40	1.536	2.57E-01	4.563
	1.61	1.283	9.59E-03	0.269	1.60	1.542	2.63E-01	4.681
	1.80	1.284	1.06E-02	0.298	1.82	1.549	2.70E-01	4.792
	2.01	1.285	1.17E-02	0.329	2.01	1.553	2.75E-01	4.878
	3.01	1.291	1.70E-02	0.477	3.06	1.571	2.92E-01	5.191
	5.04	1.300	2.64E-02	0.740	5.10	1.591	3.12E-01	5.539
	7.20	1.308	3.49E-02	0.978	7.10	1.602	3.23E-01	5.745
	10.03	1.318	4.41E-02	1.237	9.89	1.613	3.34E-01	5.933

7.2. Results of fixed-bed experiments

7.2.1. Relation of the statistical variables with process variables.

Statistical variable	Process variable	Description
A	Q_F	Feed flowrates
B	Q_R	Rinse flowrates
C	Q_V	Vacuum flowrates
D	P_V	Vacuum pressure
E	S_{RN}	Rinse breack point
F	S_{FD}	Feed breack point
G	S_{PR}	Purge breack point

7.2.2. VPSA fixed-bed results for Zeolite 5ABL

Exp.	CO_2 rec. %	CO_2 Pur. %	Prod. $g_{CO2}/(g_{ads} \cdot min)$	Energy C. kWh/kg_{CO2}
1	43.0	83.0	0.14	3.7
2	48.0	87.0	0.17	3.6
3	39.0	79.0	0.13	3.5
4	48.0	67.0	0.10	8.7
5	47.0	84.0	0.14	3.5
6	41.0	67.0	0.09	7.0
7	50.0	87.0	0.15	3.4
8	53.0	93.0	0.15	3.1
9	72.0	85.0	0.19	3.9
10	74.0	98.0	0.24	2.7
11	73.0	97.0	0.22	2.6
12	70.0	96.0	0.24	2.7
13	81.0	98.0	0.26	1.4
14	69.0	96.0	0.24	1.7
15	69.0	94.0	0.16	4.0
16	72.0	94.0	0.19	3.9

7.2.3. VPSA fixed-bed results for Zeolite 13XBL

Exp.	CO_2 rec. %	CO_2 Pur. %	Prod. $g_{CO2}/(g_{ads} \cdot min)$	Energy C. kWh/kg_{CO2}
1	43.7	95.5	0.14	2.0
2	60.9	96.0	0.25	7.3
3	53.6	93.8	0.12	1.8
4	38.7	63.7	0.17	8.1
5	68.7	93.8	0.18	2.4
6	39.1	93.3	0.15	2.8
7	53.6	93.7	0.22	5.6
8	35.1	67.8	0.06	4.2
9	88.5	96.9	0.35	3.2
10	58.5	98.0	0.07	0.4
11	77.8	99.5	0.29	1.9
12	87.4	97.7	0.28	3.9
13	61.5	98.4	0.23	1.2
14	75.5	99.3	0.08	0.5
15	63.3	98.4	0.24	1.8
16	86.6	83.8	0.31	2.5

7.3. Results of fixed-bed simulation experiments

Exp	Qfd	Qrn	sRN	sFD	sPR	PT	Purity	Recovery	Productivity
1	-1	-1	-1	-1	-1	-1	96.3%	81.9%	0.16
2	1	-1	-1	-1	-1	1	94.5%	77.1%	0.28
3	-1	1	-1	-1	-1	1	93.1%	74.5%	0.24
4	1	1	-1	-1	-1	-1	94.9%	79.8%	0.26
5	-1	-1	1	-1	-1	1	94.9%	77.0%	0.18
6	1	-1	1	-1	-1	-1	96.7%	83.9%	0.24
7	-1	1	1	-1	-1	-1	95.1%	78.3%	0.18
8	1	1	1	-1	-1	1	93.8%	75.6%	0.36
9	-1	-1	-1	1	-1	1	94.3%	75.6%	0.19
10	1	-1	-1	1	-1	-1	95.9%	75.7%	0.27
11	-1	1	-1	1	-1	-1	94.5%	72.2%	0.24
12	1	1	-1	1	-1	1	93.1%	73.9%	0.33
13	-1	-1	1	1	-1	-1	96.0%	75.4%	0.18
14	1	-1	1	1	-1	1	94.9%	76.3%	0.27
15	-1	1	1	1	-1	1	93.6%	74.1%	0.22
16	1	1	1	1	-1	-1	94.9%	73.3%	0.32
17	-1	-1	-1	-1	1	1	94.4%	78.4%	0.18
18	1	-1	-1	-1	1	-1	96.6%	90.7%	0.15
19	-1	1	-1	-1	1	-1	94.8%	80.9%	0.17
20	1	1	-1	-1	1	1	93.2%	80.0%	0.31
21	-1	-1	1	-1	1	-1	96.7%	85.3%	0.11
22	1	-1	1	-1	1	1	95.0%	78.6%	0.26
23	-1	1	1	-1	1	1	93.8%	75.5%	0.23
24	1	1	1	-1	1	-1	95.3%	87.0%	0.20
25	-1	-1	-1	1	1	-1	95.8%	75.4%	0.19
26	1	-1	-1	1	1	1	94.4%	76.5%	0.26
27	-1	1	-1	1	1	1	93.2%	77.9%	0.23
28	1	1	-1	1	1	-1	94.4%	73.8%	0.28
29	-1	-1	1	1	1	1	94.7%	76.2%	0.20
30	1	-1	1	1	1	-1	96.3%	77.1%	0.26
31	-1	1	1	1	1	-1	95.0%	73.7%	0.22
32	1	1	1	1	1	1	93.6%	75.1%	0.32

Exp	Qfd	Qrn	sRN	sFD	sPR	PT	Purity	Recovery	Productivity
33	1	-1	-1	-1	-1	-1	96.4%	83.8%	0.23
34	-1	1	-1	-1	-1	-1	94.7%	77.9%	0.22
35	-1	-1	1	-1	-1	-1	96.5%	81.9%	0.16
36	1	1	1	-1	-1	-1	95.3%	81.0%	0.26
37	-1	-1	-1	1	-1	-1	95.7%	74.5%	0.21
38	1	1	-1	1	-1	-1	94.5%	73.0%	0.31
39	1	-1	1	1	-1	-1	96.2%	76.1%	0.27
40	-1	1	1	1	-1	-1	95.1%	73.2%	0.22
41	-1	-1	-1	-1	1	-1	96.4%	84.8%	0.14
42	1	1	-1	-1	1	-1	95.0%	86.2%	0.21
43	1	-1	1	-1	1	-1	96.8%	91.2%	0.11
44	-1	1	1	-1	1	-1	95.3%	81.4%	0.17
45	1	-1	-1	1	1	-1	95.9%	76.5%	0.28
46	-1	1	-1	1	1	-1	94.6%	73.0%	0.23
47	-1	-1	1	1	1	-1	96.1%	75.7%	0.18
48	1	1	1	1	1	-1	94.9%	74.1%	0.30
49	-1	-1	-1	-1	-1	1	94.4%	76.5%	0.18
50	1	1	-1	-1	-1	1	93.3%	75.0%	0.30
51	1	-1	1	-1	-1	1	94.9%	77.5%	0.25
52	-1	1	1	-1	-1	1	93.8%	75.2%	0.24
53	1	-1	-1	1	-1	1	94.4%	76.0%	0.28
54	-1	1	-1	1	-1	1	93.2%	73.8%	0.23
55	-1	-1	1	1	-1	1	94.7%	76.0%	0.20
56	1	1	1	1	-1	1	93.5%	74.4%	0.33
57	1	-1	-1	-1	1	1	94.6%	78.0%	0.22
58	-1	1	-1	-1	1	1	93.1%	74.8%	0.21
59	-1	-1	1	-1	1	1	94.9%	77.3%	0.19
60	1	1	1	-1	1	1	93.7%	76.4%	0.31
61	-1	-1	-1	1	1	1	94.3%	76.0%	0.19
62	1	1	-1	1	1	1	93.1%	74.4%	0.33
63	1	-1	1	1	1	1	94.9%	76.9%	0.29
64	-1	1	1	1	1	1	93.6%	74.5%	0.22

Aquesta Tesi Doctoral ha estat defensada el dia ____ d_____ de 201__

al Centre_____

de la Universitat Ramon Llull, davant el Tribunal format pels Doctors i Doctores sotasignants, havent obtingut la qualificació:

President/a

_____

Vocal

_____

Vocal *

_____

Vocal *

_____

Secretari/ària

_____

Doctorand/a

(*): Només en el cas de tenir un tribunal de 5 membres